THE UNIVERSITY OF ASTON IN BIRMINGHAM

ELASTIC AND INELASTIC SCATTERING OF FAST NEUTRONS IN FUSION REACTOR MATERIALS

Thesis For Degree of Ph.D.
by

MAHDI HADI JASIM

OCTOBER 1985

SUMMARY

In this work , the angular distributions for elastic and inelastic scattering of fast neutrons in fusion reactor materials have been studied . Lithium and Lead material are likely to be common components of fusion reactor wall configuration design . The measurements were performed using an associated particle time-of-flight technique . The 14 and 14.44 Mev neutrons were produced by the T(d,n) ^{4}He reaction with deuterons being accelerated in a 150 kev SAMES type J accelerator at ASTON and in the 3 Mev DYNAMITRON at the Joint Radiation Centre , Birmingham , respectively . The associated alpha-particles and fast neutrons were detected by means of a plastic scintillator mounted on a fast focused photomultiplier tube . The samples used were extended flat plates of thicknesses up to 0.9 mean-free-path for Lithium and 1.562 mean-free-path for Lead .

The differential elastic scattering cross-sections were measured for 14 Mev neutrons for various thicknesses of Lithium and Lead in the angular range from zero to 90° . In addition , the angular distributions of elastically scattered 14.44 Mev neutrons from Lithium samples were studied in the same angular range .

Inelastic scattering to the 4.63 Mev state in ^{7}Li and the 2.6 Mev state , and 4.1 Mev state , in ^{208}Pb have been measured . The results are compared to ENDF/B-IV data files and to previous measurements .

For the Lead samples the differential neutron scattering cross-sections for discrete 3 Mev ranges and the angular distributions were measured . The increase in effective cross-section due to multiple scattering effects , as the sample thickness increased was found to be predicted by the empirical relation $\sigma = \sigma_0 \exp(\alpha x)$. A good fit to the experimental data was obtained using the universal constant " α_{uni} ".

The differential elastic scattering cross-section data for thin samples of Lithium and Lead were analyzed in terms of optical model calculations using the computer code RAROMP . Parameter search procedures produced good fits to the cross-sections .

For the case of thick samples of Lithium and Lead , the measured angular distributions of the scattered neutrons were compared to the predictions of the continuous slowing down model .

Key Words : Fusion material / Fast neutrons / Cross-sections / Elastic scattering / Inelastic scattering .

ACKNOWLEDGEMENTS

I would like to express my great appreciation to my supervisor , Dr. A. J. COX for his continued guidance , encouragement and invaluable help shown throughout this research project . I also wish to thank Dr. N. P. COOPER of the Nuclear Physics group for many helpful discussions during this work .

Thanks are also due to Mr. J. PHULL and the members of the Physics Workshop for their assistance with the experimental work .

The Birmingham Radiation Centre staff are thanked for their assistance .

I also wish to thank the MINISTRY OF HIGHER EDUCATION AND SCIENTIFIC RESEARCH OF IRAQ for providing me with leave of study throughout the period of this work .

Finally , a special thanks given to my parents , brothers and sisters for their many years of encouragement and support .

MAHDI HADI JASIM

UNIVERSITY OF ASTON IN BIRMINGHAM

1985

LIST OF CONTENTS

LIST OF TABLES

LIST OF FIGURES

CHAPTER ONE

GENERAL INTRODUCTION

CHAPTER ONE

GENERAL INTRODUCTION

1.1 FUSION REACTIONS

The most accessible reactions involving the combination of two light nuclei , like hydrogen isotopes , which are accompanied by the release of energy in thermonuclear power , are :

$$^{2}_{1}D + {}^{2}_{1}D \longrightarrow {}^{3}_{2}He + n + 3.27 \text{ Mev} \quad (1.1)$$

$$\longrightarrow {}^{3}_{1}T + {}^{1}_{1}H + 4.\emptyset3 \text{ Mev} \quad (1.2)$$

$$^{2}_{1}D + {}^{3}_{1}T \longrightarrow {}^{4}_{2}He + n + 17.6 \text{ Mev} \quad (1.3)$$

As shown in fig(1.1) D-T reaction has a much larger cross-section and produces more energy than the D-D reaction with the same incident deuteron energy .

For a power system the D-T reaction would have to be supplemented by the tritium breeding reactions in a blanket surrounding the reaction chamber ;

$$n + {}^{6}_{3}Li \longrightarrow {}^{3}_{1}T + {}^{4}_{2}He + 4.8 \text{ Mev} \quad (1.4)$$

$$n + {}^{7}_{3}Li \longrightarrow {}^{3}_{1}T + {}^{4}_{2}He + n - 2.46 \text{ Mev} \quad (1.5)$$

The cross-sections of the $^{6}_{3}Li$ and $^{7}_{3}Li$ for capture of thermal neutrons are 945 barns and 1.4 barns respectively . Natural lithium contains a-bout 7.5%of $^{6}_{3}Li$ and appears to be in abundant supply for the purpose.

One thing appears clear - the energy from thermonuclear reactions must

be recovered as heat . This fact requires the presence of a heat-recovery blanket surrounding the reactor as shown in fig(1.2) . The vacuum wall and blanket will necessarily contain a certain amount of structural material that absorbs the neutrons and gamma-rays produced. In addition , a significant multiplication of the number of neutrons is required using further nuclear reactions . LiF may be satisfactory for neutron capture and tritium recovery . However concerning possible moderator materials , beryllium is efficient and a mixture of BeF and LiF might be postulated for a homogeneous moderator behind the vacuum wall . Beryllium may also be necessary for neutron multiplication ; i.e.

$$^{9}_{4}Be + n \longrightarrow {}^{4}_{2}He + 2n \qquad (1.6)$$

Where $\sigma_{n,2n} \cong$ Ø.4 barns at 14.1 Mev .

Many heavy elements Mo , Ta , Pb , W and ^{238}U have (n,2n) cross-sections in excess of 1 barn at 14.1 Mev . Cross-sections for a number of possible material are shown in table(1.1) . For Lead , the (n,2n) cross-section at 14.1 Mev is approximately 5Ø% of the total cross-section for all processes . Therefore , if the blanket contains an appropriate heavy metal , a 14.1 Mev neutrons stands a good chance of multiplication .

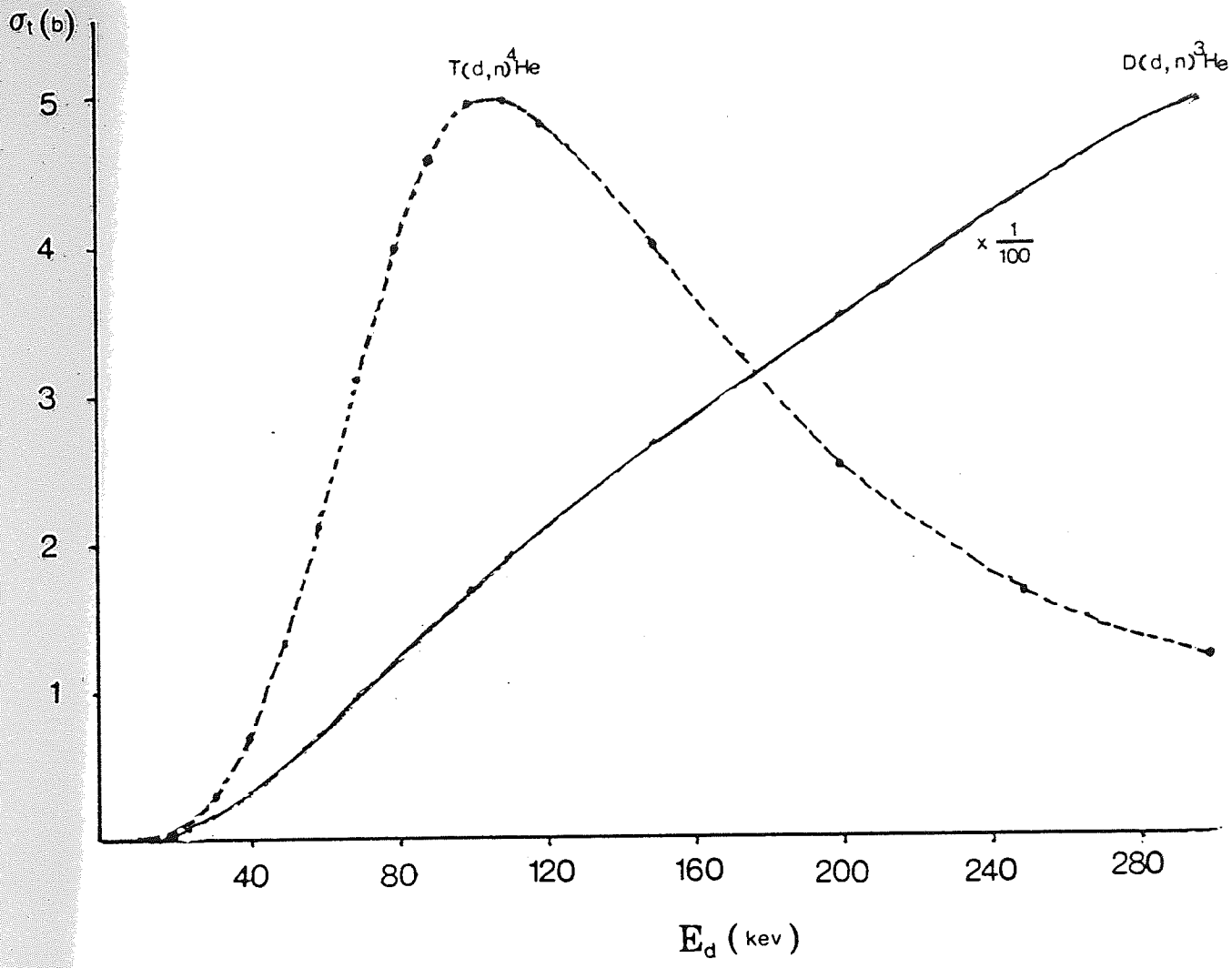

Fig(1.1) Total cross-section for the production of neutrons from the reactions $T(d,n)^4He$ and $D(d,n)^3He$. [16]

TABLE (1.1)
CROSS-SECTIONS FOR(n,2n) reactions

ELEMENTS	$\frac{\sigma\ (n,2n)\ 14Mev}{\sigma_t}$
Fe	Ø.19
Mo	Ø.39
Ta	Ø.33-Ø.5Ø
Pb	Ø.5Ø
W	Ø.53
U	Ø.31

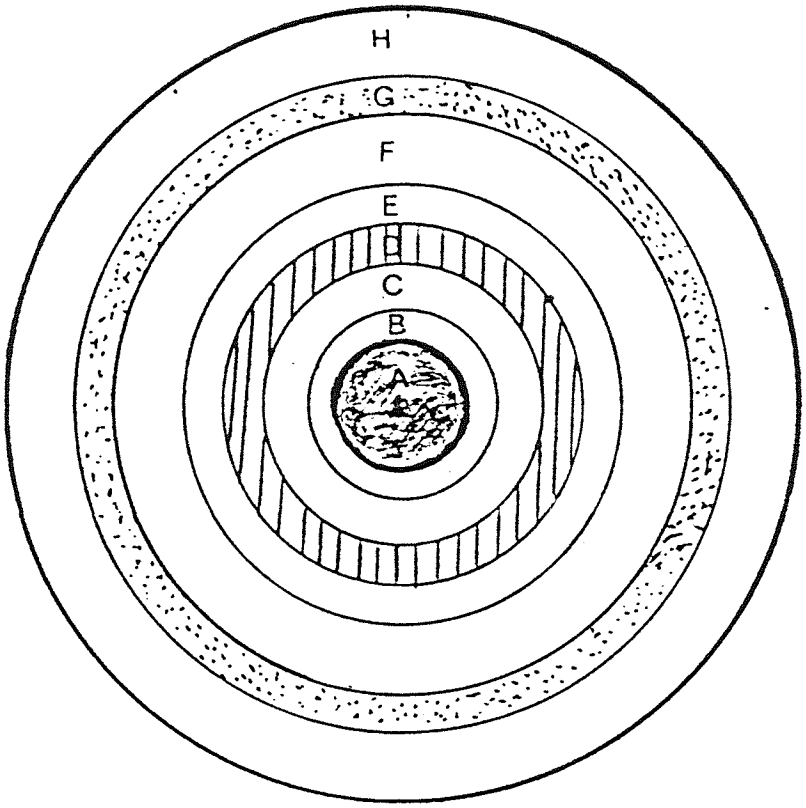

A – Plasma 10^{8} K

B – Vacuum

C – Lithium blanket

D – Graphite

E – Lithium coolant

F – Neutron shielding (water)

G – Lead gamma shield

H – Superconducting coils 4°K (– 268°C)

Fig (1.2) Section of a possible fusion reactor [104]

1.2 MODELS FOR NEUTRON-NUCLEUS INTERACTIONS

At the present time all models are simplified pictures of the neutron-nucleus interactions containing relatively few parameters that are adjusted to bring predictions into line with experimental data .

BETHE (1935) [1] began to use the real potential well model in an attempt to explain the early crude observations on the interactions of neutrons with nuclei . This model contained two adjustable parameters , the real potential and radius of the nucleus predicted two types of interactions only , elastic scattering and radiative capture . Observed resonances are classified as widely spaced [2] .

The compound nucleus model proposed by BOHR (1936)[3] , explained the observed resonances . He suggested that the interaction be considered to occur in two distinct steps , the formation of the compound nucleus (CN) and its subsequent decay . In the CN , the incoming neutron loses its identity . While the decay of the excited CN subsequently occurs through either gamma-ray emission , neutron emission , or other massive particle emission .

The cross-section for any interaction that proceeds through a CN state can be expressed in the form of the product :

$$\sigma(E,b)=\sigma_c(E)\quad(\frac{\Gamma_b}{\Gamma})_c \qquad (1.7)$$

Where $\sigma_c(E)$ is the cross-section for formation CN by an incident neutron of energy (E) and $(\frac{\Gamma_b}{\Gamma})_c$ is the probability that the CN will decay by emission of a particle b .

The black model [9] was remarkably successful in describing neutron-nucleus cross-section in the region of isolated resonances . But at high energies this model predicted that the total cross-sections averaged over resonances should be monotonically decreasing functions of energy at a fixed mass number and slowly increasing functions of mass number at a fixed energy . These predictions were not verified experimentally [5] .

WEISSKOPF et al [4] soon showed what results were to be expected for neutron cross-sections if the nucleus were weakly absorbing instead of black . This model of the nucleus which allowed partial absorption the wave associated with the incident neutron , soon came to be called the Cloudy Crystal Ball model of the nucleus [5] .

However neither the crystal model nor the black model was entirely successful in predicting even the gross behavior of neutron cross-sections , although each seemed to have some validity .

SERBER (1947) [6] introduced the optical model and was applied to neutron interactions by FERNBACH etal [7,8] . This model replaces the nucleus by a potential well that partially transmits and partially absorbs neutrons and these describe the effect of the nucleus on the incident neutron by a spherically symmetric potential well having real (U) , and imaginary (W) potentials ; i.e.

$$V(r) = U + iW \qquad \text{for} \quad r < R \qquad (1.8)$$

$$= \emptyset \qquad \text{for} \quad r > R$$

Where R is the nucleus radius .

In their pioneer work FESCHBACH et al [8] used a square well potential ; this is obviously unrealistic and in particular it has too high reflectivity . A more realistic form of potential can be obtained from a simple argument based on the form of the nucleon-nucleon interaction [87] . The first approximation in the optical model (OM) with a radial variation predicts the nuclear density quite closely ,i.e. V f(r) , where f(r) is the WOODS-SAXON form [103] ;

$$f(r) = \frac{1}{1 + \exp\left(\frac{r - R}{a}\right)} \qquad (1.9)$$

Where R is the nucleus radius , and is generally chosen to be $R_0 A^{\frac{1}{3}}$ and (a) is the surface diffuseness parameter .

This form of the potential accounts for the scattering . The imaginary or absorption potential has been taken to have a volume form , a surface form or a mixture of volume-surface . The spin-orbit form is generally taken to have the Thomas form {see chapter seven }. In the present work the experimental results for 14 Mev neutrons scattering were analyzed using the OPTICAL MODEL . The results include the differential cross-sections for elastic scattering , the total and reaction cross-sections . Most of the analyses concentrate on Lithium and Lead exeprimental data , and chapter seven is mainly devoted to review of the results .

1.3 THE RESEARCH PROGRAM

The aim of the present work was to study the differential elastic and inelastic scattering cross-sections of 14 Mev and 14.44 Mev neutrons from different sample thicknesses of Lithium and Lead . Source neutrons were provided by the $T(d,n)^4_2H$ reaction by bombarding TiT target with a deuteron beam from SAMES and DYNAMITRON accelerators .

These measurements of neutron scattering cross-sections are of importance in a number of areas related to controlled thermonuclear reactor (CTR) designs . No similar work has studied the effect of different thicknesses of Lithium and Lead material which are critical components of CTR blanket configuration , since neutron interaction with lithium and lead isotopes , may be necessary for neutron mutiplication (n,2n) and the breeding of new fuel .

The experimental results were obtained using a time-of-flight technique with a flight path of 2.13 m and a time resolution of 2.5 ± 0.2 nsec. .

The angular distributions of elastic and inelastic scattering were fitted to legendre polynomials and the expansion coefficients compared with ENDF/B-IV files .

The variation of the differential elastic and inelastic scattering cross-sections with the sample thickness , caused mainly by multiple scattering effects in the neutron distributions , was found to be characterized by a simple phenomenological formula .

The experimental elastic scattering angular distributions for the thin Lithium and Lead samples have been compared with the theoretical

predictions of the Optical Model using the computer search code RAROMP [96] .

For extended samples , the angular distributions of scattered neutrons were compared with predictions of the FERMI-AGE equation based on the continuous slowing down model .

CHAPTER TWO

GENERAL CONSIDERATIONS

CHAPTER TWO

GENERAL CONSIDERATIONS

2.1 KINEMATICS OF THE $T(d,n)^4_2He$ REACTION

An accurate knowledge of the energy and angle of the emitted neutrons in $T(d,n)\ ^4_2He$ reaction is very important for calibrating the measurement equipement and enable the interaction of fast neutrons with the fusion material to be studied . From T-D reaction , 14 Mev neutrons were produced using the reaction :

$$^2_1H + ^3_1H \longrightarrow ^4_2He + n + 17.6\ Mev \qquad (2.1)$$

This reaction gives its maximum yield of neutrons at 14 Mev when the initial deuteron particles are accelerated through a potential of about 14Ø kev .

It is possible to make an accurate calculation of the emitted neutron energy as a function of angle for a specific deuteron energy . An approximate approach is based on the Newtonian form of the conservation laws of momentum and energy . From fig (2.1) The conservation laws can be written in the form :

$$P_D = P_n \cdot \cos\theta_n + P_\alpha \cdot \cos\theta_\alpha \qquad (2.2)$$

$$Ø = p_n \cdot \sin\theta_n + p_\alpha \cdot \sin\theta_\alpha \qquad (2.3)$$

$$Q = (M_D + M_T) - (M_n + M_\alpha) = E_n + E_\alpha - E_D \qquad (2.4)$$

Where M_D , M_T , M_α and M_n = rest masses of the deuteron , tritium , ^{4}He and neutron .

θ_n = neutron emission angle in the lab-system.

θ_α = alpha-particle emission angle in the lab system .

P_D , P_α and P_n = momentum of the deuteron , ^{4}He and neutron respectively .

and Q = Q-value of the $T(d,n)^4He$ reaction.

Eliminating (θ_α) between equations (2.2) and (2.3) , and using equation (2.4) to eliminate E_α , the kinetic energy of the neutron can be obtained :

$$E_n = M_D.M_n.E_D\{ (\Gamma + \cos^2\theta_n)^{\frac{1}{2}} \pm \cos\theta_n \}^2 / (M_n + M_\alpha)^2 \qquad (2.5)$$

Where $$\Gamma = (M_n + M_\alpha) [M_\alpha - M_D + M_\alpha.Q / E_D] / (M_D.M_n) \qquad (2.6)$$

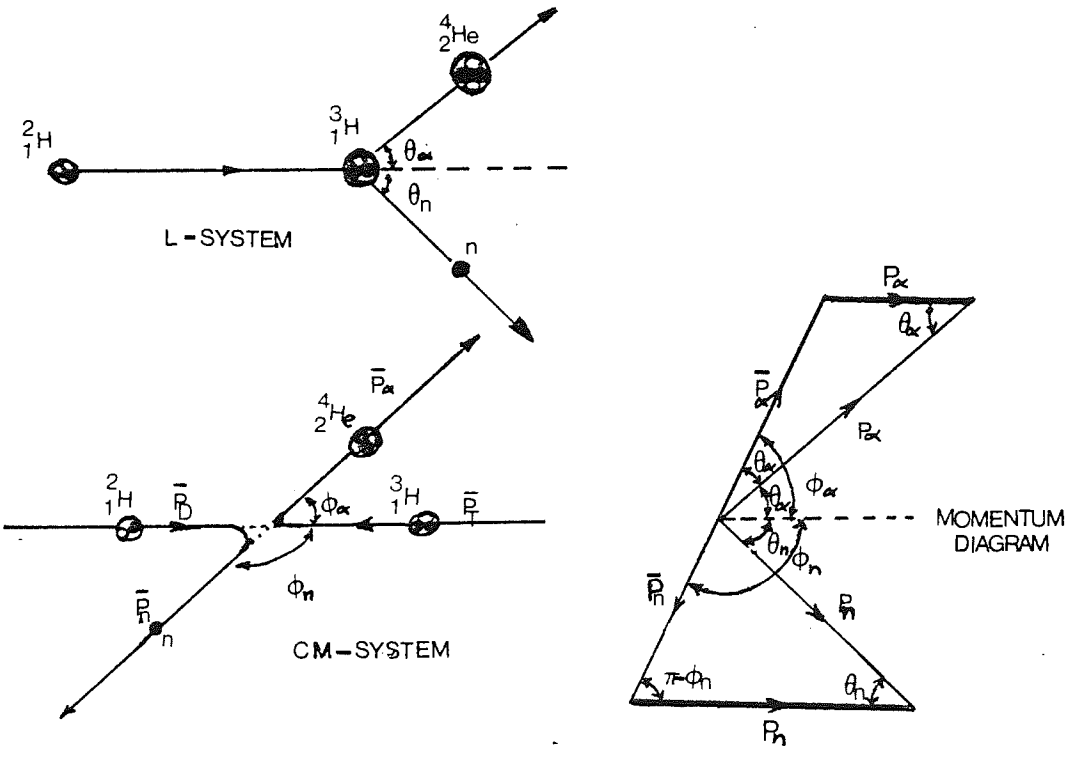

Fig(2.1) Nuclear reaction in Lab and CM system.

Fig (2.2) shows the variation of neutron energy with angle for different deuteron energies in the lab-system using the program shown in appendix A . The relation between θ_α made by alpha-particle with deuteron beam direction , and (θ_n) , made by the neutron and the beam direction , is :

$$\tan\theta_\alpha = \frac{0.5\sin 2\theta_n + \sin\theta_n \sqrt{\Upsilon^{-2} - \sin^2\theta_n}}{-\sin^2\theta_n + \cos\theta_n \sqrt{\Upsilon^{-2} + \sin^2\theta_n} - \frac{M_\alpha}{M_n}} \qquad (2.7)$$

Where $\Upsilon^{-2} = \frac{M_\alpha}{M_n} \left(\frac{M_D + M_T}{M_D}\right)\left[\frac{M_T}{M_D + M_T} + \frac{Q}{E_D}\right]$

Equation (2.7) has been evaluated for different values of deuteron bombarding energy (E_D) as shown in fig (2.3) .

The application of the condition $\left[\frac{\partial E_n}{\partial E_D} = 0\right]$ to equation (2.5) gives the following relation for the optimal value of the neutron emission angle θ_n that assures the minimal straggling in the neutron output energy :

$$\cos^2\theta_n = \frac{(M_n + M_\alpha)(M_\alpha - M_D)^2}{M_D M_n \left(M_\alpha \frac{Q}{E_D} - M_\alpha + M_D\right)} \qquad (2.8)$$

From equation (2.7) it follows that the optimal value at θ_n lies between 92.1° (E_D = 10 kev) and 98° (E_D = 140 kev) .

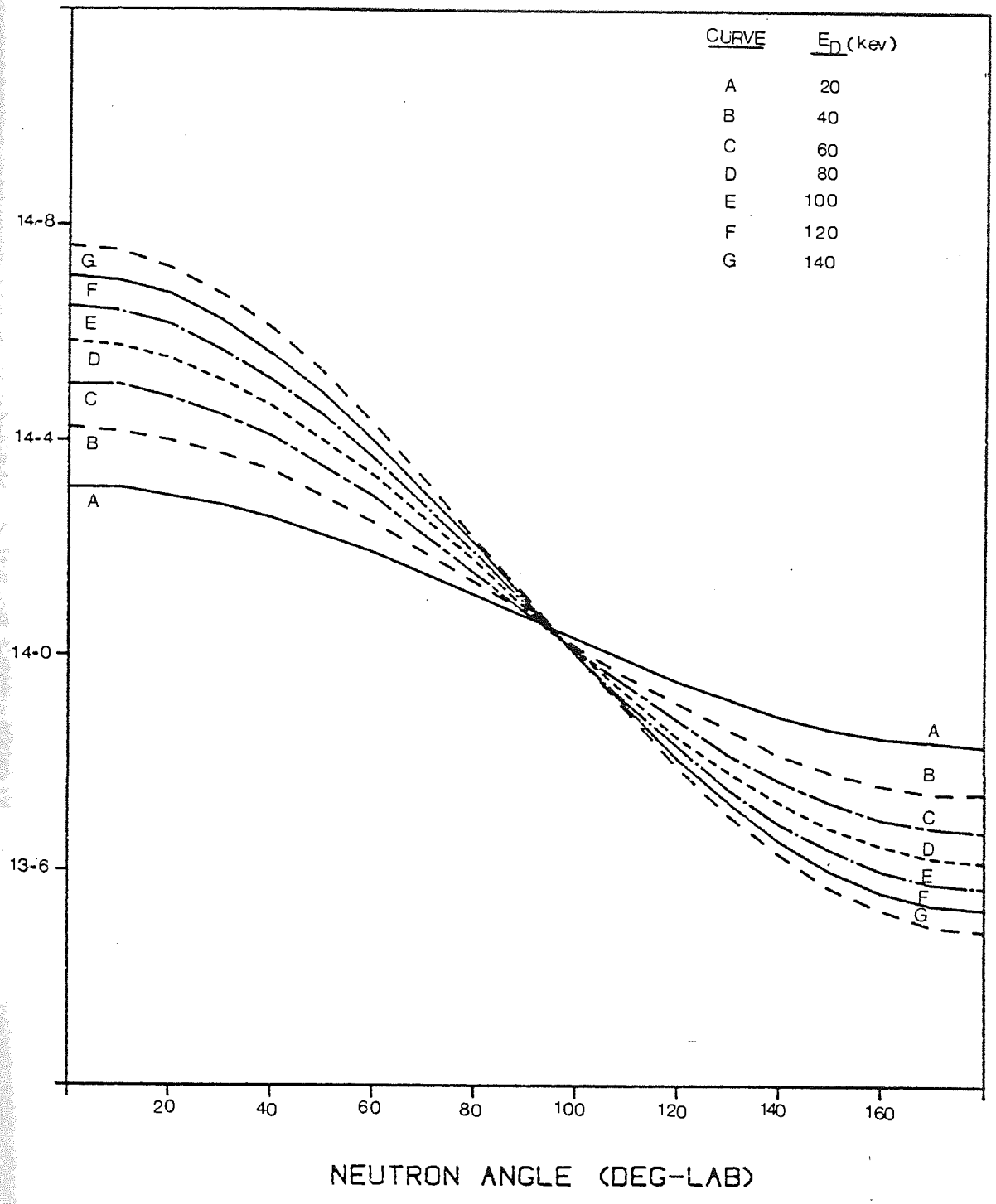

Fig (2.2) Neutron energy as a function of Laboratory angle at various incident deuteron energies.

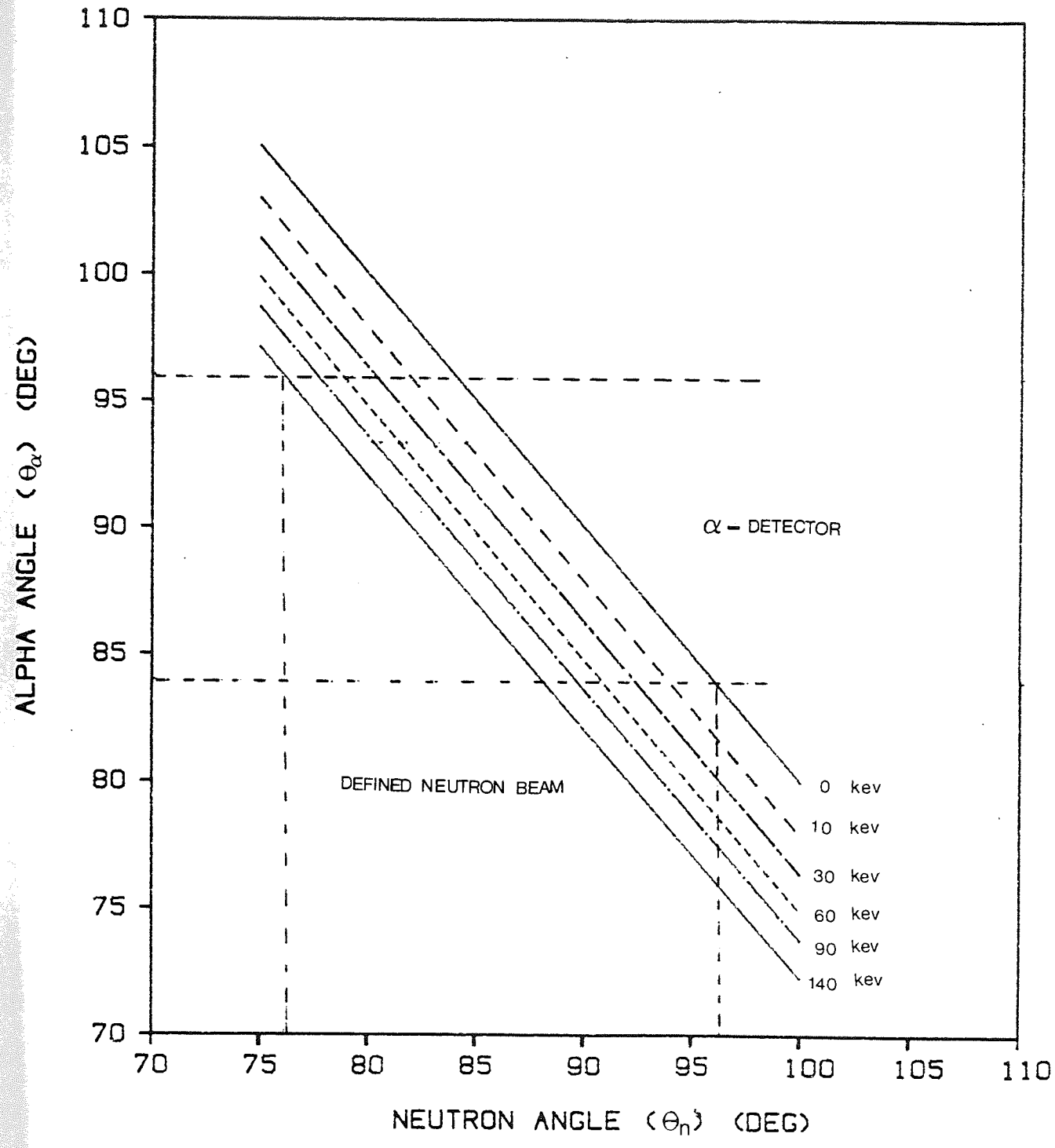

Fig (2.3) Relation between the angles made by the neutron and associated alpha-particle for a $\pm 6^{\circ}$ alpha aperture .

2.2 THE ANISOTROPY FACTOR

The most convenient coordinate system to analyze the dynamics of the T-D reaction is the centre-of-mass (CM) system . The anisotropy factor is then used to transfer from the CM-system to the laboratory (L) system in which the target nucleus is assumed to be at rest .

The relation between the solid angle , dw' , occupied by the neutron particles in the CM-system , and the corresponding , dw , in the L-system is given by :

$$\frac{dw'}{dw} = \frac{\sin\theta_n \, d\theta_n}{\sin\phi_n \, d\phi_n} \qquad (2.9)$$

Where ϕ_n and θ_n are the neutron emission angles in the CM and L-system respectively .

BENVENISTE and ZENGER [10] have shown the relation between the CM-angle (ϕ_n) and the L-angle (θ_n) with respect to the incident deuteron beam , is given by :

$$\cos\phi_n = -\gamma . \sin^2\theta_n \pm \cos\theta_n . \left(1 - \gamma^2 . \sin^2\theta_n \right)^{\frac{1}{2}} \qquad (2.10)$$

Where γ is as defined by equation (2.7) .

By differentiating equation (2.10) and subtituting into equation (2.9) gives :

$$\left(\frac{dw'}{dw}\right)_n = \frac{\gamma \left\{ \cos\theta_n + \left(\gamma^{-2} - \sin^2\theta_n \right)^{\frac{1}{2}} \right\}^2}{\sqrt{\gamma^{-2} - \sin^2\theta_n}} \qquad (2.11)$$

Equation (2.11) has been evaluated as a function of (θ_n) and for varies deuteron energies (E_D) as shown in fig (2.4) .

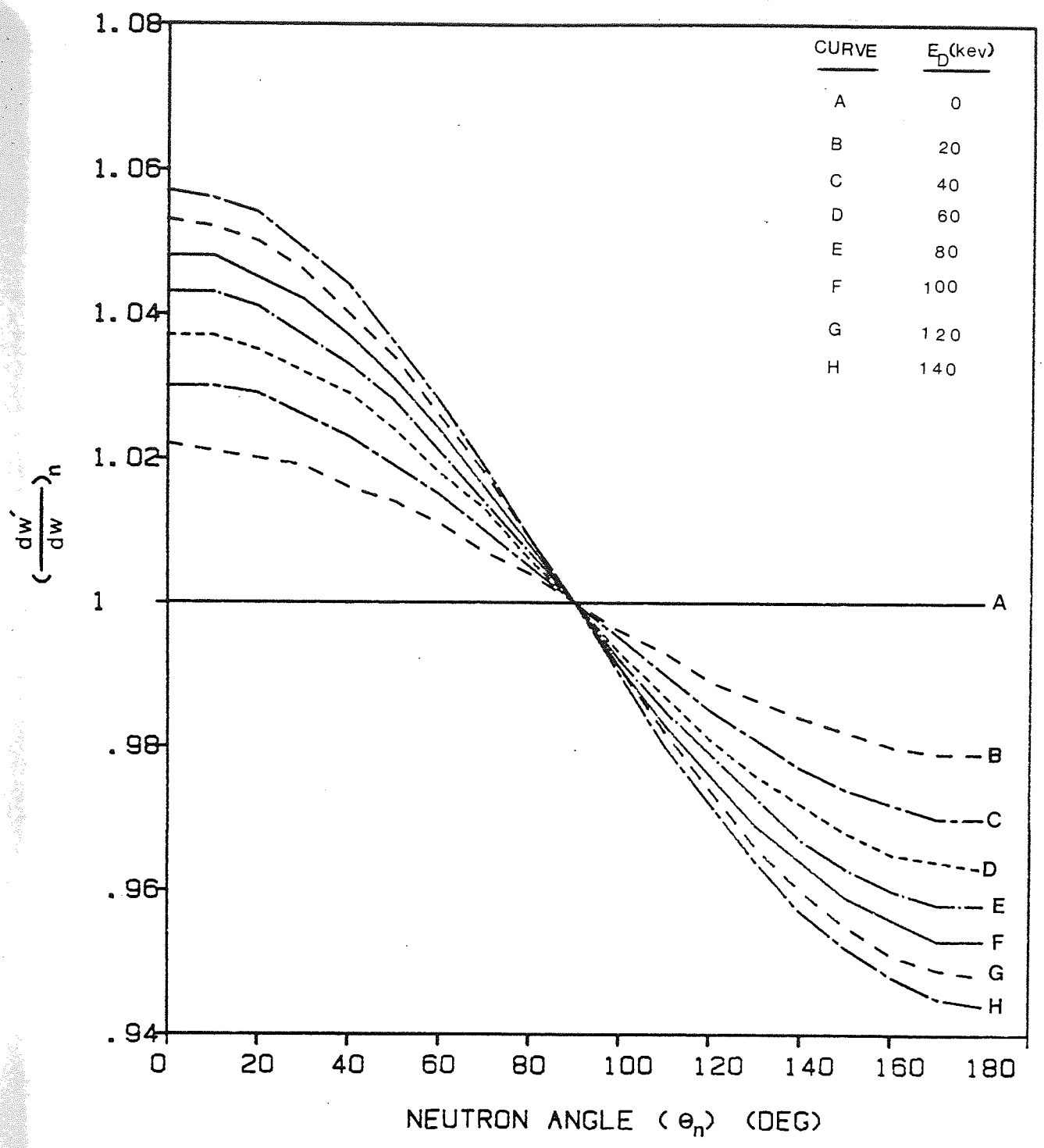

Fig (2.4) The ratio of the solid angle in CM-system (primed quantities) and L-system into which the neutron is produced as a function of the neutron angle in L - system .

2.3 THE NEUTRON YIELD CALCULATION

The recommended differential cross-section data for the production of neutrons from T-D reaction has been tabulated by earlier reviews of LISKIEN and PAULSEN (1973) [16] as shown in fig (2.5) . The approximate expression which is normally used to relate the thick target yield per unit solid angle per incident deuteron energy , to the differential cross- section is given by :

$$Y(E_D,\theta_n) = \int_0^{E_{max}} N_t \cdot \frac{d\sigma/dw}{dE/dX}\, dE \qquad (2.12)$$

Where θ_n = neutron emission angle .

E_D = the energy of the incident deuteron .

N_t = the number of the tritium nuclei per unit volume .

$\frac{d\sigma}{dw}$ = the differential cross-section per steradian at a deuteron energy (E_D) and neutron emission angle (θ_n).

$\frac{dE}{dX}$ = the rate of energy loss of deuterons of energy (E_D) in the TiT target. (in $kev/gm/cm^3$)

2.3.1 NUMBER OF TRITIUM NUCLEI PER cm^3 , " N_t "

In the present work the loading ratio (ϵ) of the TiT target contains 1.682 tritium atoms/titanium atom , then the density ρ_{TiT} of the target material is :

$$\rho_{TiT} = \frac{48 + 3\epsilon}{48} \cdot \rho_{Ti} \cdot \text{Ø}.85 = 4.18 \quad gm/cm^3 \qquad (2.13)$$

Where $\rho_{Ti} = 4.54\ gm/cm^3$

The factor Ø.85 arises from the 15% expansion of the titanium during tritiation . The number Nt of tritium atoms $/cm^3$ is then :

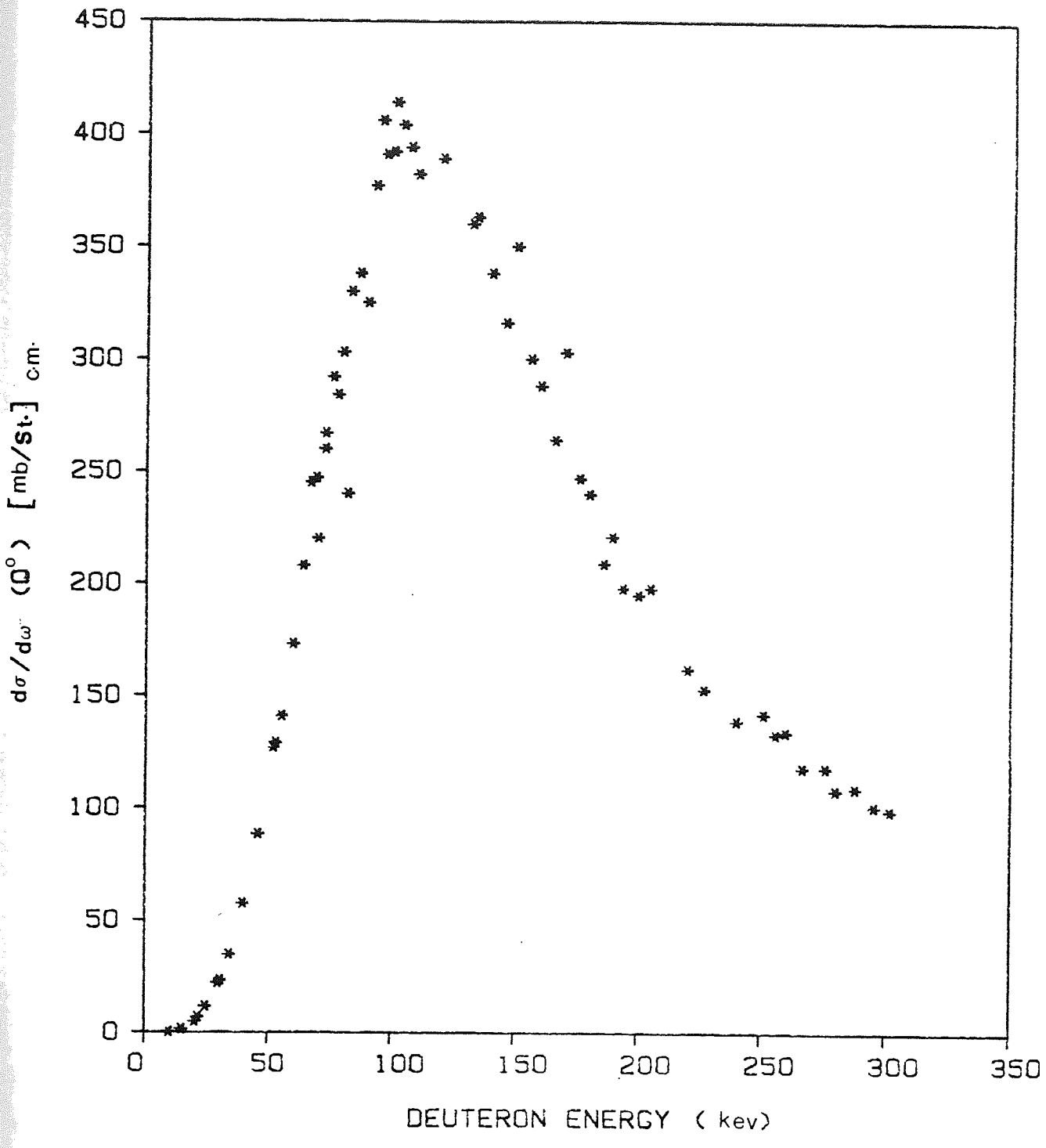

Fig (2.5) Differential cross - section for the production of neutrons from the $T(d,n)^4He$ reaction [16,15] .

$$N_t = \frac{1.68 \times \rho_{TiT} \times 6.02 \times 10^{23}}{A_{TiT}} = 8.3 \times 10^{22} \qquad (2.14)$$

2.3.2 THE ENERGY LOSS OF DEUTERONS IN TiT TARGET

There are no experimental data available on rate of energy loss for deuterons in TiT . Here the data have been evaluated by several authors [10,11,12,14] and the values are given in table (2.1) . The approximate values of $(\frac{dE}{dX})$ can be calculated by Bragg's law , which is stated , that the energy loss in a compound is the sum of the energy losses in its separate constituents [13] , as given by :

$$\frac{dE}{dX} = \frac{48}{48 + 3\epsilon} \left(\frac{dE}{dX}\right)_{Ti} + \frac{3\epsilon}{48 + 3\epsilon} \left(\frac{dE}{dX}\right)_{T} \qquad (2.15)$$

For ϵ = 1.682 tritium atoms/ titanium atoms :

$$\frac{dE}{dX} = 0.905 \left(\frac{dE}{dX}\right)_{Ti} + 0.095 \left(\frac{dE}{dX}\right)_{T} \qquad (2.16)$$

Where $(\frac{dE}{dX})_{Ti}$ represents the rate of energy loss of deuterons in titanium and $(\frac{dE}{dX})_{T}$ that in tritium . Fig(2.6) illustrates the results when equation (2.16) is applied to the values listed in table(2.1) . The numerical evalution of the integral {equation(2.12)} for incident deuteron energies 10-300 kev has been carried out using the values of $(\frac{dE}{dX})_{TiT}$, $(\frac{d\sigma}{dw})_{TD}$ and anisrotropy factor $(\frac{dw'}{dw})$, the resultant yield curve of neutron/deuteron is shown in fig (2.7) .

Table (2.1)

ENERGY LOSS VALUE FOR DEUTERONS IN Ti , T AND TiT

(Values are in kev/mg/cm^3)

E_D kev	$(\frac{dE}{dx})_{Ti}$	$(\frac{dE}{dx})_{T}$	$(\frac{dE}{dx})_{TiT}$
10	59	≃ 490	91
15	88	≃ 600	137
20	108	≃ 704	165
25	132	802	196
30	149	890	219
35	163	960	239
40	177	1023	257
45	187	1061	269
50	193	1128	282
60	210	1183	302
70	223	1238	319
80	233	1268	331
90	242	1281	341
100	252	1290	351
110	260	1294	358
120	265	1295	363
130	269	1288	366
140	273	1281	369
150	276	1270	370
160	278	1251	370
170	280	1231	370
175	280	1231	370
200	285	1211	373
225	285	1084	361
250	283	≃ 1007	352
275	279	≃ 976	345
300	272	≃ 965	338

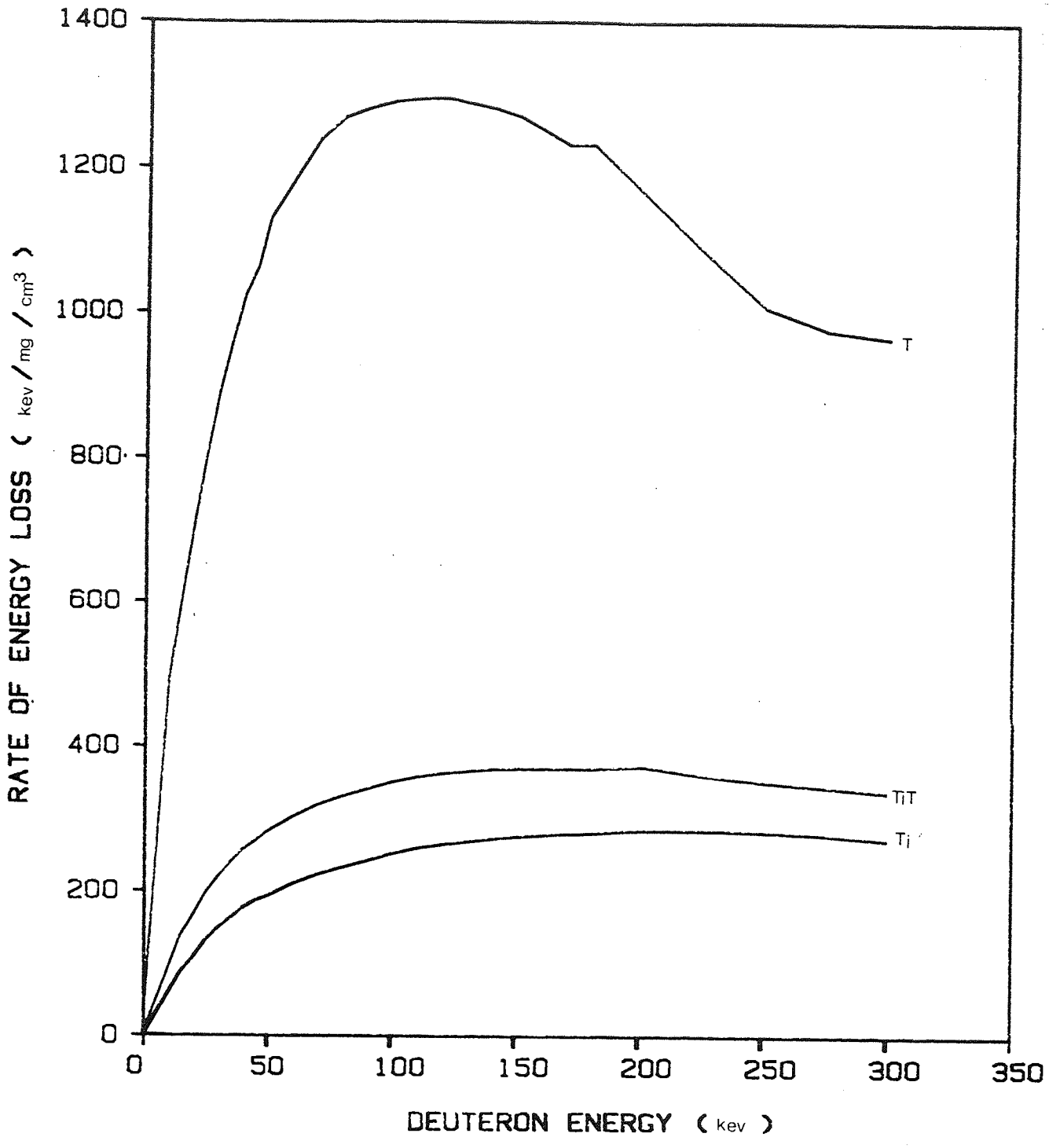

Fig (2.6) The rate of energy loss of deuterons in tritium , titanium and TiT target .

2.4 THE NEUTRON BEAM PROFILE

The shape of the relative neutron yield , is described by the neutron beam profile , produced by $T(d,n)^4He$ reaction has been analyzed at emission angle (θ_n) . In considering figures (2.3) and (2.7) , the relative neutron yield can be calculated for each neutron angle as defined by the aperture of the alpha detector (i.e.$\Delta\theta_\alpha = 6^\circ$) , and is given by :

$$s = \frac{\int_{E_1}^{E_2} Y(E_D, \theta_n)\, dE}{A_T} \qquad (2.17)$$

Where E_1 = lower limit of deuteron energy .

E_2 = upper limit of deuteron energy .

A_T = the total area under the curve , fig (2.7) from $E_D = \emptyset$ to 14Ø kev .

The calculation of equation(2.17) is carried out using 1° steps for the neutron angles as illustrated in fig (2.8) . The full width at half maximum is shown to be 12° and is centred at 82° to the incident deuteron energy .

2.5 THE NEUTRON LINE SHAPE

The neutron line shape at any particular angle shows the energy spread of the neutron striking the target . This is influenced [1Ø, 12] by both degradation of the incident deuterons in the target material and the finite geometry of the alpha-particle detector . The area under the line shape is proportional to the neutron yield in the Lab-system for deuterons of energy E ; This is given by :

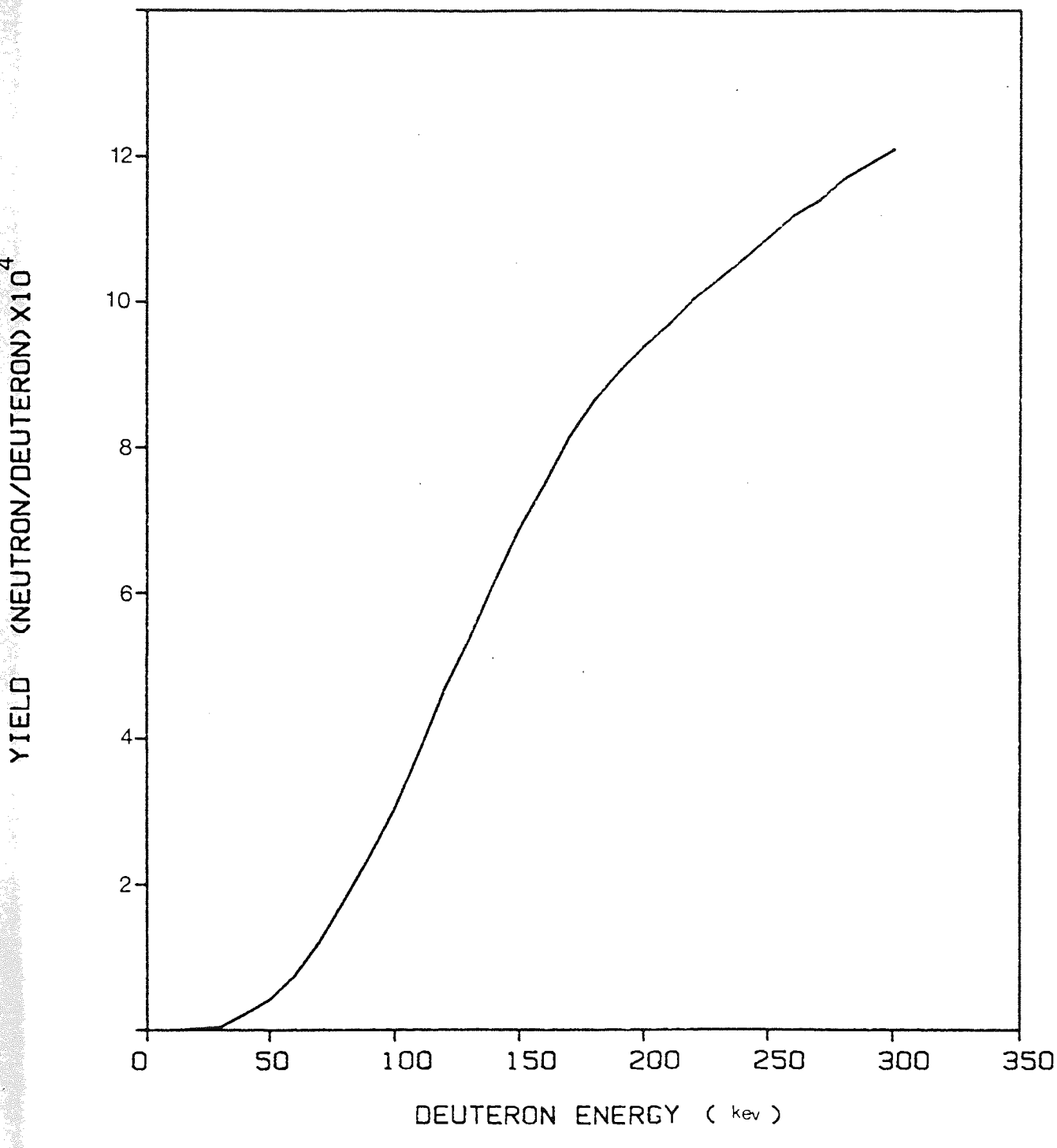

Fig (2.7) Yield of neutrons from T(d,n)^{4}He reaction produced in TiT .

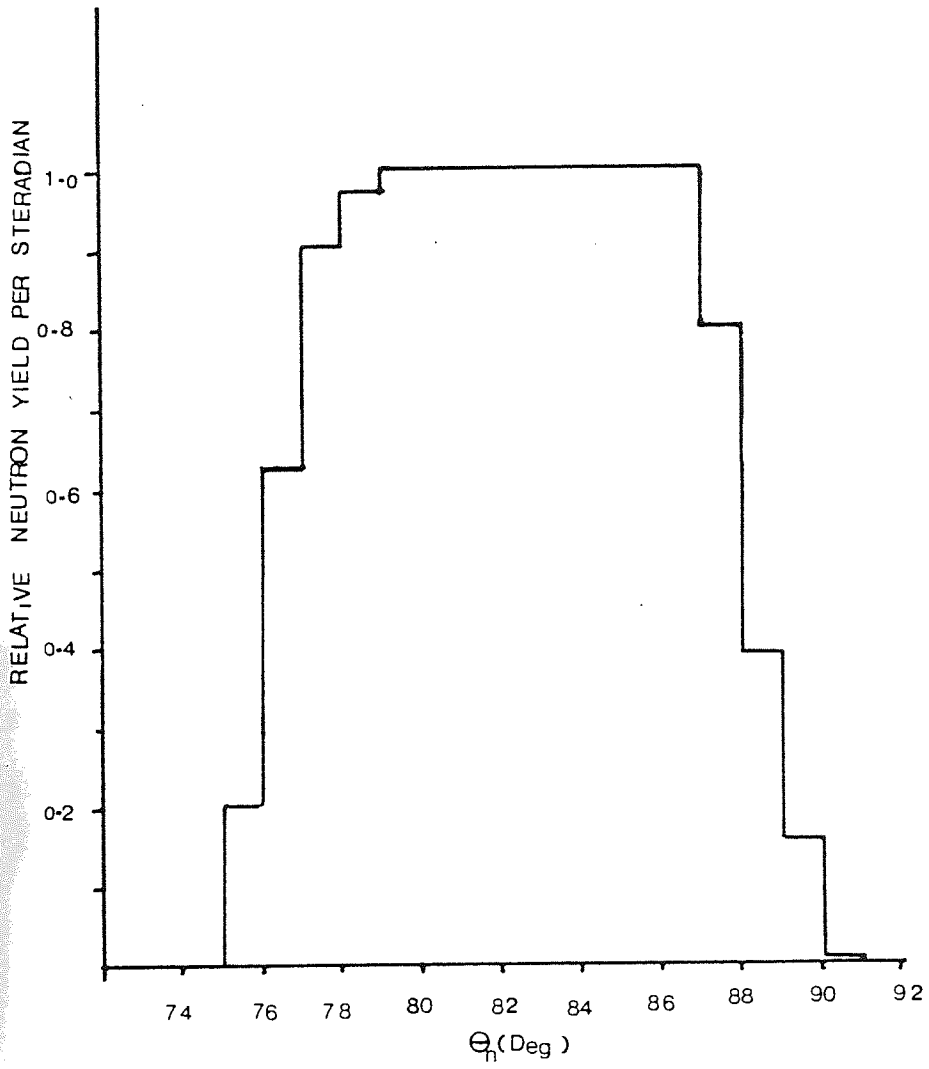

Fig (2.8) The neutron beam profile , defined by an angle $90^{\circ} \pm 6^{\circ}$ in the alpha-detector .

$$L(E_D,\theta_n) \simeq \frac{\frac{d\sigma}{dw}(E_D)}{\frac{dE}{dX}(E_D)} \cdot \frac{dw'}{dw}(\Delta E_D) \qquad (2.18)$$

The neutron line shapes calculated in this way for several angles are presented in fig (2.9) .

2.6 NEUTRON INTERACTION WITH MATTER

Neutrons carry no charge and therefore cannot interact with matter by means of the Coulomb force which dominates the energy loss mechanisms for charged particles and electrons . As a result , neutrons interact with the nucleus without difficulty. There are many different types of nuclear reactions caused by neutrons :

1 - Elastic scattering (n,n) .

2 - Inelastic scattering (n,n') .

3 - Capture reaction (n,γ) .

4 - Charged particle emission (n,α),(n,p) .

5 - Neutron production (n,2n) , (n,3n) , ...

6 - Fission (n,f) .

The first two reactions are the most significant in the present work .

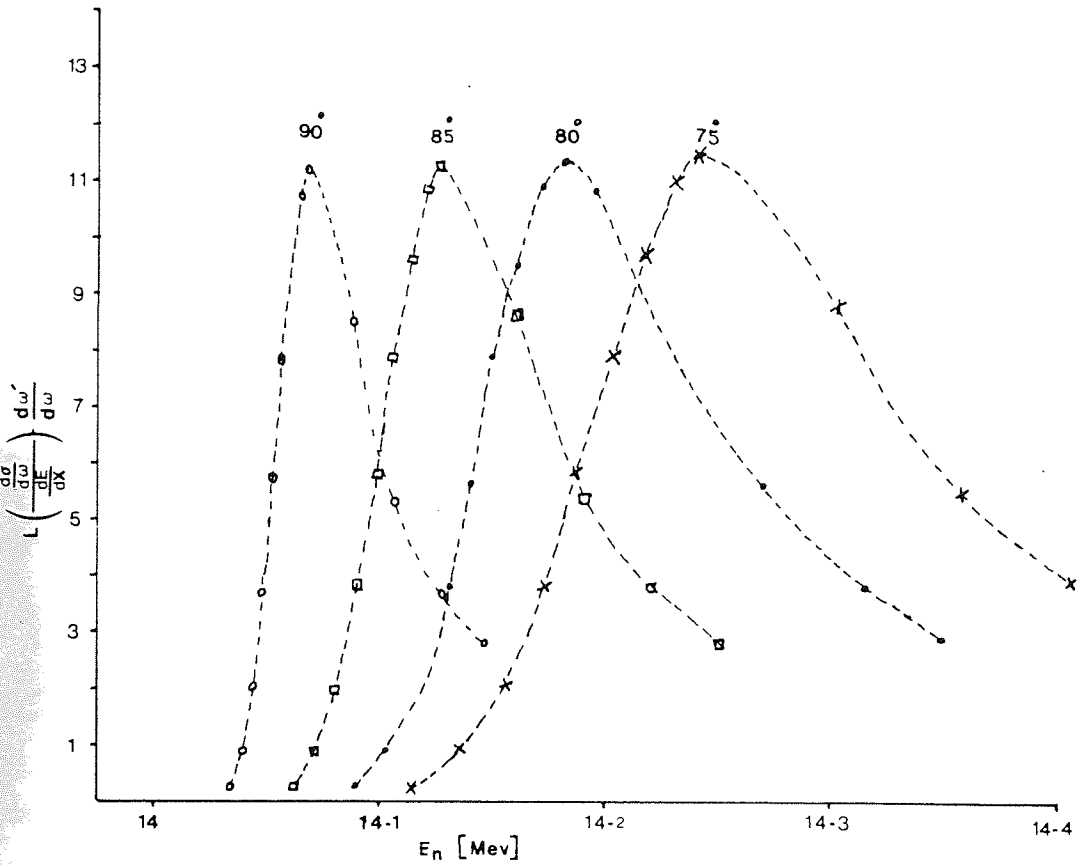

Fig(2.9) Neutron line shape . The energy distribution of neutrons coming off at an angle θ_n(Lab) with respect to the incident deuteron beam (θ_n= 75°, 80°, 85°, and 90°) .

2.6.1 ELASTIC SCATTERING(n,n)

In this process the sum of the kinetic energies of the neutron and nucleus is the same before and after the collision . It may be shown that if a neutron of kinetic energy (E_o) is deflected through an angle (ϕ_{cm}) by an elastic collision with a stationary nucleus of mass (A) , the kinetic energy (E) of the scattered neutrons is given by :

$$\frac{E}{E_o} = \frac{A^2 + 1 + 2A\cos\phi_{cm}}{(A+1)^2} \qquad (2.19)$$

The relation between the angle ϕ_{cm} in CM-system to the angle θ_L in the L-system given by :

$$\cos\theta_L = \frac{A\cos\phi_{cm} + 1}{[A^2 + 1 + 2A\cos\phi_{cm}]^{1/2}} \qquad (2.20)$$

At $\phi_{cm} = 180^o$, the neutron energy lost will be a maximum ie. E will be minimum :

$$Emin = E_o\{\frac{A-1}{A+1}\}^2 \qquad (2.21)$$

For heavy nuclei , $Emin \simeq E_o$, and there is little loss in neutron energy . On the other hand if A = 1 , Emin =0 , i.e. in a single collision the neutron will lose all its energy .

2.6.2 INELASTIC SCATTERING (n,n')

In the energy region below 20 Mev, inelastic scattering is simply one of the possible channels of compound nucleus decay. The excited compound nucleus will decay by neutron emission into an excited product nucleus that usually decays by gamma-emission and is left in its groundstate . For most elements , (n,n') reactions cannot occur unless the incident neutron energy is greater than the energy of the first excited state in the target nucleus . Therefore , the laboratory threshold energy ($\bar{E}_t$) for inelastic scattering of a neutron from a nucleus whose lowest energy level is (E^*) is given by

$$E_t = \frac{A+1}{A} E^* \qquad (2.22)$$

Where A , is the mass number of the target nucleus .

From the kinematics of inelastic scattering , the general expression for the final neutron energy (E') , in the L-system as a function of its initial energy (E) , the scattering angle (θ_L) , and the excitation energy (E^*) is [51] :-

$$E' = E \left\{ \frac{1}{A+1} \cos\theta_L + \left[\left(\frac{1}{A+1} \cos\theta_L \right)^2 + \frac{A}{A+1} \left(1 - \frac{1}{A} - \frac{E^*}{E} \right) \right]^{\frac{1}{2}} \right\}^2 \qquad (2.23)$$

The angle of emission of the inelastic neutron in the laboratory and centre-of-mass systems are related by :

$$\tan\theta_L = \frac{\sin\phi_{cm}}{\eta + \cos\phi_{cm}} \qquad (2.24)$$

Where ϕ_{cm} = scattering angle in the CM-system .

and $$\eta = \frac{1}{A}\left[\frac{A\,E}{AE-(A+1)\,E^{*}}\right]^{\frac{1}{2}} \qquad (2.25)$$

When A>>1 , the energy of the emergent neutron is practically independent of angle and equal to ($E - E^{*}$) , therefore heavy nuclei are more effective than light nuclei in slowing down neutrons at high energies for inelastic scattering .

CHAPTER THREE

THE EXPERIMENTAL METHODS

CHAPTER THREE

THE EXPERIMENTAL METHODS

3.1 THE SAMES ACCELERATOR

A SAMES accelerator type-j [fig (3.1)] was used to provide deuteron beams of up to 150 kev .

The electrostatic high voltage generator is housed in a hermetically sealed unit in a hydrogen atomosphere at 10^{-2} torr .

A current of up to 2 mamp can be delivered from the generator to the electrode terminal to produce the 150kev with a stability of ±1% [17] . The accelerator tube was constructed of insulating glass cylinders 20.32 cm long and 2.54 cm diameter . Inside the accelerating tube there is an electrode causing extraction by applying a 0-6 kv repelling voltage .

The ion source was a 100MHz radiofrequency source applied to deuterium gas passing into the ion source bottel through a palladium leak ; the power supplied to the RF oscillator was adequate to create and maintain an intense ionization of the gas . The ions are directed into the accelerating section of the generator by means of an extraction canal as shown in fig (3.2) .

3.1.1 THE BEAM TUBE

After acceleration to an energy of 150 kev , the positive ion beam transverses a 6 meter long , evacuated brass beam tube to the neutron target assembly as shown in fig (3.3).

To achieve the necessary vacuum in the tube , two vacuum pumps were used , one in the vacuum generator and the second at the end of the

Fig (3.1) S.A.M.E.S. Accelerator Type-J .

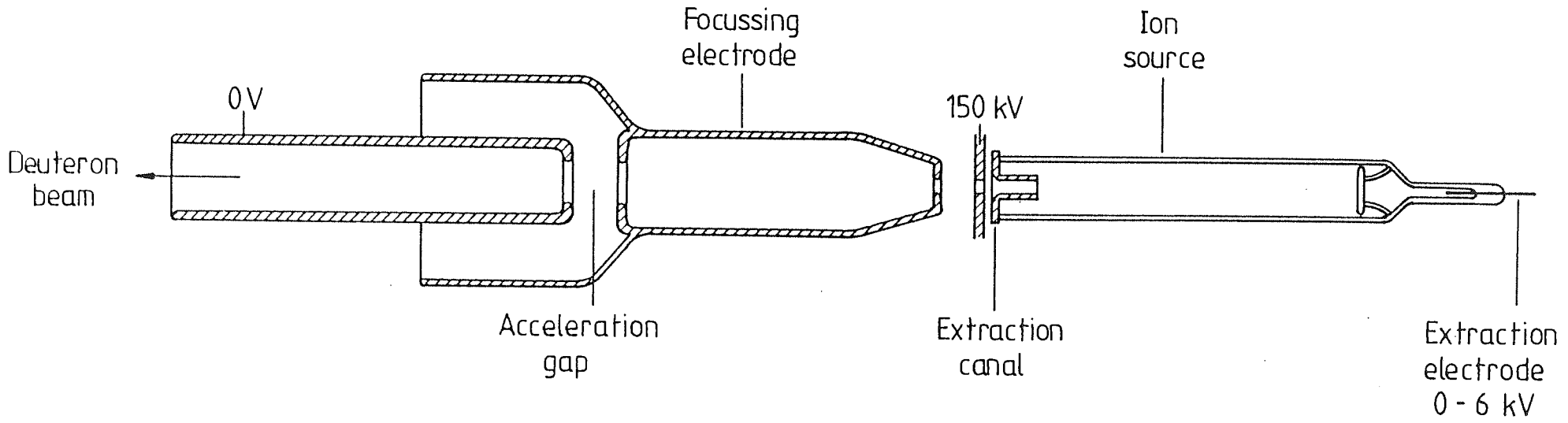

Figure (3·2) Electrode configuration of S.A.M.E.S. accelerator.

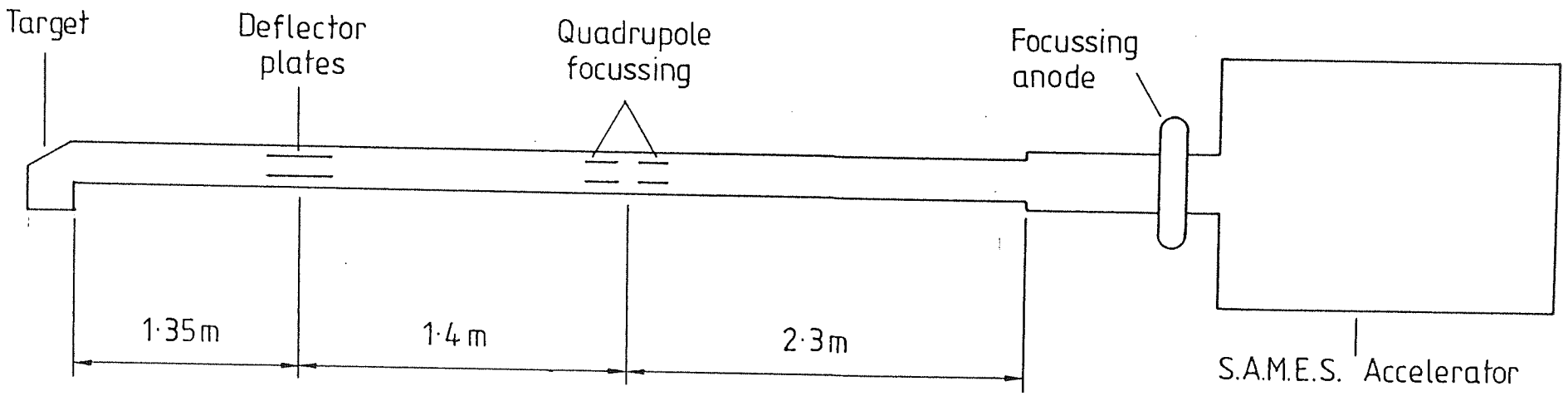

Figure (3·3) Schematic diagram of accelerator.

beam tube . Each consisted of an oil filled diffusion pump backed by a rotary pump . These two pumping systems mentioned give an overall vacuum of 2×10^{-6} torr.

A liquid nitrogen cold finger was positioned in the beam line before the target assembly stage to condense and freeze out any vapours and prevent oil depositing in the target .

Since the focussing system the SAMES accelerator was designed for use with a drift tube between 0.5 and 1.5 meters in length , a pair of auxiliary Quadrupole focussing lenses were used to focus the ion beam with a potential of ±2.2 kv .

The Quadrupole focussing system has been described in more detail by BAYNHAM (1971) [18] .

A pair of electrostatic deflector plates were positioned in the beam path ,before the target assembly ,to optimize the beam current falling onto the target .The deflector plate voltages were adjusted to -1.29 kv .

3.1.2 THE TARGET ASSEMBLY

The stainless steel target assembly* housed an annular shaped target that could be rotated at 10 r.p.m. by an electric motor to expose new target area to the deuteron beam . A thick tritiated-titanium target containing a layer of titanium tritide of thickness 2 μm backed with 152 mm diameter copper was used . The tritium concentration in the target was 4Ci/in^2 with an active area of 104 cm by 30 mm .

---

* Supplied by MULTIVOLT Ltd. SUSSEX .

Cold water flowing through the back of the target prevented any thermal outgassing of the tritium .

The deuteron beam window of the target was defined by a small brass aperture 10mm x 1mm situated 20cm behind the target . As shown in fig (3.4) the target , the aperture flange and the main beam were insulated by araldite spacing flanges , in order to maintain the suppression potentials which were produced by taking the target and the diaphragm currents to earth via large resistors .

Target and diaphragm currents were monitored by microammeters with typical values of 3 μamp and 10 μamp respectively. The NE102A alpha detector was connected to the target assembly at right angles to the main beam tube .

3.2 SCATTERING SAMPLE POSITION IN THE SAMES

As shown in fig (3.4) the alpha-detector was positioned at 90° with respect to the incident deuteron beam . The solid angle subtended by the alpha detector was defined by a 1.09cm x 1.89cm aperture in front of the alpha-particle detector located 90 mm from the TiT target , corresponding to samples 3° 28′ wide and 5° 59′ high. Due to the kinematics of the D-T reaction , the most intense part of the neutron beam was at an angle of 83° to the deuteron beam. The alpha-particle solid angle defined the cross- sectional area of the associated neutron beam which extended from 76° to 92° to the beam direction in the laboratory frame of reference . The scattering sample was centered at 83° and 190 mm distance from the target , so that it completely intercepted the defined associated neutron beam .

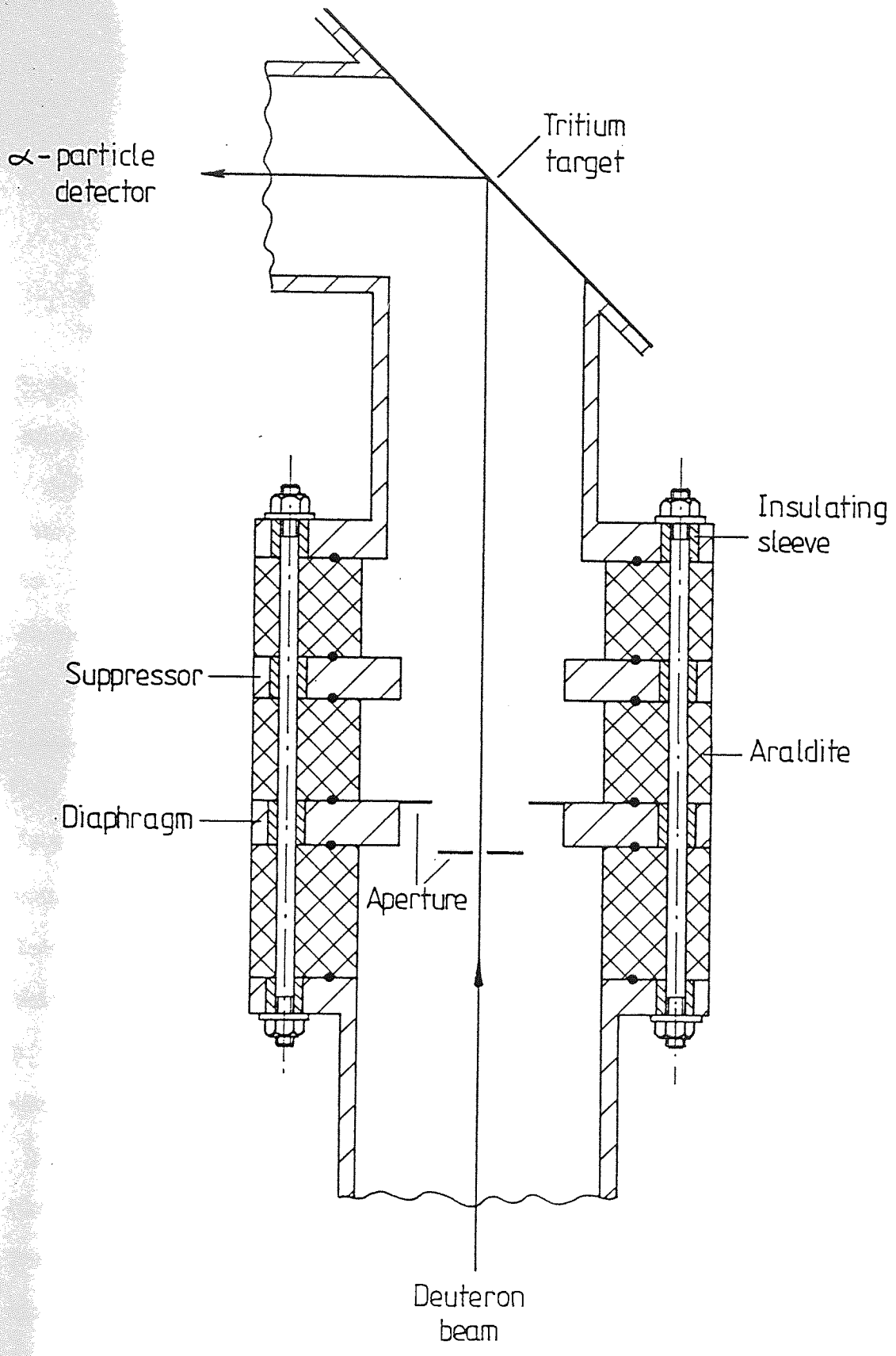

Figure (3·4) The 90° branched target assembly.

Fig (3.5) shows the target assembly with the scattering sample position .

3.3 THE DYNAMITRON ACCELERATOR

The DYNAMITRON accelerator model RPEA3.Ø is a high voltage , high current generator . The particles which are commonly accelerated by this generator are electrons , protons and deuterons , although heavy ions may also be used [19].

It is characterized by its constant potential voltage from Ø.2 Mev to 3 Mev ,continuously variable and controlled from an operating console . The maximum current is 3 mamp at 3 Mev , reduced downward to 1ØØ μamp at Ø.2 Mev and the average beam stability is ± 1Ø% [2Ø] within period 15 min after warm up for maximum current levels . The basic construction of a Dynamitron accelerator is shown in fig (3.6) . A set of 4Ø staged cascaded rectifiers is capacitively coupled to a powerful r.f. oscillator with a frequency of 13ØkHz . Inside a cylindrical outter tank , there are two large electrodes which draw power from an oscillator and induce on r.f. potential in a set of corona rings just inside the electrodes . A large-toroidal coil is connected in parallel with the r.f. elecrodes (Harthy type) The production of positive ions of the Hydrogen or Helium isotopes carried out by duoplasmatron ion source .

The accelerator tube is attached to the ion source and passes through the cascade stack and is usually evacuated from the ground potential end. The beam vacuum system consisted of ion pumps each with a baffle , a liquid nitrogen cold trap and a mechanical

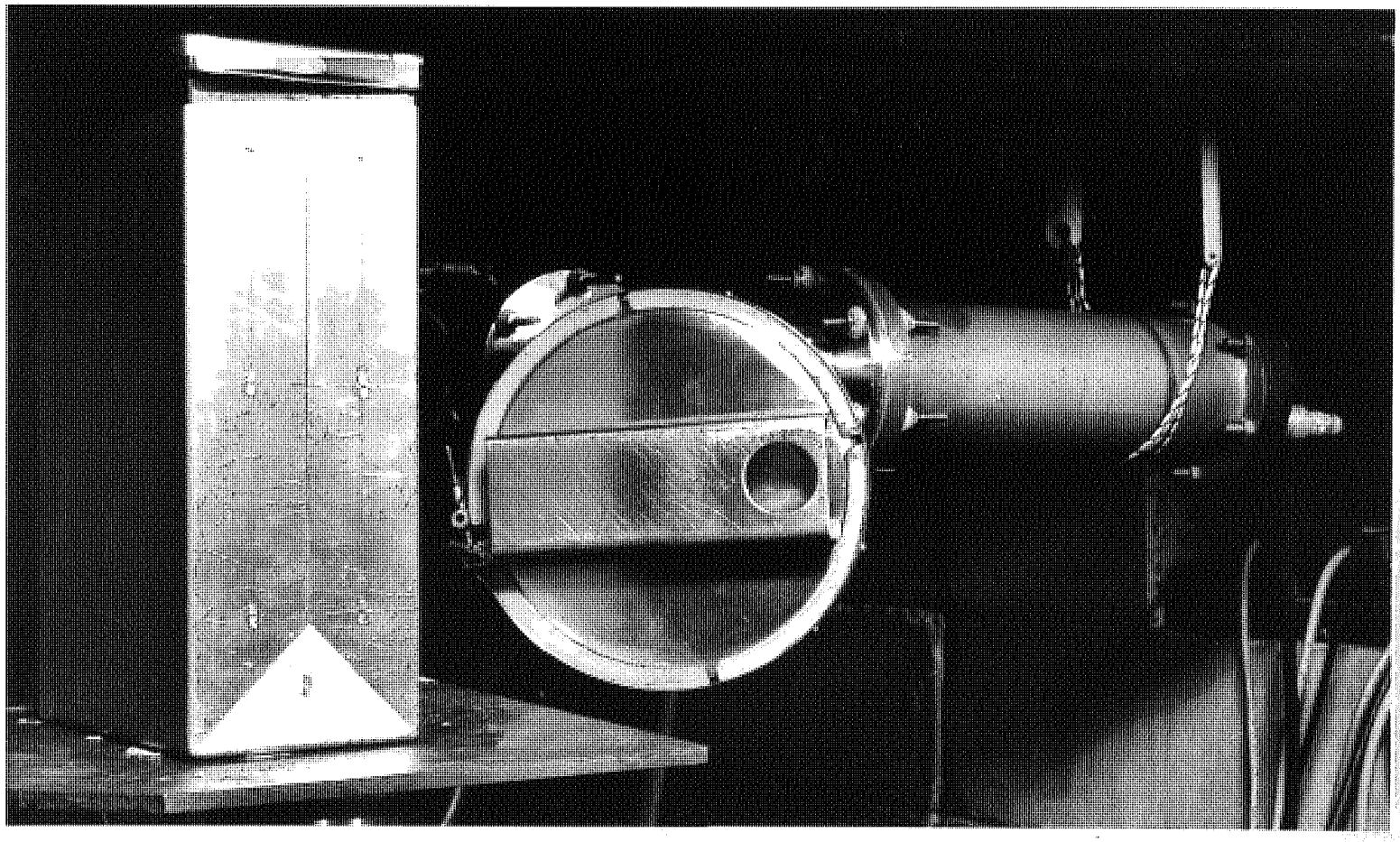

Fig (3.5) Target assembly and the scattering sample .

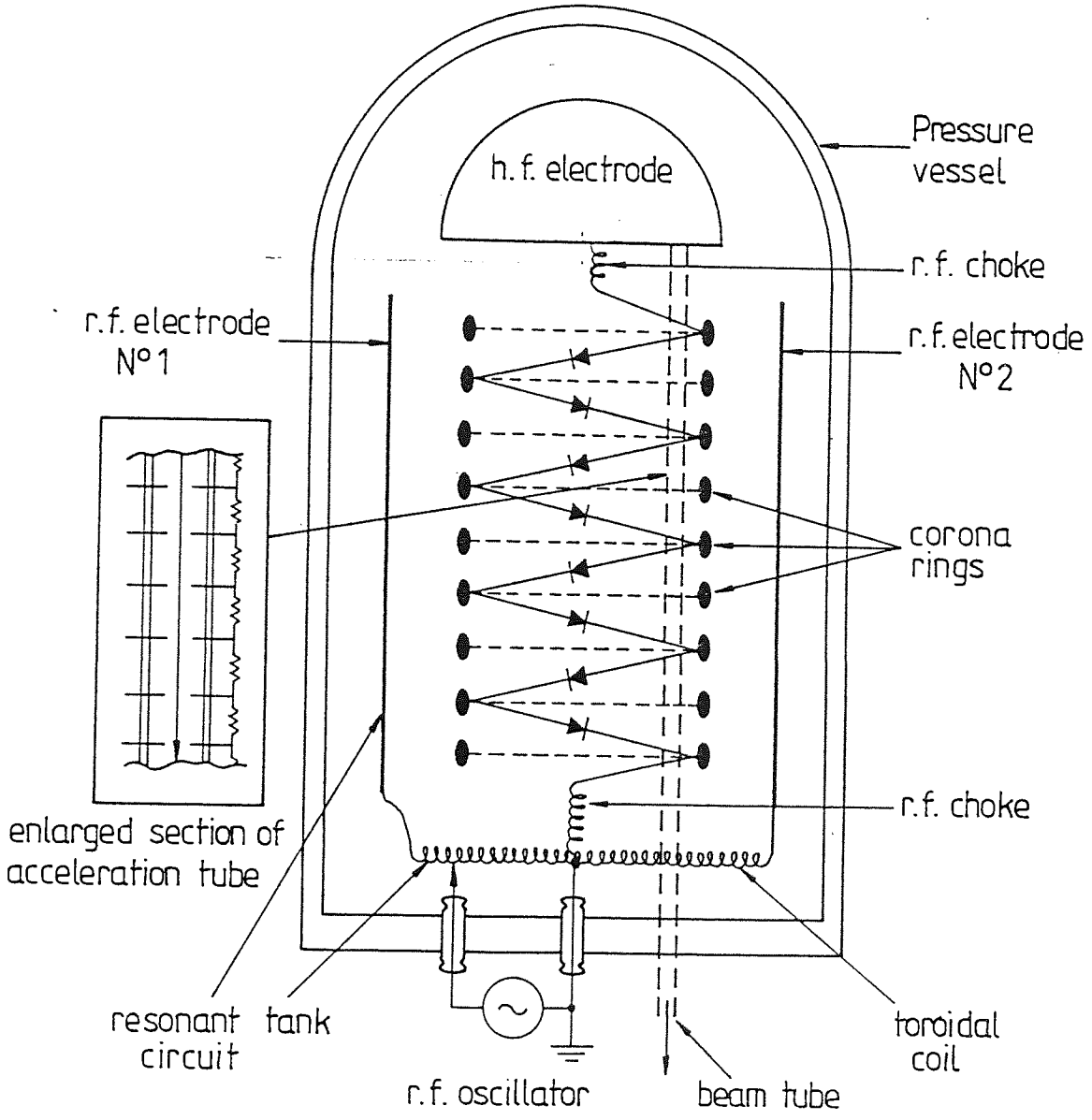

Figure (3·6) Schematic representation of a vertical section through a vertical dynamitron accelerator. [21]

backing pump .The system is capable of maintaining a base vacuum of less than 2×10^{-6} torr and an operating pressure of less than 10^{-5} torr. The beam from the ion source after passing through a crossing field analyzer is separated into its mass components . The cross field analyzer is located near the extraction electrode and utilizes permanent magnets for the H-field and variable voltage electrostatic electrodes for the crossed E-field . After the masses of the ions have been fully separated , the deuterons are deflected by a bending magnet towards the neutron producing target in the low scatter cell where the present work took place .

3.3.1 TARGET CHAMBER AND BEAM COLLIMATOR

The target was mounted inside a T-shaped stainless steel chamber situated at the end of the beam tube as shown in fig (3.7) . The TiT target foil used in the Radiation Centre was of the type TRT-51* and consisted of a 7 mg/in^2 layer of tritiated titanium on a 0.01 inch copper backing .

The foil is normally fixed at 45° to the incident deuteron beam direction and was water cooled . The area of the target struck by deuteron beam was defined by the two stainless steel and tantalum aperture plates with internal diameters of 10 mm. and 3 mm. respectively as shown in fig (3.8) .

The aperture were electrically insulated from the beam line and separated by a distance of 2 cm. The alpha-particle detector inside the T-chamber was positioned at 90° to the beam direction .

---

* Provide by Radio Chemical Centre , AMERSHAM .

Fig (3.7) Target assembly at Birmingham Radiation Centre .

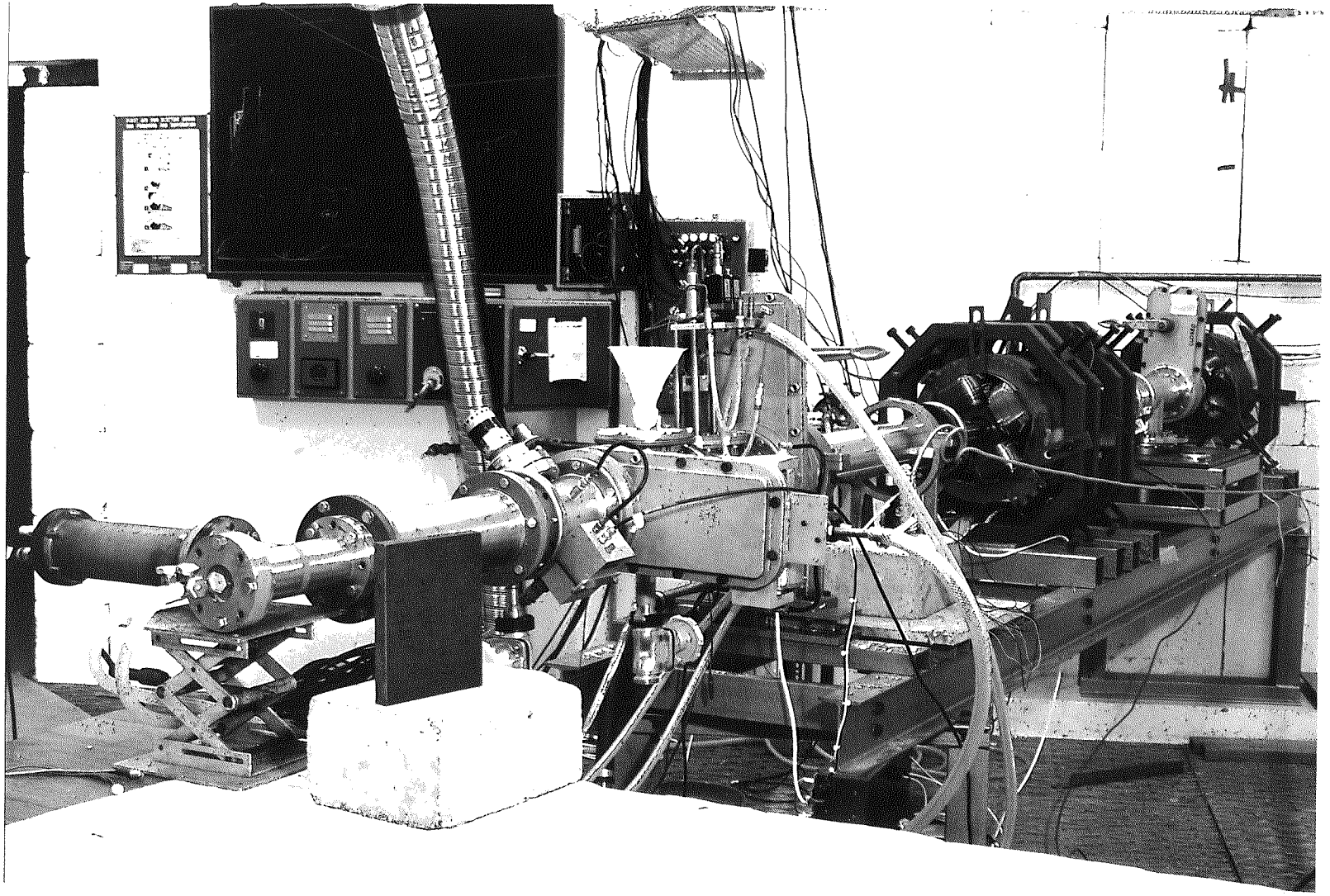

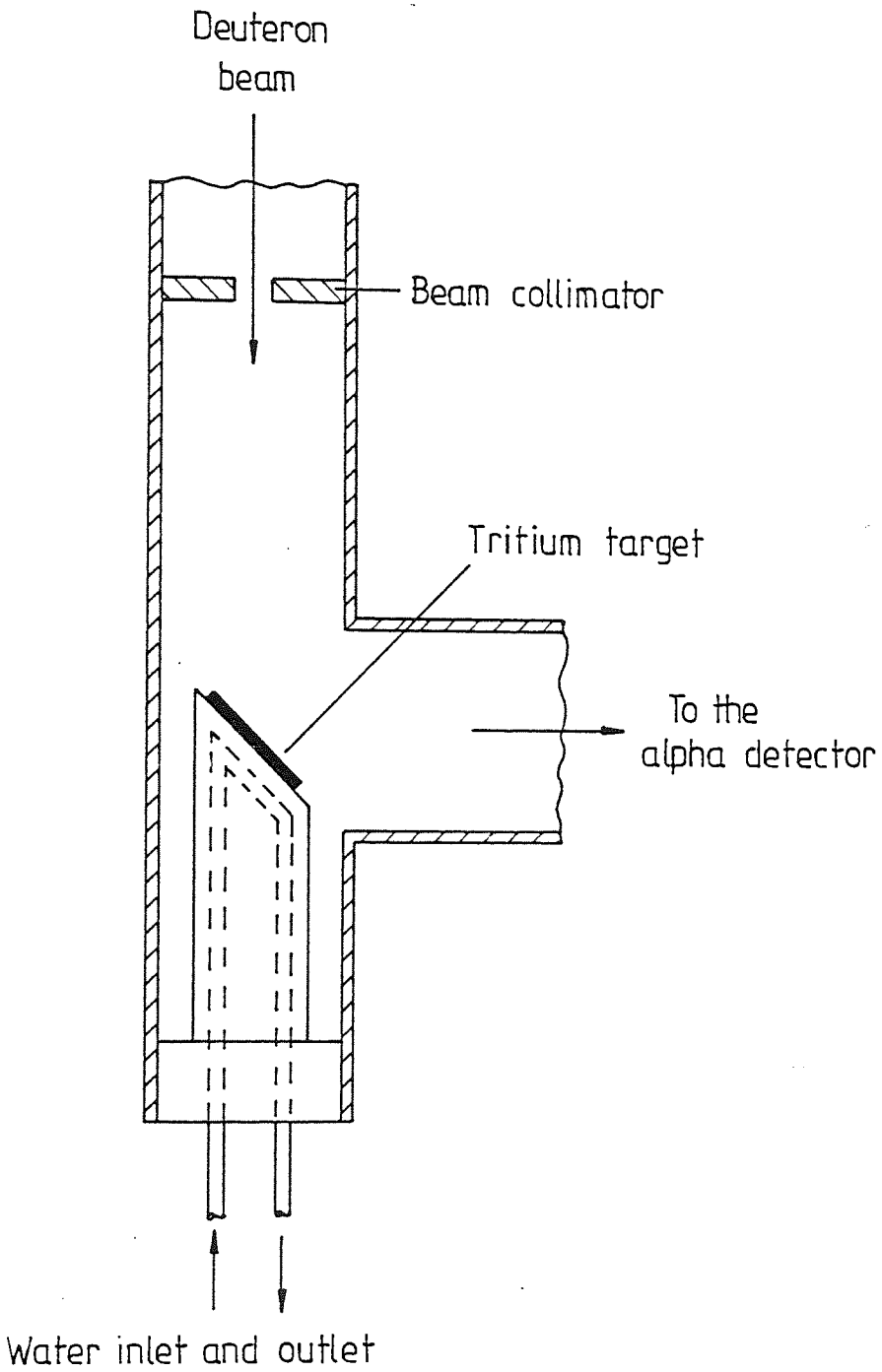

Figure 3·8 Target assembly.

3.3.2 SAMPLE POSITION AT RADIATION CENTRE

The 14.44 Mev neutrons were produced by the $T(d,n)^4He$ reaction using a 300 kev incident deuteron beam which was accelerated in the 3 Mev Dynamitron accelerator .

Due to the relativistic kinematics of the D-T reaction the neutrons were produced at an angle 78° to the incident deuteron beam . The scattering sample was placed 15 cm. from the neutron source , in order to intercept normally all the neutrons from the source associated with the alpha- particles detected at 90° to the beam direction.

3.4 SAMPLE SCATTERING GEOMETRY

The shape of the scattering sample is usually chosen as a compromise between reducing the relative background and the corrections which must be made to the experimental data .

In this work a flat plate scattering sample was used , facing the neutron beam with the neutron detector rotated about the scatterer to measure the angular distribution of neutrons .

A massive shielding was used surrounding the sample-detector system . This usually consists of a shadow bar , where a minimum solid angle subtended by the neutron detector at the source is shielded, and a massive collimator surrounding the neutron detector , providing a narrow channel through which scattered neutron can pass.

3.5 TIME-OF-FLIGHT TECHNIQUE

3.5.1 INTRODUCTION

In recent years , there have been several designs for the use of the time-of-flight technique for the study of neutron producing reactions [29-31] . They are characterized by the measurement of the time elapsed between the time when the neutron is produced at the target and the time at which it is detected .

The major improvement in this technique has been the minimization of the time resolution of the spectrometers , in order that closely spaced neutron energy groups can be resolved .

If a neutron source emits neutron pulses with an energy (En) Mev measured at a distance (L) meters from the source .

The time-of-flight in nsec of the neutrons is given by :

$$\tau_{NR} = \frac{72.298}{\sqrt{En}} \cdot L \qquad (3.1)$$

The accuracy with which energy measurements are possible with the time-of-flight method is connected with uncertainties ($\Delta\tau$) in the flight time and (ΔL) in the flight path . In this case the resolution in energy of non-relativistic neutrons is related to the time resolution by :

$$\Delta En^{NR} = 2\, En^{NR} \left[\left(\frac{\Delta\tau}{\tau} \right)^2 + \left(\frac{\Delta L}{L} \right)^2 \right]^{\frac{1}{2}} \qquad (3.2)$$

where ΔEn^{NR} = energy resolution of non-relativistic (NR) neutrons .

En^{NR} = energy of non-relativistic neutrons in Mev .

If , as is often the case , $\frac{\Delta L}{L} << \frac{\Delta\tau}{\tau}$ then :

$$\left[\frac{\Delta En}{En} \right]^{NR} \simeq 2 \frac{\Delta\tau}{\tau} = 2 v_n \frac{\Delta L}{L} \qquad (3.3)$$

In the case of relativistic neutrons ,the neutron energy En in Mev is :

$$En = E_o\left[\left(1 - \frac{v_n^2}{c^2} \right)^{-\frac{1}{2}} - 1 \right] \qquad (3.4)$$

therefore :

$$En = E_o\left[\left(1 - \frac{L^2}{\tau^2} \cdot \frac{1}{c^2} \right)^{-\frac{1}{2}} - 1 \right] \qquad (3.5)$$

The time-of-flight of relativistic neutrons [24] is :

$$\tau = \left(\frac{3.335}{\left(1 - \left[\frac{939.5}{En + 939.5} \right]^2 \right)^{\frac{1}{2}}} \right)^{*} L \qquad (3.6)$$

In the present work the difference between the relativistic and non-relativistic calculation of $\left(\frac{\tau}{L}\right)$ for the neutron energy 14 Mev and flight path of 1 meter is ($\emptyset.215 \pm \emptyset.\emptyset\emptyset6$) nsec/m .

3.5.2 PRINCIPLES OF TIME-OF-FLIGHT SPECTROMETRY

The basic principles involved in using time of flight techniques are :

1- The production of a signal giving the time zero at the start of the flight of neutron whose energy is to be measured .

2- The production of another signal corresponding to the end of its flight .

There are two different methods used for the production of the time zero :

1- A pulsed beam of particles to initiate neutron emission .

2- The detection of the associated particle emmited from the neutron producing reaction .

---

* The values of the constants are taken from the Review article of Taylor etal [23] .

3.5.2.1 THE PULSED BEAM TECHNIQUE

In this technique the beam of charged particles striking the target is modulated by radio frequency voltage . Some of these source neutrons striking the scattering sample are scattered through a known angle , and traverse a given flight path to a neutron detector. In principle ,the time of arrival of a neutron at the detector is measured relative to a pulse derived once per cycle from the r.f. voltage.

From the knowledge of this time , the neutron energy can be obtained.This method has been widely employed [25-27] in nuclear structure sutd ies by using a single detector which is sequentially arranged to make a number of measurements at various scattering angles and incident neutron energies .

There are two conditions which imposed some limitation [28] on this technique . These are :

1- The duration of the modulated charged pulse should be much shorter than the time-of-flight of the highest energy neutrons involved.

2- The repetition period of the pulse should be longer than the time-of-flight of the neutron group of lowest energy to be observed .

3.5.2.2 THE ASSOCIATED PARTICLE METHOD

The use of the associated charged particle from the neutron producing reaction $T(d,n)^4He$, to provide a zero time signal , has advantages which may make this method preferable to the use of a pulse beam method in some applications [29] .

In the most general case , where the possibility exists of deriving the neutron start signal from the associated ^{4}He recoiling nucleus for time of flight measurements , the recoil particle can be detected at an angle of 90° for example , the angle of emission , and the energy of the emitted neutrons can be determined .

The main requirement of this method is that the charged particle detector should be kept as close as possible to the neutron source in order to obtain the maximum rate of coincidence .

A great advantage of this technique is , that it offers the possibility of selecting a particular group of neutron energies in coincidence with associated charge particle . In addition , this method which achieves a maximum time resolution of the produced neutron is only limited by the scintillator , photomultiplier and electronic equipment .

3.5.3 TIME-OF-FLIGHT ELECTRONICS

A block diagram of the electronics is shown in fig (3.9) . The output signal from the neutron detector is fed through an emitter follower , with sufficient amplitude to exceed a given discriminator level setting in the constant fraction discriminator (CFD-436) . the function of the discriminator in this unit (CFD) is to permit the selection of signals of interest and to eliminate any response to smaller signals .

The negative output logic signal from CFD provides a short signal for the TIME TO PULSE HEIGHT CONVERTOR (TPHC). The signals from the alpha- particle detector pass through a 100MHz discriminator (DIS) which provides a negative logic signal for the GATE AND DELAY GENERATOR (GDG) . The GDG furnishes a standard negative delayed Marker pulse with selected amplitude and width . The delay time is continously variable from 100nsec to 110 μsec . The output from this operates as the stop signal for the TPHC .

In the TPHC , the time interval between the arrival of a start neutron signal and the next alpha-particle stop signal is converted to an output voltage .

The amplitude of the output signals is directly proportional to the time interval . The time conversion in the TPHC was adjusted to 200 nsec in this work.

The output pulses from the TPHC , analysed by a 1024 channel Pulse Height Analyzer (PHA) - type CANBERRA series-30 were used to give time interval spectra . In the dynamitron , the output pulses from the TPHC were analyzed by the ANALYZER SYSTEM 5406B through an

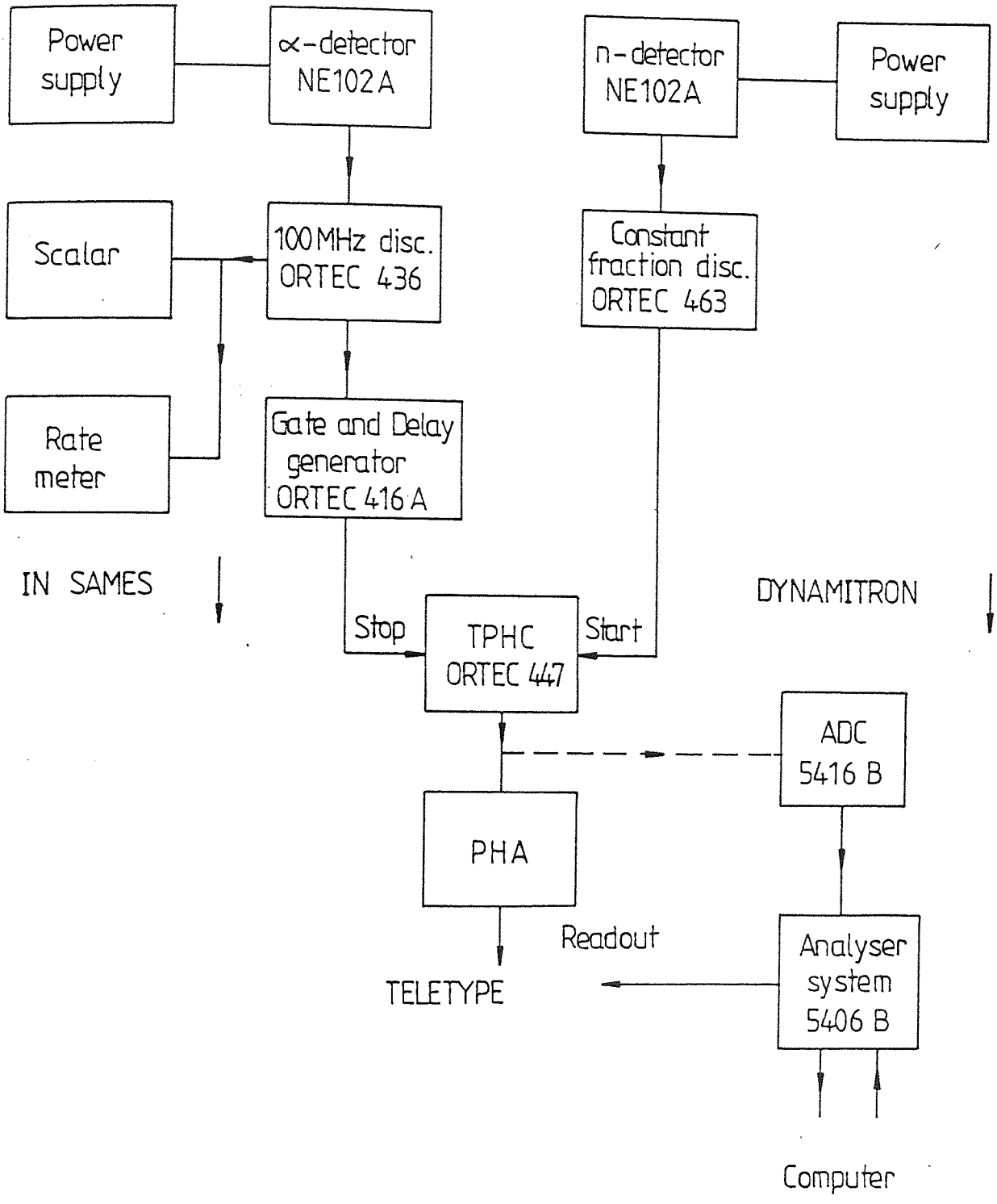

Figure (3.9) Block diagram of time-of-flight electronics

Analog-to-Digital convertor (ADC) 5416B and the output data was stored in a HEWLETT-PACKARD computer system .

A scalar type NE4681 was used with the CFD to monitor the alpha-particle count as a function of neutrons produced at the target .

3.6 THE TIME RESOLUTION OF THE SPECTROMETER

The time resolution of a time-of-flight spectrometer determines the energy separation of the elastic and inelastic neutron peaks which can be resolved . It also establishes the accuracy with which the neutron energy can be determined and indicates the limit of sensitivty of the spectrometer .

The FWHM of the neutron time distribution allows the time resolution to be estimated and can be used to measure the overall timing uncertainties [32] in the experiment .

The major timing uncertainties are :

1- Neutron production , this can be determined to an accuracy of 7Ø kev (Ø.3 nsec) this being the energy spread of alpha-particles through a 12° angular range and a 9Ø mm target to alpha-detector flight path .

2- Neutron detection time , which is related to the time variations in the formation of the detector signal originating from several sources of time uncertainties described by MOSZYNSKI and BENGTSON (1979) [32] . These include , the energy transfer from the detected nuclear particles to the optical levels in the scintillator , the finite decay time of light emitting states in the scintillator and the light yield

of the scintillator as a function of the energy of the detected radiation , the variation of the time of light collection from the scintillator at the photocathode , the variation of the transit times of photoelectrons from the photocathode to the first dynode , and the variation of the multiplication process in the electron multiplier .

3- Time variations associated with the electronic equipment , which are dependent on the effect of the electronic noise and stability .

The FWHM in fig (3.11) ,is a measure of the resolution of the system and for the 14 Mev direct neutrons may be seen to be (Ø.5±Ø.ØØ4) Mev ,i.e.(2.5±Ø.2)nsec with the fractional FWHM [E_{fwhm}/En] being 3.5 %. For 14.44 Mev neutrons the direct beam time resolution is 2.68±Ø.26 nsec as shown in fig (3.11) .

Figs (3.12) show typical time-of-flight spectra for 14 Mev neutrons scattered from 4cm carbon sample at 3Ø° . The neutron inelastic scattering from the 1st excited state of carbon (Q=-4.43 Mev) is well resolved from the elastic peak .

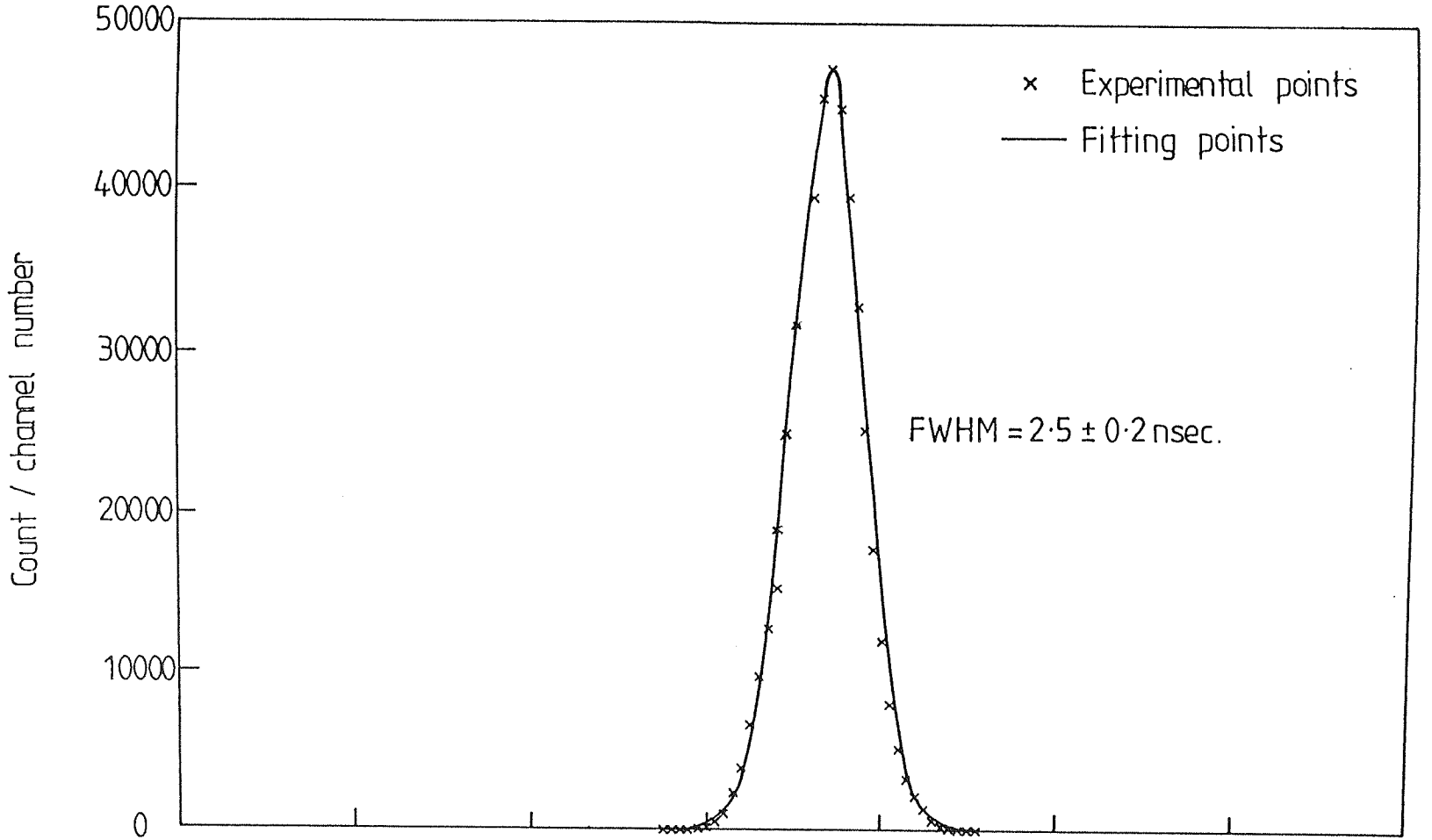

Figure (3·10) Direct beam of 14·1 MeV neutron.

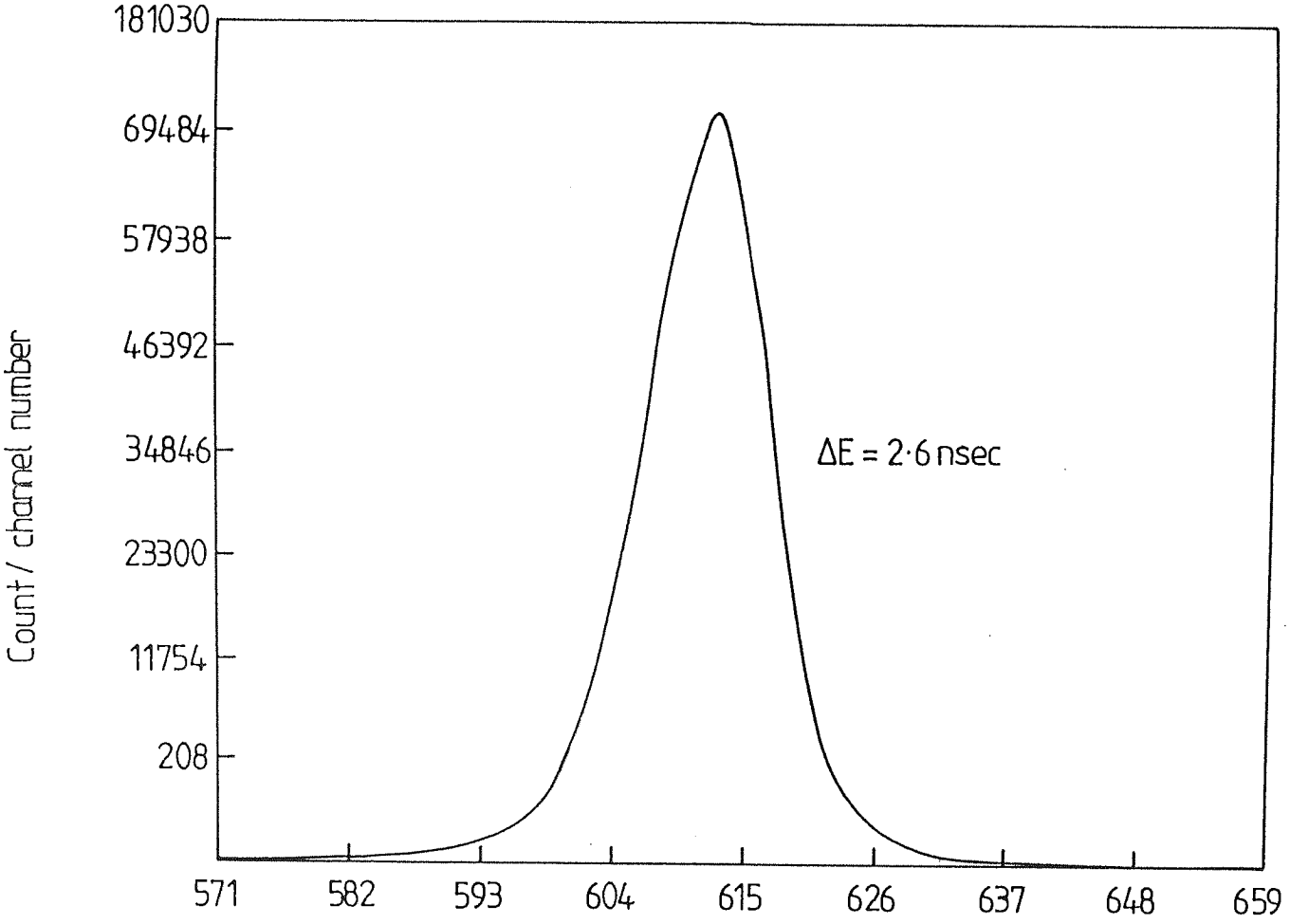

Figure (3·11) 14·44 MeV Direct beam, without sample.

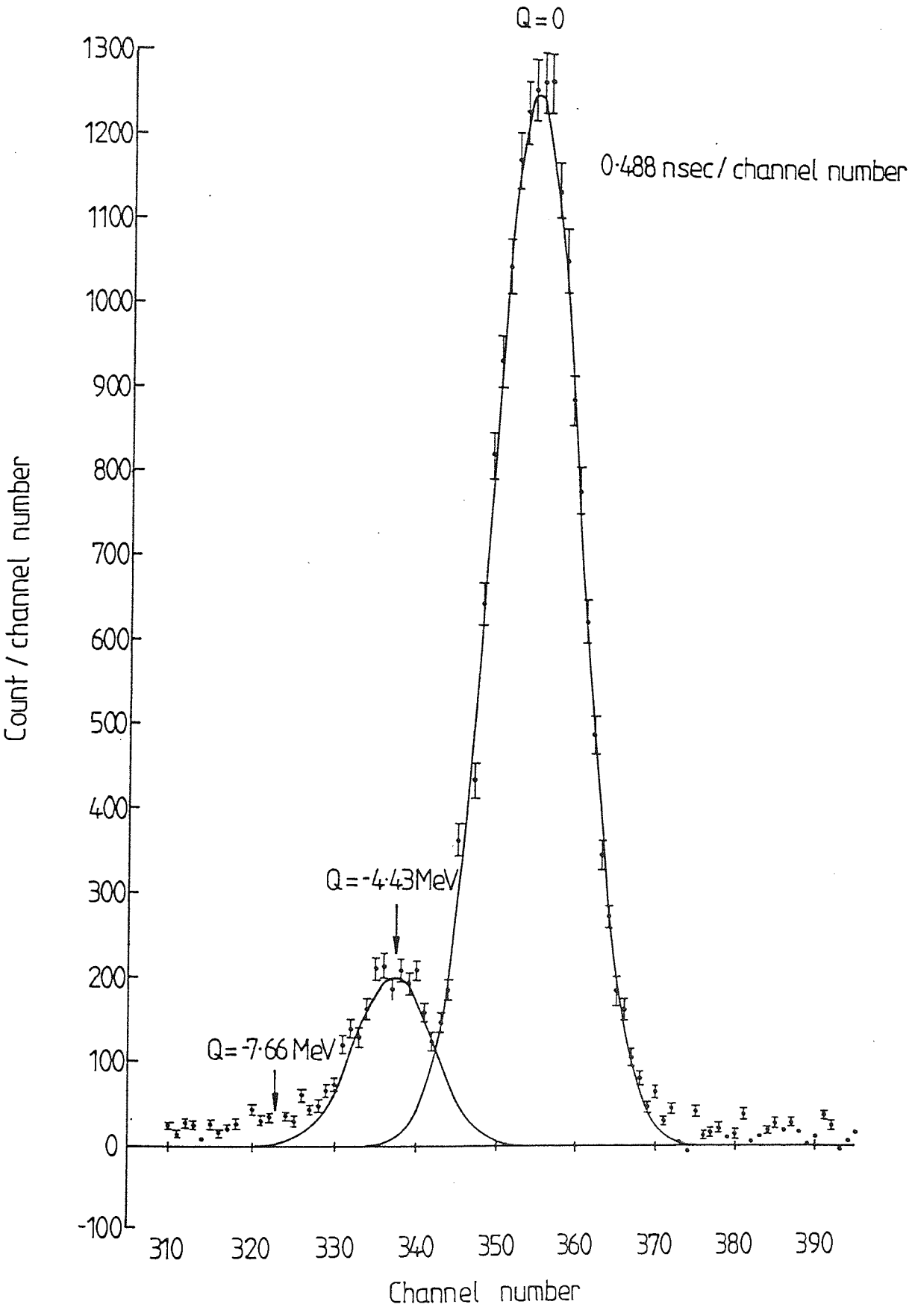

Figure (3·12) Time-of-flight spectrum from 14 MeV neutrons by C^{12} - 4 cm - at 30° Lab angle, the neutron scattered from 1st excited state Q = -4·43 MeV well resolved from elastic peak.

CHAPTER FOUR

NEUTRON AND CHARGED PARTICLE DETECTION

CHAPTER FOUR

NEUTRON AND CHARGED PARTICLE DETECTION

4.1 NEUTRON DETECTION

4.1.1 GENERAL PROPERTIES

Neutrons , being uncharged massive particles , readily penetrate the electron clouds and collide with nuclei of the detection medium . Such nuclear reactions can produce a charged particle which can be utilized for neutron detection .

One of the commonest methods for the detection of fast neutrons is to detect proton recoils from an hydrogenous absorber produced by a collision process. Devices based on this neutron interaction are often referred to as proton recoil detectors .

The n-p reaction has a large cross-section for neutron energies in the relavent range as shown in fig (4.1) .

The energy transfered to the recoil proton can range anywhere between zero and the full neutron energy , so that the average recoil proton has an energy about one half that of the original neutron .

In the elastic scattering process ,fig (4.2),the application of the principles of the conservation of energy and momentum reveals that (Ep) aquired by the proton in collision with a neutron of unit mass is given by :

$$E_R = \frac{4A}{(A+1)^2} \cdot En \cdot \cos^2\theta \qquad (4.1)$$

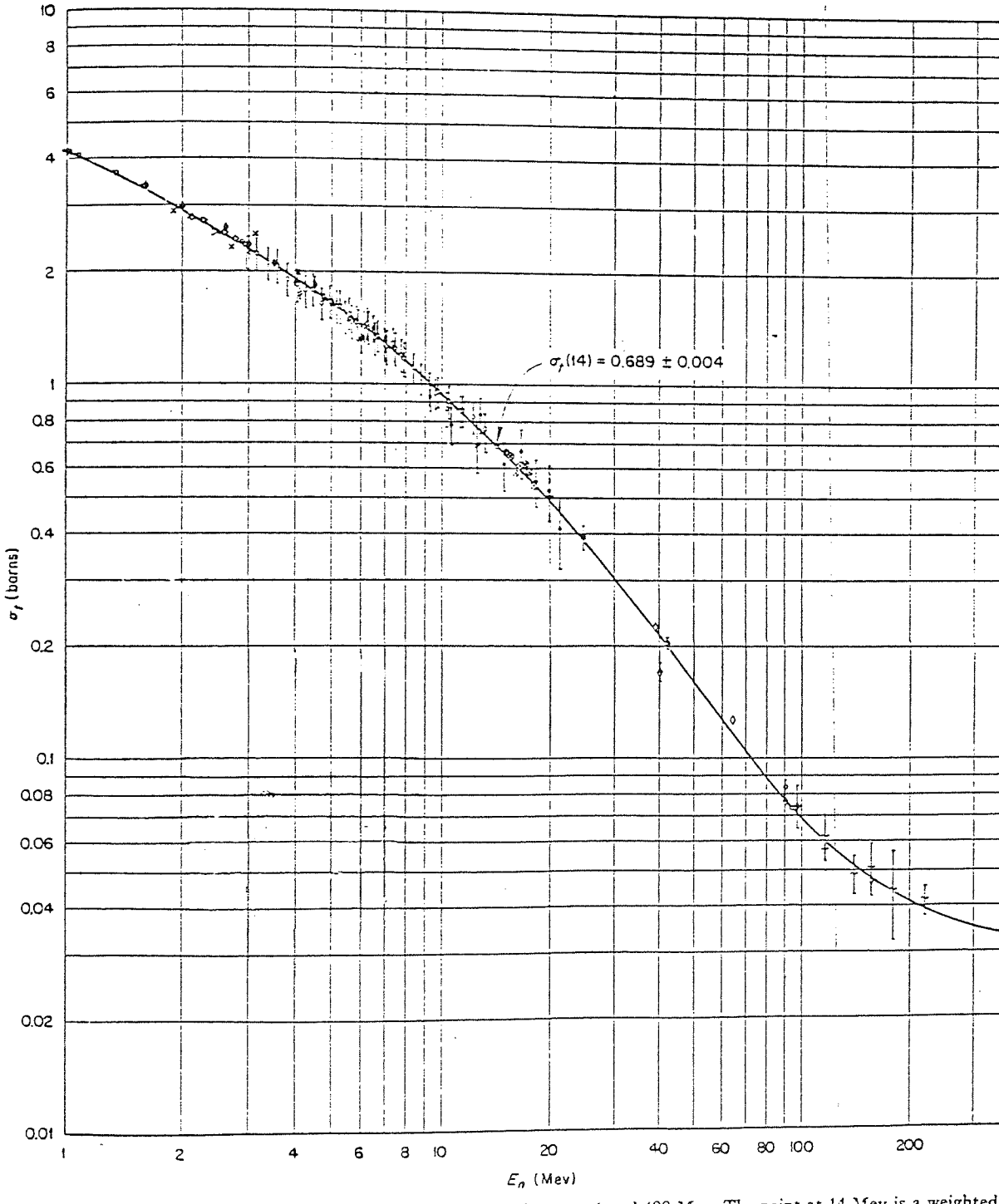

Fig(4-1)Total cross section of hydrogen for neutrons of energies between 1 and 400 Mev. The point at 14 Mev is a weighted of measurements reported in the literature (106)

and in the centre-of-mass system :

$$E_R = \frac{2A}{(A+1)^2} En.(1-\cos\Theta) \qquad (4.2)$$

Where En is the energy of the incident neutron , Θ is the scattering angle of the recoil proton in the c.m. system , θ is the scattering angle of the incident neutron in the c.m. system , and A is the mass of the proton .

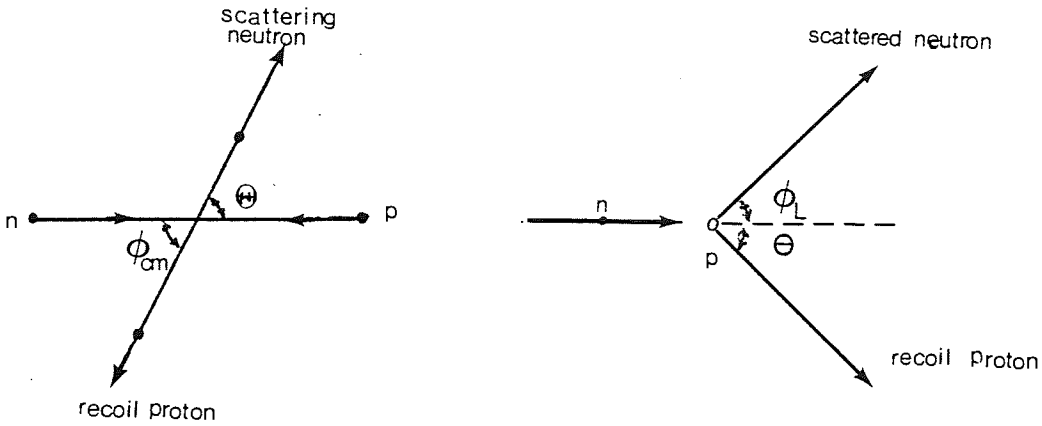

Fig (4.2) Neutron elastic scattering diagrams for c.m. and lab. system .

At a neutron scattering angle $\phi_L = \frac{\pi}{2}$ with $\theta = 0$, the incident neutron energy is wholly transfered to the struck proton in a single encounter , when the maximum possible recoil energy becomes :

$$E_R\Big]_{max} = \frac{4A}{(A+1)^2} \cdot En \qquad (4.3)$$

As shown in fig (4.3) , when the target mass increases the maximum fractional energy $(E_R / En\Big]_{max})$ transfer decreases , and this explains

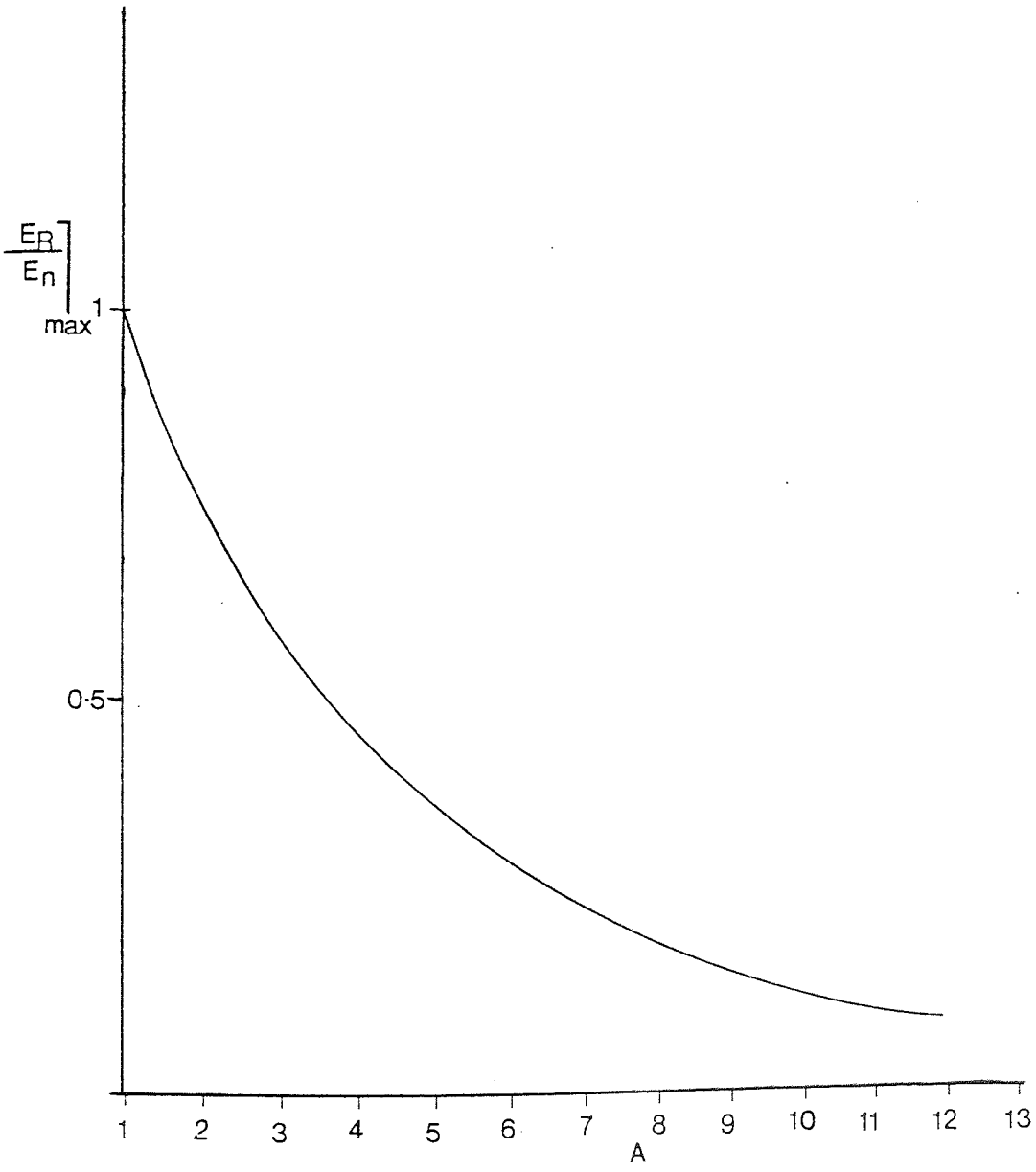

Fig (4.3) Maximum fractional energy, equation (4.3) .

why only light nuclei are of primary interest in recoil detectors , with hydrogen assuming the predominant rôle .

4.1.2 ENERGY DISTRIBUTION OF THE RECOIL PROTONS

In principle, as a result of the n-p scattering process, we expect a continuum of possible recoil energies at different scattering angles.

The probability that the neutron will be scattered into $d\Theta$ about Θ is :

$$P(\Theta).d\Theta = 2\pi \sin\Theta.d\Theta. \frac{\sigma(\Theta)}{\sigma_s} \qquad (4.4)$$

Where $\sigma(\Theta)$= the differential scattering cross-section .

Θ = neutron scattering angle in the cm system .

σ_s= total scattering cross-section integrated over all angles .

Therefore , the distribution of the recoil nucleus energies can be described by the probability $P(E_R)\, dE_R$. The probability that a proton aquires an energy between E_R and $E_R + dE_R$ is :

$$P(E_R) \cdot dE_R = 2\pi \cdot \sin\Theta \cdot \frac{\sigma(\Theta)}{\sigma_s} \cdot d\Theta \qquad (4.5)$$

Differentiating equation (4.2) and combining the result with equation(4.5) gives :

$$P(E_R) = \frac{(A+1)^2}{A} \cdot \frac{\sigma(\Theta)}{\sigma_s} \cdot \frac{\pi}{En} \qquad (4.6)$$

The shape of the recoil energy continuum, in equation (4.6), can be expected to be the same as the shape of differential scattering cross-section vs neutron scattering angle Θ in c.m. system [65].

From the known spherical symmetry of n-p scattering in the c.m. system $[\sigma(\Theta)/\ \sigma_s\ ]$ is equal to $(\frac{1}{4\pi})$. Hence :

$$P(E_R) = \begin{cases} \frac{1}{E_n} & E_R \leq E_n \\ 0 & E_R > E_n \end{cases} \qquad (4.7)$$

The expected proton recoil energy distribution is a simple rectangle, extending from zero to the full incident neutron energy En, as sketched in fig (4.4).

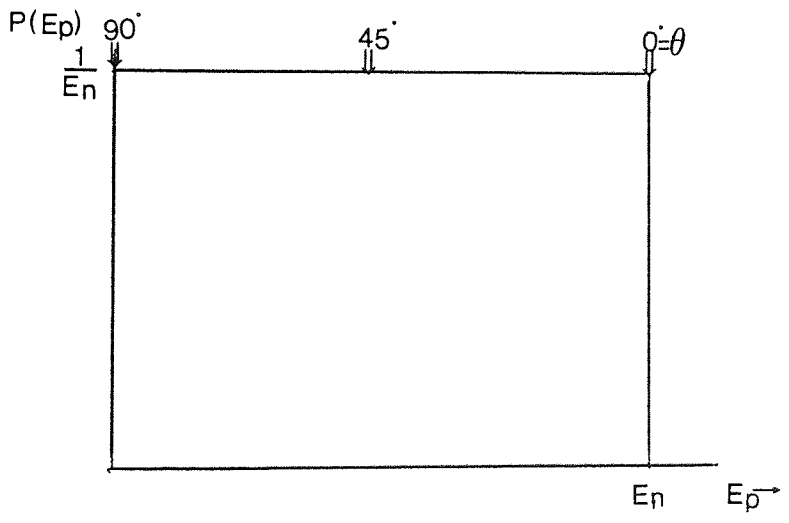

Fig (4.4) Energy distribution of recoil protons produced by monoenergetic neutrons. Recoil energies are indicated for various values of the recoil emission angle Θ as given by eq.(4.1).

4.1.3 ORGANIC SCINTILLATORS

Organic scintillators are efficient detectors of neutrons from En $\simeq$ 10 kev to 200 Mev [47], becuase of their high hydrogen content (1.1 atoms of hydrogen per atom of carbon and a density of 1.0 g/cm^3) . Several more suitable organic scintillators have been introduced within the last few years , among them liquid scintillators (e.g. NE213 , NE224, NE228) that combine an organic scintillant dissolved in a hydrogen containing an organic solvent , and plastic scintillators (e.g. NE102A , NE110) in which an organic scintillant is incorporated in a bulk matrix of polymerized hydrocarbon .

With these organic scintillators , it is possible to convert as large a fraction as possible of the incident radiation energy into detectable visible light with a high scintillation efficiency. This conversion should be linear (i.e. the light yield should be proportional to the deposited energy over as wide a range as possible.).The scintillation medium with its good optical quality and transparency to the wavelength of its own fluorescent emission , can offer a short decay time of the induced light , so that fast pulses can be generated .

The early development of organic scintillation detectors and scintillation mechanisms have been reviewed by BIRKS (1964) [48] .

4.1.4 DESIRED CHARACTERISTICS OF NEUTRON DETECTOR

The important general characteristic, which established the organic scintillators as the best detectors of fast neutrons for this work , may be summarized as :

a- In order to monitor the entire spectrum of the neutron beam the

neutron attenuation in the detector (hence , it is efficiency) should be small .

b- Since high resolution is required in the time-of-flight technique , it is essential that the detector be capable of good timing resolution .

C- If the neutron detector possesses some pulse height resolution , the contribution of background (due to gamma-rays) can be reduced by selecting only that range of pulse heights produced by the neutrons of interest .

It is desirable that the neutron detector produces a pulse height distribution which characterizes the energy of the incident neutron. This feature often complements the high energy resolution obtainable from the time-of-flight technique .

4.1.5 DETECTOR EFFICIENCY

In principle, neutron detectors will give rise to an output pulse for each neutron which interacts within their active volume . Therefore , neutrons need to have a high probability of undergoing an n-p interaction in the detector before detection is possible . Because neutrons can travel large distances between interactions , it is necessary to know the neutron detector efficiency accurately in order to relate the number of recoil protons counted to the number of neutrons incident onto the detector . If only one nucleus is present in the detector , the intrinsic efficiency is given simply by :

$$\varepsilon = 1 - \exp (-N.\sigma_s.l) = \frac{N_p}{N_i} \qquad (4.8)$$

Where , N is the number of target nuclei per unit volume , σ_s is the scattering cross-section of the recoil nuclei , l is the path length through the detector , Np is the number of recoil nuclei produced in the detector and Ni is the number of incident neutrons all of energy E_o. For a plastic scintillator of length l consisting of carbon and hydrogen , the number of recoil protons produced in a single scattering is :

$$N_1 (E_o, l) = \frac{N_o \cdot n_H \sigma_H \cdot l}{(a \cdot l)} \cdot [\, 1 - \exp (- a.l) \,] \qquad (4.9)$$

Where N_o is the incident neutron flux at energy E_o , $a = n_H.\sigma_H + n_C.\sigma_C$, l is the length of the scintillator , σ_H is the n-p scattering cross-section , σ_C is the total neutron cross-section for carbon , and n_H , n_C are the total number of hydrogen and carbon atoms per cm^3 in the scintillator , respectively .

Therefore , the efficiency of the detector can be calculated by :

$$\varepsilon_1(E_o, l) = \frac{n_H \cdot \sigma_H \cdot l \cdot \{1 - \exp(-a \cdot l)\}}{(a \cdot l)} \qquad (4.10)$$

In the plastic scintillator some of the neutrons scattered by carbon nuclei will produce recoil protons in a second scattering event . Since the number of neutrons scattered once by carbon in length l is

$$N_C(E_o, l) = \frac{N_o \cdot n_C \cdot \sigma_C}{a} \cdot [\, 1 - \exp (- a \cdot l) \,] \qquad (4.11)$$

The average neutron energy in the secondary scattering event is $\emptyset.85 E_o$ (TOMS (1971) [49] , SWARTZ (1960) [50]) and traverse an average path length $\frac{1}{a}$ in the scintillator ; hence the number of recoil protons produced in this process is :

$$N_{2C}(E_o, l, l_1) = \frac{N_C \; n_H \sigma_H}{a_1} [\; 1 - \exp\; (\; - a_1 \cdot l_1) \;] \qquad (4.12)$$

The total number of recoil protons is now $[\; N_1(E_o, l) + N_{2C}(E_o, l, l_1)]$, where l assumed to be $\frac{1}{2} l$.

The efficiency of the detector including double scattering is :

$$\mathcal{E}_2(E_o, l, l_1) = \mathcal{E}_1(E_o, l) \cdot [\; 1 + \frac{N_{2C}(E_o, l, l_1)}{N_1(E_o, l)}] \qquad (4.13)$$

Table (4.1) and fig (4.5) show the variation of $\mathcal{E}_1$ and $\mathcal{E}_2$ with neutron energy for NE102A plastic scintillator . An efficiency of 14.3 % is achieved with 50.8 mm long plastic having a density [42] of $n_H = 5.25 \times 10^{22}$ atom/cm^3 , $n_C = 4.75 \times 10^{22}$ atom/cm^3 .

4.1.6 NONLINEAR RESPONSE OF PLASTIC SCINTILLATOR NE102A

Since the output pulse height distribution from a plastic scintillator mounted on a photomultiplier tube is proportional to the flourescence output yield L of the scintillator . Therefore , the output L is directly proportional to the energy which the proton loses.

It is well known [53-54] that the differential light output $(\frac{dL}{dX})$ of a plastic scintillator is a non-linear function of the differential ionization energy loss $(\frac{dE}{dX})$ to heavily ionizing particles . BIRKS(1952) [55] has expressed this nonlinearity of response at high rates of energy loss in the form :

$$\frac{dL}{dX} = s \cdot (\frac{dE}{dX}) \cdot [\; 1 + kB \cdot \frac{dE}{dX} \;]^{-1} \qquad (4.14)$$

Where s and kB are constants .

Table (4.1)

NEUTRON DETECTOR EFFICIENCY

E (Mev)	ε_1 %	ε_2 %
1	53.2	64.7
2	45.Ø	52.3
3	39.3	44.5
4	32.1	38.2
5	3Ø.6	34.4
6	27.8	31.1
7	25.5	28.2
8	23.Ø	25.8
9	2Ø.8	23.6
1Ø	19.3	21.9
11	17.8	2Ø.3
12	16.5	19.Ø
13	15.3	17.7
14	14.3	14.6
15	13.4	15.7

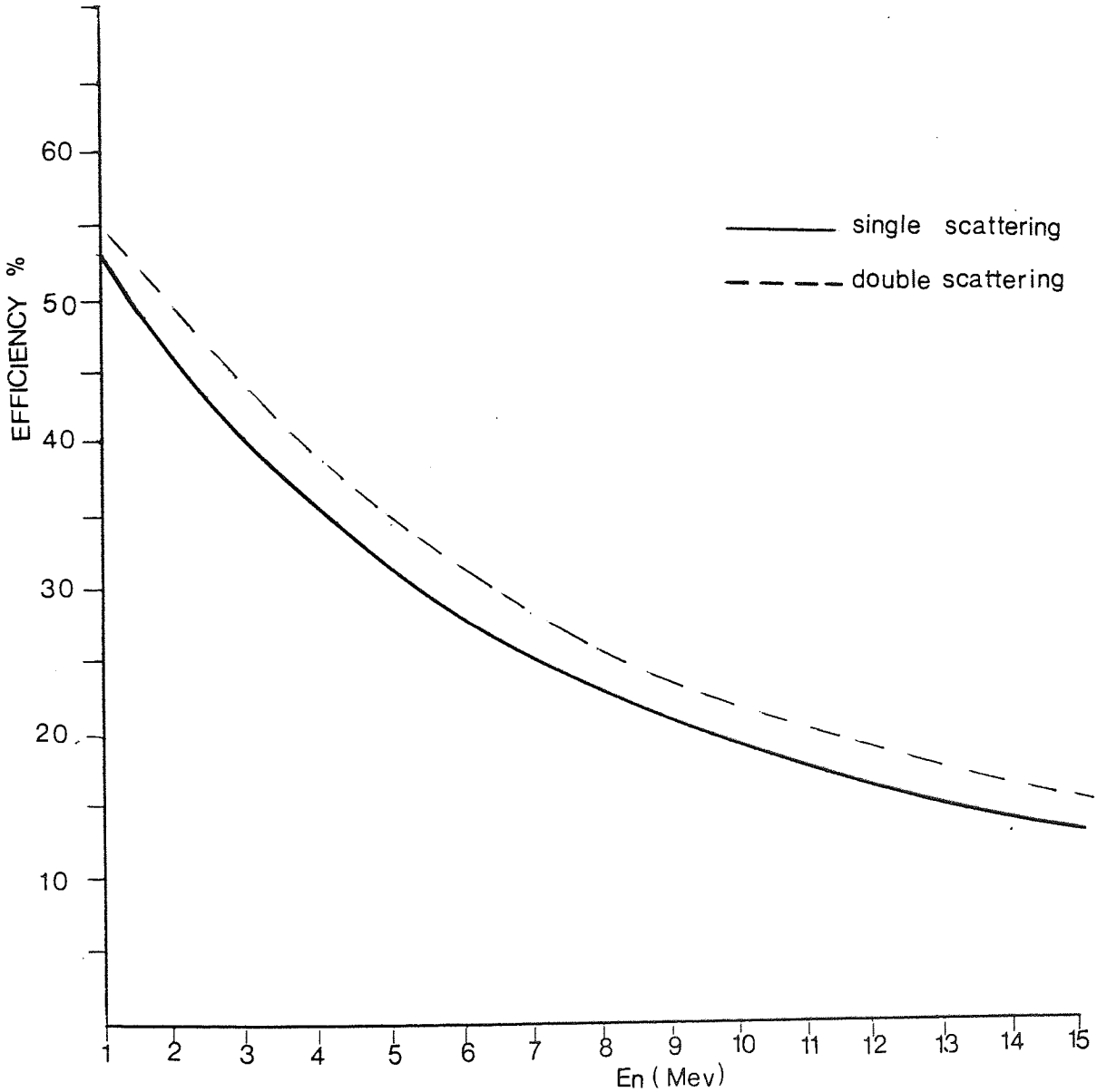

Fig (4.5) Efficiency of NE102A Plastic scintillator.*

* The values of σ_H and σ_C in eq.(4.10) have been taken from REFS [50-52].

CHOU (1952) [56] proposed a modified form of equation (4.14) to fit the experimental data at high values of $\frac{dE}{dX}$:

$$\frac{dL}{dX} = S\left(\frac{dE}{dX}\right)\left[\, 1 + kB\,\frac{dE}{dX} + C\left(\frac{dE}{dX}\right)^{2}\,\right]^{-1} \qquad (4.15)$$

Where C is a constant chosen to give the best fit to the data .

In 1953 , WRIGHT [57] using a different mechanism , suggests :

$$\frac{dL}{dX} = A\,\ln\left[\, 1 + \alpha\left(\frac{dE}{dX}\right)\,\right] \qquad (4.16)$$

Equation (14.16) reduces to equation (14.14) at low values of $\frac{dE}{dX}$ when constants A and α become $\left(\frac{S}{kB}\right)$ and (2kB) respectively . These three formula fit the experimental data equally well [47,52] . In the present work BIRK'S formula has been used to calculate the plastic scintillator pulse height output . The range-energy relationship for $CH_{1.105}$, which is the composition of the plastic scintillator NE1Ø2A , was taken as that for CH given by the tables of RICHARD and MANDEY (1954) [58] , and ZIEGLER (1977) [59] . The energy loss $\left(\frac{dE}{dX}\right)$ can be calculated by the following formula and is listed in table (4.2) : -

$$\left(\frac{dE}{dX}\right)_{1.105} = Ø.917\,\left(\frac{dE}{dX}\right)_{C} + Ø.ØØ8\,\left(\frac{dE}{dX}\right)_{H} \qquad (4.17)$$

For energies in the range 1 to 15Ø Mev GOODING and PUGH (1960) [60] have used the following range-energy relationships to compute the response of the plastic scintillator NE1Ø2A to different particles which agrees well with equation (4.17) :

$$\frac{dE}{dX} = 16.94\ x^{-0.448} \qquad \text{(for protons)} \qquad (4.18)$$

Where the energy is in the Mev and the range x is in gm/cm^2.

We can represent the scintillator output by the variable p = L/s and rewrite BIRK's formula ,equation (4.14),in terms of dP/dE as follows

$$\frac{dP}{dE} = S^{-1}\frac{dL}{dE} = \left(1 + kB \frac{dE}{dX}^{-1}\right) \qquad (4.19)$$

In the case of protons with energies of a few Mev ,dE/dX cannot be neglected , therefore the pulse height (P) must be determined by integrating equation(4.19) numerically between zero and E_p :

$$P = \int_0^{Ep} \left(1 + kB \frac{dE}{dX}\right)^{-1} dE \qquad (4.20)$$

For fast electrons of sufficiently large values of E_e impinging on an organic scintillator , dE/dX is small , and equations (4.19) and (4.20) become :

$$dP/dE = 1 \qquad : \qquad P = Ee \qquad : \quad kB = 10 \pm 1 \qquad (4.21)$$

The calculation of dP/dE and P has been carried out for NE102A scintillator with $(10 \pm 1) \times 10^{-3}$ g/cm^2.Mev taken from EVANS and BELLAMY(1958)[62] and others [54]. The results of this calculation are presented in figures (4.6) and (4.7) and listed in table (4.2) . The variation of (dL/dX) with (dE/dX) [equation (4.14)] is plotted in fig (4.8) at a relative value of S = 0.82 ± 3 % which has been taken from PRESCOTT(1961) [54] and KNOLL (1979) [65] .

Suppose the number of recoil protons with energies E and E + dE is :

$$dN = N(E)\ dE \qquad (4.22)$$

Hence , the number of pulses between P and P + dP is :

$$dN = N(p)\ dp \tag{4.23}$$

From equations (4.22) and (4.23) we can obtain :

$$N(E) = N(P)\ (dP/dE) \tag{4.24}$$

The relation between N(E) and N(P) with a neutron energy E = 14.1 Mev is shown in figure (4.9) and table (4.2) . The area under the pulse height spectrum N(P) at an energy greater than E (which is fixed by the discriminator level - see section (4.1.7)) , is equal to the area under the proton recoil spectrum N(E) .

4.1.7 NEUTRON DETECTION THRESHOLD

In order to supress undesired pulses which arise spontoneously from neutron and gamma-ray backgrounds , noise inherent in the photomultiplier and the counting system , only pulses above a suitable discriminator level , defining the detection threshold are allowed to be counted . Because the light output of the plastic scintillator NE102A for electrons is always higher per unit energy than that for heavy charged particles , see fig (4.10) , the gamma-rays and other background may dictate the discriminator level . The low z- value of the constituents of the NE102A scintillation results in a very low photoelectric output , so that virtually all gamma-ray interactions are Compton scatterings and the Compton edge is the only distinguishable feature of these resultant spectrum .

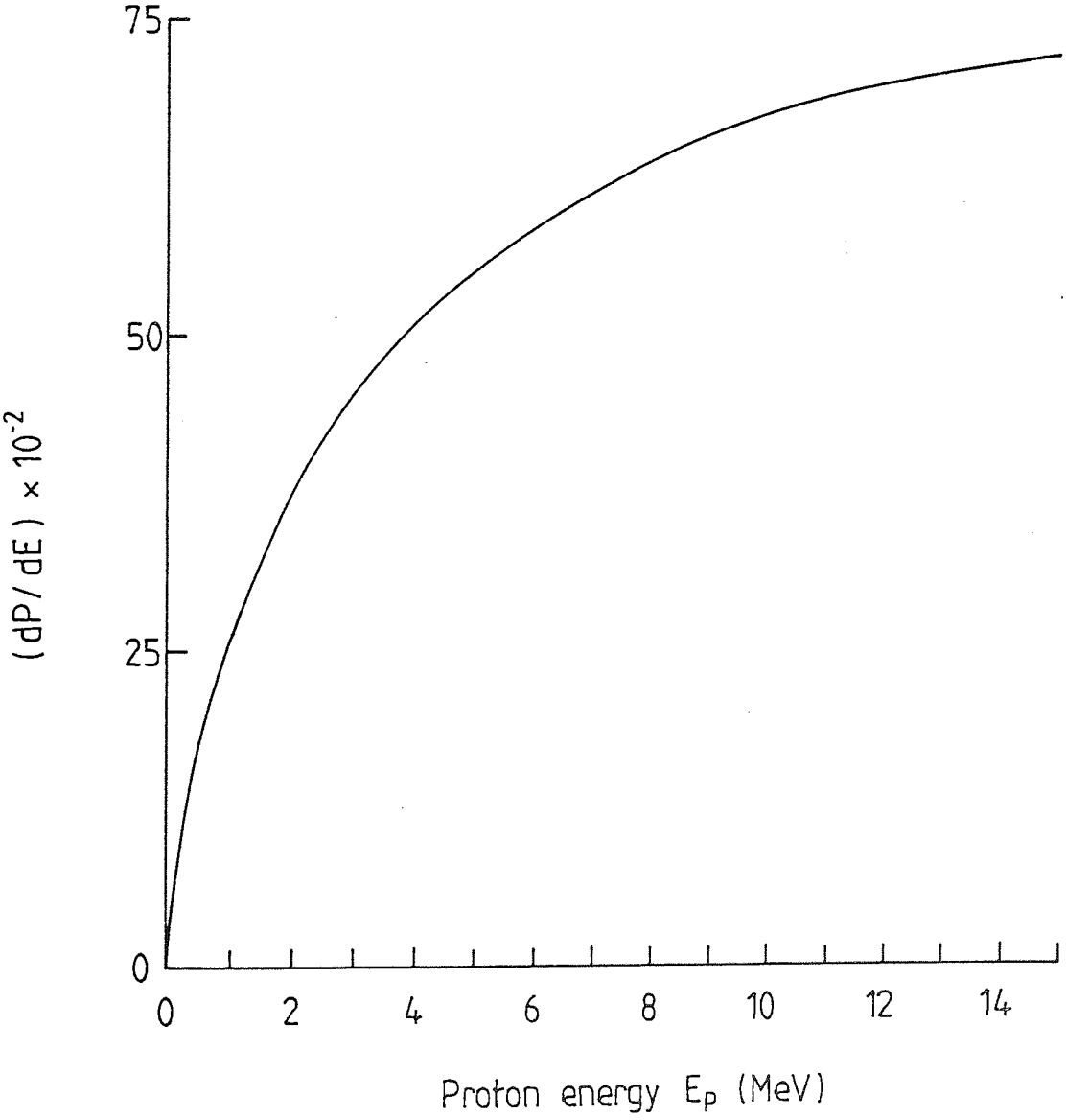

Figure (4.6) Variation of dP/dE with different proton energies in NE102A scintillator.

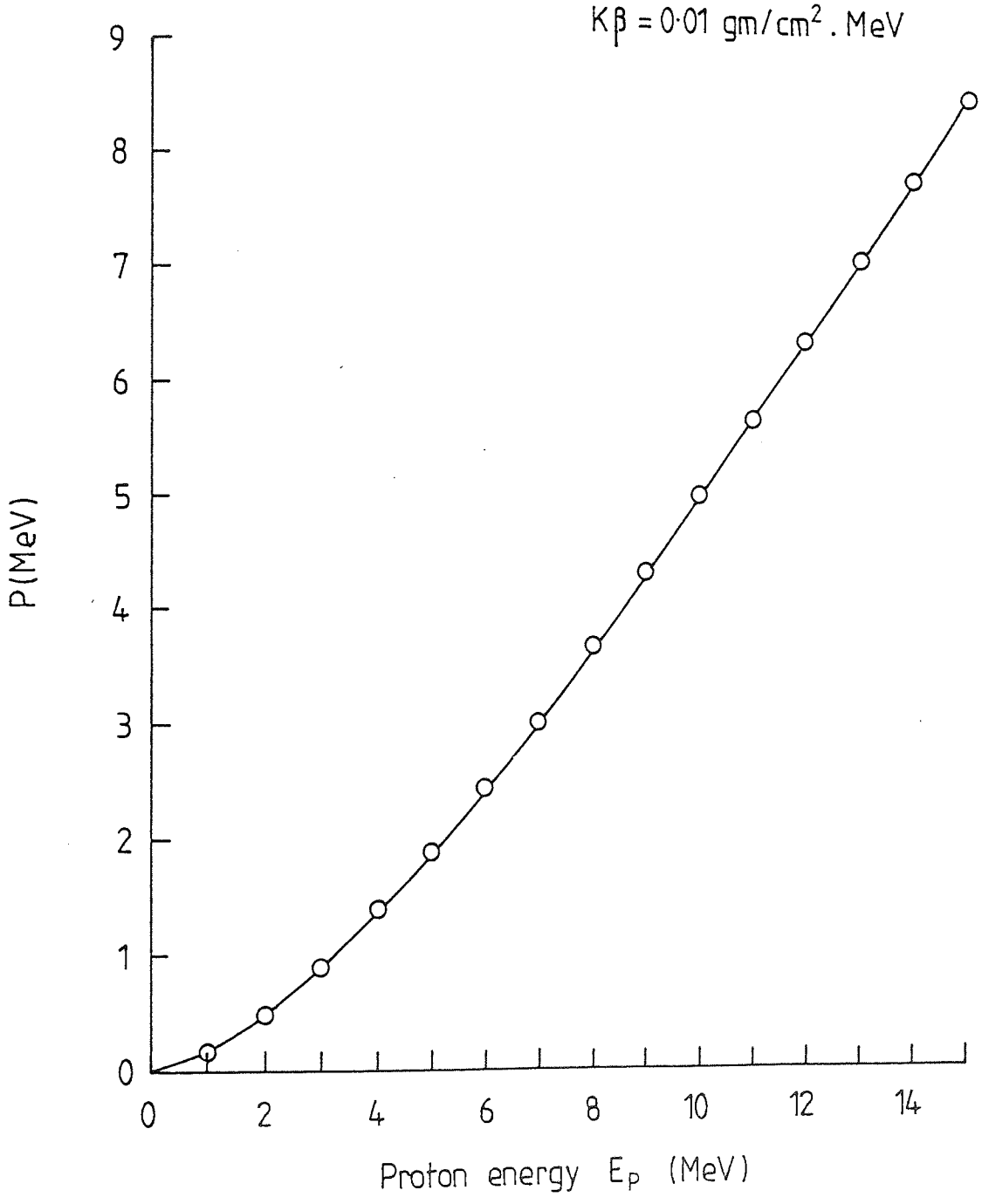

Figure (4·7) Pulse height of proton in NE102A plastic scintillator.

Table (4.2)

PULSE HEIGHT SPECTRUM OF NE102A PLASTIC SCINTILLATOR

E (Mev)	dE/dX kev.cm^2/mg	dP/dE	P (Mev)	dL/dX	N(P)
1	275.7	0.266	0.160	60.2	3.759
2	167.4	0.374	0.480	51.3	2.674
3	121.8	0.451	0.892	45.0	2.218
4	94.3	0.515	1.375	39.8	1.943
5	81.8	0.550	1.907	36.9	1.818
6	71.7	0.582	2.473	34.2	1.717
7	63.8	0.610	3.069	31.9	1.640
8	56.0	0.641	3.694	29.4	1.560
9	49.5	0.669	4.349	27.1	1.495
10	45.8	0.685	5.026	25.8	1.456
11	43.2	0.700	5.718	24.7	1.432
12	40.6	0.711	6.420	23.7	1.405
13	39.8	0.715	7.130	23.4	1.398
14	37.2	0.729	7.852	22.2	1.372
15	35.5	0.738	8.586	21.5	1.355

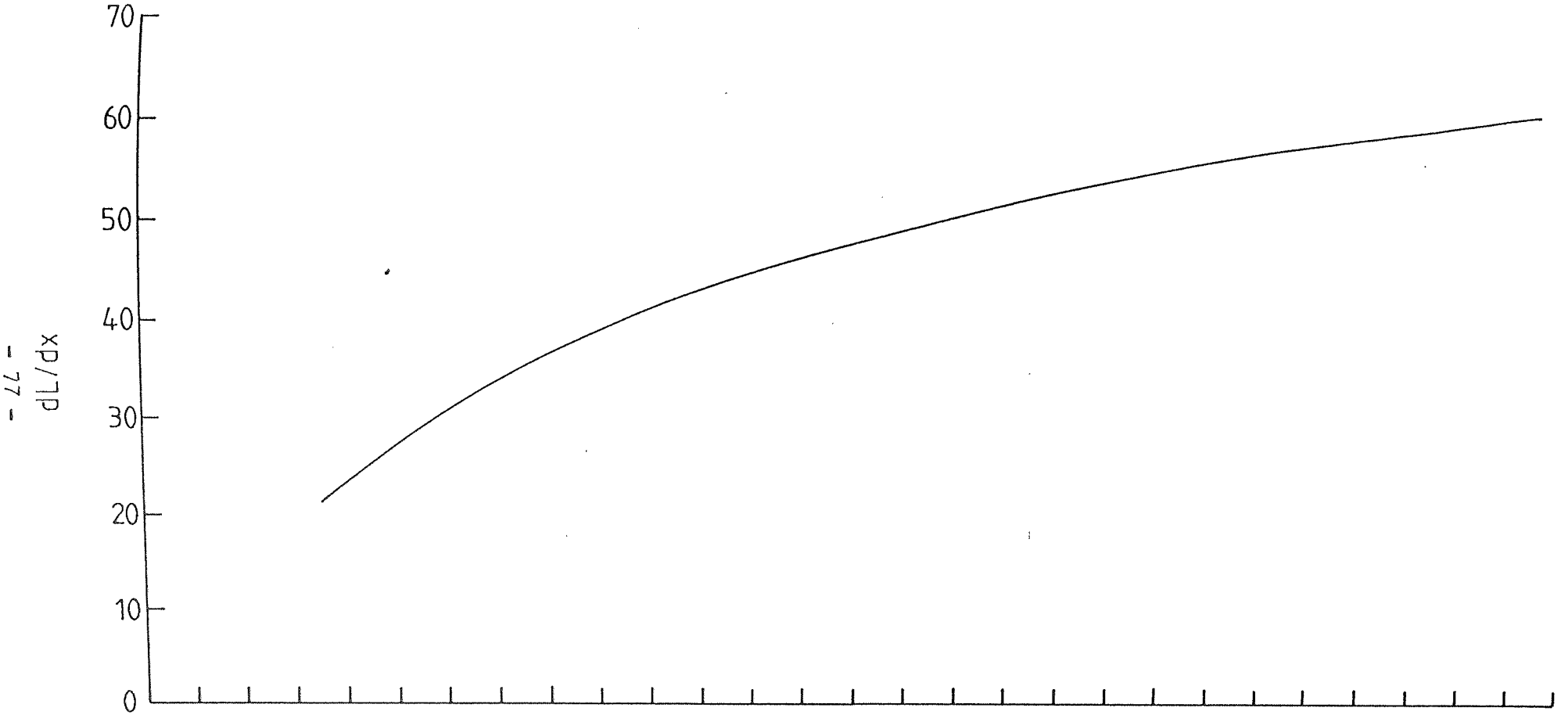

Figure (4·8) Variation of the specific fluorescence dL/dx [expressed in arbitrary units per cm^2/gm] with specific energy loss dE/dx in NE102A plastic scintillator.

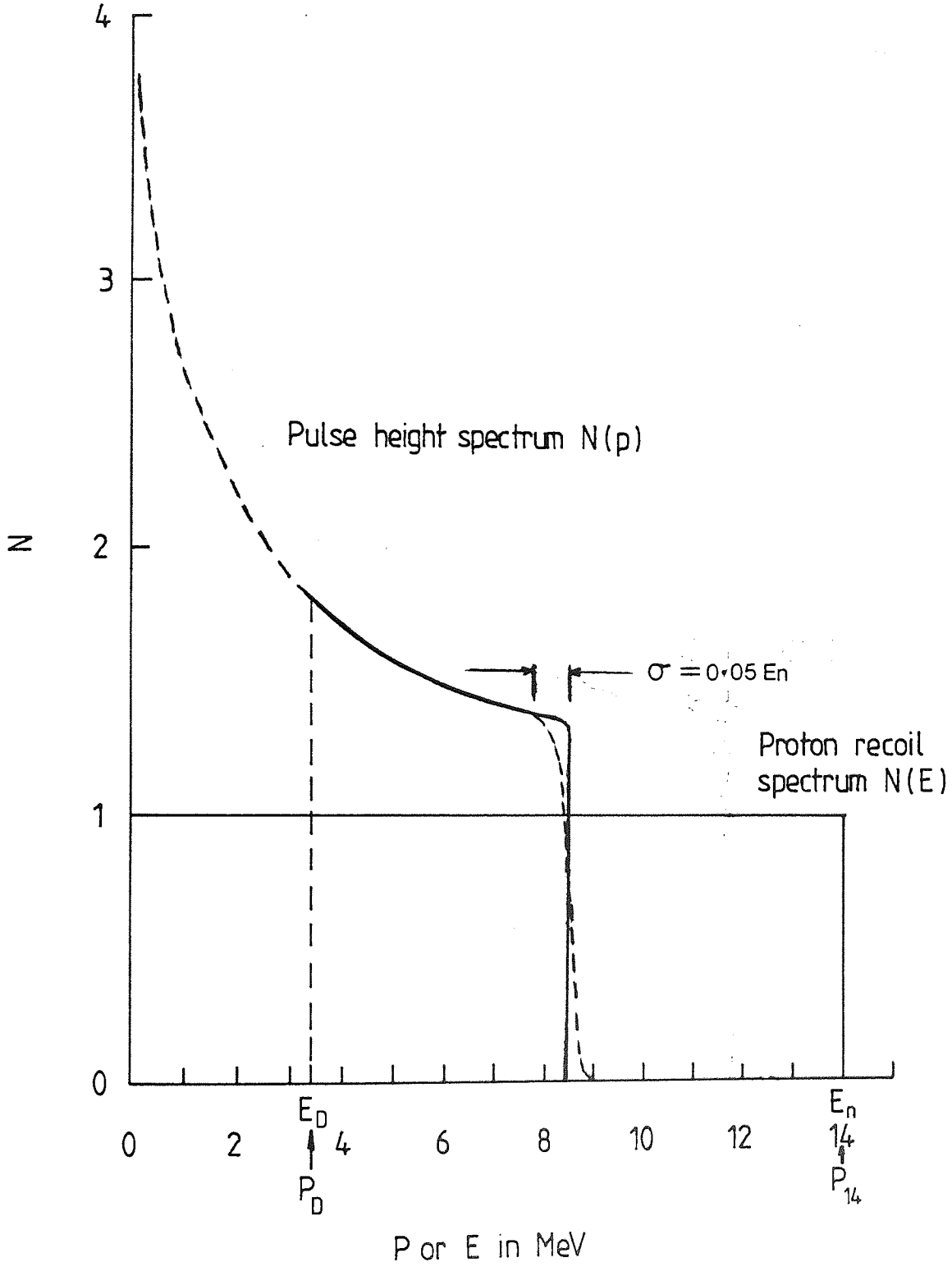

Figure (4.9) Calculated pulse height spectrum for 14 MeV neutron energy, including a distortion by the non linear response of NE 102A plastic scintillator. The dashed line represents the effect of the scintillator and phototube statistics with standard deviation $\sigma = 0{\cdot}05\ E_n$ (50).

In the block diagram [fig (4.11)] a constant fraction discriminator (ORTEC 463) is used with a ^{60}Co source of gamma-rays with energies of 1.17 Mev and 1.33 Mev , and the gamma-ray source positioned infront of the neutron detector .

A spectrum for the interacting gamma-rays was measured by plotting,counts in successive intervals as a function of the discriminator level as shown in fig (4.12) . The maximum recoil electron energy E_{max} = 1.115 Mev can be obtained by using :

$$E_{max} = \frac{E_o}{\left(1 + \frac{m_o c^2}{2 E_o} \right)} \qquad (4.25)$$

where E_o = 1.33 Mev

From equation (4.21) the equivalent to the proton pulse height of 1.115 Mev gamma-rays can be found . The pulse height of the Compton edge [fig (4.12)] is taken for convenience at a channel number which corresponds to one half of the maximum energy of the Compton recoil electrons (FLYNN 1964 [63]) and with an energy equal to 104% of the maximum compton electrons energy [50] (i.e. 1.159 Mev). Referring to fig (4.7) a gamma-ray pulse amplitude P = 1.159 Mev is seen to correspond to a proton energy of E = 3.4 Mev from which the detection threshold can be obtained .

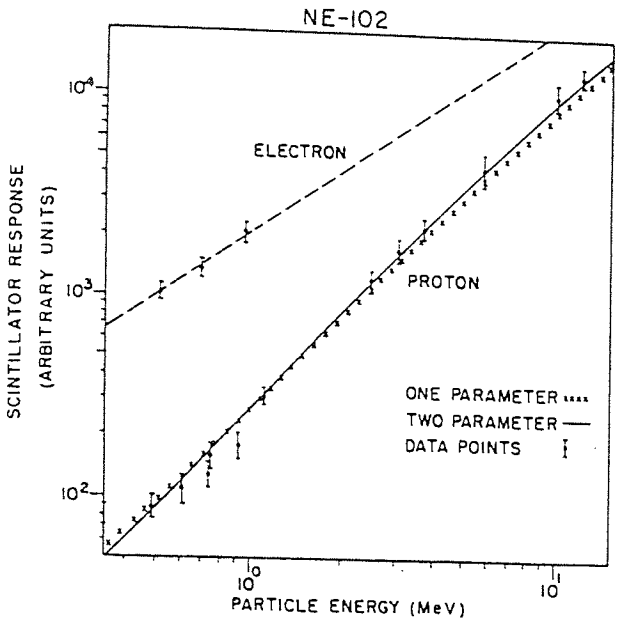

FIGURE (4·10)The scintillation light yield for a commercially available plastic scintillator (NE 102) when excited by electrons and protons. [26,105]

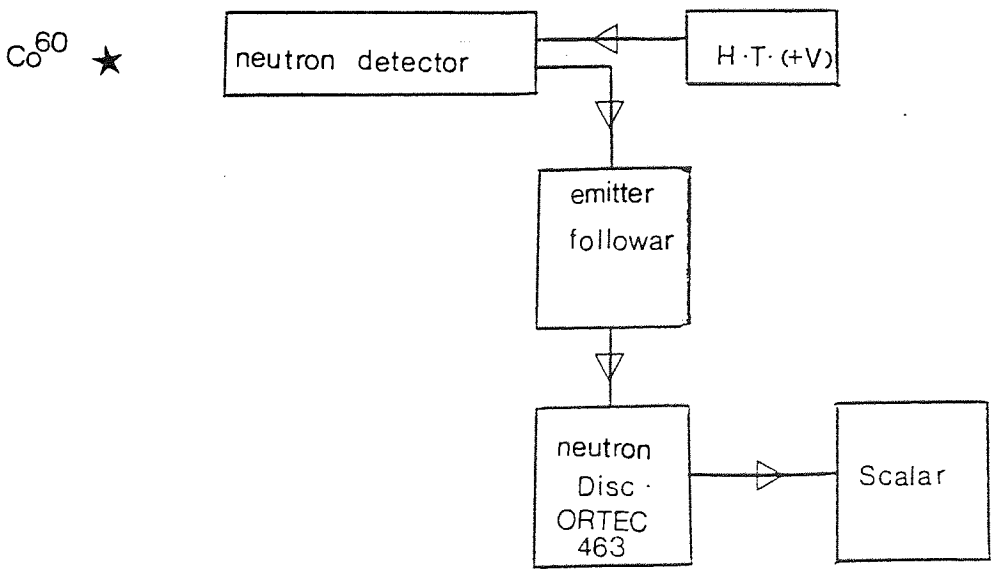

Fig (4.11) Block diagram of the electronics used to set the neutron discriminator level .

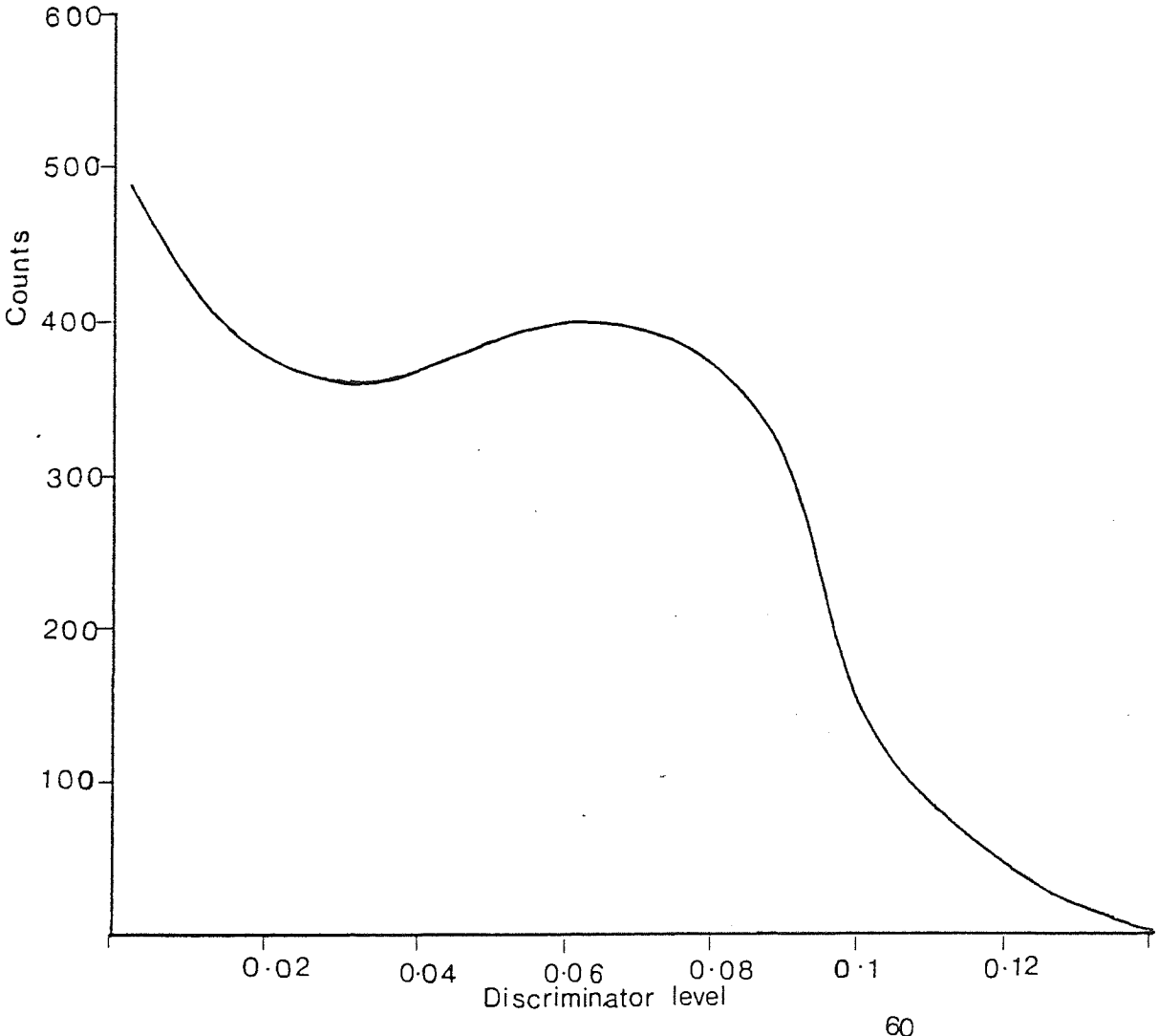

Fig (4.12) Differential Compton spectrum for ^{60}Co gamma-ray .

4.1.8 CALCULATION OF THE DETECTOR EFFICIENCY

In section(4.1.5), the neutron detector efficiency was calculated by assuming that all pulses are counted . This is sometimes called " Zero-bias efficiency " .

When a finite discrimination level (P_D) is used , the detector always has a somewhat lower efficiency , particularly at low neutron energies . For 14 Mev neutrons , the neutron detector efficiency with a discrimination level {corresponding to a proton of energy 3.4 Mev} fixed to eliminate all pulse amplitude below P_D is given by :

$$\varepsilon(14) = \varepsilon_2(14)\ \left(\frac{A_{14} - A_{PD}}{A_T}\right) \qquad (4.26)$$

Where $\varepsilon(14)$ = detector efficiency without discrimination for 14 Mev neutrons as calculated in equation(4.10) .

$(A_{14} - A_{PD})$ = area under the pulse height spectrum between P_D and P_{14} [see fig (4.9)] .

A_T = total area under the pulse height spectrum [fig(4.9)]

At a neutron energy (E) the detector efficiency can be calculated by

$$\varepsilon(E) = \varepsilon_2(E)\ \left(\frac{A_E - A_{PD}}{A_T}\right) \cdot \frac{14}{E} \qquad (4.27)$$

The effect of the discrimination level P_D on neutron detector efficiency is shown in fig (4.13).

4.1.9 DETECTION SYSTEM

The time resolution which can be achieved by time-of-flight techniques is limited only by the type of scintillator and photomultiplier (PM) employed .

In the scintillator-PM assembly the rise time of a pulse produced at the anode by neutrons incident on the scintillator is determined by

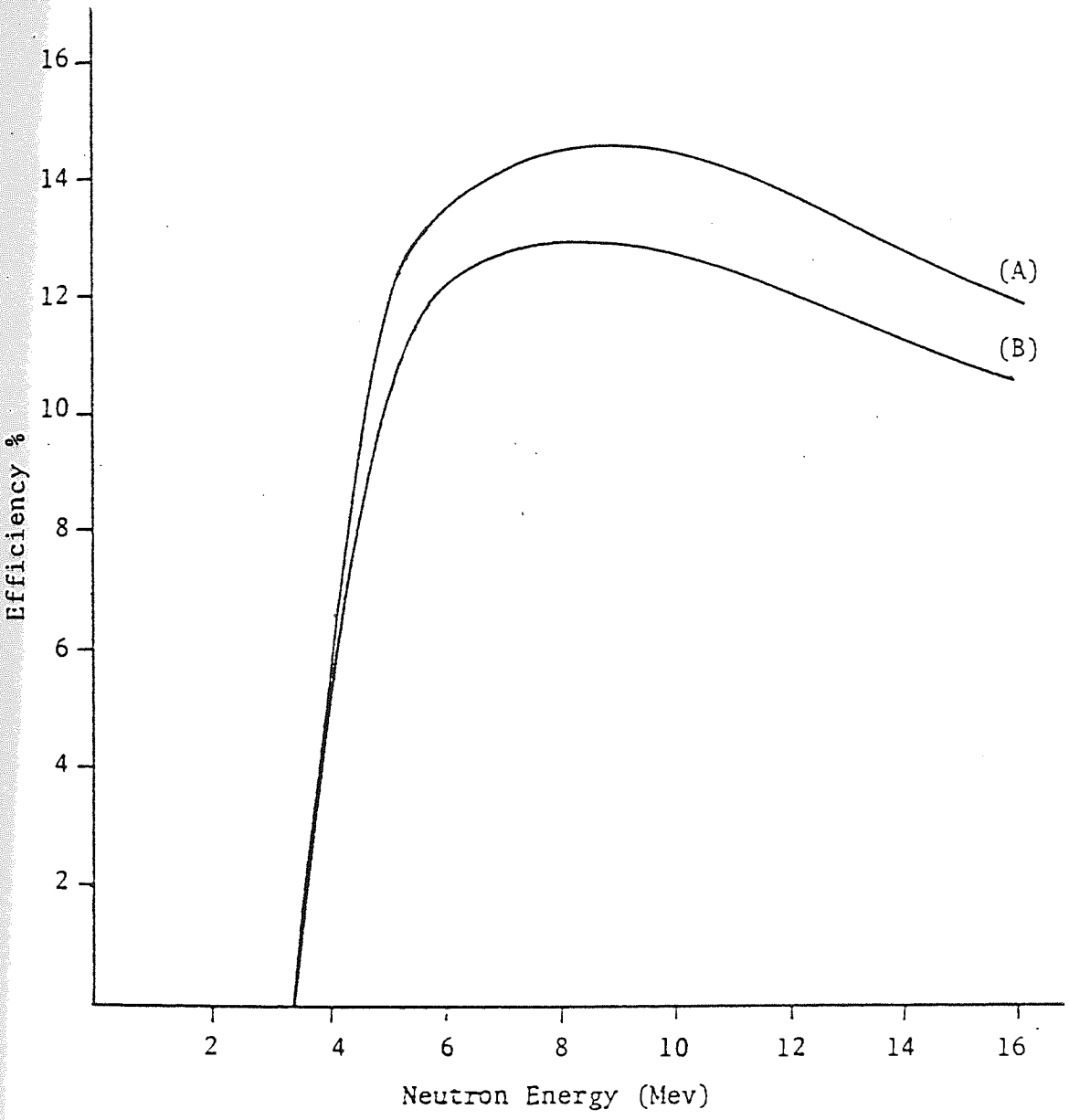

(A) - Including scattering from Carbon and Hydrogen

(B) - No multiple scattering

Figure (4-13) Calculated efficiency of the NE 102A Scintillator with a discriminator level of 3.4 Mev .

the decay time of the fluorescence in the scintillator and the transit time spread of the electrons through the PM .

In the present work a Philips 56AVP PM , 5 cm. diameter is coupled to the plastic scintillator NE102A , 10 cm. diameter. It has a transit time spread of 0.5 nsec FWHM [18] giving a high gain of approximately 10^8 through 14 stages of amplification when operated at 2 kV .

Fig (4.14) shows a typical wiring diagram for the base of a 56AVP PM tube in which the dynode voltages were supplied by the resistor chain with a 2.3 mA d.c. current at + 2 kV operating voltage .If the internal current at the peak of a pulse is between 10 - 50 μA (BAYNHAM 1971 [18]) and therefore comparable with resistor chain current , the voltages of the dynodes , in the last four stages , will begin to deviate from their equilibrium values , leading to a drift in the PM tube gain. For this reason it was necessary to provide stablizing capacitors for the last stages of the divider chain to prevent these fluctuations . The load resistor RL and the coupling capacitor Cc values were chosen to give an output pulse of suitable amplitude and duration .

4.1.9.1 MAGNETIC SHIELDING

In the 56AVP PM , electron trajectories in the cathode-S1 {see fig (4.14)} space are particularly sensitive to magnetic fields and are easily deflected . If the tube is to be moved in the earth's field or brought near equipment with stray magnetic fields , it is essential that a magnetic shield be provided to prevent gain shifts in the PM tube (BIRKS 1964 [48]) .

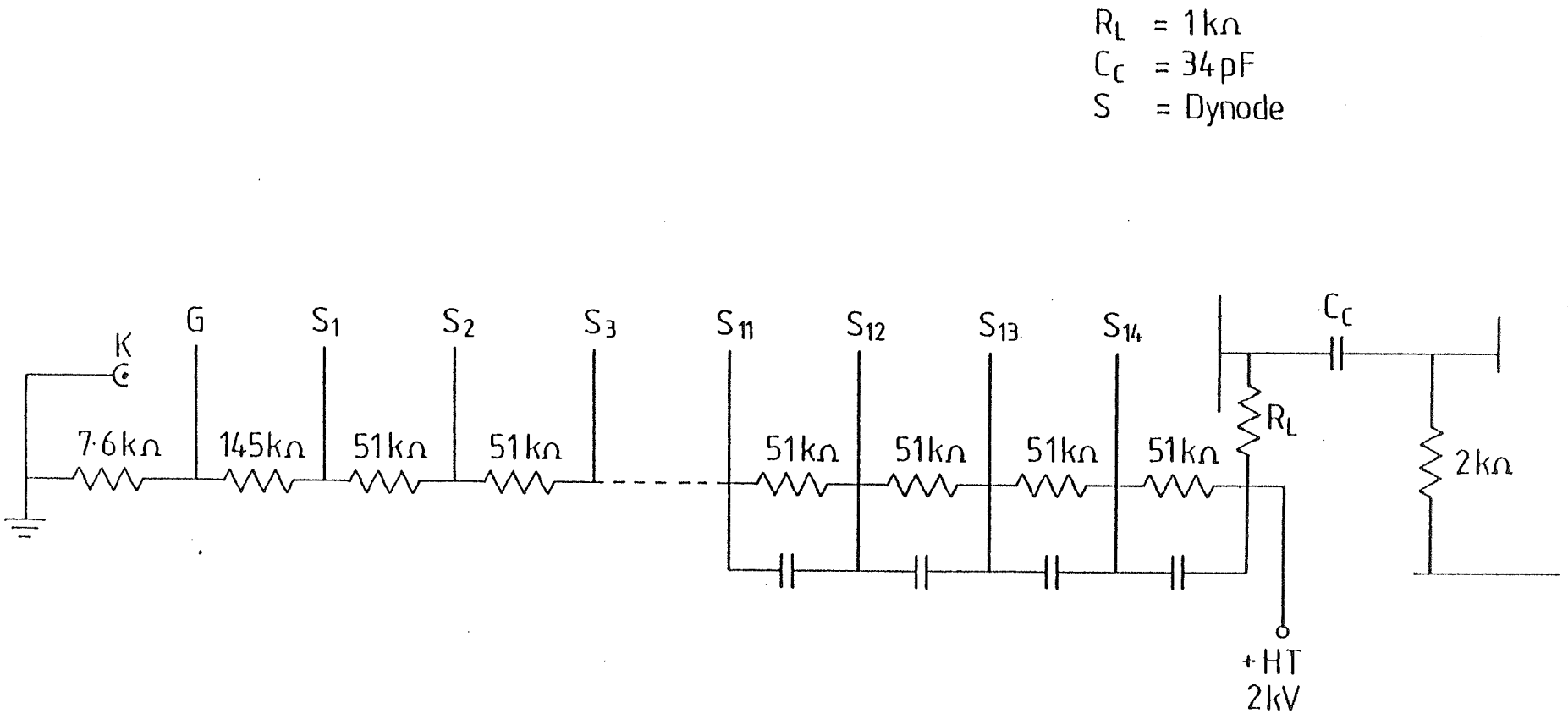

Figure(4·14) 56 AVP photomultiplier dynode chain.

To eliminate this effect and minimize transit time spread a thin cylindrical-μ-metal shield No.56131 was used , which fits closely around the outside glass envelope of the 56AVP PM tube.

4.1.9.2 THE LIGHT GUIDE

It is desirable that most of the light quanta produced in the scintillator should be collected at the photocathode . Two factors , which may prevent this are the self absorption , which will introduce losses in the large volume of the scintillator (GARG 1960 [64]) , and the internal reflection of the light at the scintillator surface of 104% [48] from the total an isotropic light source at the centre of the scintillator .

In the present work a perspex light pipe was employed to match the 10 cm diameter NE102A scintillator to the 5 cm diameter 56AVP PM . The internal reflection at the lower surface of the scintillator is limited by the optical coupling , which is produced using a non-drying silicon immersion oil between the light pipe and PM .

To ensure effective light transmission between the NE102A and the PM tube , an optical cement type NE580 with a refractive index (μ=1.58) was used , matching closely to the NE102A plastic scintillator .

4.1.10 NEUTRON DETECTOR SHIELDING

Neutron scattering experiments require the detector to be carefully shielded both from the direct beam and spurious background radiaton from the surrounding the neutron producing facilities .

The shielding in a time-of-flight technique usually consists of a massive movable shielding collimator surrounding the neutron

detector as shown in fig (4.15) and a shadow bar shielding the target from the neutron producing target .

The selection of the appropriate type of shielding material depends on the neutron attenuation , which varies as (Ns / [Ni.exp($-\sum_a$.x)]) , where Ns is the number of neutrons per unit time scattered into the neutron detector by the scattering sample , Ni is the number of neutrons per unit time from the primary source , and exp($-\sum_a$.x) is the absorption factor for a shield of thickness x .

For materials containing a high percentage of hydrogen such as paraffin wax , water , polyethylene etc , where elastic scattering dominates an average energy degradation of 5Ø % per elastic collision is provided . As indicated in fig (4.16) the attenuation coefficient for hydrogen, based on the total cross-section ,is dominant for En<3 Mev .

However , once the neutron has been moderated , the capture process $^{1}_{1}H(n,\gamma)^{2}_{1}D$ occuring leads to the liberation of a 2.23 Mev gamma-ray with a reaction cross-section of 33Ø mbarns , and in the case of paraffin a 4.43 Mev gamma-ray emmited by inelastic scattering with carbon in wax which has a very small cross-section .

Construction of the detector shielding has been described in detail by CONNEL 1972 [33] , where a paraffin wax cylinder of 15.Ø cm side thickness and 33.Ø cm length was used to shield the detector

Lithium carbonate (Li_2Co_3) and boric oxide (B_2O_3) are the best shielding materials (GLASGOW 1974 [34]) for the absorption of the moderated neutrons and should be located near the inner surface of the parffin wax . The elements ^{6}Li and ^{10}B in these compounds have high capture neutron cross-sections at low energies (94Ø barns and

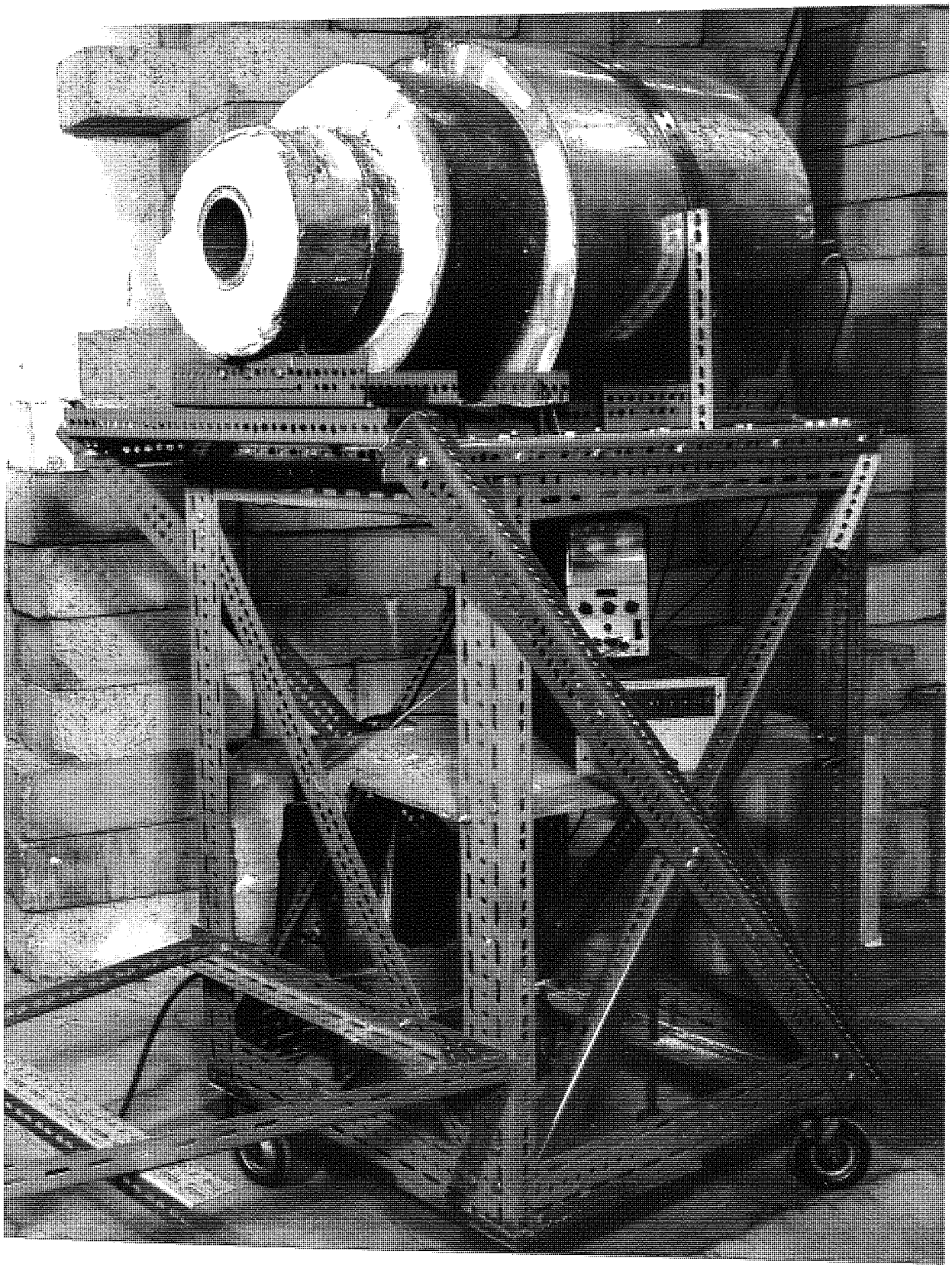

Fig (4.15) Neutron Detector Shielding .

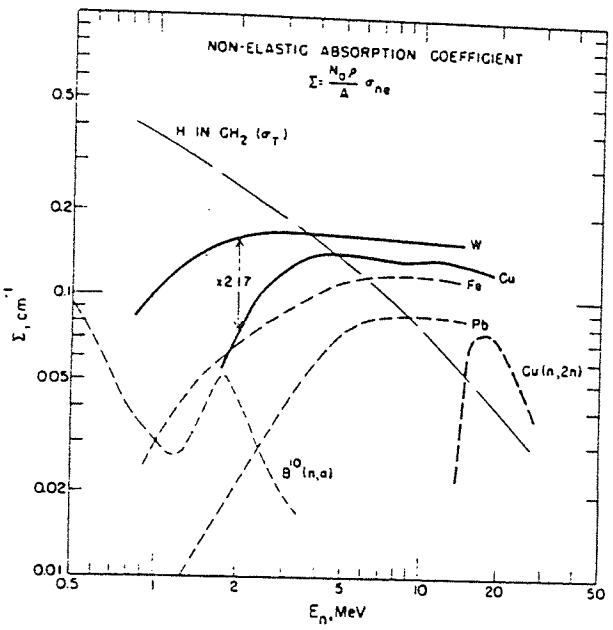

Fig (4.16) Absorption coefficients by B , Fe , Cu , W , and Pb calculated using non-elastic cross-section and for H in the density of Paraffin Wax using the total cross-section . [35,37]

3838 barns respectively at thermal energy) and the main absorption reaction is (n ,α) , where the product nucleus ^{7}Li gives Ø.48 Mev gamma-ray .

As shown in fig (4.16) ^{10}B and H dominate over the energy range of En < Ø.7 Mev , while for the heavy materials (e.g. Fe,Cu,W, and Pb),the dominate reaction is non-elastic neutron scattering for En > 4 Mev .

Since the differential cross-sections for heavy materials are highly peaked in the forward direction , scattering provides little energy loss .

Secondary gamma-rays produced by the neutrons in the paraffin wax and boric oxide in the shielding were absorbed by a lead layer of 5.5 cm thickness and length 12.5 cm at the front of neutron detector The lead shield has an attenuation factor of (Ns/Ni $\simeq$ Ø.2) for the 2.23 Mev gamma-rays of the $^{1}_{1}H\ (n,\gamma)\ ^{2}_{1}D$ reaction and Ø.22 for 4.43 Mev gamma-rays of the $^{12}C(n,n'\gamma)^{12}C$ reaction .

By using the time-of-flight technique , the background resulting from the direct beam was found to be a critical function of the shadow shielding location which agrees with HOPKINS 1967 [35] as shown in fig (4.17) . A movable paraffin wax shadow bar was used to prevent the primary neutron source from irradiating the front and throat of the neutron detector shield .

Table (4.3) illustrates how the properties of the shielding materials [36] used in the present experiment compare with other commonly avaliable materials for neutron detector shielding .

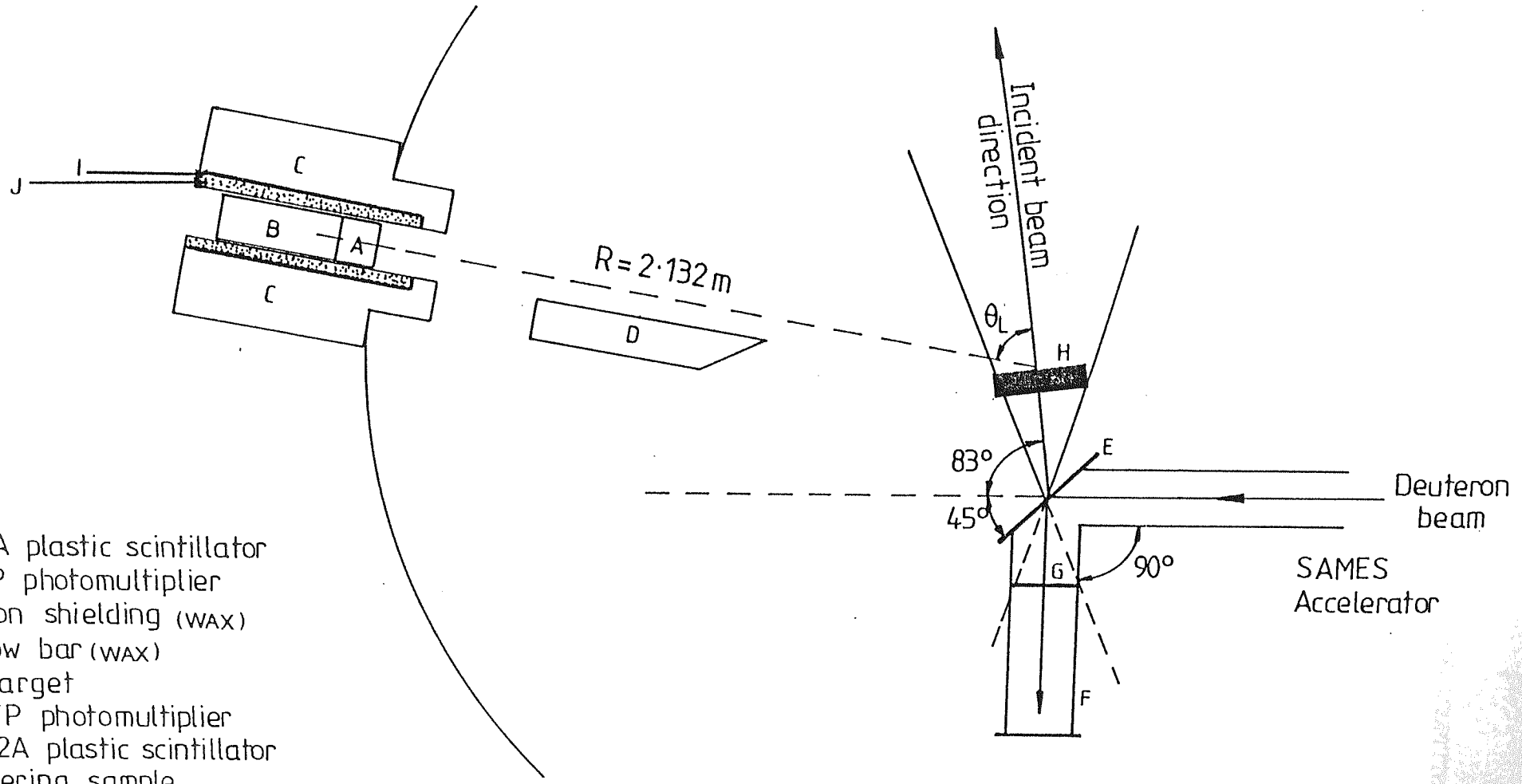

A:- NE102A plastic scintillator
B:- 56AVP photomultiplier
C:- Neutron shielding (WAX)
D:- Shadow bar (WAX)
E:- TiT target
F:- 56AVP photomultiplier
G:- NE102A plastic scintillator
H:- Scattering sample
I:- B_2O_3
J:- Pb

Figure (4·17) Experimental arrangement

Table (4.3)

PHYSICAL AND CHEMICAL PROPERTIES OF SHIELDING CONSTITUENTS

MODERATION MATERIAL FOR FAST NEUTRONS		ABSORPTION MATERIAL OF SUBSEQUENTLY MODERATED FOR SLOW NEUTRONS	
COMPOUND	NUMBER* OF H (Nuclei/cm^3) x 10^{22}	COMPOUND	NUMBER* OF B or Li (Nuclei/cm^3) x 10^{22}
Paraffin(CH)	7.8 - 8	LiF	6.12
H_2O	6.7	Li_2CO_3	3.44
Wood(Celluose)	2.5	B_2O_3	3.26

[*] $n = \frac{\rho_{compound}}{\text{molecular weight}} \cdot \text{number of} \begin{vmatrix} H \\ B \\ Li \end{vmatrix} \times 6.02 \times 10^{23}$

4.2 THE ALPHA-PARTICLE DETECTOR

Plastic scintillator and semiconductor detectors have become the choice for detecting highly ionizing charged particles like alpha particles , (MUGA etal (1972) [38]). Because of their high ionization , they can be detected with 100% efficiency and they lose all their energy in a thin (1mm) scintillator (GEISSEL etal 1977[39).

The selected alpha particle detector in the present work requires the following characteristics :

1 - A 100% detection efficiency of the alpha-particles .

2 - A low detection efficiency for neutrons and gamma-rays .

3 - Fast response time for the pick-off (timing) pulse in the time-of-flight measurement .

The plastic scintillator was used rather than a semiconductor detector (surface barrier) because of the following advantages , firstly the plastic scintillator with a high gain , focussed , photomultiplier tube , does not need to be used with a pulse amplifier which is normally required with a semiconductor detector. Secondly the scintillator detector is less susceptible to radiation damage than the surface barrier detector,which causes the energy resolution to deteriorate rapidly as described by DEARNALEY(1963)[40] and HANSER etal (1970) [41] .

The plastic scintillator NE102A meets these requirements . It has high light transmission with a very short decay time of 2 nsec and is relatively insenstive to gamma-rays as well as neutrons .

The range of 3.5 Mev alpha-particles in a scintillator is 0.025 mm as shown in fig (4.18) , therefore a thin sheet of NE102A with a

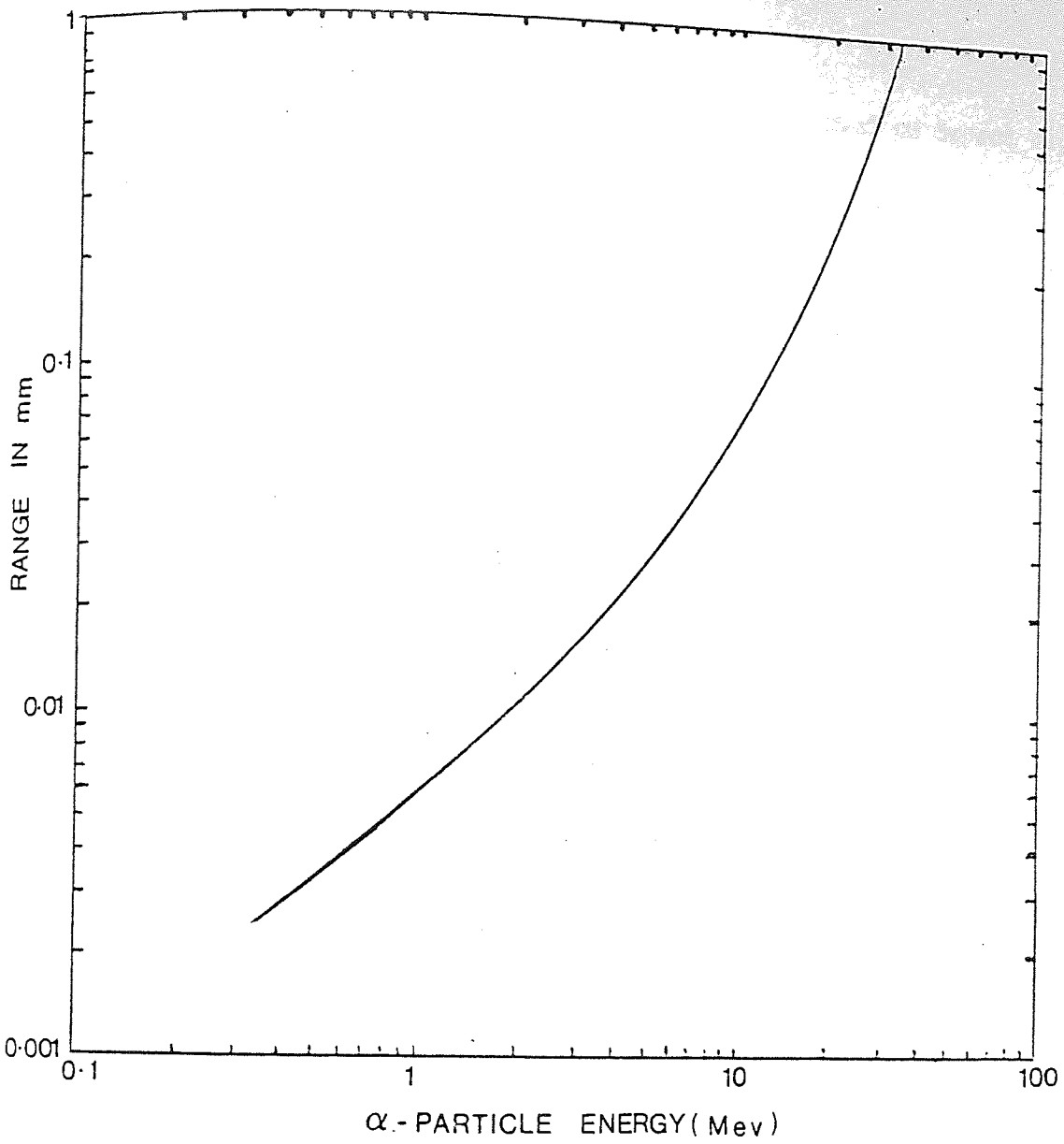

Fig (4.18) Range of α-particle in NE102A Plastic Scintillator

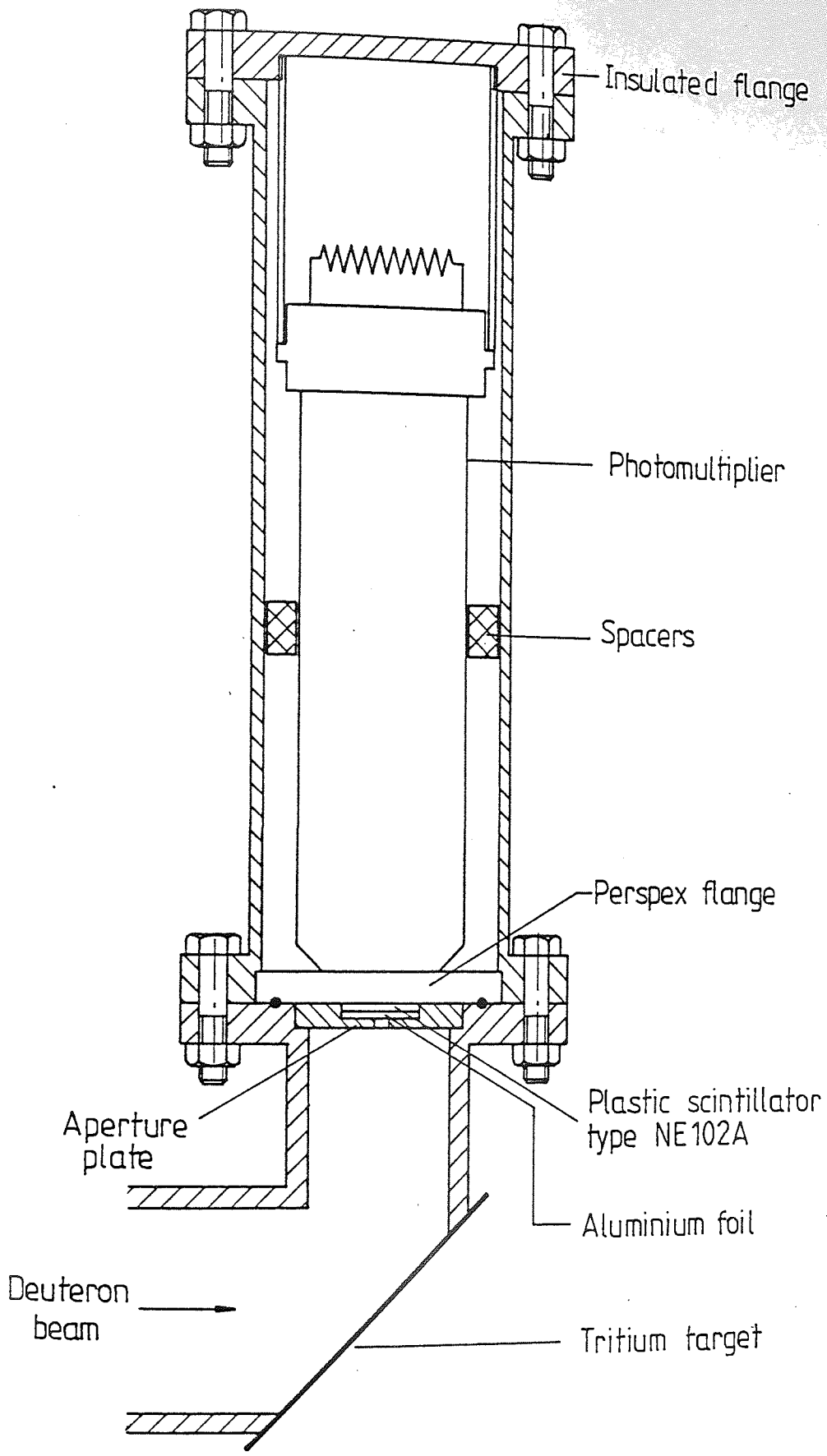

Figure (4·19) The α-particle detector system.

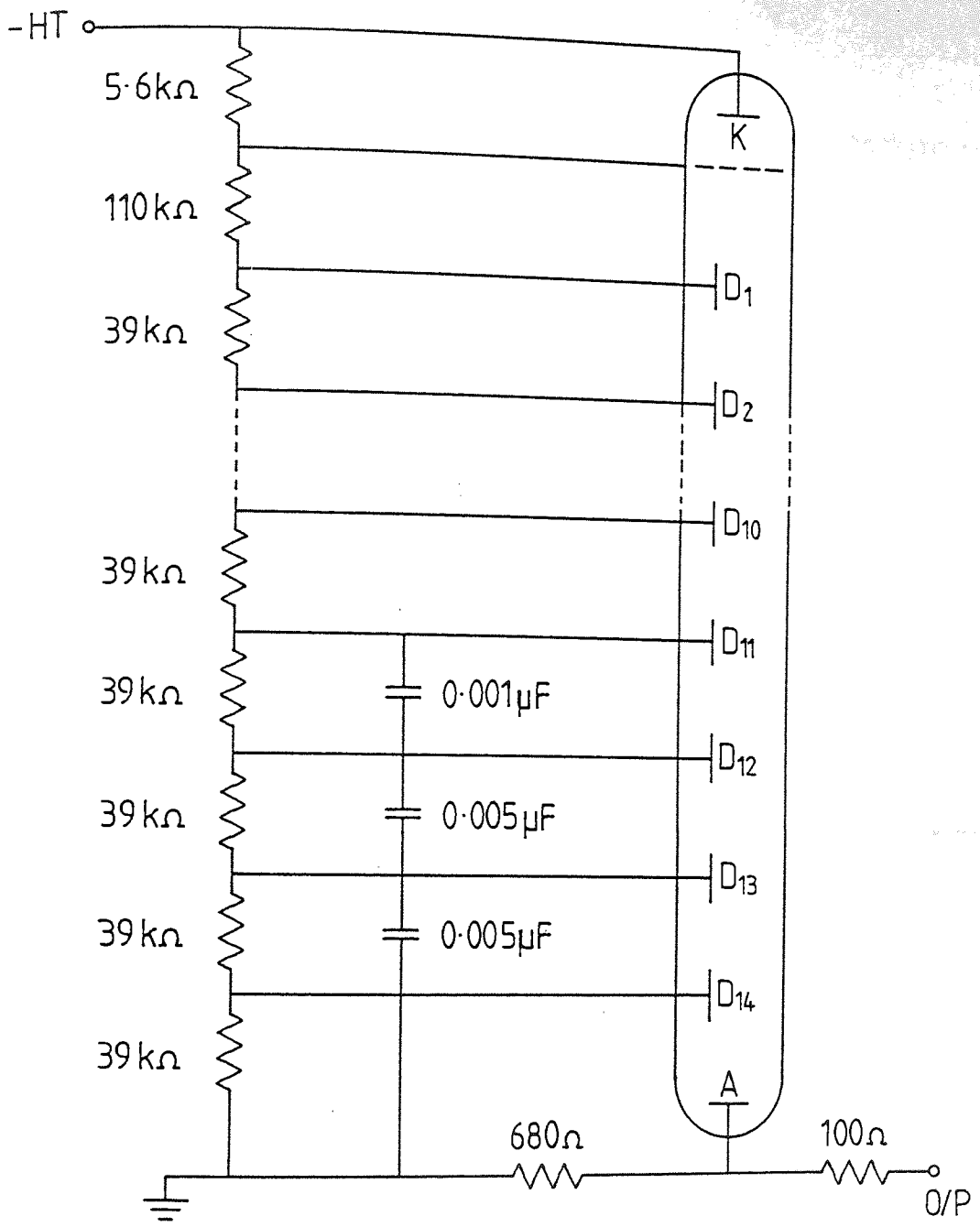

Figure (4·20) The Dynode resistor chain for alpha-detector.

4.2.1 THE ALPHA-DETECTOR SHIELDING

It was necessary to shield the detector against the background radiation from the scattering of 140 kev deuterons , the activated target holder and the beta-particles emitted from the tritium in the target .

The β^--particles produced in the decay of the tritium have an energy of around 18.6 kev with a range in aluminium of about 0.0022mm [43] .

Deuterons scattered through 90° into the alpha-particle detector carry an energy of less than 140 kev , and have a range in aluminium (density 0.52 mg/cm^2) of approximately 0.002 mm [44,46] .

Therefore , an aluminium foil of thickness 0.0044 mm was used to shield the alpha detector completely from both the beta particles and scattered deuterons , while having a negligible effect on the alpha-particles . The range of 3.5 Mev apha- particles in aluminium of density 0.045 mg/cm^2 is 0.017 mm [45] .

4.2.2 SETTING THE α-PARTICLE DETECTOR DISCRIMINATION LEVEL

The α-particle pulses were discriminated in order to reject energies below 3.5 Mev . The experimental arrangement is shown in fig (4.21) . The detector output pulse was amplified by a linear amplifier and the resulting pulses were gated by the output of the discriminator . Up to the discriminator level the linear gate remained unopened , therefore remaining the lower energy pulses .

Fig (4.22) shows the α-particle pulse height spectrum from T-D reaction .

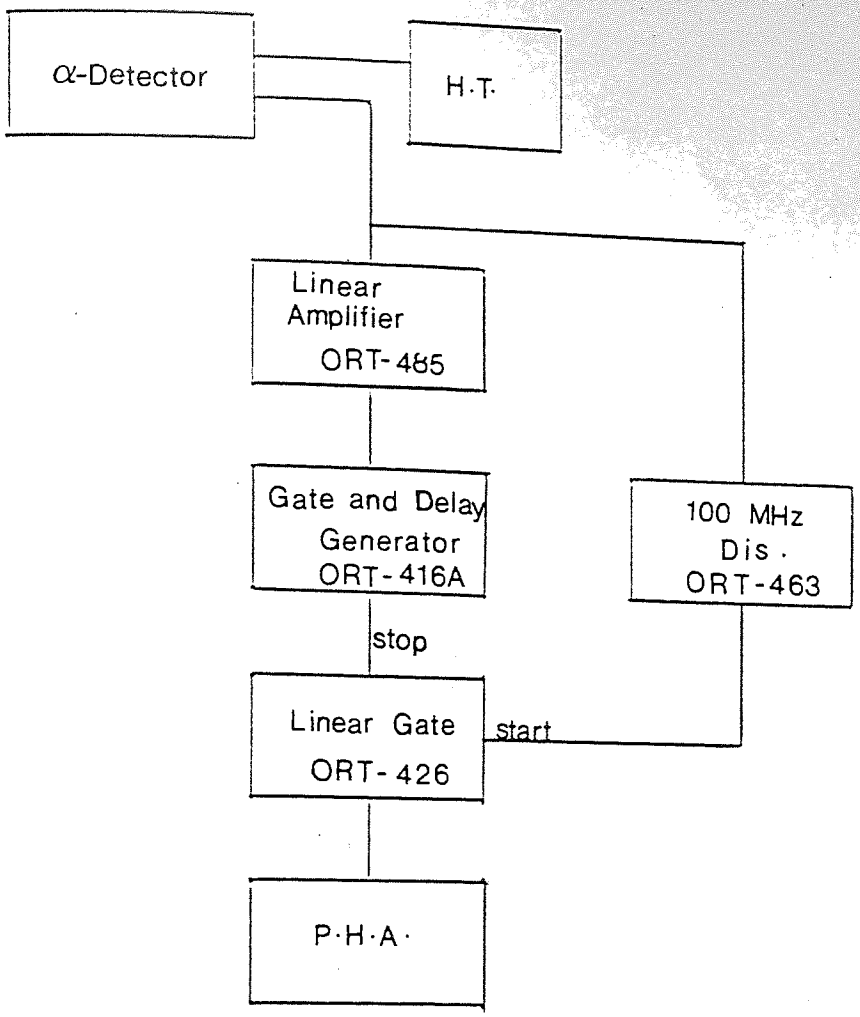

Fig(4.21) Block diagram of the electronics used for setting the α- particle discriminator level .

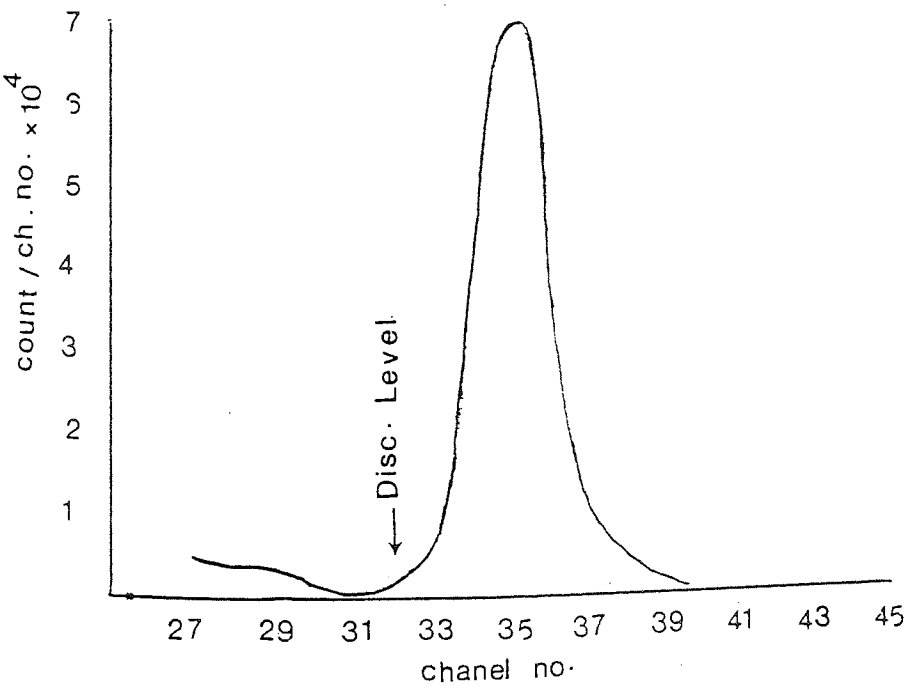

Fig(4.22) α-particle pulse height spectrum .

CHAPTER FIVE

EXPERIMENTAL RESULTS

CHAPTER FIVE

EXPERIMENTAL RESULTS

5.1 THE DIFFERENTIAL CROSS-SECTION

When fast neutrons interact with nuclei they are not scattered isotropically , it is therefore useful to define a cross-section which is a function of the direction in which the neutron is emited.

This is called the differential cross-section $\sigma(\theta)$ which is defined as the probability of scattering per unit solid angle at a specified angle (θ) to the incident neutron beam .

The cross-section for scattering the incident neutron into the solid angle ($d\Omega$) by a single target nucleu is :

$$d\sigma(\theta) = \sigma(\theta) \cdot d\Omega \tag{5.1}$$

For the spherically symmetric case :

$$d\Omega = 2\pi \cdot \sin\theta \cdot d\theta \tag{5.2}$$

; Equation (5.1) then becomes :

$$d\sigma(\theta) = 2\pi \cdot \sin\theta \cdot \sigma(\theta) \cdot d\theta \tag{5.3}$$

Hence the total scattering cross-section is :

$$\sigma_t = 2\pi \int_0^{\pi} \sigma(\theta) \cdot \sin\theta \cdot d\theta \tag{5.4}$$

Which gives the total probability of scattering in any direction of θ.

5.2 RELATION BETWEEN CROSS-SECTIONS IN THE LABORATORY AND CENTRE OF MASS SYSTEM

The relation between the differential cross-section in the lab and c.m system can be obtained from the principle that the same number of neutrons are scattered into the solid angle $d\Omega_L$ about (θ_L) in the lab system as are scattered into $(d\Omega_C)$ about (θ_C) in the c.m system providing that the angles correspond in both systems.

hence

$$\sigma(\theta_L)\cdot \sin\theta_L \cdot d\Omega_L = \sigma(\theta_C)\cdot \sin\theta_C \cdot d\Omega_C \qquad (5.5)$$

However the relation between angles in the lab and c.m. sytem is given by :

$$\theta_C = \theta_L + \sin^{-1}\left(\gamma \cdot \sin\theta_L\right) \qquad (5.6)$$

The differential cross-section for elastic scattering can be written as :

$$\sigma(\theta_L) = \frac{\left\{1+\gamma^2+2\gamma\cos\theta_C\right\}^{\frac{3}{2}}}{\left\{1+\gamma\cos\theta_C\right\}} \cdot \sigma(\theta_C) \qquad (5.7)$$

Where γ = M1/M2 ; M1 is the mass of the incident neutron and M2 is the mass of the target nucleus .

5.3 THE DIFFERENTIAL CROSS-SECTION MEASUREMENT

Consider a total number (n) of neutrons incident on a sample of thickness (t) containing (N) nuclei per unit volume , then the total number of interactions is given by :

$$Y = n \left[1 - \exp (- N.\sigma_T.t) \right] \qquad (5.8)$$

Where $\left[1 - \exp (- N.\sigma_T.t) \right]$ = attenuation of the neutron beam in the sample.

σ_T = neutron total cross-setion.

If elastic scattering is only one of the reactions take place ,the probability of neutrons being elasticaly scattering is :

$$Y = n \cdot \left[1 - \exp (- N.\sigma_T.t) \right] . \frac{\sigma_E}{\sigma_T} \qquad (5.9)$$

Where σ_E is the neutron elastic scattering cross-section at enrgy (E). The probability of neutron scattering into a solid angle ($d\Omega$) and centered at an angle (θ_L) to the incident beam is :

$$Y = n \cdot \left[1 - \exp (- N.\sigma_T.t) \right] . \frac{1}{\sigma_T} \int_{\Omega} \frac{d\sigma(\theta)}{d\Omega} d\Omega \qquad (5.10)$$

If the integral is over a very small solid angle ($d\Omega$) , the integral may be replaced by the product $\left(\frac{d\sigma(\theta)}{d\Omega} \right) . \Delta\Omega$.

Equation (5-1Ø) can be written in terms of the differential cross-section as :

$$\frac{d\sigma(\theta)}{d\Omega} = \frac{Y(\theta)\cdot\sigma_T}{n\cdot\{\ 1 - \exp(-N\cdot\sigma_T\cdot t)\ \}\ .\Delta\Omega} \qquad (5.11)$$

The differential elastic scattering cross-sections which are defined in equation (5-11) require several additional corrections concerning the detector and geometry . These are discussed in the next section .

5.3.1 CORRECTION FACTORS FOR SCATTERED NEUTRONS FROM THE SAMPLE

To estimate the correction factors , consider a slab of material of thickness (t) containing (N) number of nuclei per unit volume located in the neutron beam of intensity (n_i) . The neutron detector is placed at an angle of (θ) to the beam direction. In a layer of thickness (dx) within the slab , a reduction of the neutron intensity occurs due to the interaction of the beam with total cros-section (σ_T) .

The resulting fractional reduction of the beam intensity , $(-\frac{dn}{n_i})$, is proportional to the :

$$-\frac{dn_i}{n_i} = N\cdot\sigma_T\cdot dx \qquad (5.12)$$

Inegrating equation (5.12) and assumed (n_i) is the beam intensity incident on the slab , one obtains the intensity transmitted through the sample :-

$$n(t) = n_i \cdot \exp\left(-N.\sigma_T.t\right) \qquad (5.13)$$

When the scattered neutron traverses different thicknesses of the sample in the nearby detector, a correction factor $(\frac{n(t)}{n_i})$ has to be applied for each thickness . Therefore the sample-detector geometry was drawn at a different scattering angles and the path length in the sample estimated for each Ø.5 cm. slice of the sample .

The average neutron path length (Δx) of the scattered neutron beam in each sample , was calculated for each specific neutron scattering angle (θ) .

The average correction factor for the scattered neutrons from the sample of a specific thickness at an angle (θ) is :

$$c(t) = \frac{n(t)}{n_i} = \frac{\sum_{\Delta x=0.5}^{\Delta x=t} \exp\{-N.\sigma_T.\Delta x\}}{\text{Total number of 0·5 slices}} \qquad (5.14)$$

When the neutron traverses different parts of the sample {see fig (5.1)} , a different correction factor (c(t)) has to be used .

Figure (5.2) shows the variation between the percentage areas from which the neutrons are scattered through the front and side faces of the sample respectively at different neutron scattering angles (θ_L).

5.3.2 WEIGHTED SAMPLE THICKNESS

When the neutron beam is incident on the scattering sample , the thickness traversed by each neutron differs for different values of neutron emission angle (ϕ_n) . The neutron beam profile {see fig(2.8)} shows that the relative yield of the neutrons varies over an angular range of 17 degrees . Therefore it is necessary to

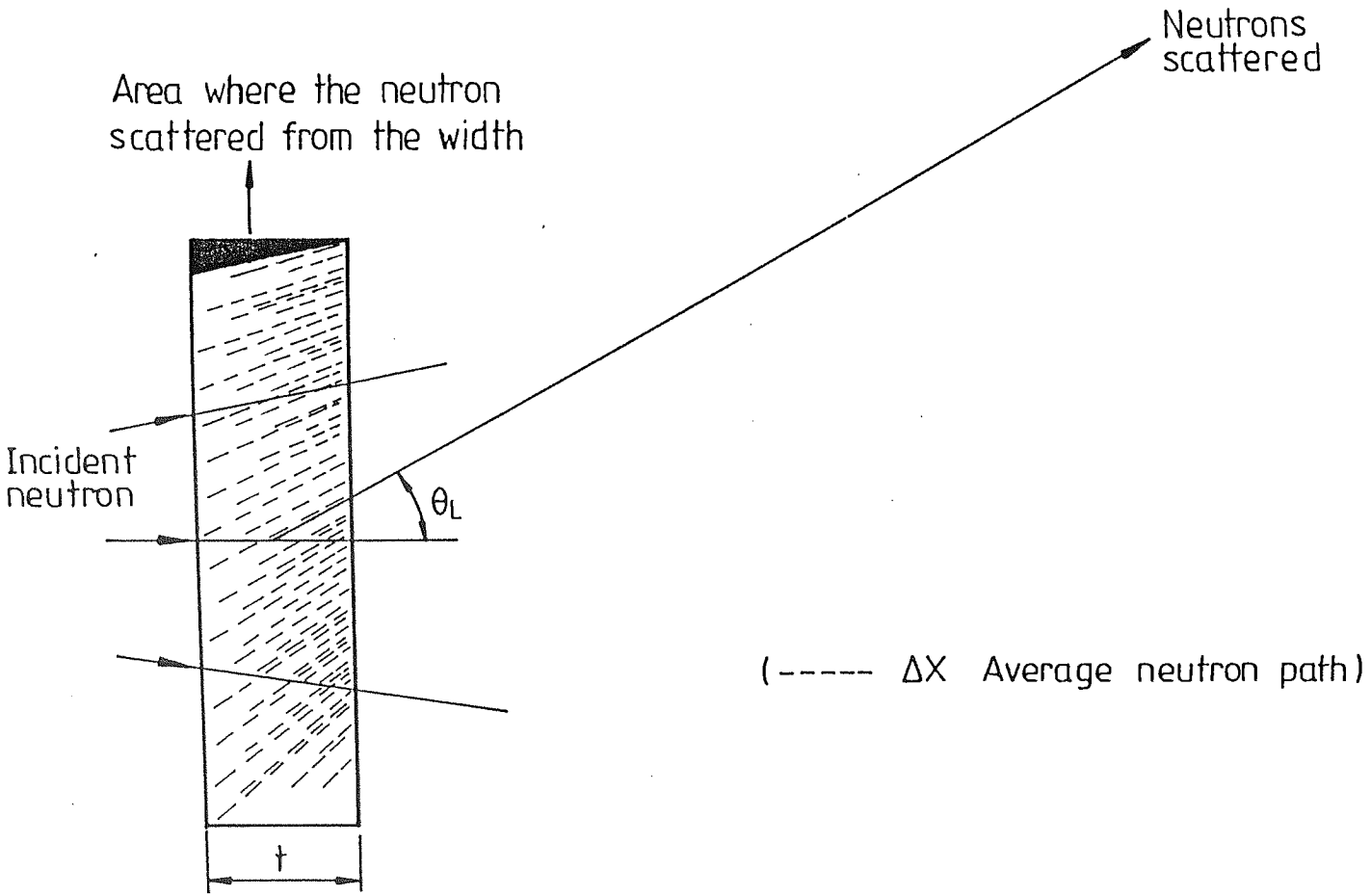

Figure (5·1) The sample geometry used to measure the path length (ΔX) of the scattered neutrons.

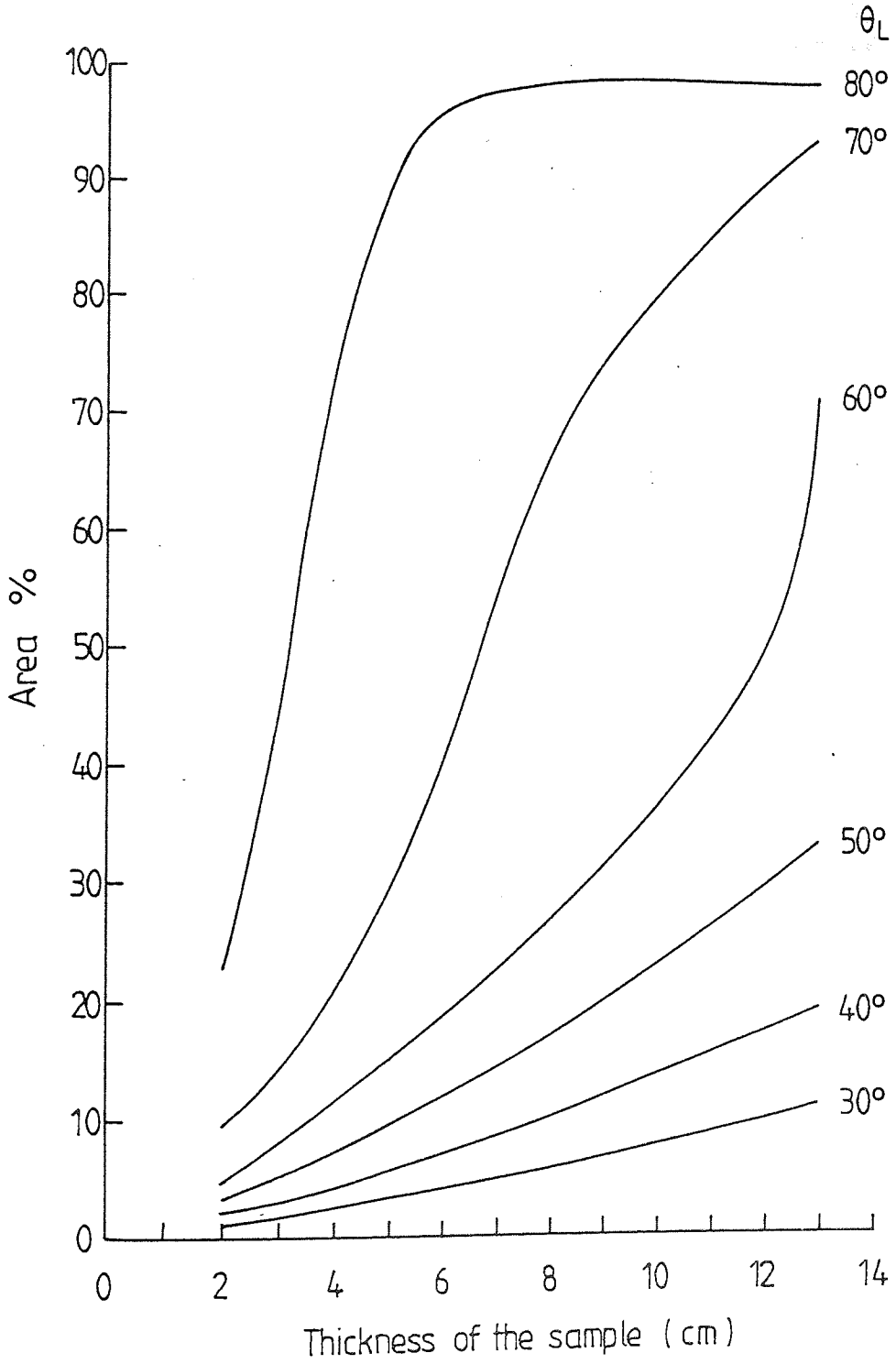

Figure (5·2) The relation between the sample thickness and area % from which the neutrons scattered through the width at different scattering angles (θ_L)

calculate the weighted average sample thickness ($\bar{x}$) over this angular range of neutron emission .

The weighted average thickness of the sample can be calculated by the equation :

$$\bar{x} = \frac{\sum f_i \cdot x_i}{\sum_i f_i} \qquad (5.15)$$

Where x_i = the sample thickness , which depends on the neutron emission angle (ϕ_n) , as shown in figure (5.3) .

f_i = the weighting fraction which is proportional to the area under the curve {figure (2.8)} in 1 degree steps over the neutron scattering angle range $77^\circ < \phi_n < 93^\circ$.

$\sum_i f_i$ = the total area under the neutron beam profile .

Figure (5.3) shows the geometrical dependence of the sample thickness , on neutron angle (ϕ_n) .

The average weighted sample thickness ($\bar{x}$) was calculated by the equation :

$$\bar{x} = (1.\emptyset\emptyset6 \pm \emptyset.\emptyset\emptyset5) \cdot t \qquad (5.16)$$

Where t = is the actual sample thickness .

5.3.3 CORRECTION TO THE ALPHA-PARTICLE COUNTS

During the experimental work, background radiation affects the total count in the alpha detector .

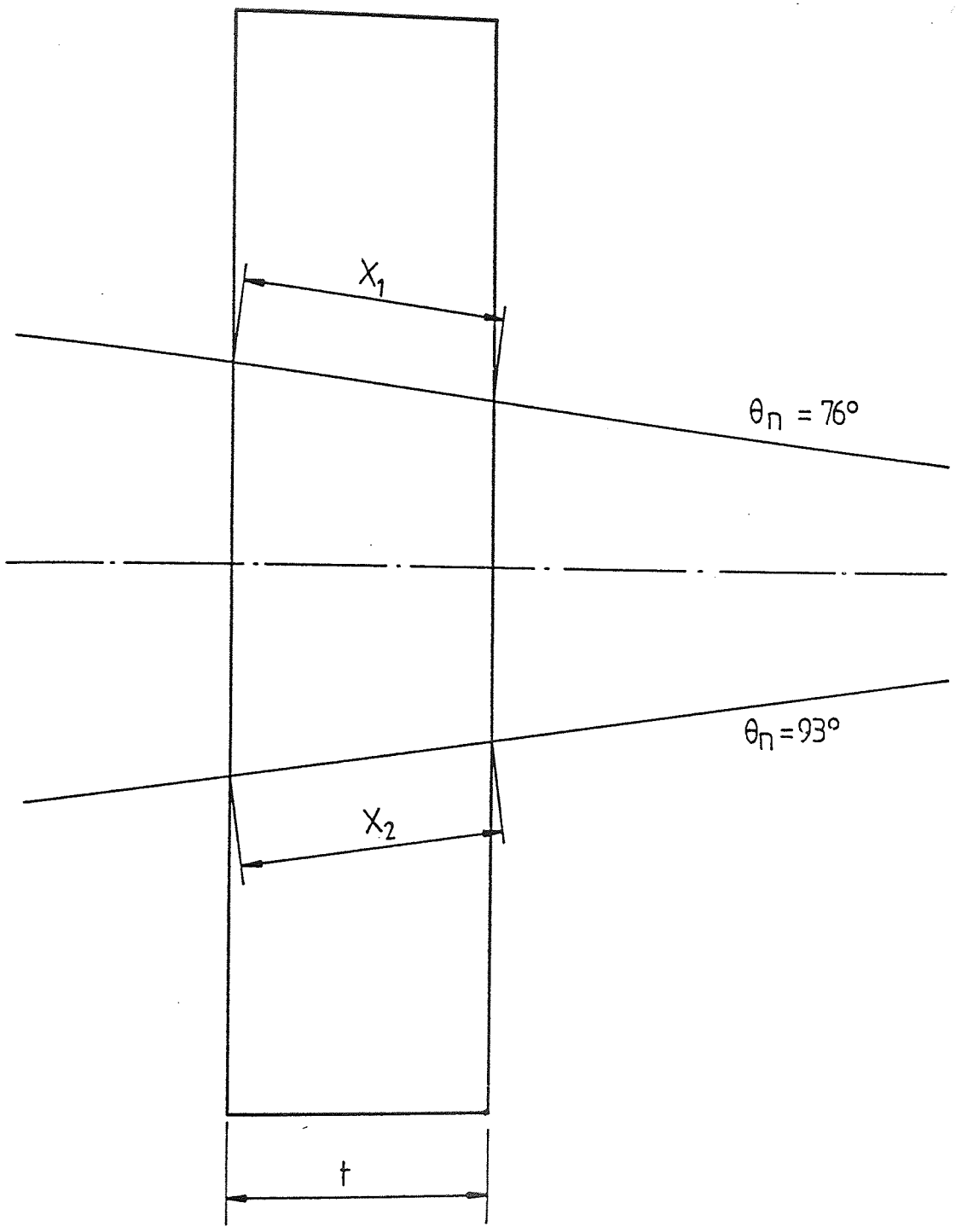

$$\bar{X} = \frac{t}{\cos \theta_n} \qquad 76^\circ < \theta_n^\circ < 83^\circ$$

$$\bar{X} = \frac{t}{\cos \theta_n} \qquad 83^\circ < \theta_n^\circ < 93^\circ$$

Figure (5·3) Calculation of the weighted sample thickness ($\bar{X}$)

The background correction can be divided into two components . The first is due to the neutrons in the direct beam being scattered from the target itself and the materials of the target assembly (mainly iron , copper and zinc) .

The second component of the correction is due to γ-rays and β-particles resulting from the activation of the target assembly .

CONNEL (1972) [33] , investigated the γ-ray spectrum produced by the target which consisted of peaks at Ø.511 Mev , Ø.845 Mev , 1.81 Mev and 2.13 Mev .The Ø.511 Mev had a half life of approximately 1Ø min. , whereas the others had half lives of several hours .

The dominant activation reaction with iron is the $^{56}Fe(n,p)^{56}Mn$ reaction , which has a cross-section of 11Ø.Ø mb at 14 Mev .^{56}Mn decays with a mean half life of 2.576 hr. and acounts for the higher γ-ray energies mentioned above .

Activation of Zn and Cu take place mainly by the (n,2n) reaction which then produces a Ø.511 Mev annihillation γ-ray . The main component is produced by the β-decay of the ^{62}Cu which has a half life of 9.73 min.

The $^{63}Cu(n,2n)^{62}Cu$ reaction has a cross-section of 55Ø mb at 14 Mev .

The decay modes of the unstable zinc isotpes produce very few γ-rays .

The background due to the activation of the target has been measured after switching off the deuteron beam immediately after each run , where the background count rate in the alpha-monitor was noted for 2Ø sec .The background count rate is usually found to be in the range of 269±16 count/sec which is used to correct the data .

Since the alpha-partical count is in the range of 60-70 kn/sec , the background mentioned above represents an effect of between 0.38% - 0.45% .

The remainder of the background is due to the direct neutron beam from the T(d,n) ^{4}He reaction which leaves the target at 83° to the deuteron beam .

This was also measured experimentally by switching the deuteron beam on , and monitoring the alpha count rates at various values of target current . After switching the machine off , the alpha-particle detector aperture was replaced by an aluminum plate of 1 mm thickness which was sufficient to stop 3.5 Mev alpha-particles with a range of 0.017 mm [67] reaching the detector .

The estimated error in the determination of the neutron background was less than 0.5% .

The total correction factor for both background effects was found to be :

$$F = 0.945 \pm 0.005$$

5.3.4 NEUTRON ABSORPTION IN THE TARGET ASSEMBLY

Neutrons produced in T(d,n) ^{4}He reaction must pass through the target assembly before reaching the scattering sample . Hence they must pass through (2.5±0.03)mm of steel and (1.3+0.03)mm of water . The data shown table (5.1) taken from CONNELL(1974) [33] for 14 Mev neutrons , have been used for the iron and water .

Table(5.1)

TOTAL CROSS-SECTION FOR Fe , O AND H

MATERIAL	CROSS-SECTION (barns)
IRON	2.316±Ø.Ø31
OXYGEN	1.523±Ø.Ø22
HYDROGEN	Ø.646±Ø.Ø14

The fraction of neutrons escaping the target , F_2 , can be calculated as :

$$F_2 = \exp - [\Sigma_{Fe} \cdot x_{Fe} + (\Sigma_O + \Sigma_H) \cdot x_{H_2O}] \qquad (5.17)$$

Where Σ_{Fe}, Σ_O , Σ_H are the macroscopic total cross-sections for iron , oxygen and hydrogen respectively and x_{Fe} and x_{H_2O} are the thicknesses of iron and water.

The fraction of source neutrons escaping the target was calculated as (Ø.96Ø±Ø.ØØ3) , where the error is due to the uncertainties in the cross-sections and the thicknesses of steel and water .

5.3.5 GEOMETRY FACTOR

As already explained in chapter three , the area of the sample which is in radiated by neutron source is defined by the alpha-detector aperture . The neutron beam is $5^{\circ}59'$ half angle high and a $3^{\circ}38'$ half angle wide .These angles define the effective irradiated area A_F in the sample , from which the scattered neutrons are directed to the neutron detector .

Since the neutron detector has a finite area , not all the scattered neutrons leaving the thick sample at a specific scattering angle enter the detector . Because of this , a correction factor must be calculated after first drawing the sample geometry {figure (5.4)} to define the effective area .The geometry factor was determined by the equation :

$$G = \frac{A_P}{A_D} = \frac{A_S}{A_D} \cdot \sin\Theta \qquad (5.18)$$

Where A_P = projected area of the sample .

A_S = radiative area of the sample .

A_D = area of the detectror .

Θ = angle of neutron detector with respect to the sample's position .

5.3.6 DETERMINATION OF THE NUMBER OF COUNTS IN THE NEUTRON PEAK N(Θ)

Most of the experimental spectra involved in this work consist of a primary Gaussian peak for neutron elastic scattering with a small additional tailing on the low energy side of the peak , and secondary Gaussian peaks for neutron inelastic scattering . The energies of the scattered neutrons are determined from the peak positions , while the areas under the peaks are used to determine the differential cross-sections . For this reason an accurate determination of the Gaussian parameters for the area of the peak is often required . The calculation of these parameters is usually performed by a least squares method [68-69] , (APPENDIX-B) , which is

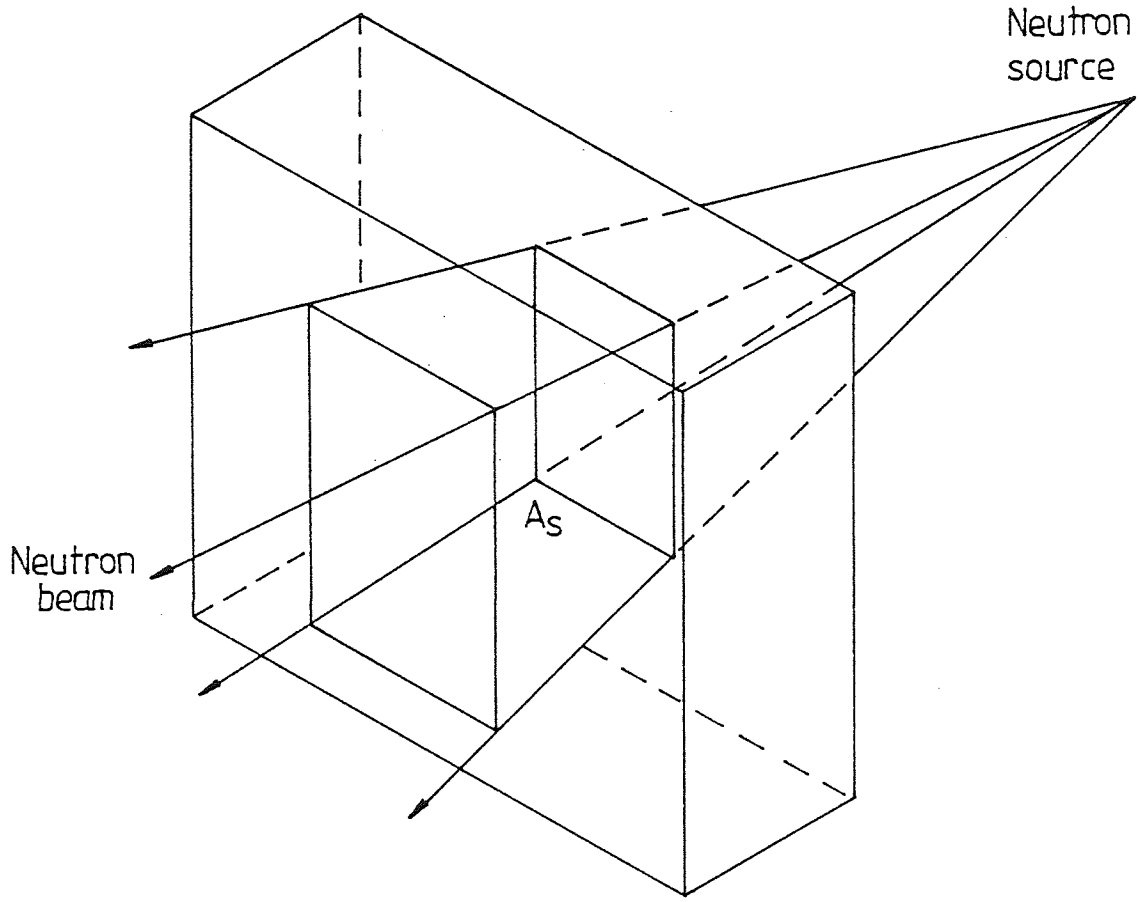

Figure (5.4) Sample geometry factor calculation

used to fit the function . The area is then derived after subtraction of the background under the peak channel-by-channel to reduce the error for the individual peak . The method of Gaussian fitting is illustrated in the computer program called GAUSSIAN (APPENDIX-B).

A typical fitting of neutron spectra at 14 Mev shown in figure (5.5) , and the results obtained by this method are listed in table (5.2) .

Table (5.2)

GAUSSIAN PARAMETERS OF FIG (5.5)

REACTION	Y_0	X_0	σ	χ^2
Q = Ø.Ø	557±41	329±Ø.12	1.893±Ø.ØØ2	Ø.7Ø8
Q = -4.43Mev	21Ø±24	311±Ø.Ø5	1.669±Ø.ØØ3	Ø.Ø36

5.4 DIFFERENTIAL CROSS-SECTION FORMULA

The formula used to determine the differential cross-section for scattering neutrons of energy En , after applying all correction factors , is :

$$\frac{d\sigma}{d\Omega} = \frac{N(\Theta)\cdot\sigma_T\cdot G}{n\cdot F_1\cdot F_2\cdot\{\,1-\exp(-N\cdot\sigma_T\cdot t)\,\}\cdot\Delta\Omega\cdot\exp(-N\cdot\sigma_T\cdot t)} \qquad (5.19)$$

Where all the terms have been previously defined .

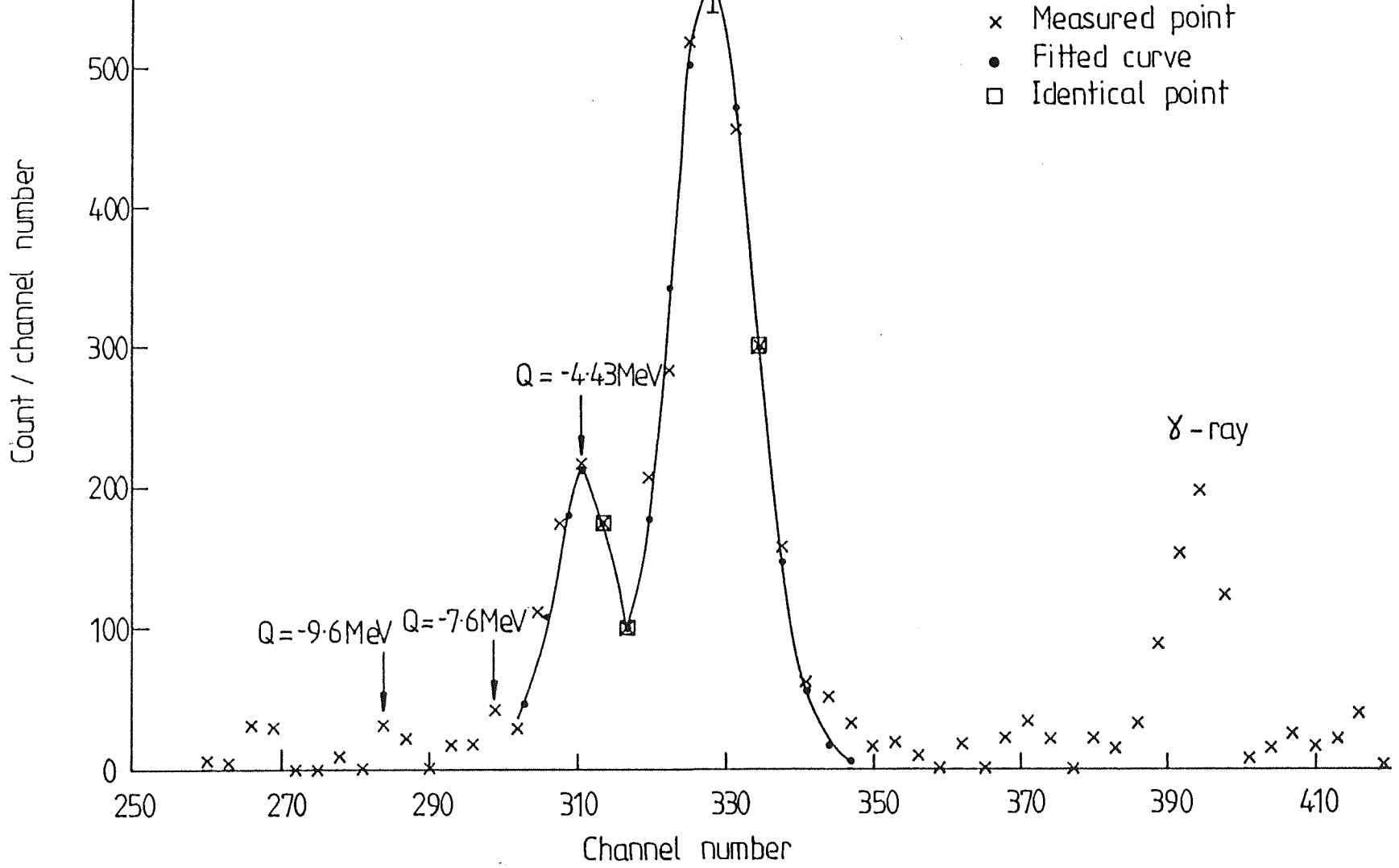

Figure (5·5) Time-of-flight spectra of ^{12}C at 14·1 MeV at scattering angle 50°

5.5 NEUTRON DETECTOR EFFICIENCY MEASUREMENT

The energy dependence of the neutron detector efficiency is required , for 14 Mev and 14.44 Mev neutrons ,in order to determine the neutron differential cross-sections. It was measured in two ways.The first called the absolute efficiency ,is where the neutron detector is placed at a distance of 20 cm. from the target , located on the center line of the neutron beam profile to ensure that the neutron detector was fully covered by the neutron source . The total number of pulses were recorded in both the alpha-particle and neutron detectors , the alpha counter giving the total number of incident neutrons on the detector . The absolute efficiency was then determined by :

$$\mathcal{E}(En) = \frac{Nr}{Ns} \cdot \frac{d\Omega_{\alpha}}{d\Omega_{n}} \qquad (5.20)$$

Where Nr = total number of pulses recorded .

Ns = total number of incident neutrons defined by the alpha detector .

$d\Omega_n$= solid angle subtended by the neutron detector at the source .

$d\Omega_{\alpha}$= solid angle subtended by the alpha-detector aperture .

The absolute efficiency obtained was (9.74±0.3)% at 14.1 Mev and (9.7±0.2)% at 14.44 Mev . The second method of efficiency measurement , called the relative efficiency , is where an n-p scattering experiment is performed using a dewar filled with water giving 0.25 mean-free-path . The relative efficiency of the neutron detector at energies lower than 14 Mev can be determined by measuring the number of

scattered neutrons from the hydrogen in the water at detection angles between 30° and 50° .

Alternative runs were made with an empty dewar in position to subtract both the random background and the background due to scattering from the dewar . Figure (5.6) and figure (5.7) show typical time- of-flight spectra at 30° and 40° . The efficiency of the neutron detector may be written as :

$$\varepsilon_R(En) = \frac{N(\theta) \cdot \sigma_t \cdot G}{n.F_1.F_2.\{1 - \exp(-N.\sigma_t.\bar{x})\} \cdot \frac{d\sigma}{d\Omega}(\theta) \cdot \Delta\Omega} \qquad (5.21)$$

Where $\frac{d\sigma}{d\Omega}(\theta)$ = the differential cross-section in the lab-system for scattering neutrons from hydrogen .

The other parameters are as previously defined .

The relative efficiency was calculated using the n-p total cross-section {fig(5.8)} and the various ${}^{1}_{1}H(n,n){}^{1}_{1}H$ differential cross-section data from ENDF/b-IV {fig (5.9)} . The experimental results obtained for $\varepsilon_R(En)$ are presented in table (5.3) and are shown plotted as a funtion of neutron energy in fig(5.10) . The error on $\varepsilon_R(En)$ was estimated to be 2.9 % at each of the data points . This is the result of summing in quadrature . The possible errors estimated for each term of equations (5.21) is listed in table (5.4). The smooth curve shown in fig (5.9) is the result of a polynomial [109] fit to the data yielding the equation :

$$\varepsilon_R(En) = 8.66\ 10^{-4} . En^3 . f_2 - 7.78 f_1 \qquad (5.22)$$

Where $f_1 = 8.33 - 4.84.En + En^2$

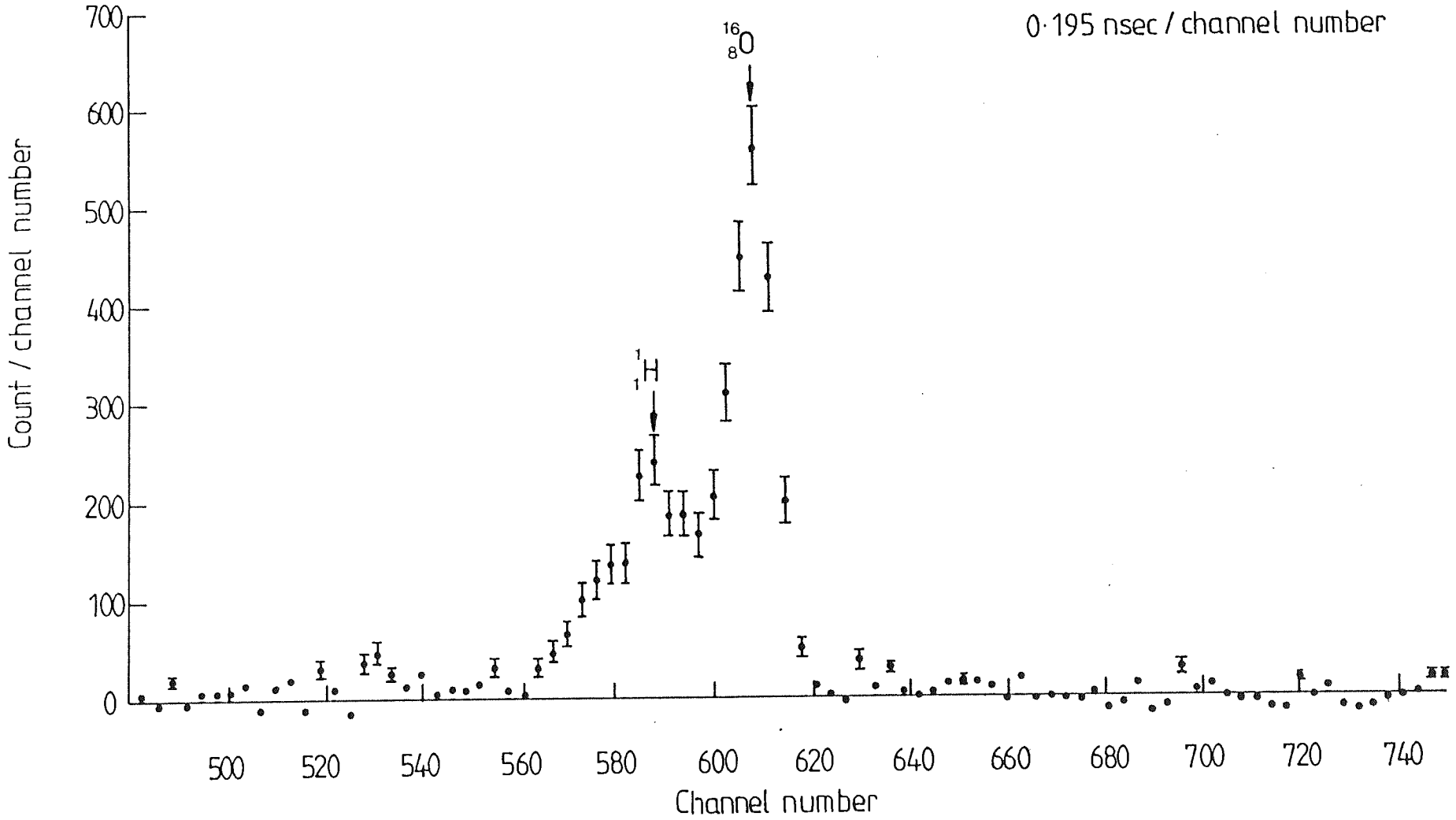

Figure (5·6) Neutron time-of-flight spectrum showing 14 MeV neutrons scattered from 0·25 mfp thickness of water at scattering angle 30°

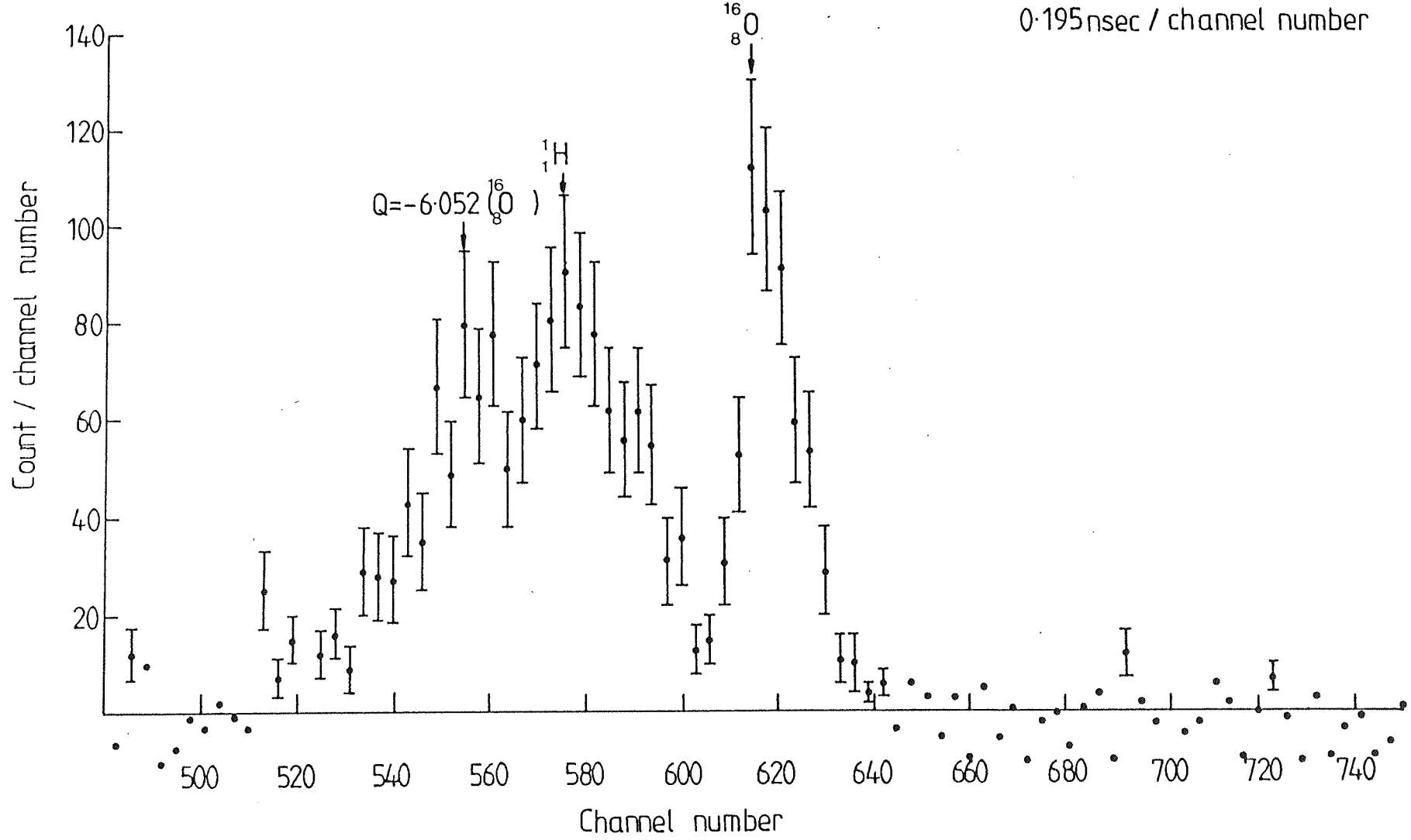

Figure (5·7) Neutron time-of-flight spectrum showing 14 MeV neutrons scattered from 0·25 mfp thickness of water at scattering angle 40°

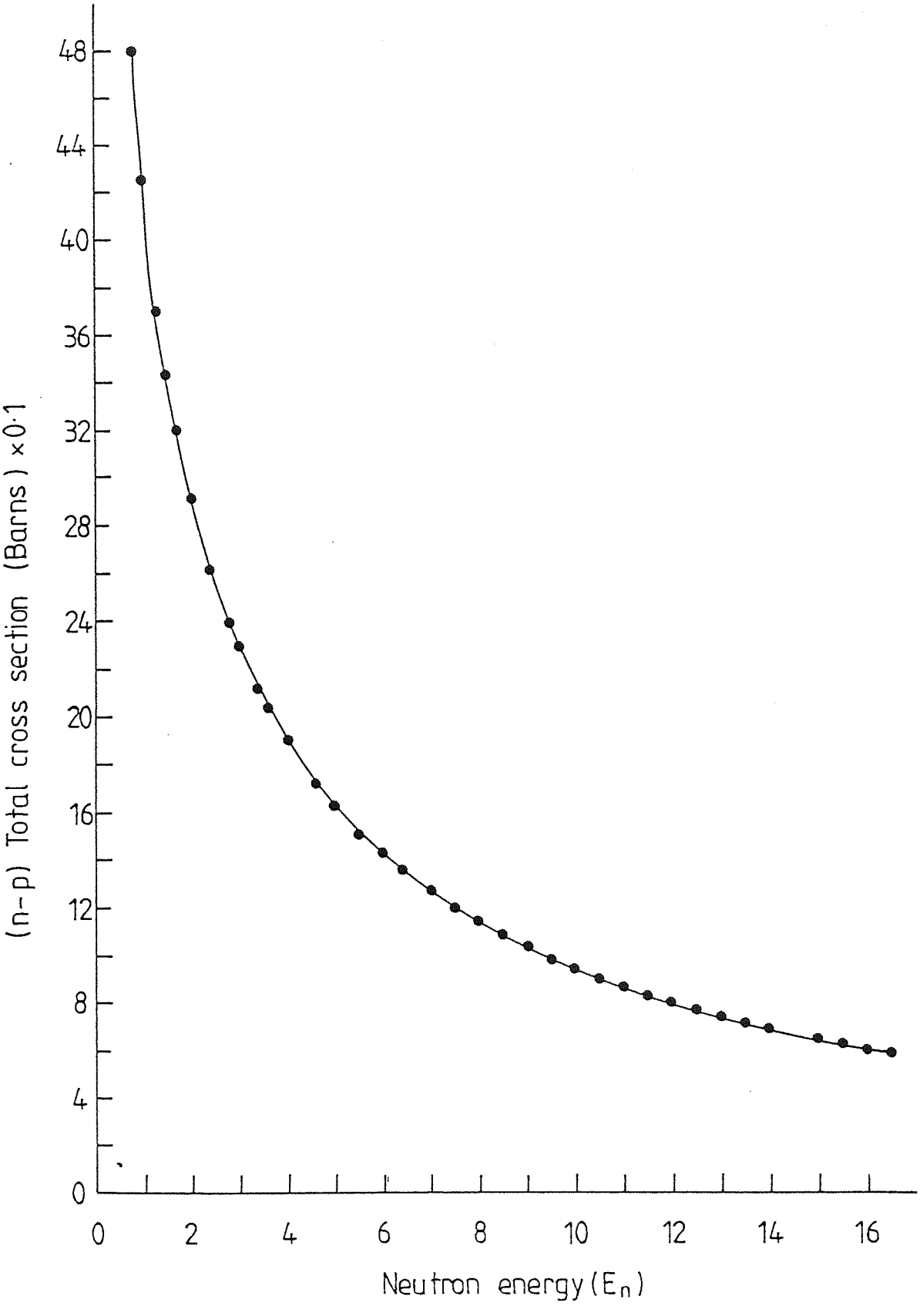

Figure (5·8) Total cross section of hydrogen for neutrons of energies between 0·8 and 16 MeV, from ENDF/B-IV [66]

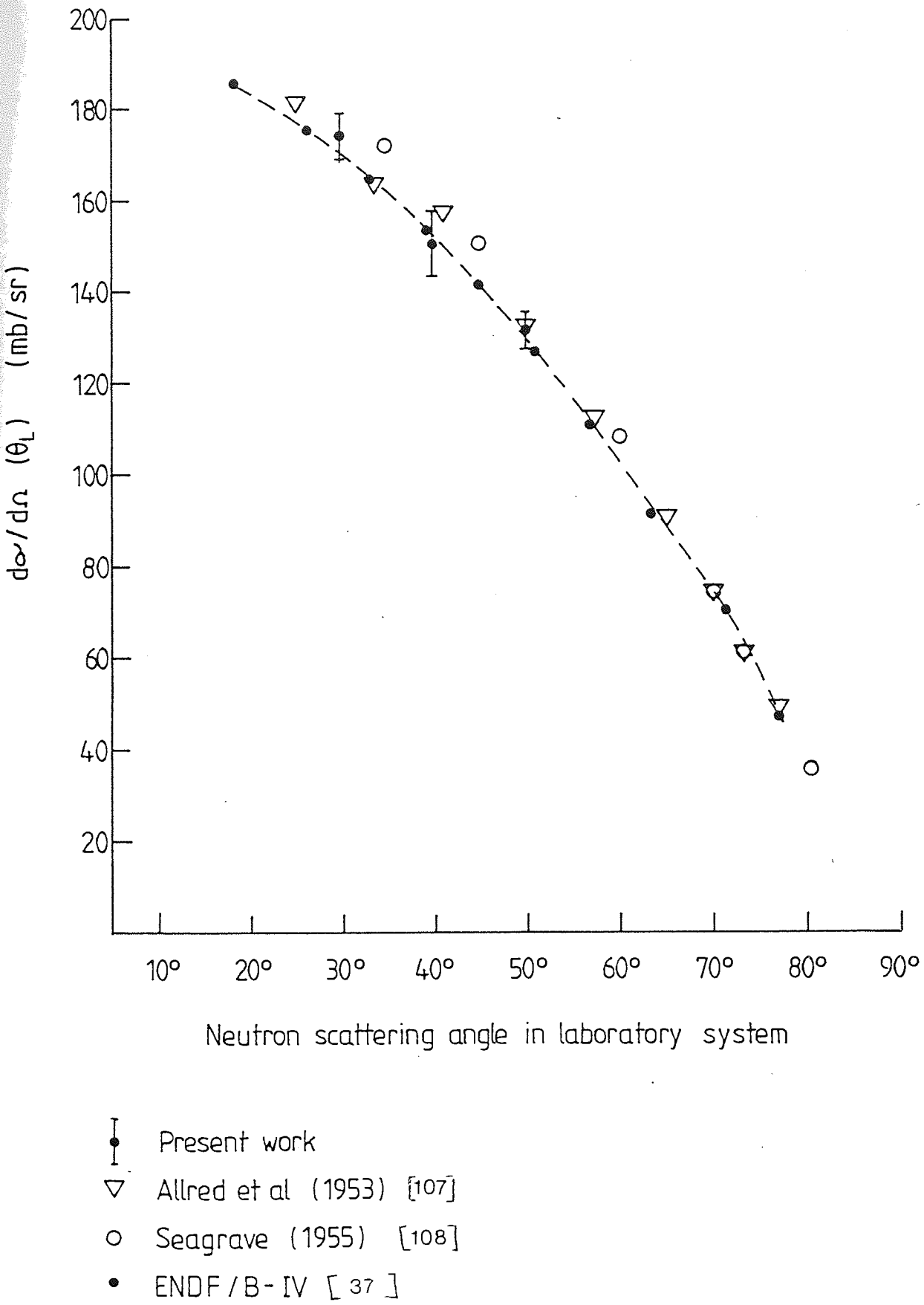

Figure (5.9) n-p differential x-section in laboratory system as a function of scattering angle (θ_L) at 14·1 MeV

$$f_2 = 937.159 - 48.708 \cdot En + En^2$$

Table (5.3)

NEUTRON DETECTOR EFFICIENCY

θ_L	En(Mev)	ε_R(En) %
×Ø°	14.ØØ±Ø.5Ø	×9.74±Ø.31
3Ø°	5.76±Ø.29	8.2Ø±Ø.3Ø
4Ø°	8.2Ø±Ø.3Ø	9.8Ø±Ø.3Ø
5Ø°	1Ø.2Ø±Ø.4Ø	1Ø.2Ø±Ø.29

×) DIRECT BEAM MEASUREMENT OF EFFICIENCY.

Measurements of the n-p differential cross-sections were made at an incident neutron energy of 14.1 Mev on hydrogen and with detection angles of 3Ø°, 4Ø°, and 5Ø°. The comparison of the present data with the published values of ENDF/B-IV[37], ALLERD etal (1953) [107] and SEAGRAVE (1955) [108], shows significant agreement of 1.6 % to 2.5 % with higher values at 3Ø° and 5Ø°, and systematically lower values (1.95 %) at 4Ø° as shown in fig (5.9).

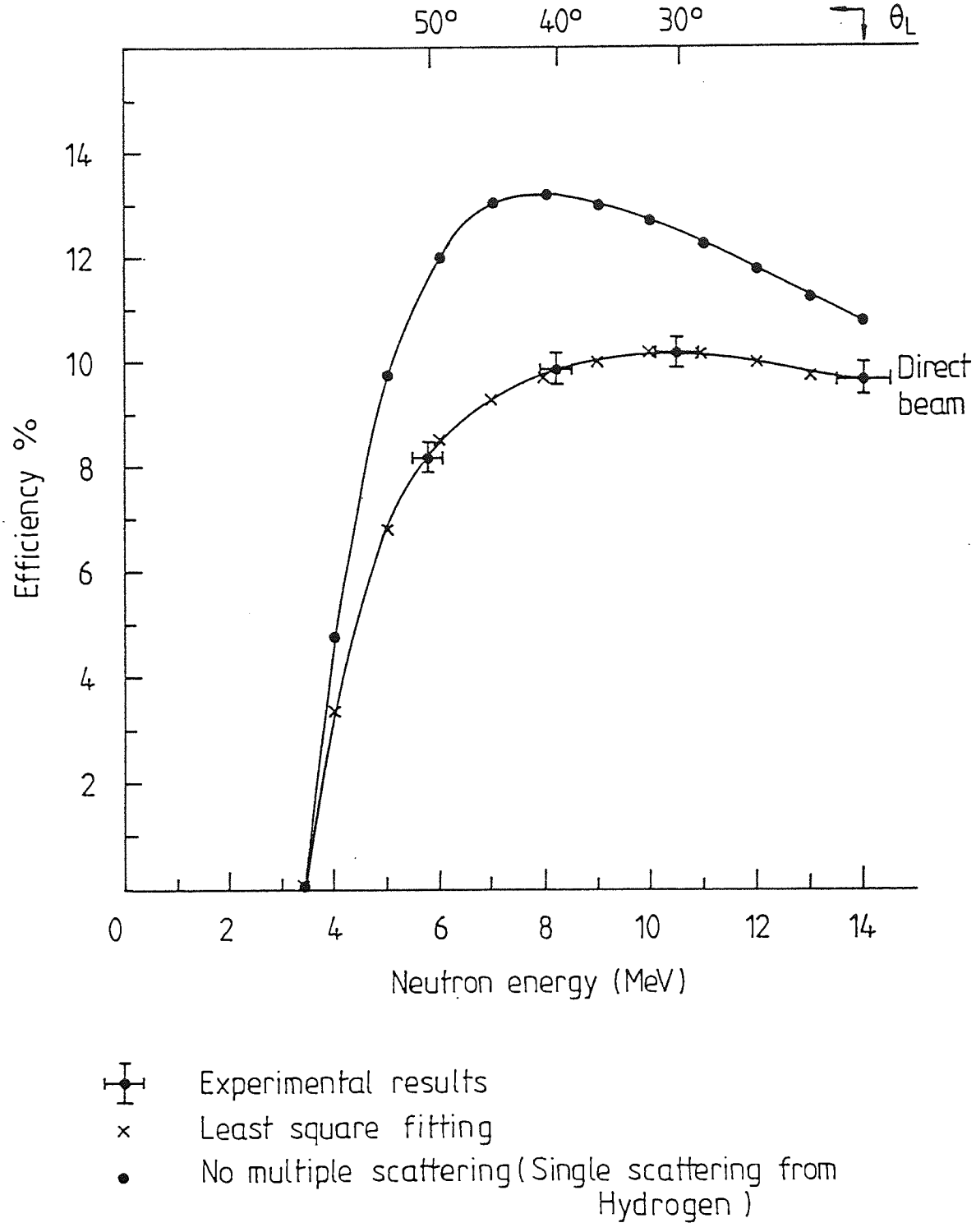

Figure (5·10) Neutron detector efficiency as a function of neutron energy.

Table (5.4)

EXPERIMENTAL ERRORS IN EACH TERM OF EQUATION (5.21)

PARAMETER	ESTIMATED ERROR (%)
$N(\Theta)$	6.5
σ_T	< 1 [52]
n	Ø.38 - Ø.45
$\Delta\Omega$	1.12
$\bar{x}$	< 1
F_1 , F_2	Ø.3 - Ø.5
$\frac{d\sigma}{d\Omega}(\Theta)_H$	4.3

CHAPTER SIX (PART ONE)

LITHIUM DIFFERENTIAL CROSS-SECTION MEASUREMENTS

CHAPTER SIX

LITHIUM DIFFERENTIAL CROSS-SECTION

6.1 LiF SAMPLES

The scattering sample consisted of powdered lithium fluoride with natural lithium (92.5% ^{7}Li and 7.5% ^{6}Li) and fluorine (100% ^{19}F) . The powder samples were canned in thin aluminium containers in slab geometry . An empty aluminium container was used for background measurements . Five different thicknesses of LiF were used in the work as listed in table (6.1)

Table (6.1)

DIMENSIONS OF LiF SCATTERING SAMPLES USED IN THE PRESENT WORK

Length (cm.)	Width (cm.)	Thickness	
		(cm.)	(mfp)
25	14	2	Ø.14
25	14	4	Ø.27
25	14	6	Ø.41
25	14	9	Ø.62
25	14	13	Ø.89

For the work on the dynamitron , three samples of thickness 4 cm , 9 cm , and 13 cm respectively were used .

6.2 TIME-OF-FLIGHT SPECTRA

In order to explain the observed spectra it is necessary to consider the energy level diagrams of both ^{7}Li and ^{19}F . These are shown in fig (6.1) . Due to the kinematics of the reaction , the neutrons elastically scattered respectively from ^{7}Li and ^{19}F have an energies of 13.64 Mev and 14 Mev at 30° , and 10.575 Mev and 12.69 Mev at 90° in the laboratory system . Therefore , the peaks due to ^{7}Li overlap peaks of the ^{19}F spectrum at different angles .
The calculation of the differential elastic scattering cross-section in lithium therefore required correction for the contribution of the elastic and inelastic scattering for the 1.554 Mev level of the ^{19}F .

Figs (6.2) and (6.3) show typical time spectra corresponding to the laboratory angles 27.81° and 80° respectively for different sample thicknesses and fig(6.4) shows a typical time spectrum at En=14.44 Mev at 45° scattering angle .

6.3 EXPERIMENTAL RESULTS FOR THE DIFFERENTIAL ELASTIC SCATTERING CROSS-SECTIONS

6.3.1 NEUTRON ENERGY - 14 Mev

The differential cross-sections for each sample were calculated using equation (5.21) .
The neutrons corresponding to elastic scattering in lithium were calculated after correcting the LiF results for elastic and inelastic scattering in fluorine .

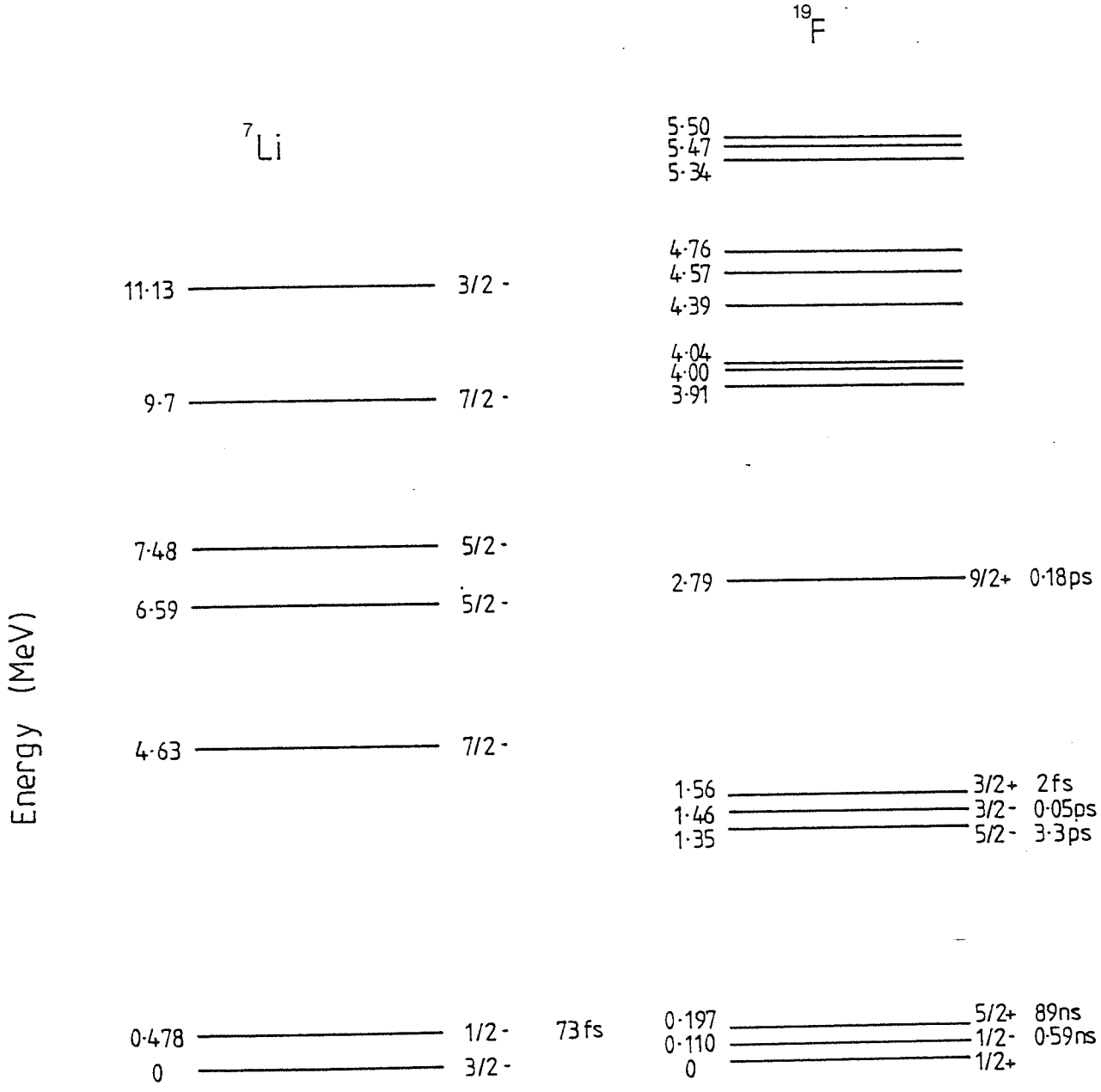

Figure 6·1 Level diagrams of ^{7}Li and ^{19}F

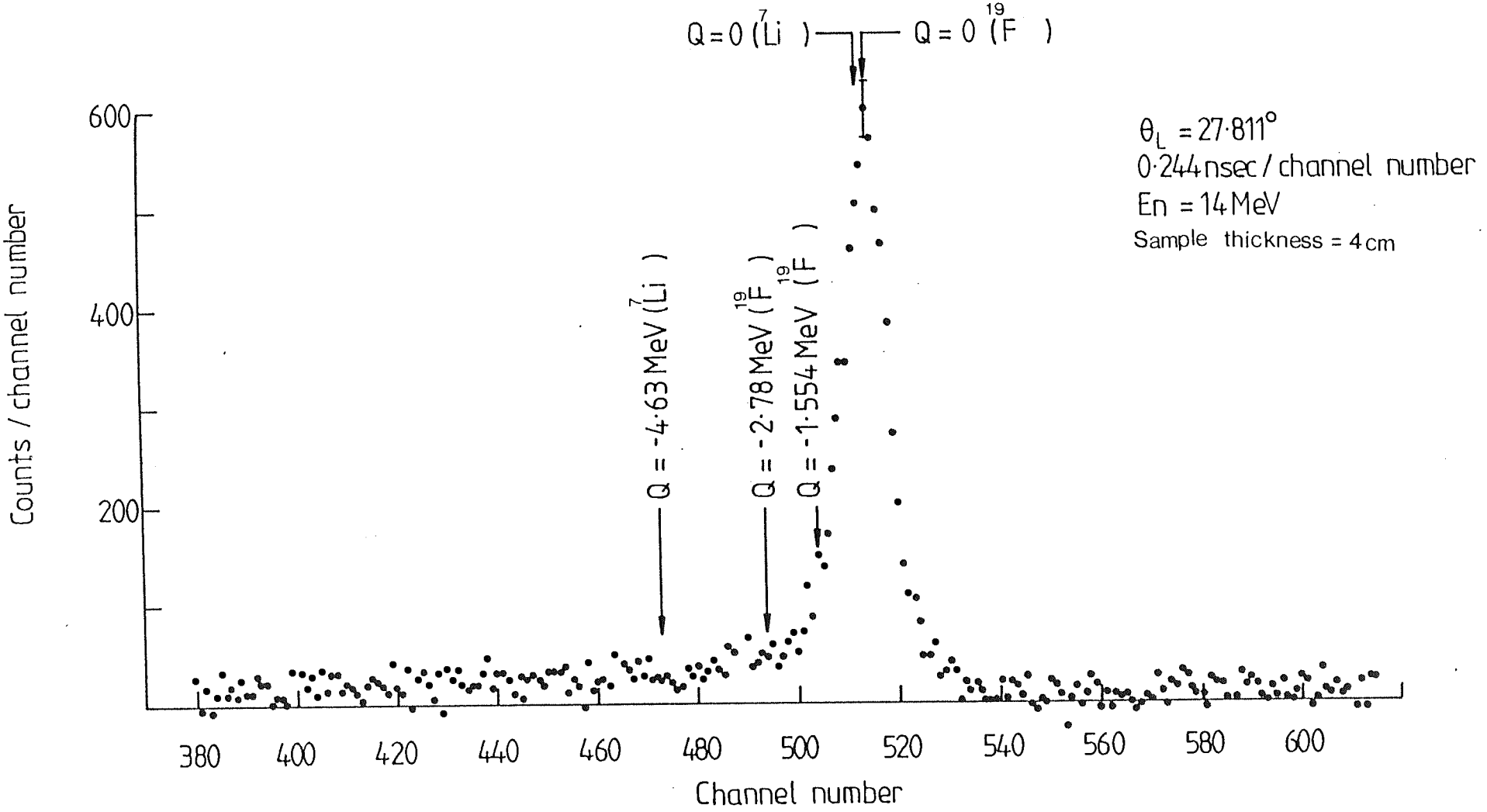

Figure 6·2 Time-of-flight spectrum for neutron scattering from LiF. The energy of the scattered neutrons decrease from right to the left. The arrows show the calculated positions of the peaks corresponding to known states in fluorine and ^{7}Li.

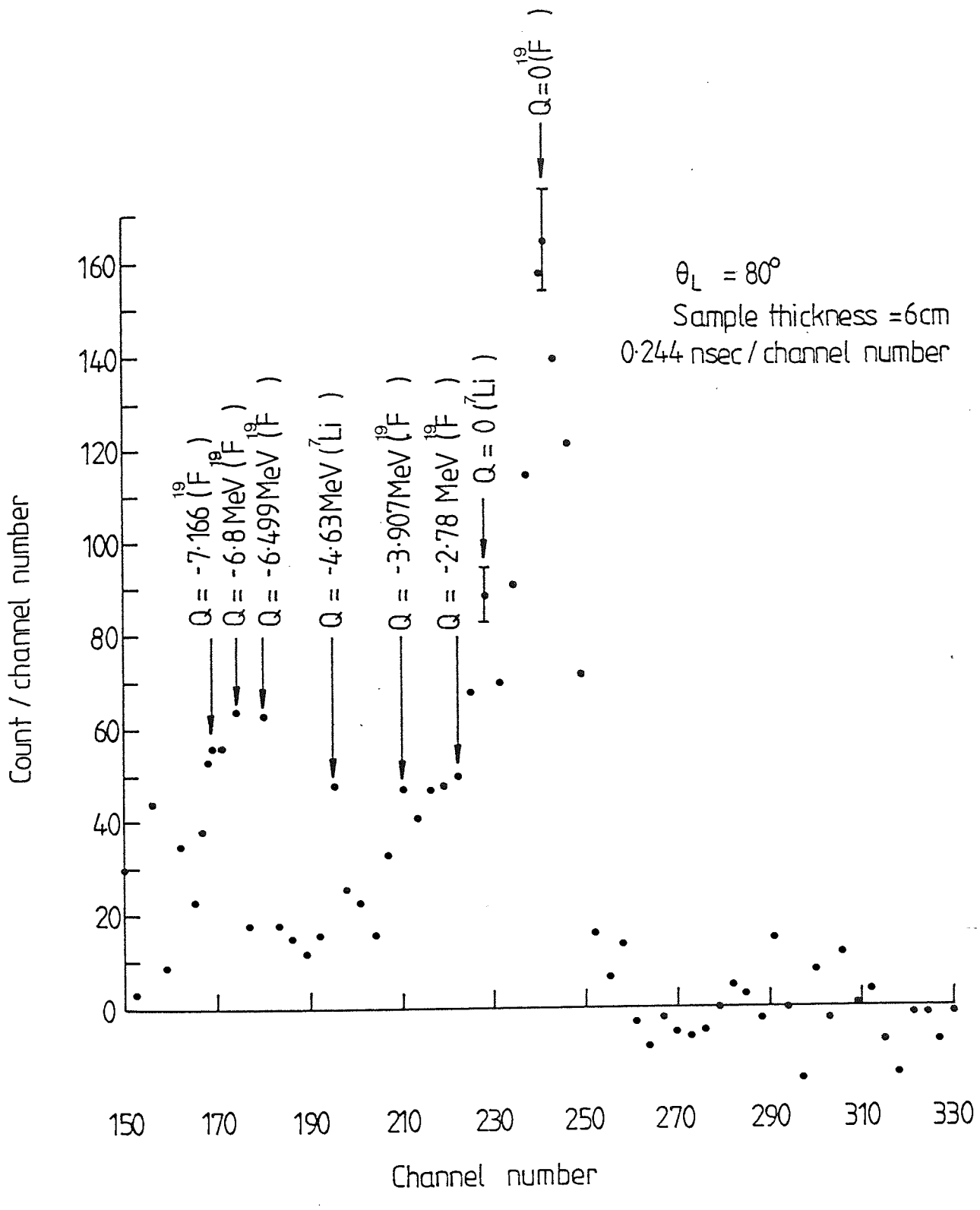

Figure 6·3 Time-of-flight spectrum for neutrons scattered by LiF (En =14·0 MeV)

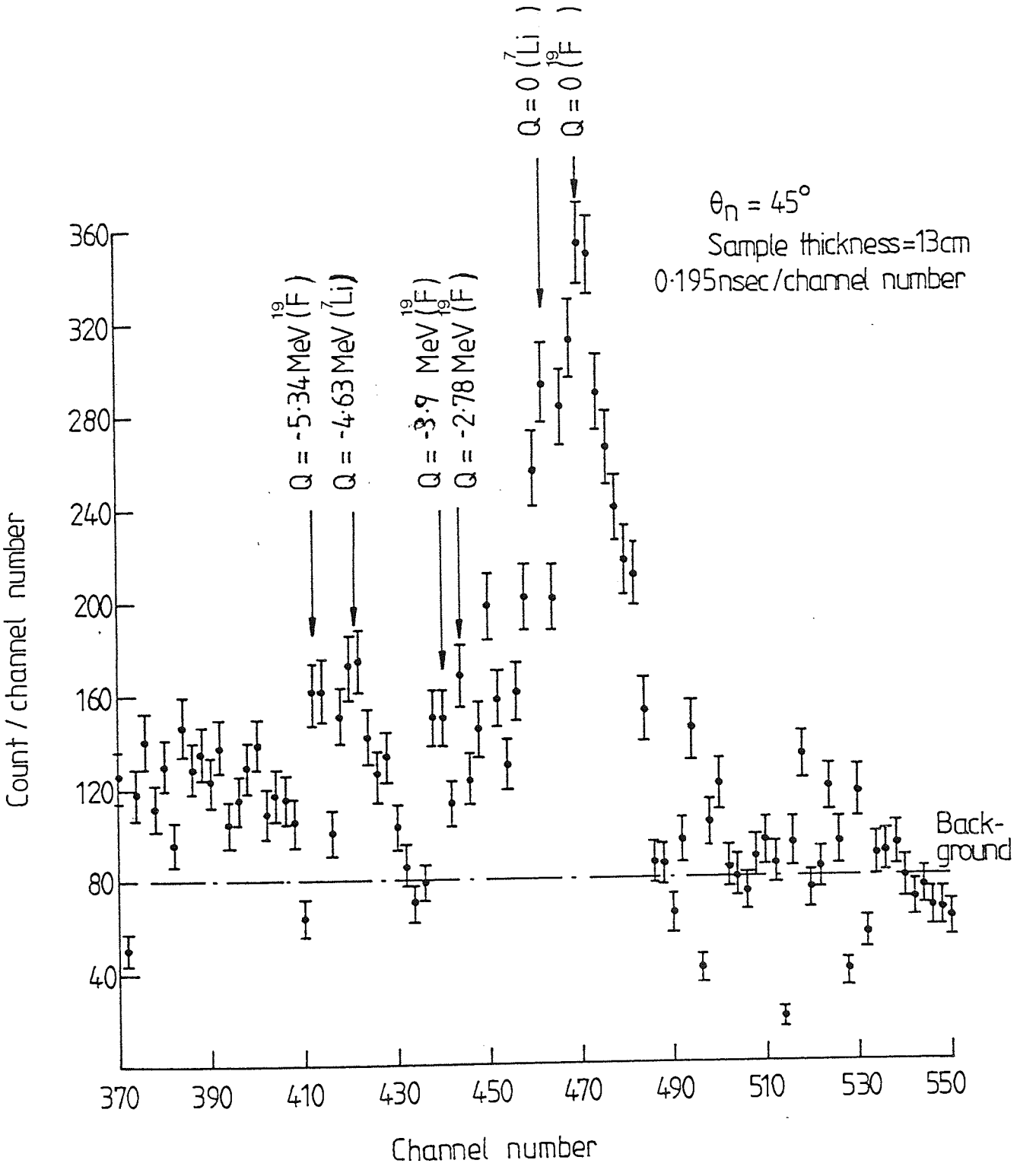

Figure 6·4 Time-of-flight spectrum for neutrons scattered by LiF (En = 14·44 MeV)

Figs (6.5) and (6.6) show the results for each scattering angle [77,78].

Table (6.2) shows the differential elastic cross-section for 14 Mev neutrons from the lithium samples with the errors calculated using equation (5.21) and indicated in table (6.3) .

Fig (6.7) gives the angular distributions of neutrons from the scattering from the ground state of the lithium samples up to 90° in the lab-system .

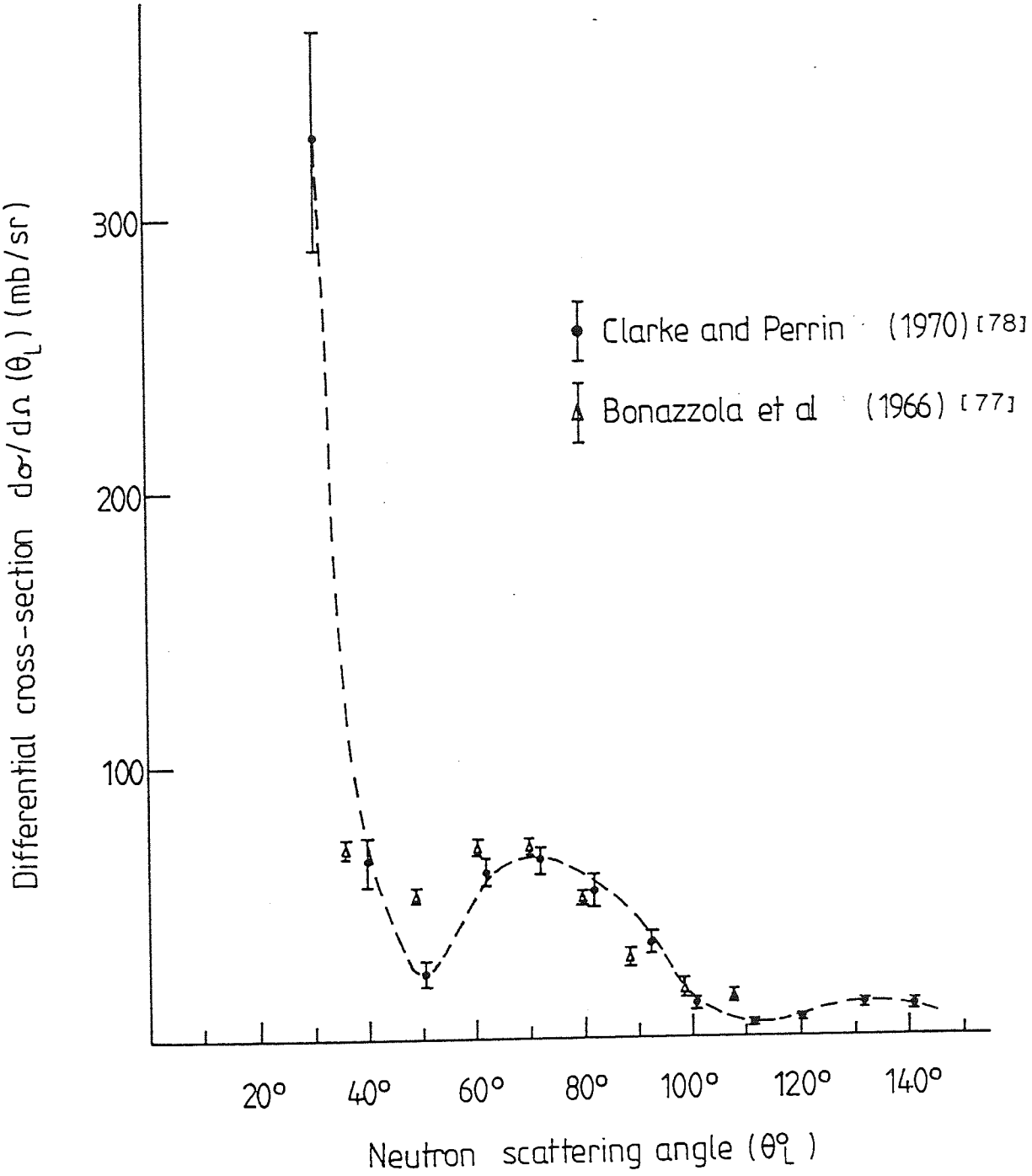

Figure 6·5 Differential cross-sections of neutrons elastically scattered from ^{19}F .

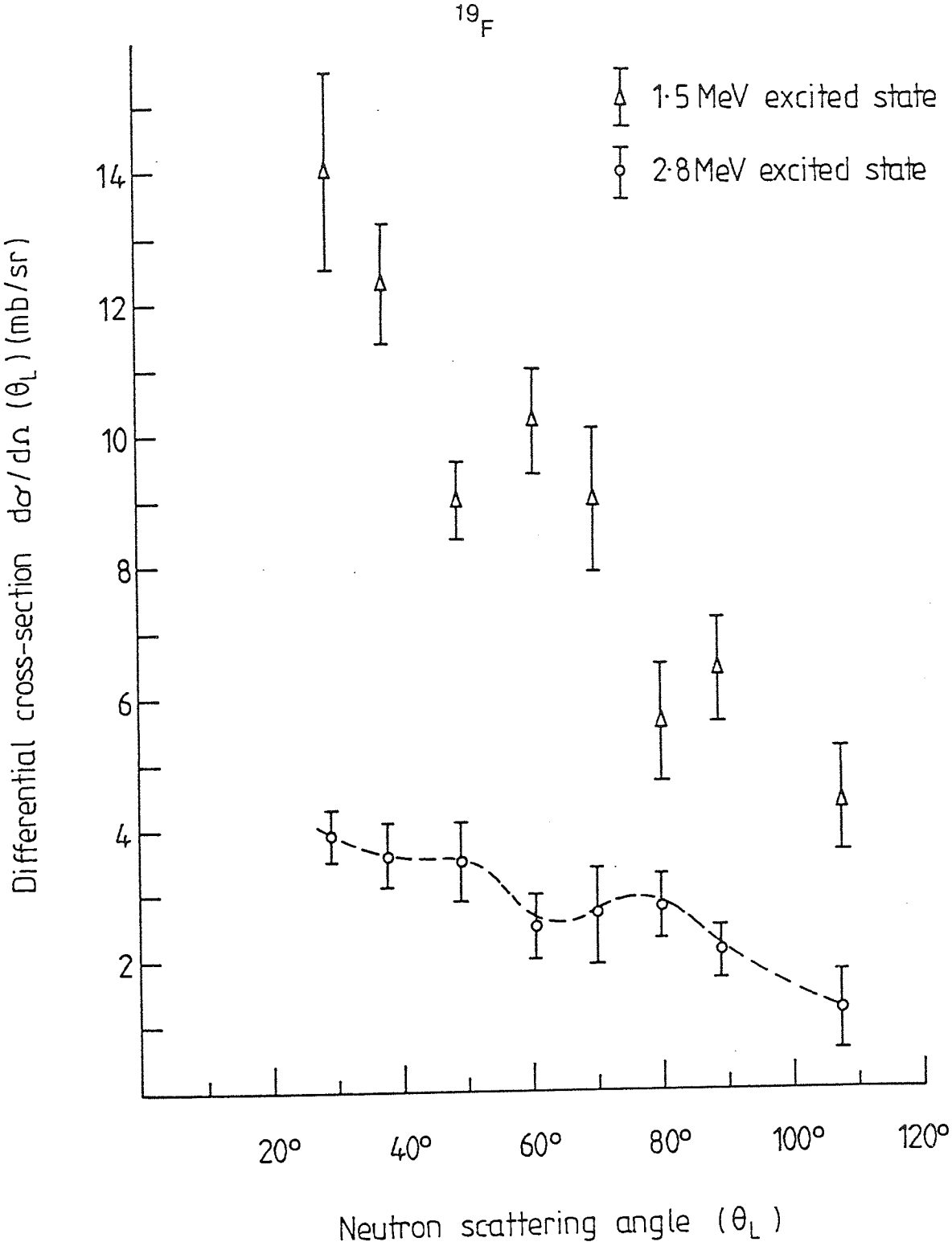

Figure 6.6 Differential cross-sections for the two groups of neutrons found at 1·5 MeV and 2·8 MeV. The data has been taken from reference (77).

Table (6.2)

LITHIUM DIFFERENTIAL ELASTIC SCATTERING CROSS-SECTION DATA OF 14 MEV NEUTRONS

NEUTRON SCATTERING ANGLE (Deg. Lab)	SAMPLE THICKNESS (cm)	(mfp)	DIFFERENTIAL ELASTIC SCATTERING CROSS-SECTION(mb/st.)
27°48'	2 ±0.004	0.14 ±0.001	415 ± 47
	4 ±0.008	0.27 ±0.01	500 ± 63
	6 ±0.02	0.41 ±0.01	513 ± 69
	9 ±0.02	0.62 ±0.02	613 ± 56
	13 ±0.03	0.89 ±0.02	634 ± 63
30°	2 ±0.004	0.14 ±0.001	400 ± 35
	4 ±0.008	0.27 ±0.01	408 ± 53
	6 ±0.02	0.41 ±0.01	409 ± 25
	9 ±0.020	0.62 ±0.02	425 ± 38
	13 ±0.030	0.89 ±0.02	432 ± 42
35°	2 ±0.004	0.14 ±0.001	257 ± 33
	4 ±0.008	0.27 ±0.01	304 ± 33
	6 ±0.020	0.41 ±0.01	287 ± 26
	9 ±0.020	0.62 ±0.02	316 ± 29
	13 ±0.030	0.89 ±0.02	353 ± 21
40°	2 ±0.004	0.14 ±0.001	248 ± 25
	4 ±0.008	0.27 ±0.01	258 ± 34
	6 ±0.020	0.41 ±0.01	249 ± 24
	9 ±0.020	0.62 ±0.02	299 ± 44
	13 ±0.030	0.89 ±0.02	309 ± 33
45°	2 ±0.004	0.14 ±0.001	126 ± 14
	4 ±0.008	0.27 ±0.01	135 ± 16
	6 ±0.020	0.41 ±0.01	143 ± 18
	9 ±0.020	0.62 ±0.02	187 ± 23
	13 ±0.030	0.89 ±0.02	201 ± 20
54° 20'	2 ±0.004	0.14 ±0.001	67 ± 14
	4 ±0.008	0.27 ±0.01	75 ± 15
	6 ±0.020	0.41 ±0.01	80 ± 15
	9 ±0.020	0.62 ±0.02	100 ± 13
	13 ±0.030	0.89 ±0.02	107 ± 23

table(6.2) , continue

70°	2 ±0.004	0.14 ±0.001	33 ± 8
	4 ±0.007	0.27 ±0.01	55 ± 12
	6 ±0.020	0.41 ±0.01	78 ± 12
	9 ±0.020	0.62 ±0.02	83 ± 15
	13 ±0.030	0.89 ±0.02	88 ± 18
80°	2 ±0.004	0.14 ±0.001	29 ± 4
	4 ±0.007	0.27 ±0.01	23 ± 4
	6 ±0.020	0.41 ±0.01	45 ± 7
	9 ±0.020	0.62 ±0.02	48 ± 6
	13 ±0.030	0.89 ±0.02	57 ± 7
90°	2 ±0.004	0.14 ±0.001	28 ± 3
	4 ±0.007	0.27 ±0.01	20 ± 4
	6 ±0.020	0.41 ±0.01	33 ± 6
	9 ±0.020	0.62 ±0.02	49 ± 7
	13 ±0.030	0.89 ±0.02	56 ± 8

Table (6.3)

EXPERIMENTAL ERRORS IN THE CALCULATION OF THE DIFFERENTIAL ELASTIC SCATTERING CROSS SECTION OF LITHIUM

FACTOR	ESTIMATED ERROR %
E_1 , E_2 , n	< 1
$N(\theta)$	$[\sum (Acc - B.G.)_i^2]^{\frac{1}{2}}$
$\Delta\Omega$, G	1.75
$\bar{\varepsilon}(En)$	5
$\bar{X}$	<1
ATTENUATION FACTOR	1.1

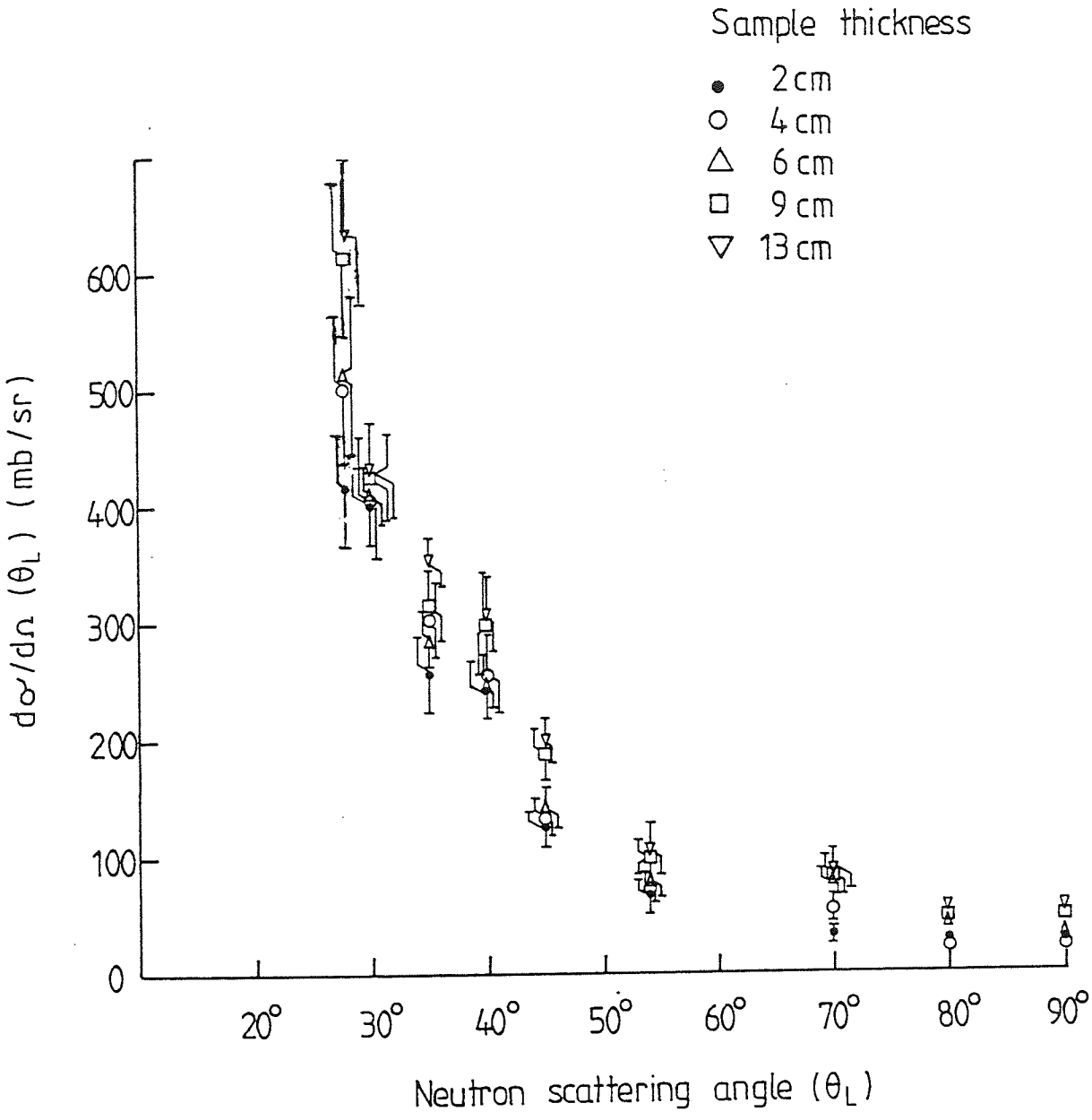

Figure 6.7 Differential elastic scattering cross-section of 14MeV neutrons on Lithium.

The variation of the differential cross-section results as a function of neutron scattering angle obtained from present work can be characterized in terms of expansion coefficients of a LEGENDRE POLYNOMIAL [22,83] :

$$\frac{d\sigma}{d\Omega}\left[E,\mu\right] = \frac{\sigma_{el}(E)}{4\pi}\sum_{l=0}^{l_{max}}\left\{1+\beta_l(E)\,P_l(\mu)\right\} \qquad (6.1)$$

and $$\sigma_{el}(E) = 2\pi\int_{-1}^{+1}\frac{d\sigma}{d\Omega}\left[E,\mu\right]d\mu \qquad (6.2)$$

the total elastic scattering cross-section at a laboratory energy (E) . Here $\mu = \cos\theta$, θ is the lab-scattering angle and $P_l(\mu)$ is the Ith Legendre Polynomial in terms of the variable .

The differential elastic scattering cross-section data given in table (6.2) were fitted to the Legendre Polynomial as shown in fig (6.8) . The Legendre Polynomial coefficients are given in table (6.4) together with theoretical calculations of the integrated elastic scattering cross-sections .The fitting terms were improved by specifying only even terms in the polynomial in accordance with the statistical model of the nucleus .

A more complete discussion of the use of Legendre Polynomial program (LEGFIT) is given in appendix C .

6.3.1.1 <u>THE VARIATION OF MEASURED $\sigma(\theta)$ WITH LITHIUM SAMPLE THICKNESS</u>

The experimental results of the differential elastic scattering cross-section for different sample thicknesses are given in table (6.2) . It can be seen from this table that the measured cross-section increases with the increasing sample thickness .This indicated the effect of multiple scattering of the incident neutrons in the sample ,

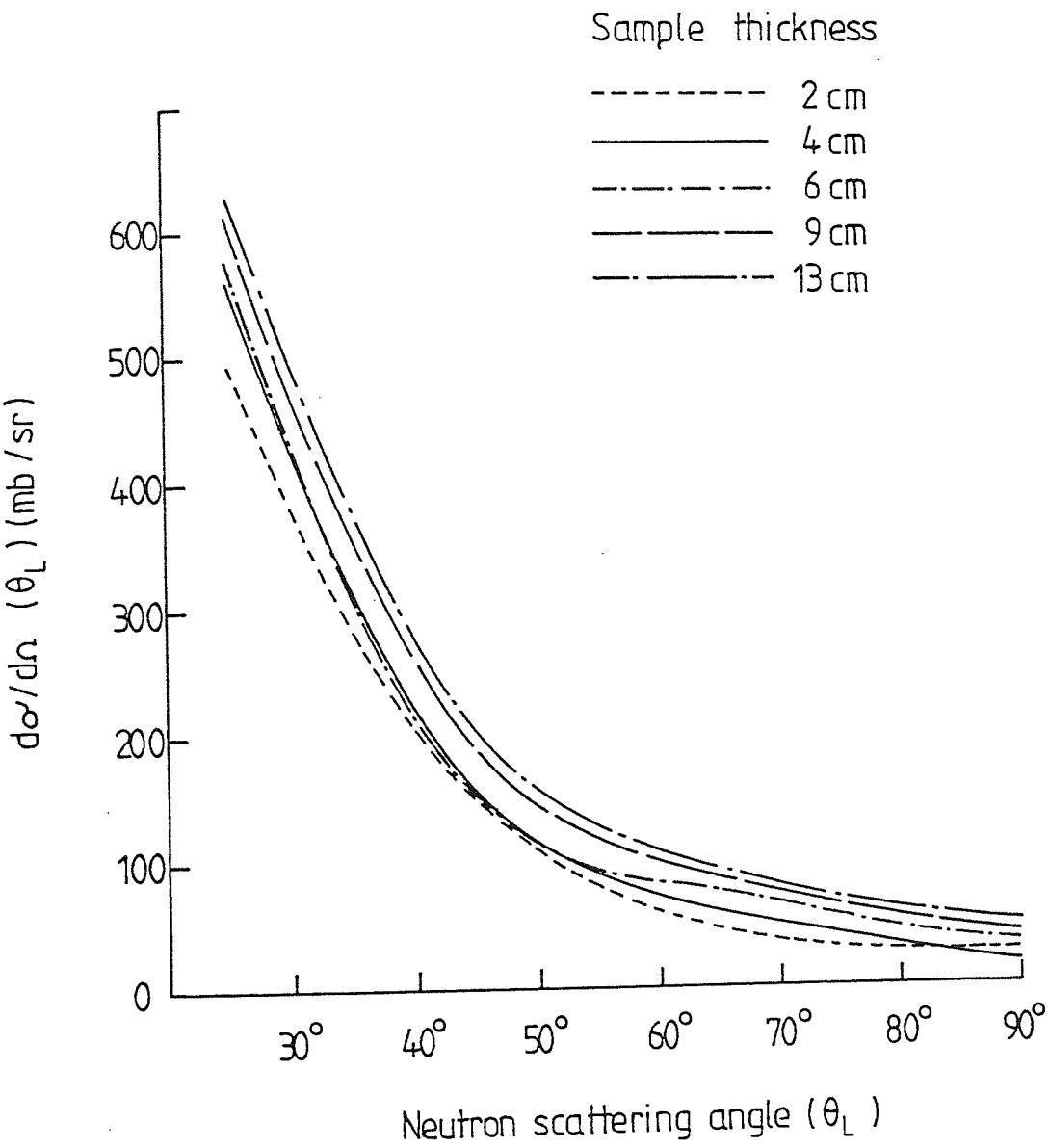

Figure 6.8 Legendre polynomial fitting of $d\sigma/d\Omega(\theta_L)$ for 14 MeV neutrons on Lithium.

Table (6.4)

LEGENDRE POLYNOMIAL COEFFICIENTS AND INTEGRATED CROSS-SECTIONS FOR ELASTIC NEUTRON SCATTERING FROM LITHIUM

SAMPLE THICKNESS (cm)	σ_{el} (mb)	B_2^*	B_4	B_6	B_8	χ^2_ν
2 ±Ø.ØØ4	999±58	2.6±Ø.1	1.7±Ø.2	Ø.6±Ø.3	Ø.2±Ø.Ø5	Ø.8
4 ±Ø.ØØ8	1Ø85±67	2.7±Ø.1	1.9±Ø.2	Ø.7±Ø.2	———	Ø.8
6 ±Ø.ØØ2	1167±57	2.4±Ø.1	1.7±Ø.2	Ø.8±Ø.1	———	1.1
9 ±Ø.Ø2Ø	1262±69	2.4±Ø.1	1.6±Ø.2	Ø.6±Ø.2	———	1.5
13±Ø.Ø3Ø	1352±73	2.3±Ø.1	1.4±Ø.2	Ø.5±Ø.2	———	1.5

* Incuded is the value of standard deviation .

and therefore the probability of neutron scattering interactions , generally increased with increasing the sample thickness .

The variation of $(\frac{d\sigma}{d\Omega}(\theta_L))$ with the sample thickness was fitted to an equation of exponential form :

$$\frac{d\sigma}{d\Omega}[\theta]\Big]_t = \frac{d\sigma}{d\Omega}[\theta]\Big]_o \cdot \exp(\alpha \cdot t) \qquad (6.3)$$

Where $\frac{d\sigma}{d\Omega}[\theta]\Big]_t$ = the measured differential cross-section .

$\frac{d\sigma}{d\Omega}[\theta]\Big]_o$ = the differential cross-section as the sample thickness approaches zero .

α = constant determined from the experimental results .

and t = the sample thickness in units of mean-free-path (mfp).

By taking the logarithm of equation (6.3) ,

$$\log_e\left(\frac{d\sigma}{d\Omega}[\theta]\Big]_{t=t}\right) = \log_e\left(\frac{d\sigma}{d\Omega}[\theta]\Big]_{t=o}\right) + \alpha \cdot t \qquad (6.4)$$

Since equation (6.4) is a linear , the values of $\log_e(\frac{d\sigma}{d\Omega}[\theta]\Big]_{t=o})$ and α can be determined from the experimental results .

As shown in figs (6.9) and (6.1Ø) , for the lithium results , α was determined as :

$$\alpha_{Li} = Ø.36 \pm Ø.12 \quad (mfp)^{-1}$$

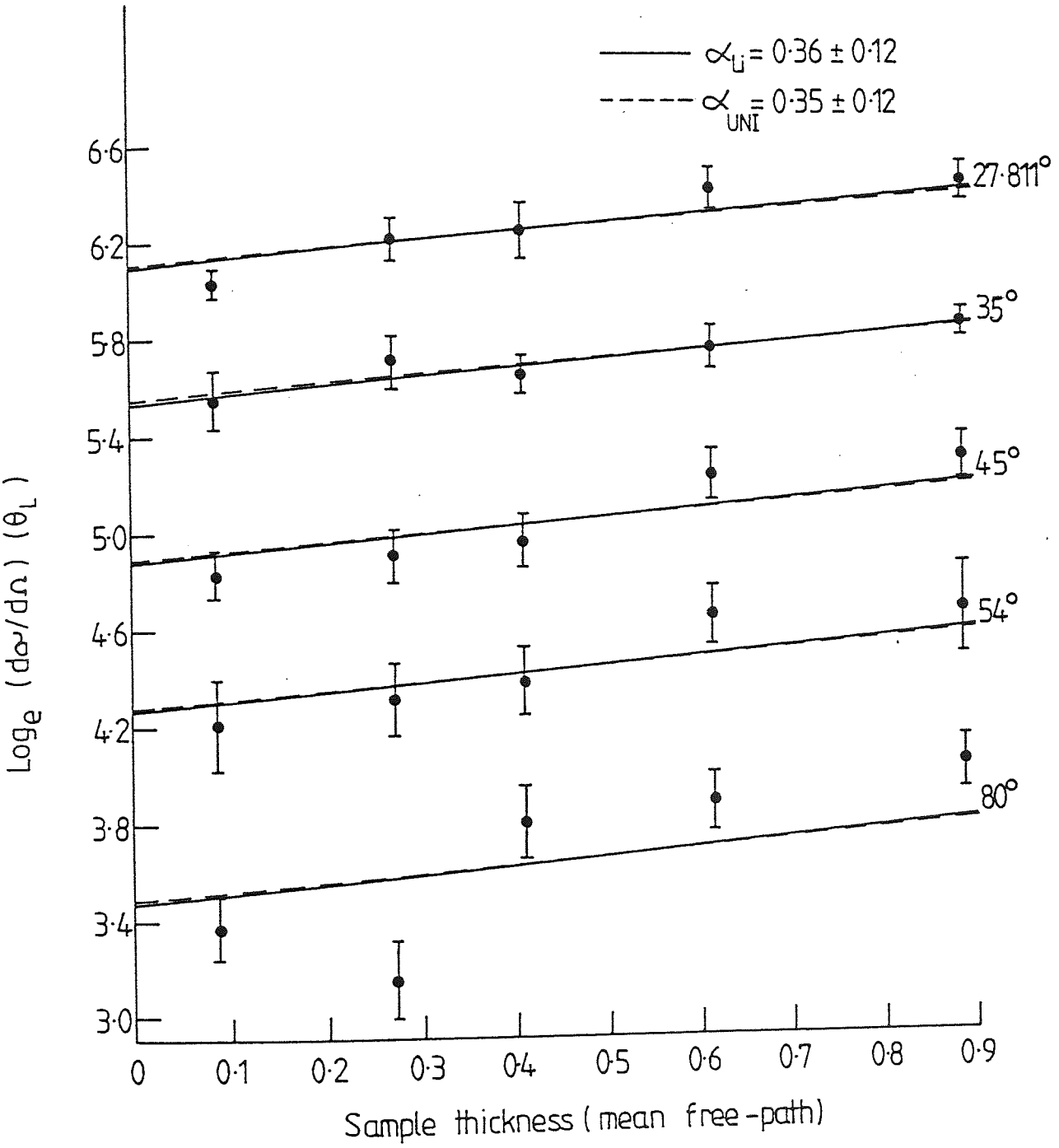

Figure 6·9 The variation of the measured differential cross-section from Lithium samples with the sample thickness at various angles. The lines represent least squares fit to equation (6·4).

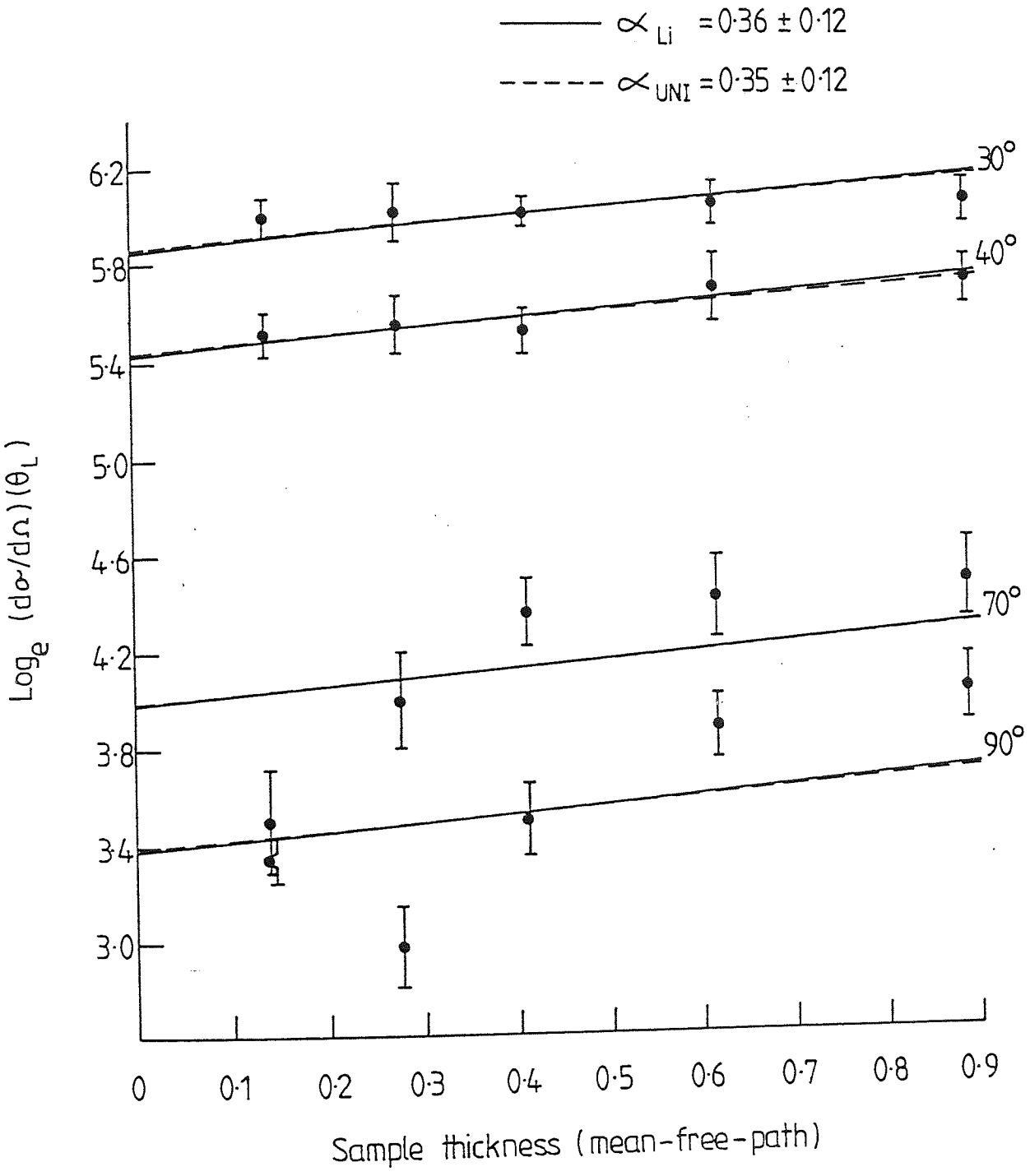

Figure 6·10 The variation of the measured differential cross-section from Lithium samples with the sample thicknesses at various angles. The lines represent least squares fit to equation (6·4).

6.3.2 NEUTRON ENERGY - 14.44 Mev

Using the same technique as described in the previous section but with the experiment performed on the Dynamitron , the differential elastic scattering cross-sections for LiF samples at 14.44 Mev were determined. Table (6.5) shows the differential cross-section for elastic scattering of 14.44 Mev neutrons . The angular distribution for scattering from the ground and Ø.48 Mev state in ^{7}Li is shown in fig (6.11) for different thicknesses . Whereas fig (6.12) shows the differential cross-section for neutron scattering from a thin sample . The data presented in table (6.5) were fitted to Legendre Polynomial using equation (6.1). The coefficients given in table (6.6) were fitted by Legendre polynomials using equation (6.1) together with integrated elastic cross-section .

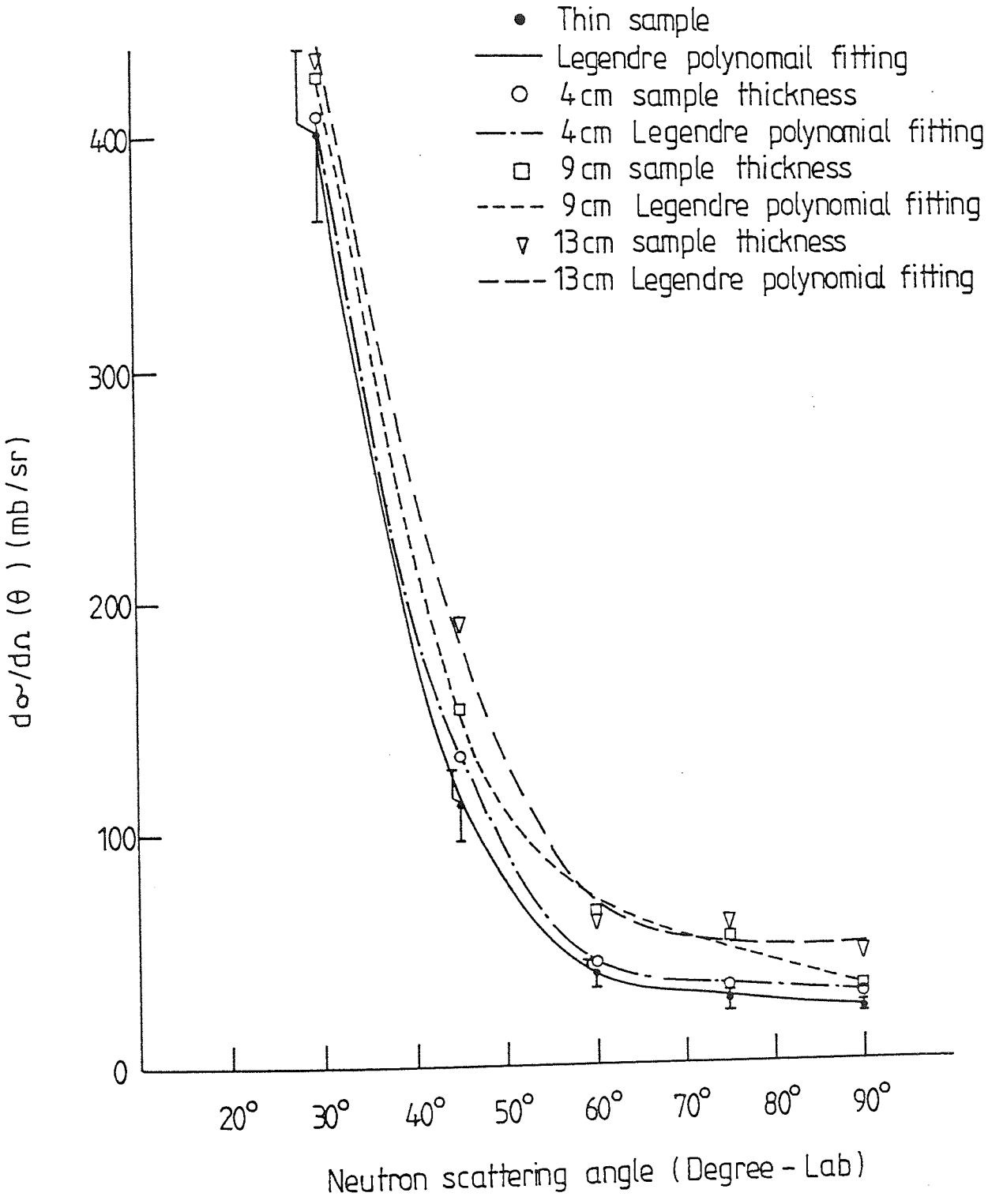

Figure 6.11 Differential elastic scattering cross-section of 14.44 MeV neutrons on Lithium

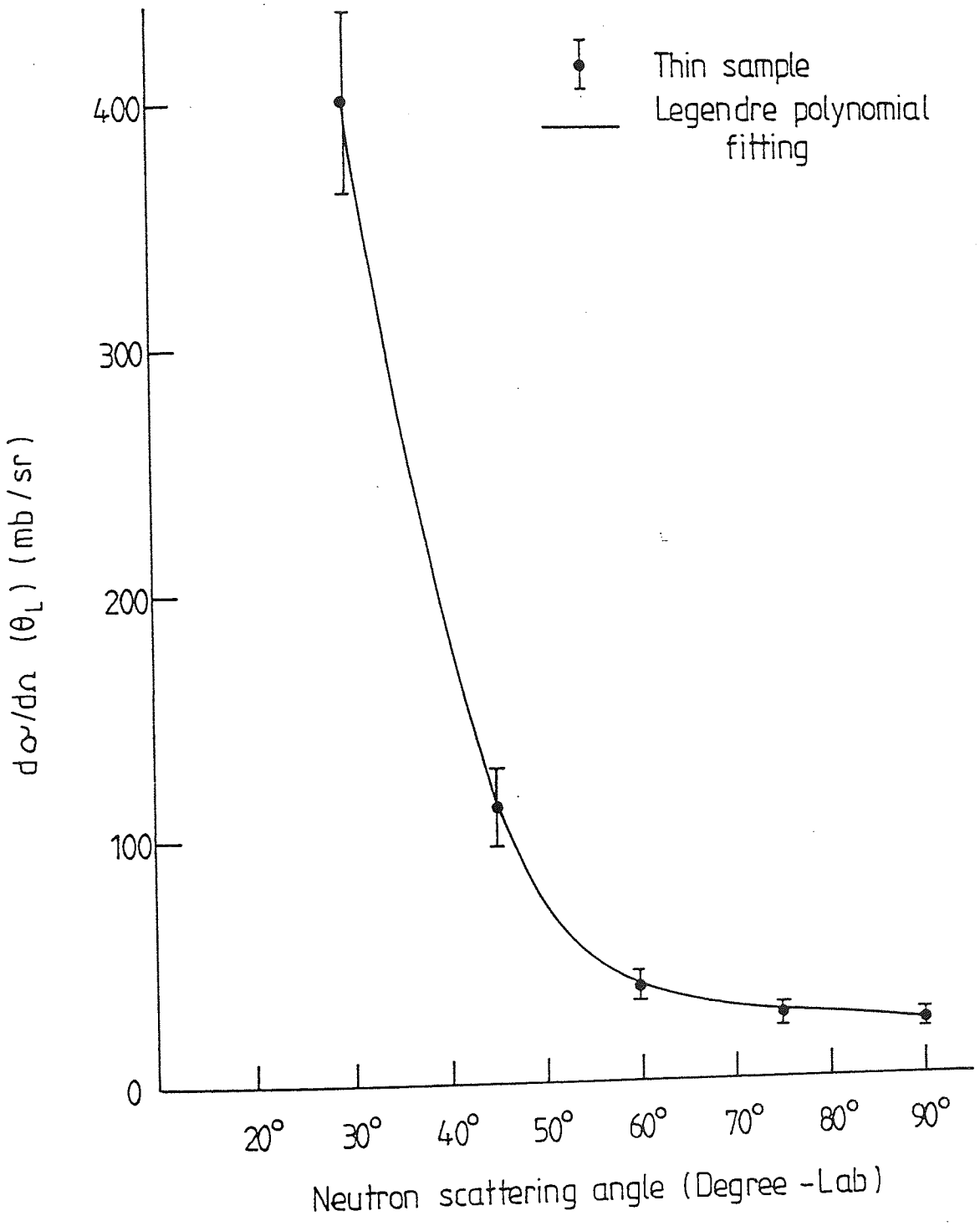

Figure 6·12 Differential cross-section for 14·44 MeV elastic and inelastic (Q = -0·48 MeV) scattering on Lithium.

Table (6.5)

LITHIUM DIFFERENTIAL ELASTIC SCATTERING

CROSS-SECTION DATA OF 14.44 Mev NEUTRONS

Θ_L (Degree)	THICKNESS cm	THICKNESS mfp	$d\sigma/d\Omega$ (mb/st)
30°	4±0.007	0.27 ±0.01	408 ± 53
	9±0.020	0.62 ±0.02	425 ± 47
	13±0.030	0.89 ±0.02	432 ± 42
45°	4±0.007	0.27 ±0.01	134 ± 16
	9±0.020	0.62 ±0.02	155 ± 19
	13±0.030	0.89 ±0.02	191 ± 15
60°	4±0.007	0.27 ±0.01	44 ± 7
	9±0.020	0.62 ±0.02	66 ± 8
	13±0.030	0.89 ±0.02	64 ± 6
75°	4±0.007	0.27 ±0.01	33 ± 5
	9±0.020	0.62 ±0.02	55 ± 6
	13±0.030	0.89 ±0.02	60 ± 7
90°	4±0.007	0.27 ±0.01	29 ± 4
	9±0.020	0.62 ±0.02	32 ± 5
	13±0.030	0.89 ±0.02	47 ± 7

Table (6.6)

LEGENDRE POLYNOMIAL COEFFICIENTS AND INTEGRATED CROSS-SECTIONS

FOR ELASTIC NEUTRON SCATTERING FROM LITHIUM (En=14.44 Mev)

THICKNESS (cm)	$\sigma_{el}(E)$ (mb)	β_2 *)	β_4	β_6	χ^2_ν **)
THIN	964 ± 47	2.9±0.08	2.1±0.1	0.7±0.1	0.250
4 ± 0.007	1004 ± 48	2.7±0.09	1.9±0.2	0.5±0.1	0.016
9 ± 0.020	1133 ± 51	2.6±0.09	1.7±0.2	0.6±0.1	1.360
13 ± 0.030	1141 ± 52	2.3±0.10	1.3±0.2	0.2±0.1	3.300

*) Incuded the standard deviatons .
**) ν - degree of freedom .

6.3.2.1 THE VARIATION OF MEASURED CROSS-SECTION WITH SAMPLE THICKNESS

The variation of the differential elastic cross-section for Lithium [table (6.5)] with the thickness was analysed using equation (6.2) . By applying the least squares method , the constant (α) for lithium results was determined as :

$$\alpha_{Li} = 0.45 \pm 0.17 \quad (mfp)^{-1}$$

Fig (6.13) shows the variation of the measured differential cross-section with the sample thickness , in units of mean-free-path (mfp) , for lithium in the angular range studied at 14.44 Mev neutron energy .

6.4 EXPERIMENTAL RESULTS FOR THE DIFFERENTIAL INELASTIC SCATTERING CROSS-SECTIONS

Neutrons produced by the inelastic scattering from the excited state at 4.63 Mev of ^{7}Li were observed and the differential cross-section were calculated and corrected for the contribution of the excited state (Q=-4.7 Mev) in ^{19}F . The data for the excited state at 4.7 Mev was taken from BONAZZOLA etal (1966) [77] .

Table (6.7) shows the differential inelastic scattering cross-sections for 14 Mev neutrons for different lithium thicknesses which are also shown in fig (6.14) .

The data were fitted to the Legendre Polynomials using equation (6.1) with the coefficients given in table (6.8) . The value of $\chi_\nu < 1$ is

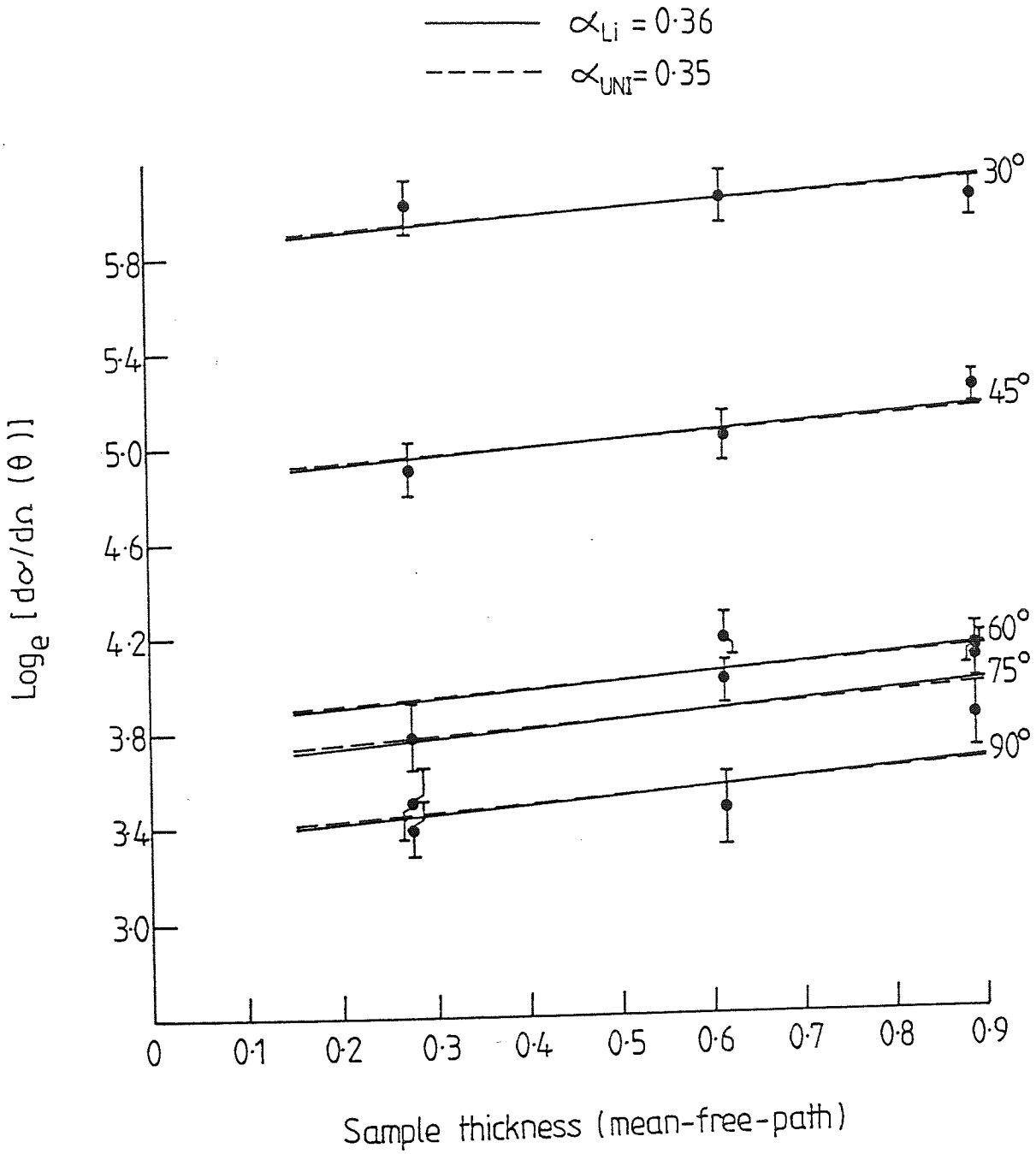

Figure 6·13 The variation of the measured differential elastic scattering cross-section with the sample thickness for 14·44 MeV neutrons. The lines represent least square fit.

Table (6.7)

INELASTIC SCATTERING CROSS-SECTION FOR

THE EXCITED STATE 4.63 Mev IN ^{7}Li

θ_L (Degree)	THICKNESS (cm)	THICKNESS (mfp)	$d\sigma / d\Omega$ (mb/st)
27° 48′	2	Ø.14	12.Ø ± 2.2
	4	Ø.27	12.Ø ± 2.1
	6	Ø.41	11.7 ± 1.7
	9	Ø.62	11.2 ± 1.7
	13	Ø.89	12.6 ± 2.6
3Ø°	2	Ø.14	11.7 ± 2.6
	4	Ø.27	1Ø.5 ± 2.2
	6	Ø.41	14.6 ± 3.2
	9	Ø.62	14.8 ± 3.6
	13	Ø.89	14.2 ± 3.4
35°	2	Ø.14	13.3 ± 2.9
	4	Ø.27	11.1 ± 2.3
	6	Ø.41	9.Ø ± 1.8
	9	Ø.62	1Ø.1 ± 1.8
	13	Ø.89	15.4 ± 2.6
4Ø°	2	Ø.14	1Ø.Ø ± 1.9
	4	Ø.27	13.7 ± 2.7
	6	Ø.41	13.4 ± 2.2
	9	Ø.62	11.1 ± 1.8
	13	Ø.89	15.7 ± 3.Ø
45°	2	Ø.14	8.3 ± 1.3
	4	Ø.27	1Ø.5 ± 1.6
	6	Ø.41	12.9 ± 2.3
	9	Ø.6	15.1 ± 3.5
	13	Ø.89	16.6 ± 3.7
5Ø.3°	2	Ø.14	8.9 ± 1.7
	4	Ø.27	13.9 ± 2.4
	6	Ø.41	9.1 ± 1.9
	9	Ø.62	1Ø.5 ± 1.7
	13	Ø.89	11.3 ± 2.9
7Ø°	2	Ø.14	8.7 ± 1.8
	4	Ø.27	12.1 ± 2.2
	6	Ø.41	13.6 ± 2.7
	9	Ø.62	13.6 ± 2.6
	13	Ø.89	1Ø.6 ± 2.4

table(6.7) , continue

80°	2	Ø.137	6.9 ± 1.8
	4	Ø.274	6.6 ± 1.4
	6	Ø.41Ø	6.2 ± 1.2
	9	Ø.616	12.1 ± 2.7
	13	Ø.889	8.2 ± 2.1
9Ø°	2	Ø.137	6.9 ± 1.6
	4	Ø.274	6.8 ± 1.2
	6	Ø.41Ø	8.Ø ± 1.7
	9	Ø.616	1Ø.Ø ± 2.1
	13	Ø.889	8.5 ± 1.8

Table (6.8)

LEGENDRE POLYNOMIAL COEFFICIENTS AND INTEGRATED INELASTIC SCATTERING CROSS-SECTIONS FOR THE EXCITED STATE 4.63 Mev in ^{7}Li

THICKNESS (cm)	$\sigma_{el}(E)$ (mb)	β_2	β_4	χ^2_ν
2	11Ø ± 8	Ø.4±Ø.1Ø	—	Ø.3
4	124 ± 8	Ø.2±Ø.Ø2	-(Ø.5±Ø.2)	Ø.8
6	12Ø ± 8	Ø.4±Ø.1	-	1.5
9	142 ±1Ø	(Ø.ØØØ2± Ø.ØØØØ5)	-	Ø.5
13	145 ± 11	Ø.5+Ø.1	-	Ø.4

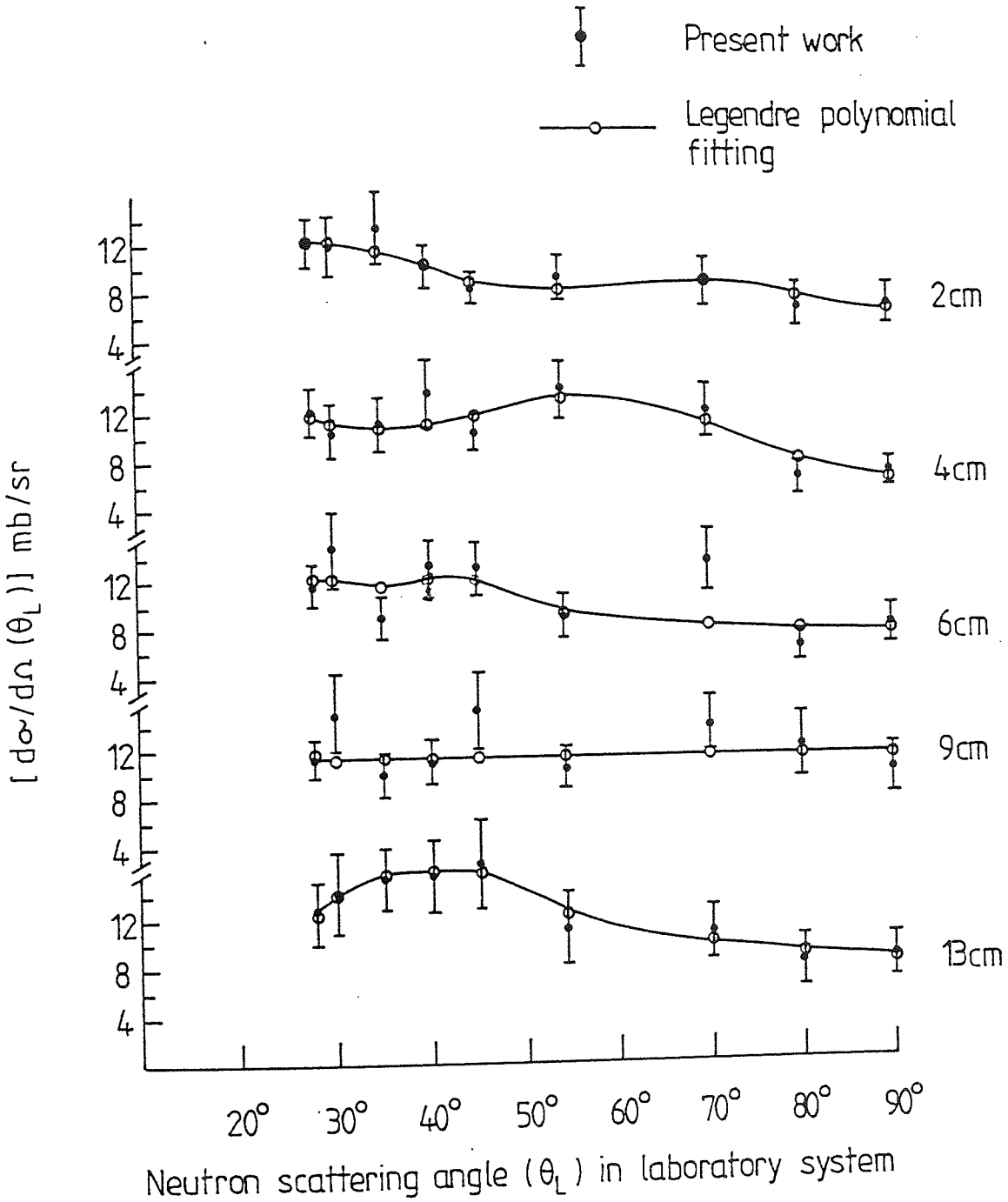

Figure 6.14 Inelastic differential scattering cross-section of 14 MeV neutrons on Lithium-7. (Q = - 4.63 Mev)

acceptable within the estimated experimental errors for the coefficients of the even terms , in the angular range from 20° to 90° in the lab-system . The integrated inelastic scattering cross-section for different lithium samples was calculated by the program LEGFIT (Appendix C) and the results are presented in table (6.8) .

The variation of the measured inelastic cross-sections $\frac{d\sigma}{d\Omega}(\theta)$ with the sample thickness given in terms of mean-free-path is shown in figs (6.15) and (6.16) . The constant was determined as :

$$\alpha = 0.29 \pm 0.11 \quad (mfp)^{-1}$$

The average constant for the lithium for all results is :

$$\alpha_{Li} = 0.36 \pm 0.23 \quad (mfp)^{-1}$$

A comparison of this average constant with the values obtained by AL-SHALABI (1981) [80] and ANVARIAN (1982) [81] is shown in table (6.9) .

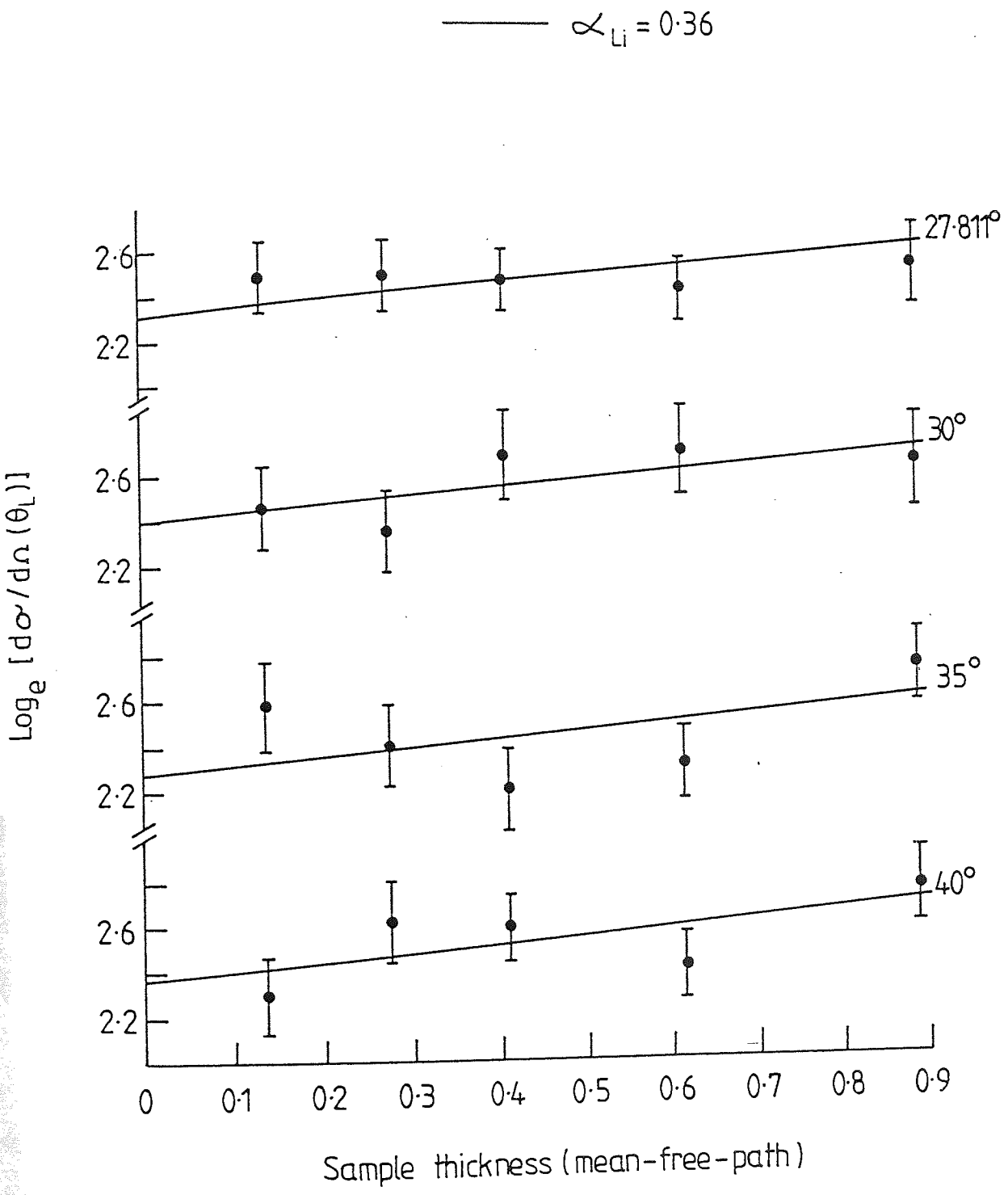

Figure 6·15 The variation of the measured differential inelastic scattering cross-section for the excited state 4·63 MeV in ^{7}Li with the sample thickness for 14 MeV neutrons.

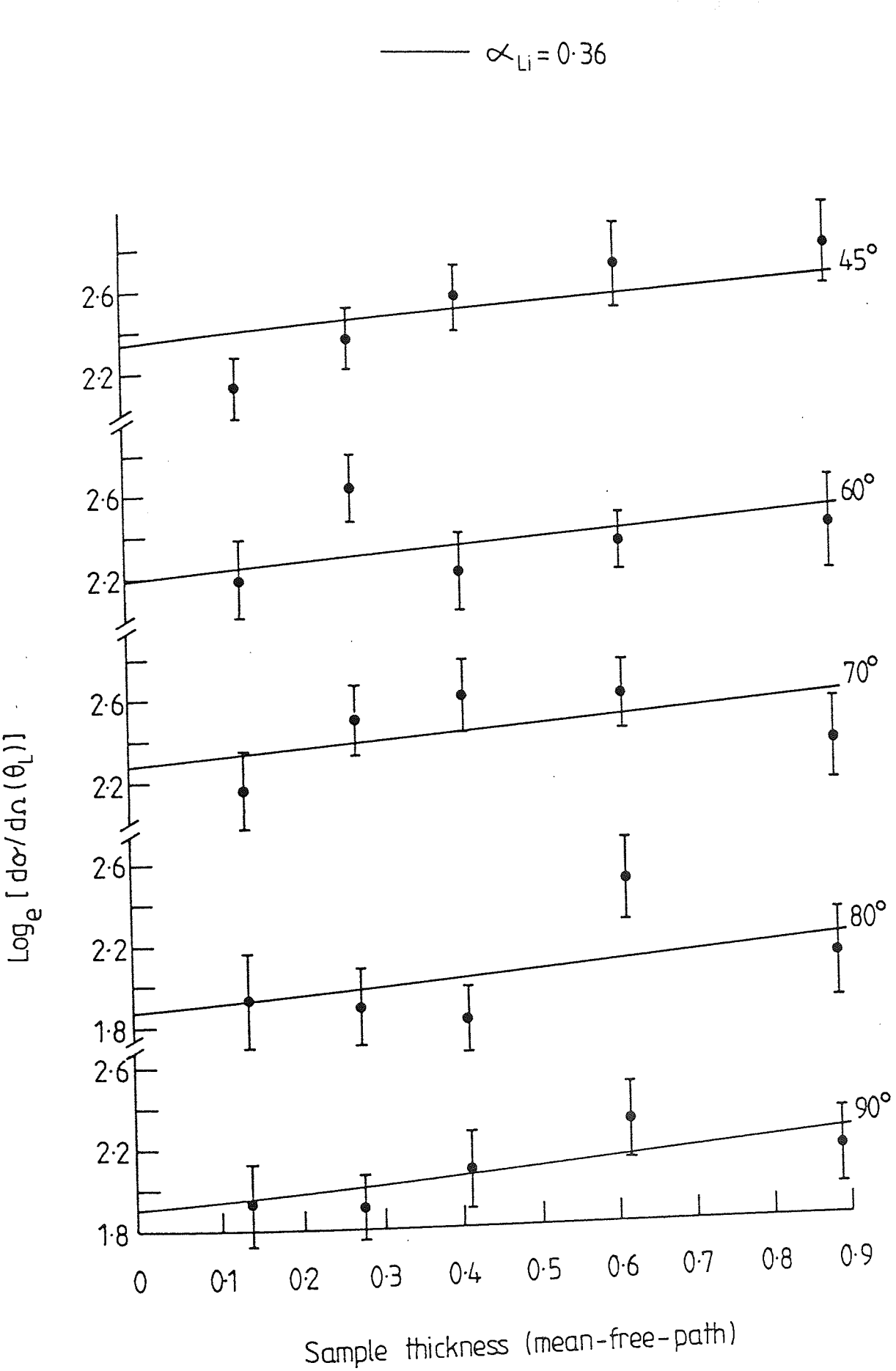

Figure 6.16 The variation of the measured differential inelastic scattering cross-section for the excited state 4·63MeV in ^{7}Li, with the sample thickness for 14 MeV neutrons.

6.5 THIN SAMPLE RESULTS

The results of the differential elastic and inelastic scattering cross- sections for thin samples of lithium were calculated using equation (6.3) for each scattering angle and the data converted to the center-of-mass system [equation (5.7)] . These are presented in tables (6.1Ø) and (6.11) with other published data .

Fig (6.17) gives a comparsion of our data with other measurements . The smooth line through the distribution is the result of fitting the Legendre Polynomial series , shown at equation (6.4) , to the experimental points :

$$\frac{d\sigma}{d\Omega}\left(E,\mu\right)_n = \sigma_n(E)\sum_{l=0}^{l_{max}} \frac{[2l+1]}{4\pi} f_l(E)\, P_l(\mu) \qquad (6.5)$$

An eighth order series was found most suitable for the elastic scattering using the data of HOGUE (1979) [74] for scattering angles greater 1ØØ° in the CM-system . The inelastic scattering data for 4.63 Mev state of ^{7}Li fitted to a second order Legendre series agreed well with the data of HOGUE [74] beyond 1ØØ° . The values of the coefficients from the fit are given in table (6.12) , and are chosen to minimize the value of chi-squared :

Where
$$\chi^2 = \sum_{i=1}^{N} \left\{ \frac{\frac{d\sigma}{d\Omega}(\mu_i)_f - \frac{d\sigma}{d\Omega}(\mu_i)_e}{\Delta \frac{d\sigma}{d\Omega}(\mu_i)_e} \right\}^2 \qquad (6.6)$$

and $\frac{d\sigma}{d\Omega}(\mu)_f$ = fitted differential cross-section .

$\frac{d\sigma}{d\Omega}(\mu)_e$ = experimental differential cross-section .

$\Delta \frac{d\sigma}{d\Omega}(\mu_i)_e$ = experimental relative error at angle μ_i, where $\mu_i = \cos\phi_i$ and ϕ_i is the scatering angle in the cm-system .

N = is the number of angles at which data were taken .

The maximum coefficients of order (lmax) were chosen on the following criteria :

1 - χ^2_ν-per degree of freedom , i.e. $\chi^2/(N-lmax-1)$, is a minimum .

2 - Wick's limit [82 , 2 , 87] is a very useful expression for setting a lower limit on the differential elastic scattering cross-section in the forward direction and has the form :

$$\frac{d\sigma}{d\Omega}(\phi=0) \geq \left[\frac{\sigma_T \cdot k}{4\pi}\right]^2 = \sigma_W \qquad (6.7)$$

$$\left\{ \frac{\sigma_{el}(E)}{4\pi} \sum_{l=0}^{lmax} (2l+1)\, f_l(E) \right\} \geq \sigma_W \qquad (6.8)$$

WHERE σ_T = total integrated cross-section for all interactions .

k = wave number ,

$$k = \frac{\sqrt{2\bar{\mu}E}}{\hbar}$$

$$\bar{\mu} = \frac{M1 \cdot M2}{M1+M2} = \text{reduced mass} .$$

M1 = mass of the neutron .

M2 = mass of the target .

E = the energy of the reduced mass $= \frac{M2}{M1+M2} E_o$

3 - The coefficients f_l for $l \leq lmax$ are significant .

The Wick's limit at 14 Mev neutron energy for lithium was calculated as σ_W = 692.2 mbarn , and $\frac{d\sigma}{d\Omega}$ the differential elastic scattering cross-sections in the forward direction were calculated from the summation of the Legendre Polynomial coefficients as 854 ± 71 mbarn with

$\chi^2_\nu = 0.6$. The integrated elastic and inelastic scattering cross-sections were obtained from :

$$\sigma_{int} = 4\pi a_o \qquad (6.9)$$

Where a_o = the polynomial coefficient at 90^o (Appendix C) .

The results of these integrated cross-sections, compared with other measurements, are presented in table (6.13) .

Table (6.9)

AVERAGE CONSTANT α FOR THE VARIATION OF THE $\frac{d\sigma}{d\Omega}(\theta)_L$ vs SAMPLE THICKNESS

ELEMENT	En (Mev)	α (1/mfp)	REACTION	AUTHOR
^{7}Li	14	0.36 ± 0.12	(n,n)	present work
^{7}Li	14	0.29 ± 0.11	(n,n')	present work
^{7}Li	14.44	0.45 ± 0.17	(n,n)	present work
AVERAGE CONSTANT α_{Li} = 0.36 ± 0.23 (1/MFP) (present work)				
CONCRETE	14	0.45 ± 0.20	(n,n'γ)	REF [80]
CONCRETE	14	0.38 ± 0.14	(n,n)	REF [81]
^{56}Fe	14	0.26 ± 0.10	(n,n)	REF [81]
^{56}Fe	14.44	0.36 ± 0.13	(n,n)	REF [81]
AVERAGE CONSTANT α_{Pb} = 0.37 ± 0.12 (PRESENT WORK)				

Table (6.1Ø)

LITHIUM DIFFERENTIAL ELASTIC SCATTERING

CROSS-SECTION DATA FOR A THIN SAMPLE OF LITHIUM

θ_{cm} (deg)	PRESENT WORK (mb/s)	ARMSTRONG etal (mb/s) [72]	WONG etal (mb/s)[70]	HOLLAND etal (mb/s)[79]
22° 48′	–	376 ± 71	–	405 ± 25
25° 26′	–	–	438 ± 19	–
31° 36′	364 ± 46	–	–	–
34° 6′	285 ± 2Ø	267 ± 4Ø	–	261 ± 17
36° 18′	–	–	3Ø6 ± 1Ø	–
39° 42′	2Ø9 ± 14	–	–	–
43° 22′	–	–	2Ø1 ± 9	–
45° 12′	186 ± 2Ø	16Ø ± 32	–	126 ± 8
5Ø° 48′	11Ø ± 8	–	–	–
53°	–	–	113 ± 3	–
56° 17′	–	55 ± 13	–	75 ± 5
61° 6′	66 ± 4	–	–	–
67° 7′	–	63 ± 25	38 ± 3	35 ± 3
77° 42′	3Ø ± 4	2Ø ± 1Ø	–	26 ± 3
88° 6′	22 ± 2	15 ± 8	–	24 ± 3
98° 12′	25 ± 2	22 ± 8	–	25 ± 3

Table (6.11)

DIFFERENTIAL INELASTIC SCATTERING

CROSS-SECTON FOR 4.63 Mev STATE IN ^{7}Li

θ_{cm} (deg)	PRESENT WORK (mb/s)	θ_{cm} (deg)	HYAKUTAKE etal (mb/s) [73]	θ_{cm} (deg)	HOGUE etal (mb/s) [74]
31°36′	10.1 ± 1.5	24°	8.5 ± 1.0	29°45′	10.3 ± 1.8
34°6′	11.0 ± 1.2	35°	7.0 ± 1.0	35°27′	12.8 ± 1.4
39°42′	9.7 ± 0.9			41°6′	10.8 ± 1.2
45°12′	10.6 ± 0.8	47°	8.0 ± 0.8	46°48′	9.5 ± 1.5
50°48′	10.4 ± 0.8			52°24′	13.0 ± 3.5
61°6′	9.0 ± 0.7	63°	10.0 ± 1.0	63°3′	10.5 ± 1.4
77°42′	9.8 ± 0.8	80°	5.2 ± 1.0	79°45′	9.1 ± 1.1
88°6′	7.0 ± 1.2	90°	3.7 ± 0.8	90°12′	8.1 ± 1.0
98°12′	7.0 ± 1.4	100°	3.8 ± 0.8	100°18′	8.4 ± 1.0

Table (6.12)

COEFFICIENTS OBTAINED FROM FITS TO THE LITHIUM ELASTIC AND INELASTIC SCATTERING ANGULAR DISTRIBUTIONS AT 14Mev NEUTRON ENERGY (THIN SAMPLE)

(1) ELASTIC AND 0.478 Mev INELASTIC

$f_i(E)$	PRESENT WORK	ENDF/B-IV [84]	HOGUE [74]	GUANREN [85]
f_0	1 ± 0.062	1	1	1 ± 0.037
f_1	0.667 ± 0.014	0.674	0.670	0.640 ± 0.028
f_2	0.435 ± 0.024	0.422	0.443	0.406 ± 0.020
f_3	0.270 ± 0.026	0.228	0.260	0.236 ± 0.013
f_4	0.137 ± 0.028	0.072	0.105	0.089 ± 0.007
f_5	0.070 ± 0.024	0.009	0.022	0.009 ± 0.003
f_6	0.035 ± 0.020	- 0.002	0.006	—
f_7	0.017 ± 0.012	- 0.005	—	—
f_8	0.005 ± 0.007	- 0.0003	—	—
f_9	—	0.003	—	—
χ^2_ν	0.7	—	—	—

(2) INELASTIC SCATTERING (4.63 Mev STATE)

AUTHOR	f_0	f_1	f_2	χ^2_ν
PRESENT WORK	1 ± 0.09	0.148 ±0.029	- (0.139 ± 0.032)	0.105
HOGUE [74]	1	0.184	—	—

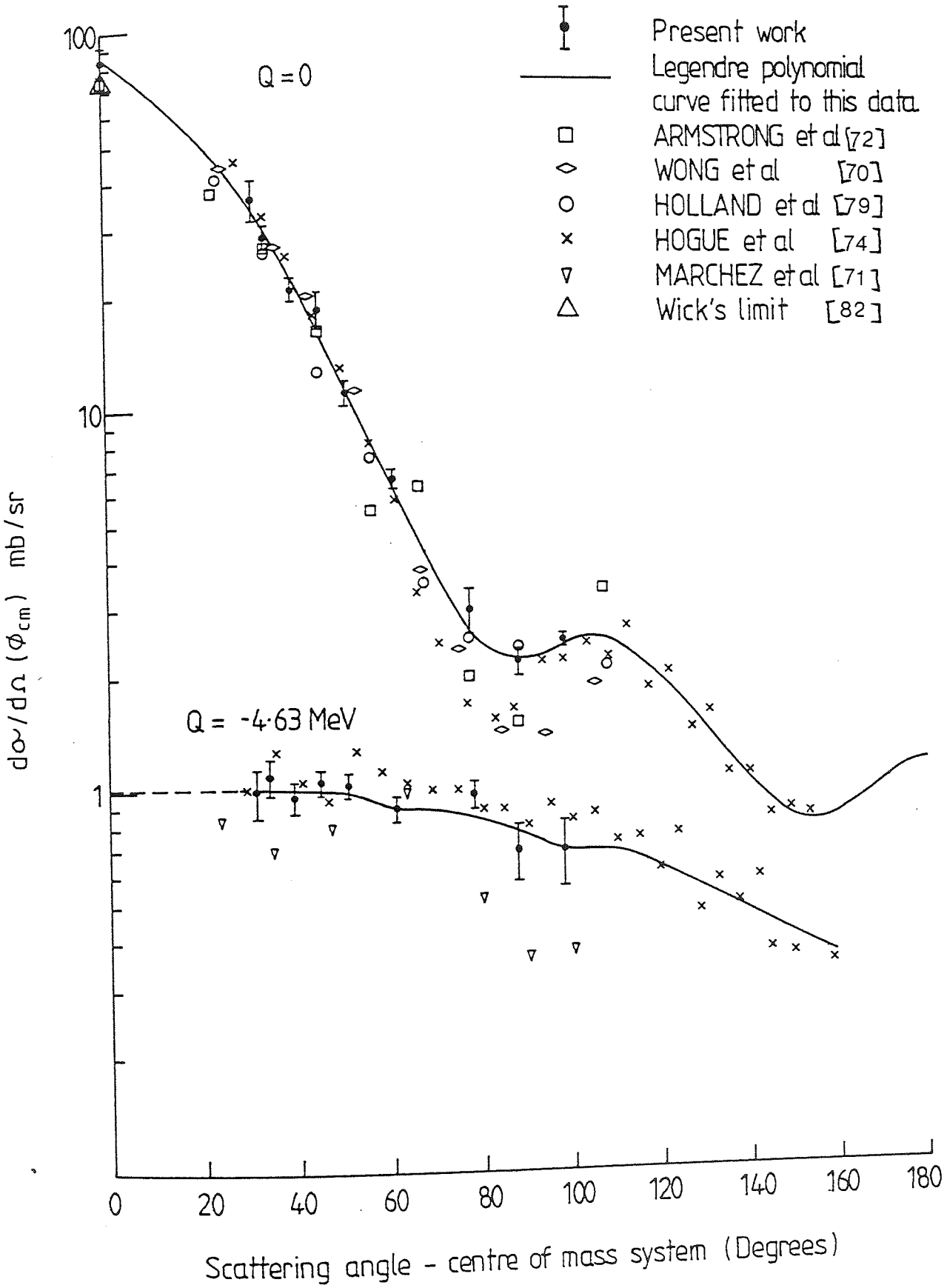

Figure 6·17 Elastic and inelastic scattering angular distributions from the groundstate pluse (1/2-) state and the (7/2-) state of Lithium-7.

Table (6.13)

EXPERIMENTAL VALUES OF INTEGRATED

ELASTIC AND INELASTIC SCATTERING

(1) ^{7}Li - INTEGRATED ELASTIC

$\sigma_{el}(E)$ (mbarn)	AUTHOR
1037 ± 37	PRESENT WORK
958	WONG etal (1962) [70]
975 ± 90	MERCHEZ etal (1965) [71]
969 ± 110	ARMSTRONG etal (1964) [72]
1044 ± 110	ARMSTRONG etal (1964) [72]
980	PENDLERBURY (1964) [76]
1034	CONLON (1972) [75]
974	ENDF/B-IV (1974) [84]
988 ± 51	HYAKUTAKE etal (1974) [73]
958 ± 51	HYAKUTAKE etal (1974) [73]
1064 ± 80	HOGUE etal (1979) [74]
1087 ± 29	GUANREN etal (1984) [85]

(2) ^{7}Li - INTEGRATED INELASTIC (4.63 Mev STATE)

98 ± 9	PRESENT WORK
90	WONG etal (1962) [70]
90 ± 25	ARMSTRONG etal (1964) [72]
135 ± 20	MERCHEZ etal (1965) [71]
69 ± 4	HYAKUTAKE etal (1974) [73]
80	ENDF/B-IV (1974) [84]
107 ± 8	HOGUE etal (1979) [74]

CHAPTER SIX (PART TWO)

LEAD DIFFERENTIAL CROSS-SECTION

CHAPTER SIX (PART TWO)

THE LEAD DIFFERENTIAL CROSS-SECTION

6.6 LEAD SAMPLES

The element lead has four naturally occuring isotopes . The natural abundances and the isotopic masses of these are given in table (6.14) .

Table (6.14)

PROPERTIES OF THE NATURAL OCCURING LEAD ISOTOPES

ISOTOPE	FRACTIONAL ABUNDANCE	ISOTOPIC MASS
^{204}Pb	Ø.Ø12 (Ø.Ø)*	2Ø3.97
^{206}Pb	Ø.236 (Ø.24)	2Ø5.97
^{207}Pb	Ø.226 (Ø.23)	2Ø6.97
^{208}Pb	Ø.523 (Ø.53)	2Ø7.97

* Effective abundances used in cases where the contribution from ^{204}Pb is neglected .

The experimental arrangement here is similar to that described for LiF at 14 Mev incident neutron .

As in the case of lithium slab-shaped samples of dimensions given in table (6.15) were used .

Table (6.15)

DIMENSIONS OF SCATTERING SAMPLES ,NATURAL LEAD

LENGTH (cm)	WIDTH (cm)	THICKNESS (cm)	(mfp)
26	15.5	Ø.9	Ø.187
26	15.5	3.2	Ø.667
26	15.5	5.Ø	1.Ø41
26	15.5	7.5	1.562

6.7 TIME-OF-FLIGHT SPECTRA

In order to analyze the time of flight spectra it is necessary to know the properties of the energy levels of the lead isotopes . The energy levels of ^{206}Pb , ^{207}Pb and ^{208}Pb are given in table (6.16) . The energy levels are mostly those given by FU AND PEREY (1975)[86] . The measurements on lead were performed the SAMES accelerator with the same technique as used in the lithium work . Enough data were accumulated in order to yield counting statistics between 5% for neutron scattering angles up to 6Ø° but less than 1Ø% was achieved for angles greater than 6Ø° . The sample out background was accumulated after each run and was subtracted from the sample-in spectra . Typical examples of the time-of-flight spectra of 14 Mev neutrons scattered from Pb are shown in figs (6.18) , (6.19) and (6.2Ø) . The errors indicated represent those due to statistical uncertainties in accumulations and background subtraction .

Table (6.16)

ENERGY LEVELS OF LEAD ISOTOPES

1) ENERGY LEVELS OF ^{206}Pb

LEVEL	EXCITATION ENERGY (Mev)	SPIN-PARITY	LEVEL	EXCITATION ENERGY (MEV)	SPIN-PARITY
1	Ø.Ø	$Ø^+$	26	3.25Ø	(6^-)*
2	Ø.8Ø3	2^+	27	3.28Ø	5^-
3	1.175	$Ø^+$	28	3.3ØØ	(1^-)
4	1.341	3^+	29	3.4Ø4	5^-
5	1.462	2^+	3Ø	3.453	(3^-)*
6	1.682	4^+	31	3.5ØØ	(3^+)*
7	1.7ØØ	1^+	32	3.56Ø	(5^-)*
8	1.762	2^+	33	3.6ØØ	(5^+)*
9	1.998	4^+	34	3.7Ø8	(5^-)*
1Ø	2.16Ø	(2^+)*	35	3.721	(2^+)*
11	2.2ØØ	7^-	36	3.75Ø	(4^+)*
12	2.21Ø	(3^+)*	37	3.776	(5^-)*
13	2.25Ø	(1^+)*	38	3.9ØØ	(6^+)*
14	2.385	6^-	39	3.961	(4^-)*
15	2.5ØØ	$(Ø^+)$*	4Ø	4.Ø05	(3^-)*
16	2.526	(3^-)*	41	4.Ø75	(4^-)*
17	2.634	3^-	42	4.125	(4^-)*
18	2.783	5^-	43	4.128	(2^+)*
19	2.8ØØ	(3^+)*	44	4.191	(5^-)*
2Ø	2.82Ø	(4^+)*	45	4.253	(5^-)*
21	2.94Ø	(4^-)*	46	4.259	(6^-)*
22	3.Ø17	6^-	47	4.368	(4^+)*
23	3.Ø5Ø	(2^+)*	48	4.382	(6^-)*
24	3.125	(5^+)*	49	4.386	(6^+)*
25	3.2ØØ	4^+	-	-	-

* REF [86]

Table (6.16) continued.

2) ENERGY LEVELS OF ^{207}Pb

LEVEL	EXCITATION ENERGY (Mev)	SPIN-PARITY	LEVEL	EXCITATION ENERGY (Mev)	SPIN-PARITY
1	Ø.ØØØ	$1/2^-$	26	3.725	$(9/2^+)$*
2	Ø.57Ø	$5/2^-$	27	3.817	$(11/2^+)$*
3	Ø.898	$3/2^-$	28	3.854	$(3/2^+)$*
4	1.633	$13/2^+$	29	3.891	$(9/2^+)$*
5	2.34Ø	$7/2^-$	3Ø	3.989	$(5/2^+)$*
6	2.624	$5/2^+$	31	4.Ø4Ø	$(7/2^+)$*
7	2.662	$7/2^+$	32	4.Ø6Ø	$(9/2^+)$*
8	2.726	$9/2^+$	33	4.Ø89	$(3/2^-)$*
9	3.Ø57	$(3/2^+)$*	34	4.113	$(15/2^-)$*
1Ø	3.18Ø	$(11/2^+)$*	35	4.12Ø	$(11/2^+)$*
11	3.2Ø2	$(5/2^+)$*	36	4.127	$(5/2^-)$*
12	3.222	$(13/2^+)$*	37	4.14Ø	$(5/2^+)$*
13	3.267	$(7/2^+)$*	38	4.16Ø	$(7/2^+)$*
14	3.298	$1/2^+$	39	4.181	$(9/2^+)$*
15	3.382	$(9/2^+)$*	4Ø	4.2ØØ	$(11/2^+)$*
16	3.4Ø9	$9/2^-$	41	4.22Ø	$(7/2^-)$*
17	3.426	$(3/2^+)$*	42	4.24Ø	$(9/2^-)$*
18	3.471	$(5/2^+)$*	43	4.26Ø	$(11/2^-)$*
19	3.499	$(11/2^+)$*	44	4.288	$(7/2^-)$*
2Ø	3.5Ø3	$(7/2^+)$*	45	4.3ØØ	$(11/2^+)$*
21	3.522	$(9/2^+)$*	46	4.31Ø	$(9/2^+)$*
22	3.58Ø	$(7/2^+)$*	47	4.314	$(7/2^+)$*
23	3.62Ø	$(9/2^+)$*	48	4.339	$(11/2^-)$*
24	3.632	$(5/2^+)$*	49	4.38Ø	$(13/2^-)$*
25	3.645	$(11/2^+)$*	5Ø	4.388	$5/2^+$

* ASSUMED REF [86]

Table (6.16) continued .

3) ENERGY LEVELS OF ^{208}Pb

LEVEL	EXCITATION ENERGY (Mev)	SPIN-PARITY	LEVEL	EXCITATION ENERGY (MEV)	SPIN-PARITY
1	Ø.ØØØ	$Ø^+$	3Ø	4.76Ø	(6^-)*
2	2.615	3^-	31	4.78Ø	(3^-)*
3	3.198	5^-	32	4.8ØØ	(3^+)*
4	3.475	4^-	33	4.82Ø	(4^+)*
5	3.7Ø8	5^-	34	4.839	(2^+)*
6	3.92Ø	6^-	35	4.859	$Ø^+$
7	3.946	(5^-)*	36	4.863	(7^+)*
8	3.961	(4^-)*	37	4.91Ø	(4^+)*
9	3.998	(6^-)*	38	4.92Ø	(4^+)*
1Ø	4.Ø38	7^-	39	4.934	(2^+)*
11	4.Ø5Ø	(4^-)*	4Ø	4.953	(5^+)*
12	4.Ø76	2^+	41	4.974	(3^-)*
13	4.125	(4^-)*	42	5.Ø1Ø	(4^-)*
14	4.161	5^-	43	5.Ø38	(2^-)*
15	4.2Ø4	(6^-)*	44	5.Ø6Ø	(3^+)*
16	4.231	(2^-)*	45	5.Ø77	(5^+)*
17	4.243	(3^-)*	46	5.Ø95	(5^-)*
18	4.253	(5^-)*	47	5.127	(2^-)*
19	4.136	(4^-)*	48	5.14Ø	(6^+)*
2Ø	4.323	4^+	49	5.162	(1^+)*
21	4.357	4^-	5Ø	5.18Ø	(6^+)*
22	4.382	6^-	51	5.2ØØ	(6^+)*
23	4.435	6^+	52	5.211	(7^+)*
24	4.48Ø	6^-	53	5.22Ø	(4^-)*
25	4.6Ø8	8^+	54	5.236	$Ø^+$
26	4.65Ø	(3^-)*	55	5.245	(3^-)*
27	4.698	(3^-)*	56	5.26Ø	(5^-)*
28	4.72Ø	(4^-)*	57	5.281	$Ø^-$
29	4.74Ø	(5^-)*	58	5.288	1^-

*ASSUMED REF [86]

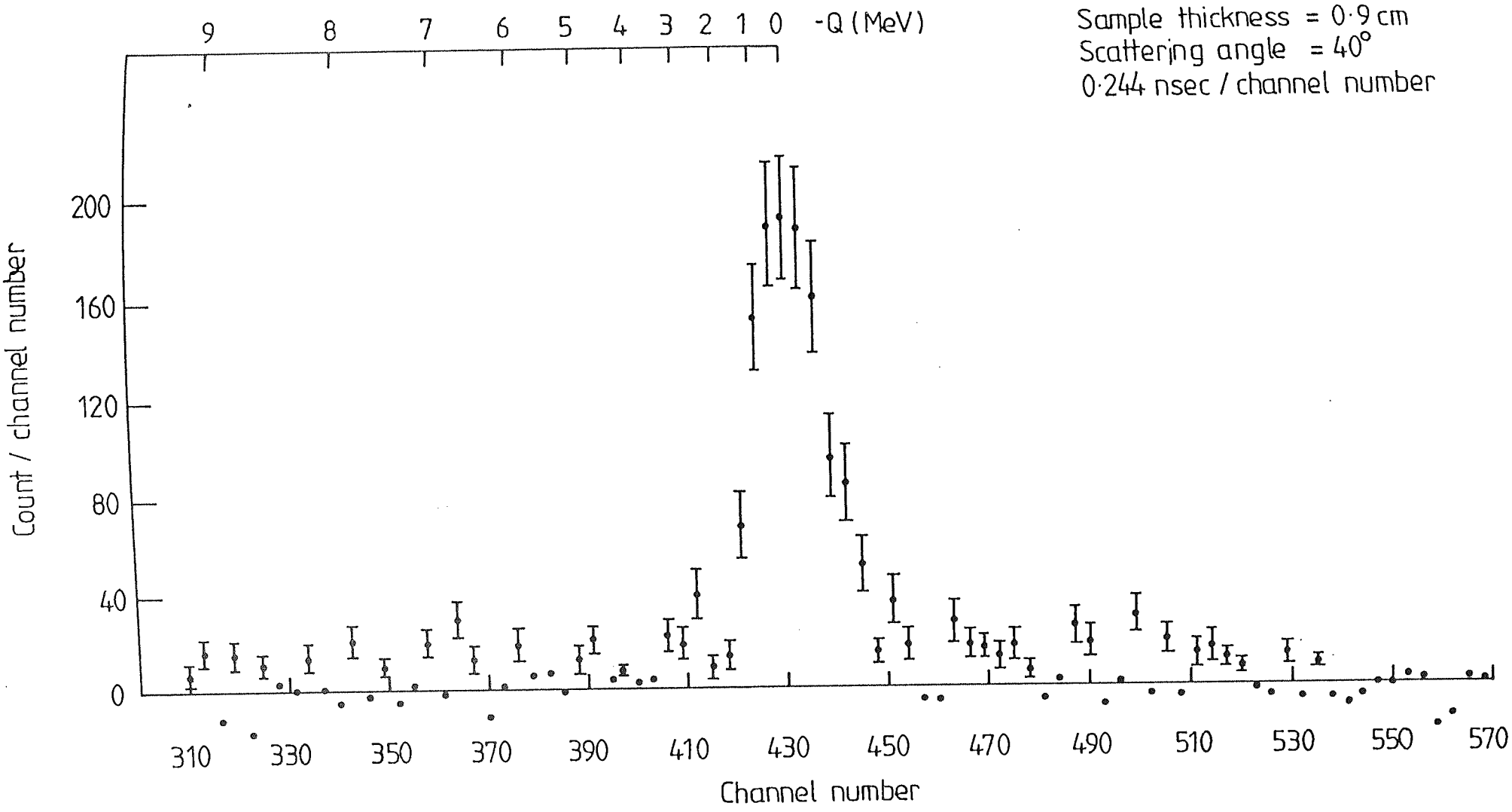

Figure 6·18 The spectrum of neutrons scattered by Lead

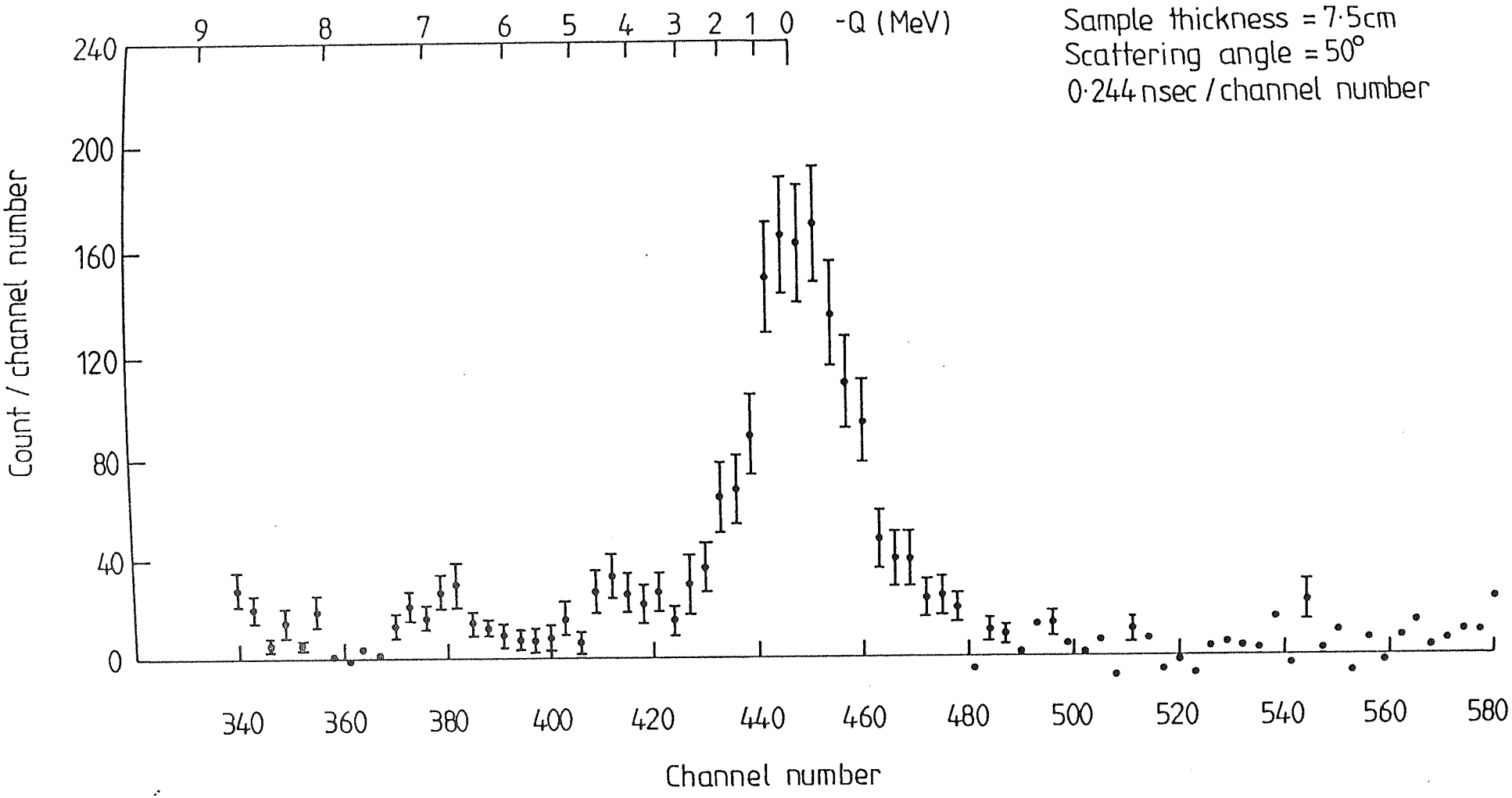

Figure 6·19 The spectrum of neutrons scattered by Lead.

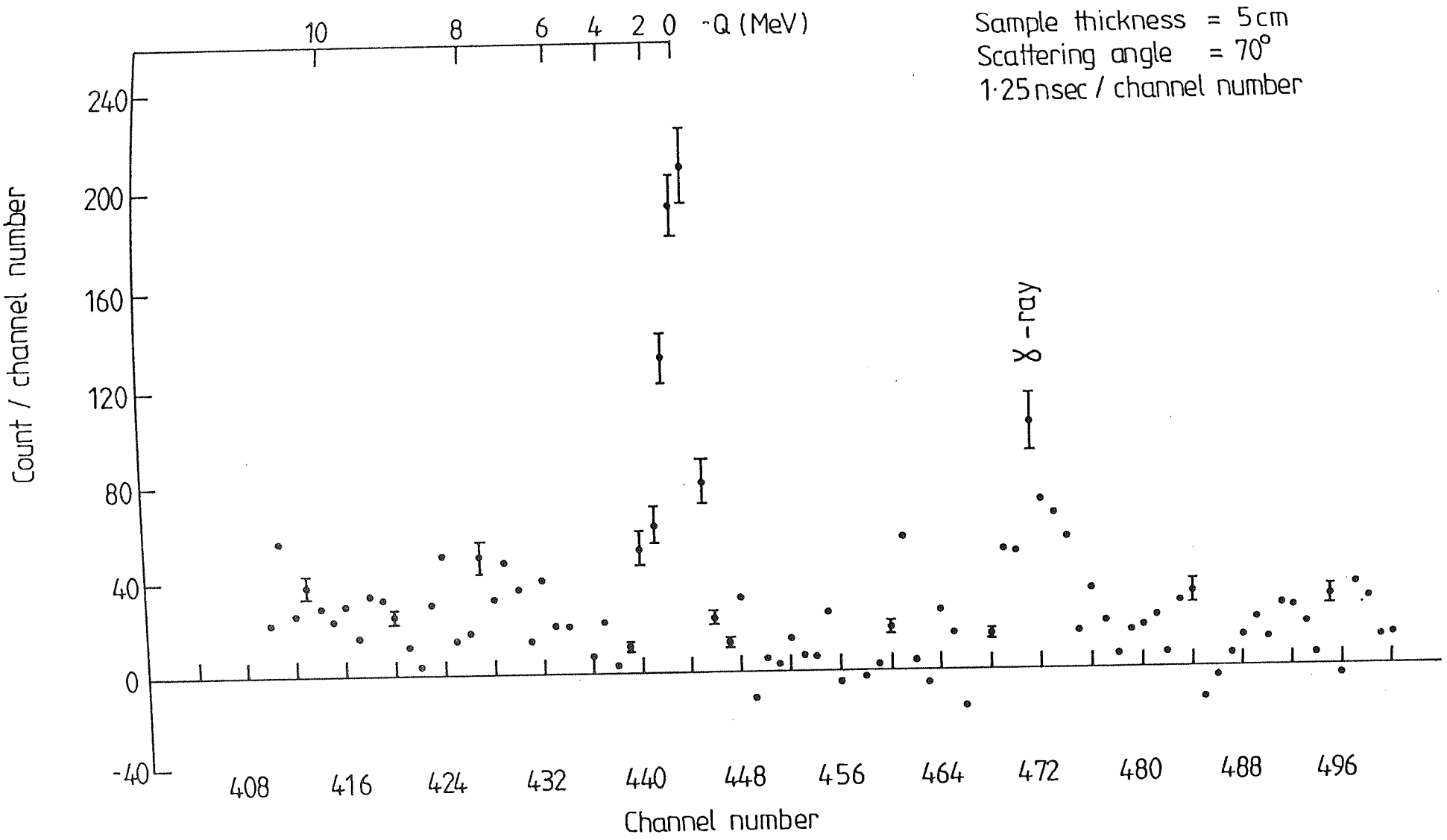

Figure 6·20 The spectrum of neutrons scattered by Lead

6.8 EXPERIMENTAL RESULTS FOR THE DIFFERENTIAL ELASTIC SCATTERING CROSS-SECTION

Using equation (5.21) the differential elastic scattering cross-sections for the Lead samples were calculated . Applying the same procedure as discussed in section (6.3.1) for lithium , the number of elastically scattered neutrons was obtained using the normal error curve program .

Table (6.17) shows the results of the differential elastic scattering cross- sections for the lead samples with the corresponding errors . The experimental errors indicate the total errors in each term of equation (5.21) , as shown in table (6.18) .

Fig (6.21) gives the angular distributions of the neutrons elastically scattered from the ground state of the natural lead samples for angles up tp 90 degrees in the Lab-system . The data were fitted to Legendre Polynomials as before .

Table (6.17)

ELASTIC SCATTERING CROSS-SECTION

DATA FOR 14 Mev NEUTRONS

θ_1 (Deg)	THICKNESS (cm)	DIFFERENTIAL ELASTIC SCATTERING CROSS-SECTION (mb/s)
30°	Ø.9	367 ± 31
	3.2	449 ± 33
	5.Ø	5Ø3 ± 37
	7.5	686 ± 44
40°	Ø.9	574 ± 46
	3.2	6ØØ ± 42
	5.Ø	687 ± 33
	7.5	67Ø ± 44
5Ø°	Ø.9	247 ± 18
	3.2	245 ± 2Ø
	5.Ø	38Ø ± 35
	7.5	544 ± 55
6Ø°	Ø.9	9Ø ± 11
	3.2	1Ø3 ± 19
	5.Ø	93 ± 1Ø
	7.5	263 ± 3Ø
7Ø°	Ø.9	1Ø4 ± 12
	3.2	13Ø ± 2Ø
	5.Ø	26Ø ± 31
	7.5	385 ± 44
8Ø°	Ø.9	54 ± 7
	3.2	133 ± 15
	5.Ø	334 ± 34
	7.5	432 ± 48
9Ø°	Ø.9	33 ± 5
	3.2	14Ø ± 19
	5.Ø	184 ± 23
	7.5	192 ± 28

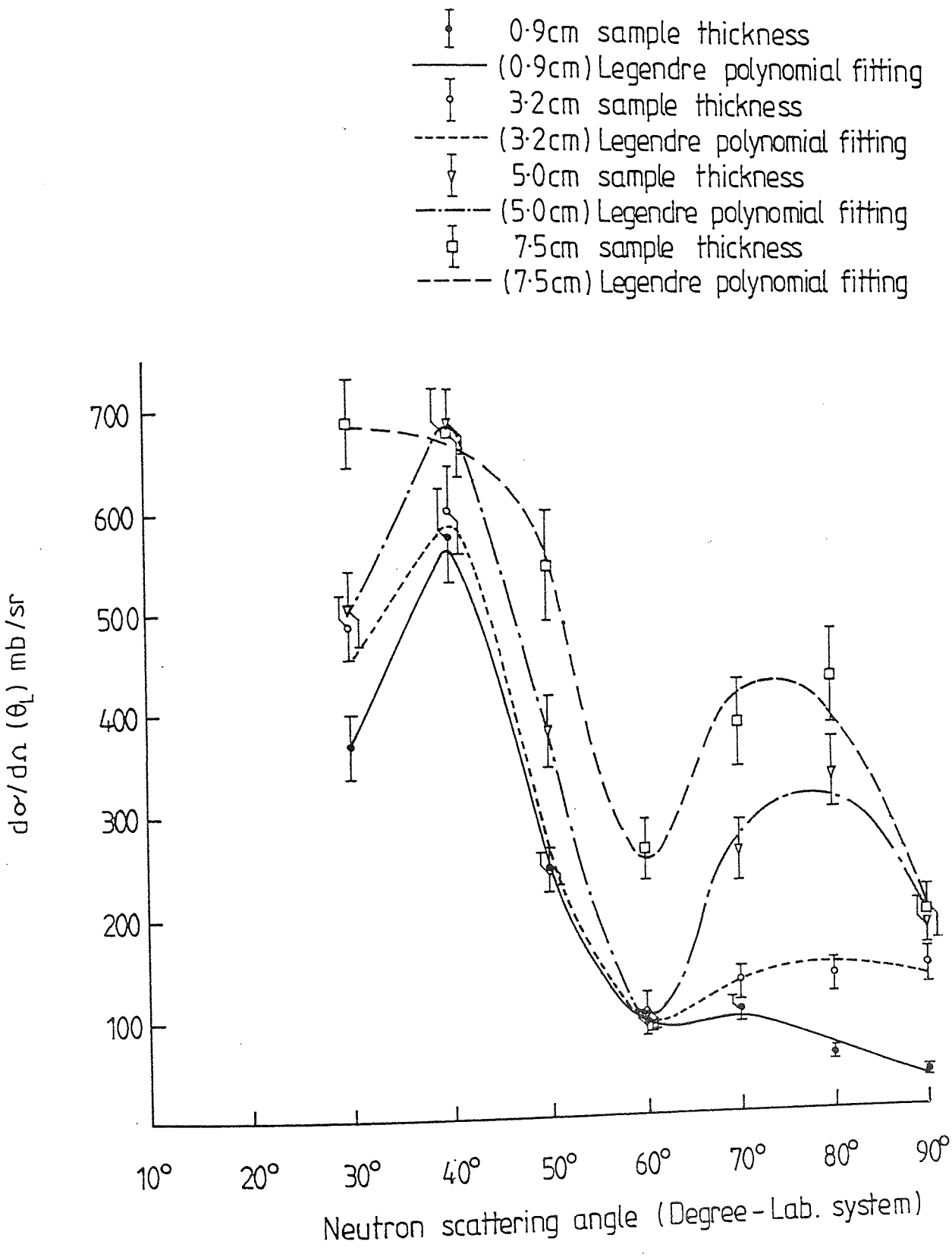

Figure 6.21 Differential elastic scattering cross-sections of 14 MeV neutrons for Lead for different sample thicknesses.

6.9 EXPERIMENTAL RESULTS FOR THE DIFFERENTIAL INELASTIC SCATTERING CROSS-SECTION

The neutrons corresponding to inelastic scattering from the 2.6 Mev and 4.1 Mev excited states in lead were observed and the differential cross-sections calculated as before . These are tabulated in tables (6.19) and (6.2Ø) for different scattering samples . The experimental errors for each term of equation (5.23) is shown in table (6.18) . As shown in figs (6.22) and (6.23) the angular distributions for neutrons scattered from the 2.6 Mev and 4.1 Mev excited states were fitted to Legendre Polynomials [equation (6.1)] using program LEGFIT [Appendix C] .

Because of the difficulty of resolving individual peaks the measured angular distributions for neutrons in different energy intervals are shown in tables (6.21) through to (6.24) and plotted in figs (6.24) through to (6.27) . Each figure gives the angular distributions for each energy interval corresponding to different scattering thicknesses The data were fitted to Legendre Polynomials as before .

Table (6.18)

EXPERIMENTAL ERRORS IN THE CALCULATION OF THE DIFFERENTIAL ELASTIC AND INELASTIC SCATTERING CROSS-SECTION

FACTOR	ESTIMATED FACTOR %
$F_1, F_2,$ $N(\theta)$	< 1 $[(\text{ACC.}-\text{B.G.})^2]^{\frac{1}{2}}$
$\Delta\Omega, G$	1.75
$\xi(En)$	5.Ø
$\bar{x}$	< 1
ATTENUATION FACTOR	1.1

Table (6.19)

DIFFERENTIAL INELASTIC SCATTERING CROSS-SECTION DATA

FOR THE EXCITED STATE 2.6 Mev IN LEAD

θ_L (Deg)	THICKNESS (cm)	DIFFERENTIAL INELASTIC SCATTERING CROSS-SECTION (mb / s)
30°	0.9	9.3 ± 1.7
	3.2	14.0 ± 2.9
	5.0	21.6 ± 4.2
	7.5	23.3 ± 3.1
40°	0.9	10.7 ± 2.4
	3.2	6.6 ± 1.3
	5.0	15.0 ± 3.2
	7.5	17.1 ± 2.5
50°	0.9	8.4 ± 2.0
	3.2	9.2 ± 2.3
	5.0	19.2 ± 4.3
	7.5	14.8 ± 4.3
60°	0.9	8.4 ± 2.2
	3.2	7.6 ± 2.7
	5.0	13.0 ± 2.3
	7.5	24.0 ± 4.1
70°	0.9	3.4 ± 0.6
	3.2	10.5 ± 3.8
	5.0	23.9 ± 4.2
	7.5	19.0 ± 4.7
80°	0.9	11.5 ± 3.9
	3.2	14.6 ± 4.4
	5.0	18.8 ± 4.4
	7.5	24.7 ± 4.1
90°	0.9	7.5 ± 1.4
	3.2	14.6 ± 3.3
	5.0	15.8 ± 3.6
	7.5	21.8 ± 4.6

Table (6.2Ø)

DIFFERENTIAL INELASTIC SCATTERING CROSS-SECTION DATA

FOR THE 4.1 Mev EXCITED STATE IN LEAD

θ_L (Deg)	THICKNESS (cm)	DIFFERENTIAL INELASTIC SCATTERING CROSS-SECTION (mb /s)
3Ø°	Ø.9	12.9 ± 2.3
	3.2	13.1 ± 2.1
	5.Ø	21.5 ± 4.3
	7.5	1Ø.7 ± 2.7
4Ø°	Ø.9	5.8 ± Ø.7
	3.2	5.4 ± 1.Ø
	5.Ø	7.6 ± 1.3
	7.5	6.8 ± 1.6
5Ø°	Ø.9	9.6 ± 2.3
	3.2	1Ø.5 ± 3.2
	5.Ø	18.8 ± 4.3
	7.5	16.3 ± 4.6
6Ø°	Ø.9	6.3 ± 1.5
	3.2	7.3 ± 2.1
	5.Ø	7.6 ± 1.1
	7.5	1Ø.4 ± 3.5
7Ø°	Ø.9	13.5 ± 3.9
	3.2	6.7 ± 1.8
	5.Ø	13.Ø ± 3.3
	7.5	11.4 ± 2.7
8Ø°	Ø.9	12.5 ± 3.1
	3.2	18.2 ± 4.6
	5.Ø	18.8 ± 5.Ø
	7.5	17.Ø ± 4.5
9Ø°	Ø.9	9.2 ± 2.4
	3.2	21.2 ± 4.6
	5.Ø	18.6 ± 5.4
	7.5	17.4 ± 4.7

Table (6.21)

DIFFERENTIAL CROSS-SECTION DATA FOR

THE ENERGY RANGE 11 - 14 Mev IN LEAD

θ_L (Deg)	THICKNESS (cm)	$d\sigma/d\Omega$ (mb/s)
30°	0.9	371 ± 24
	3.2	439 ± 27
	5.0	629 ± 33
	7.5	679 ± 50
40°	0.9	545 ± 24
	3.2	542 ± 38
	5.0	642 ± 28
	7.5	551 ± 37
50°	0.9	230 ± 18
	3.2	261 ± 18
	5.0	368 ± 24
	7.5	508 ± 44
60°	0.9	118 ± 8
	3.2	157 ± 10
	5.0	188 ± 17
	7.5	246 ± 31

θ_L (Deg)	THICKNESS (cm)	$d\sigma/d\Omega$ (mb/s)
70°	0.9	105 ± 9
	3.2	115 ± 9
	5.0	270 ± 18
	7.5	390 ± 65
80°	0.9	26 ± 4
	3.2	116 ± 10
	5.0	110 ± 14
	7.5	143 ± 17
90°	0.9	35 ± 3
	3.2	113 ± 6
	5.0	82 ± 9
	7.5	83 ± 9

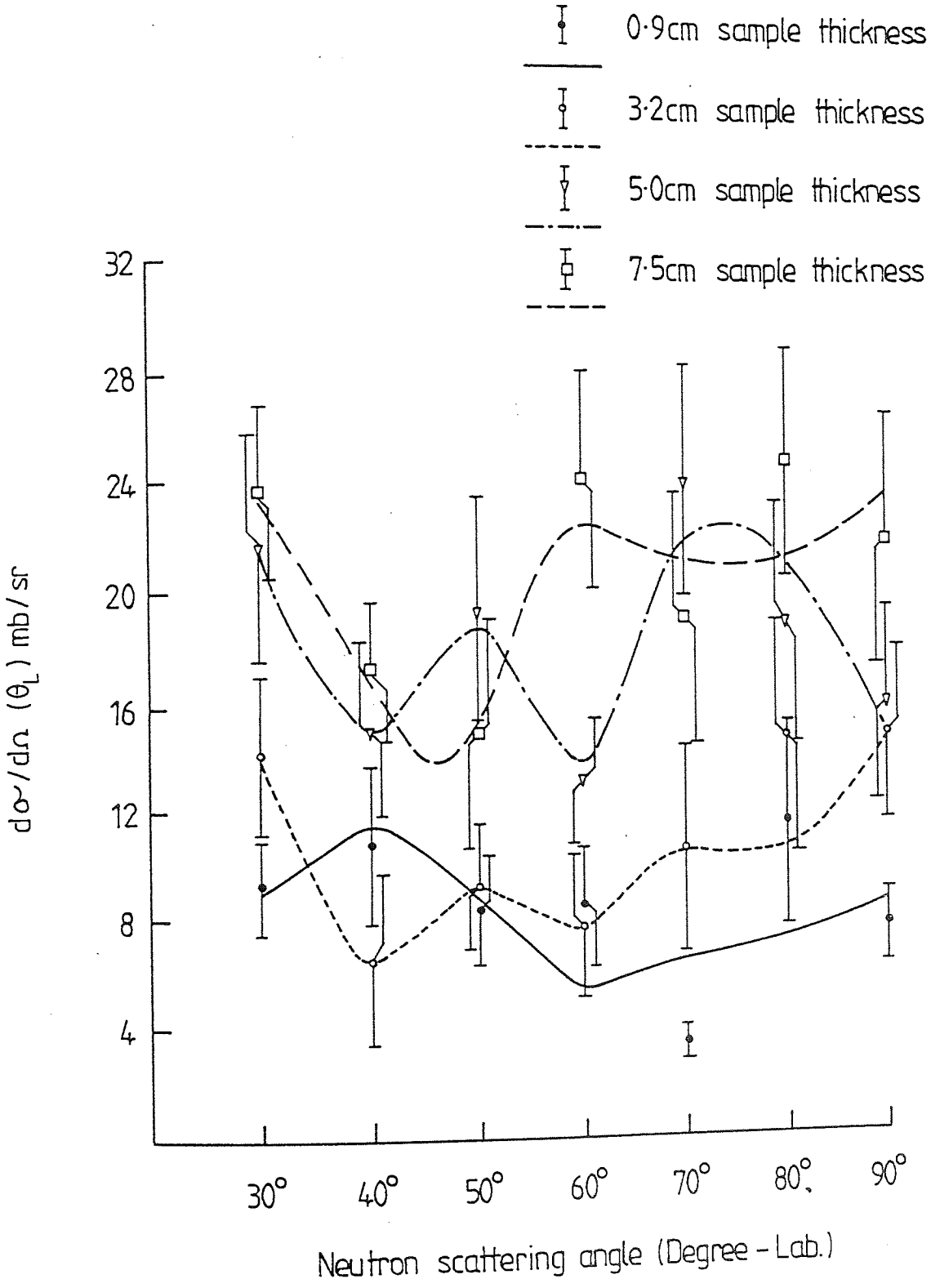

Figure 6·22 Angular distributions for the Pb(n,n′) reaction at 14MeV incident neutron energy for the state 2·6MeV for different sample thicknesses.

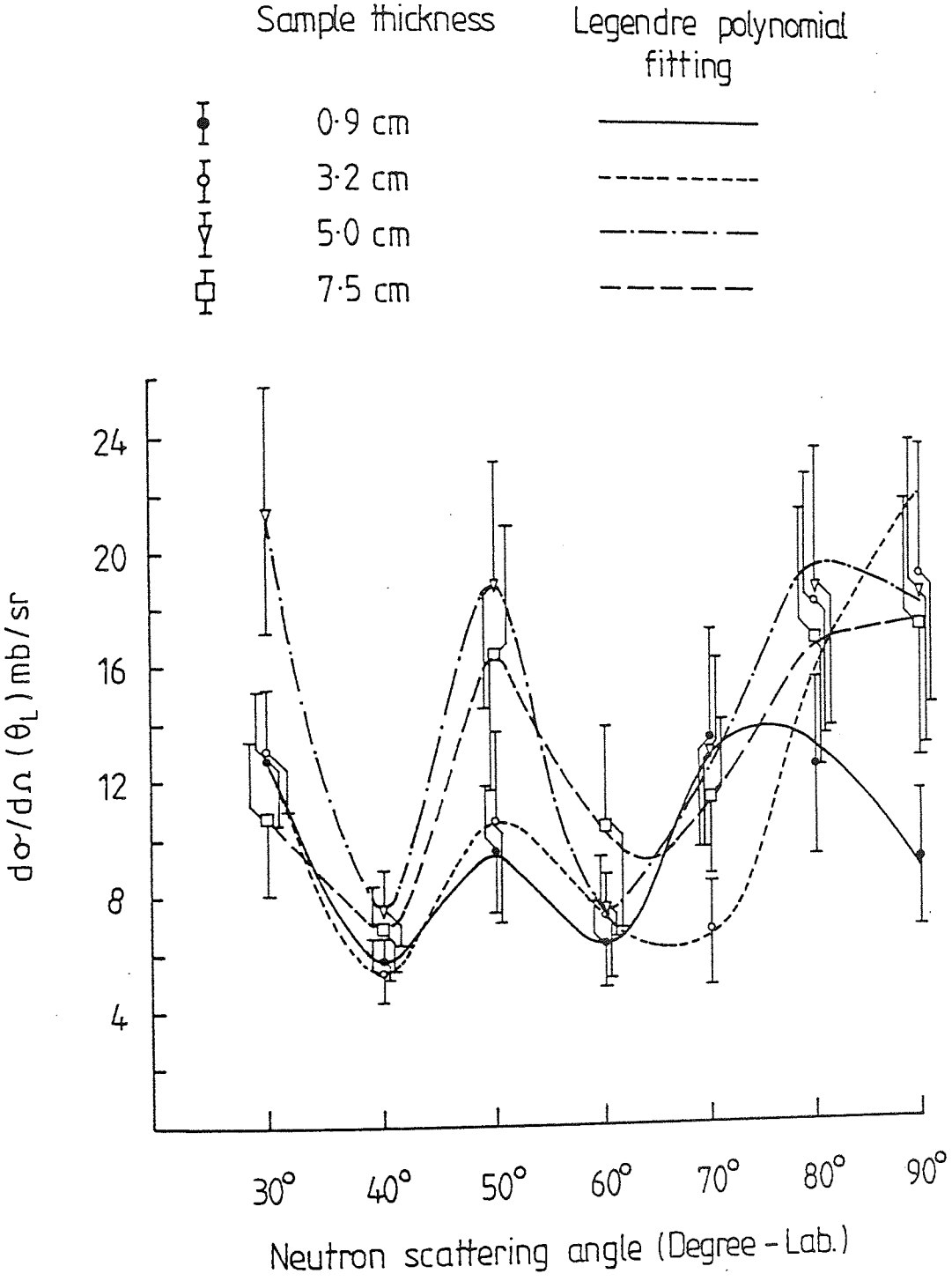

Figure 6·23 Angular distributions for the Pb(n,n') reaction at 14MeV incident neutron energy for the state 4·1MeV for different sample thicknesses.

Table (6.22)

DIFFERENTIAL CROSS-SECTION FOR THE ENERGY RANGE 8-11 Mev IN LEAD

θ_L (Deg)	THICKNESS (cm)	$d\sigma/d\Omega$ (mb/s)
30°	Ø.9	46.1 ± 7.2
	3.2	52.Ø ± 6.5
	5.Ø	56.6 ± 6.4
	7.5	47.Ø ± 6.5
40°	Ø.9	32.2 ± 4.7
	3.2	5Ø.1 ± 6.2
	5.Ø	53.7 ± 4.1
	7.5	64.Ø ± 6.9
5Ø°	Ø.9	22.Ø ± 3.7
	3.2	33.2 ± 4.3
	5.Ø	52.Ø ± 4.7
	7.5	58.4 ± 7.7
6Ø°	Ø.9	24.1 ± 3.Ø
	3.2	32.5 ± 3.2
	5.Ø	42.Ø ± 4.2
	7.5	63.2 ± 9.4

θ_L (Deg)	THICKNESS (cm)	$d\sigma/d\Omega$ (mb/s)
7Ø°	Ø.9	18.6 ± 2.5
	3.2	14.7 ± 2.1
	5.Ø	44.7 ± 6.3
	7.5	66.Ø ± 8.Ø
8Ø°	Ø.9	1Ø.4 ± 1.4
	3.2	32.Ø ± 4.1
	5.Ø	18.Ø ± 4.1
	7.5	66.Ø ± 6.5
9Ø°	Ø.9	15.Ø ± 2.5
	3.2	28.3 ± 5.4
	5.Ø	4Ø.Ø ± 7.1
	7.5	28.3 ± 5.7

Table (6.23)

DIFFERENTIAL CROSS-SECTION DATA FOR

THE ENERGY RANGE 5 - 8 Mev IN LEAD

θ_L (Deg)	THICKNESS (cm)	$d\sigma/d\Omega$ (mb/s)
30°	Ø.9	51.6 ± 8.4
	3.2	42.5 ± 6.3
	5.Ø	75.2 ± 8.Ø
	7.5	62.6 ± 6.7
40°	Ø.9	53.5 ± 6.7
	3.2	6Ø.9 ± 9.Ø
	5.Ø	67.Ø ± 7.4
	7.5	58.3 ± 5.1
50°	Ø.9	2Ø.2 ± 4.Ø
	3.2	21.1 ± 3.2
	5.Ø	19.5 ± 2.4
	7.5	4Ø.1 ± 4.9
60°	Ø.9	29.Ø ± 3.2
	3.2	52.1 ± 6.2
	5.Ø	38.Ø ± 6.1
	7.5	6Ø.8 ± 6.5

θ_L (Deg)	THICKNESS (cm)	$d\sigma/d\Omega$ (mb/s)
70°	Ø.9	4Ø.5 ± 4.8
	3.2	42.1 ± 4.8
	5.Ø	72.3 ± 7.7
	7.5	41.8 ± 5.Ø
80°	Ø.9	13.2 ± 1.4
	3.2	65.6 ± 8.2
	5.Ø	54.2 ± 7.9
	7.5	79.8 ± 11.6
90°	Ø.9	22.3 ± 3.1
	3.2	46.Ø ± 6.2
	5.Ø	26.Ø ± 4.7
	7.5	48.Ø ± 6.2

Table(6.24)

DIFFERENTIAL CROSS-SECTION DATA FOR

THE ENERGY RANGE 2 - 5 Mev IN LEAD

θ_L (Deg)	THICKNESS (cm)	$d\sigma/d\Omega$ (mb/s)
30°	Ø.9	14.3 ± 2.1
	3.2	34.8 ± 5.3
	5.Ø	4Ø.Ø ± 5.4
	7.5	42.Ø ± 4.3
4Ø°	Ø.9	3Ø.4 ± 2.4
	3.2	4Ø.Ø ± 3.8
	5.Ø	4Ø.2 ± 5.1
	7.5	47.6 ± 6.Ø
5Ø°	Ø.9	14.1 ± 2.8
	3.2	11.9 ± 2.4
	5.Ø	22.2 ± 4.1
	7.5	32.4 ± 6.8
6Ø°	Ø.9	41.3 ± 6.8
	3.2	51.8 ± 6.6
	5.Ø	35.1 ± 6.5
	7.5	34.4 ± 5.5

θ_L (Deg)	THICKNESS (cm)	$d\sigma/d\Omega$ (mb/s)
7Ø°	Ø.9	59.6 ± 9.6
	3.2	6Ø.7 ± 8.6
	5.Ø	67.8 ± 8.2
	7.5	67.8 ± 7.4
8Ø°	Ø.9	42.5 ± 5.1
	3.2	63.8 ± 7.5
	5.Ø	57.1 ± 6.9
	7.5	78.Ø ± 9.6
9Ø°	Ø.9	2Ø.1 ± 4.4
	3.2	48.8 ± 6.3
	5.Ø	58.Ø ± 7.3
	7.5	87.Ø ± 9.2

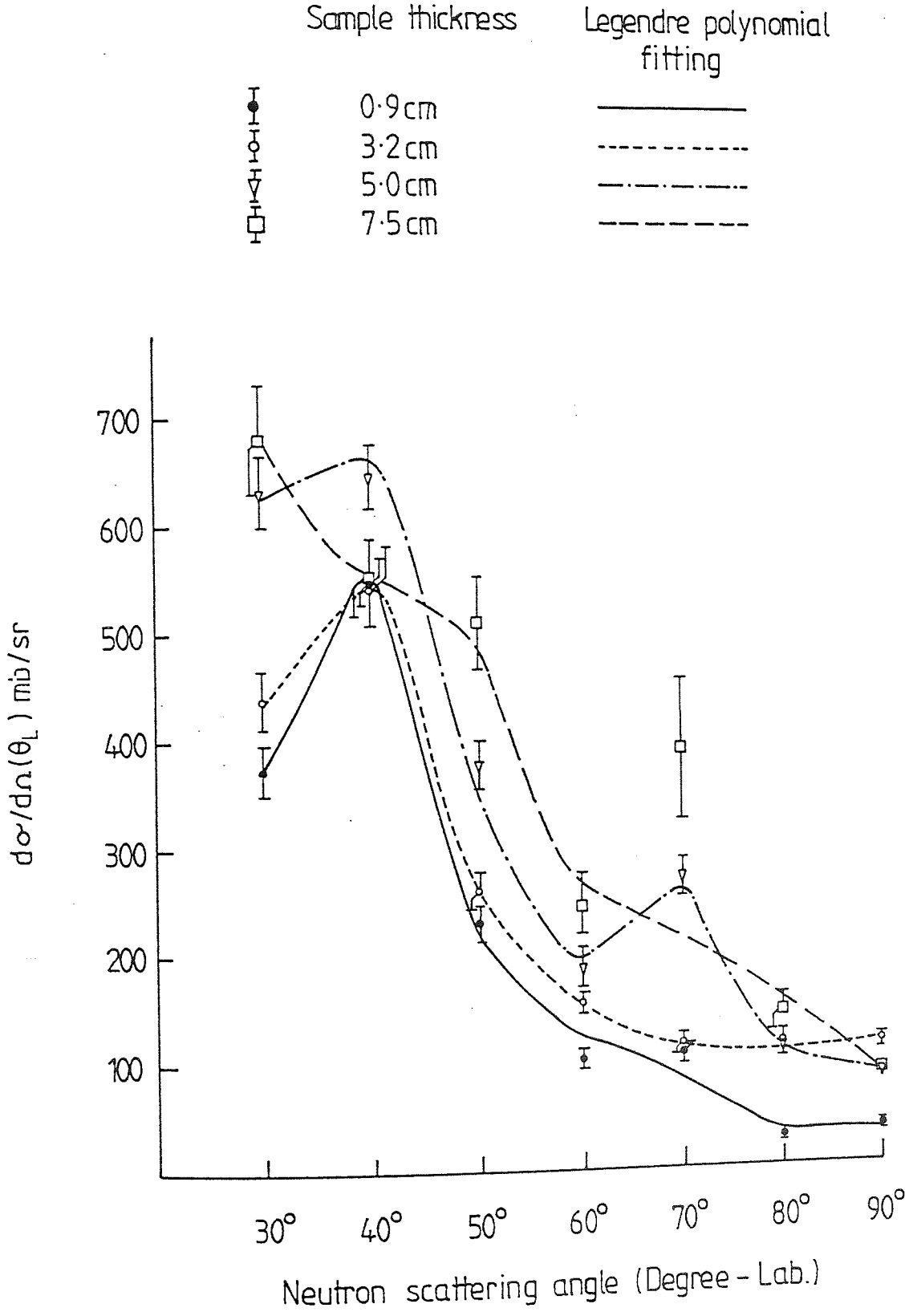

Figure 6·24 Angular distributions for the energy range 11 - 14 MeV at 14 MeV incident neutrons for Lead at different sample thicknesses.

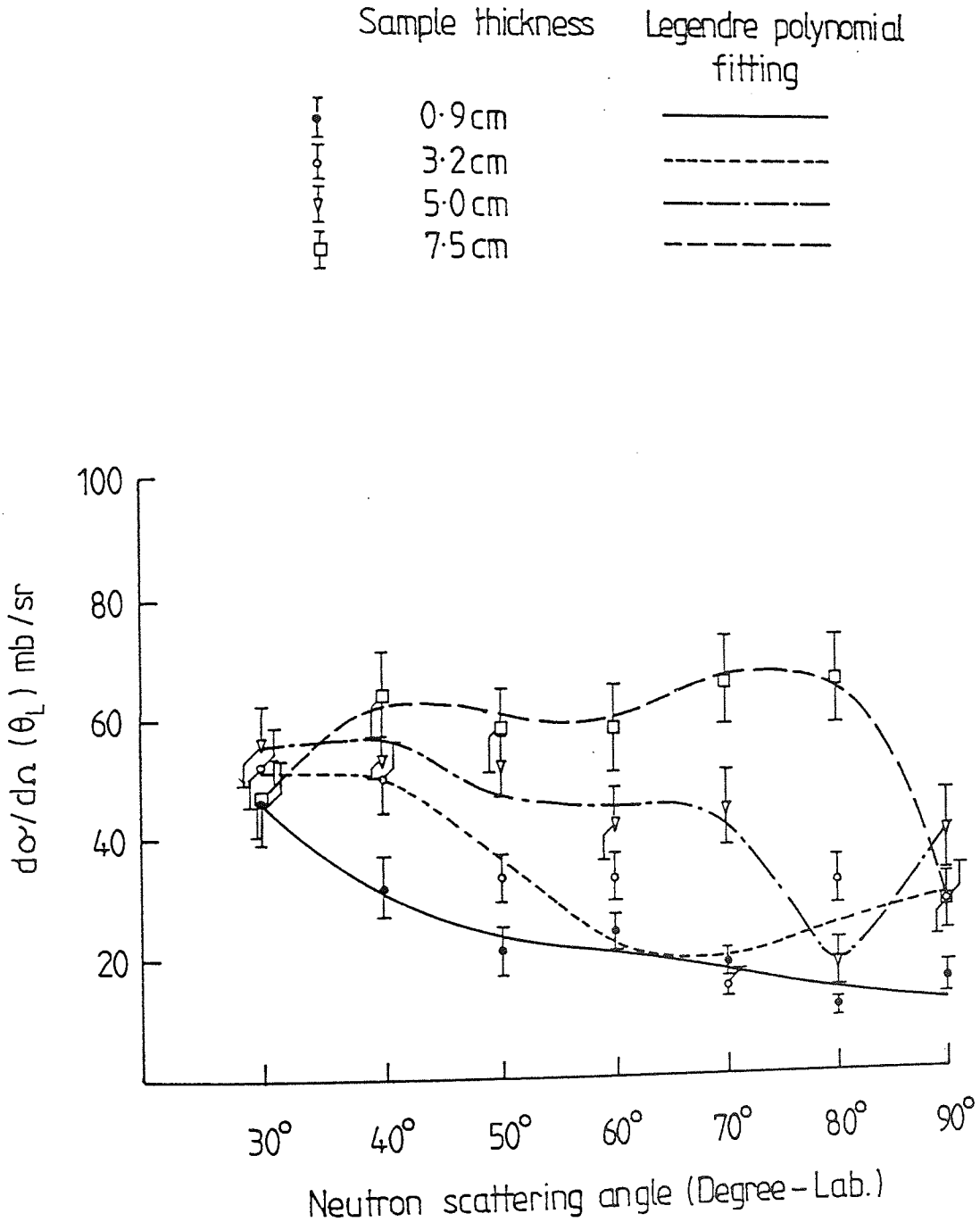

Figure 6·25 Angular distributions for the energy range 8 - 11 MeV at 14 MeV incident neutrons for Lead at different sample thicknesses.

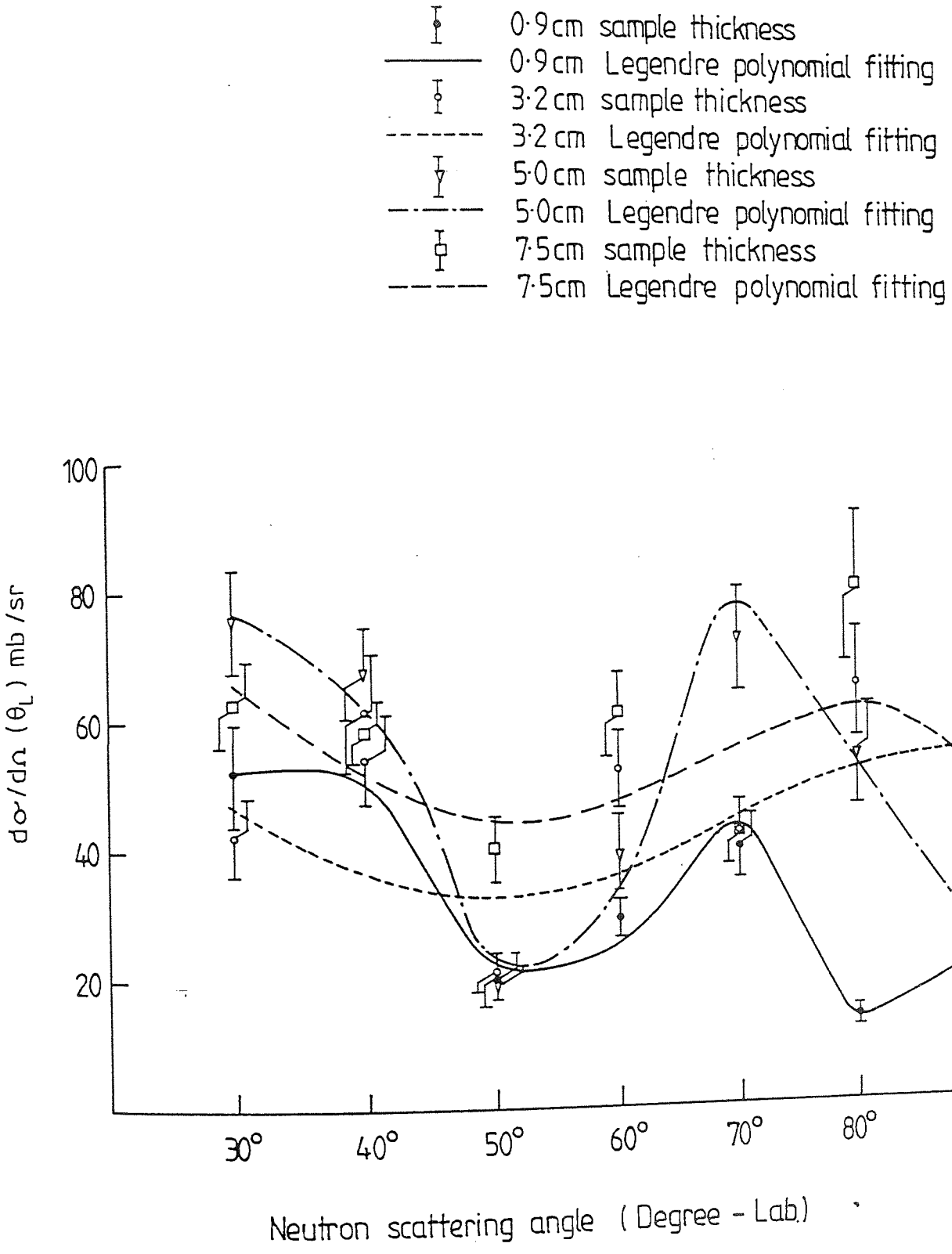

Figure 6·26 Angular distributions for the energy range 5-8 MeV at 14 MeV incident neutrons for Lead at different sample thicknesses.

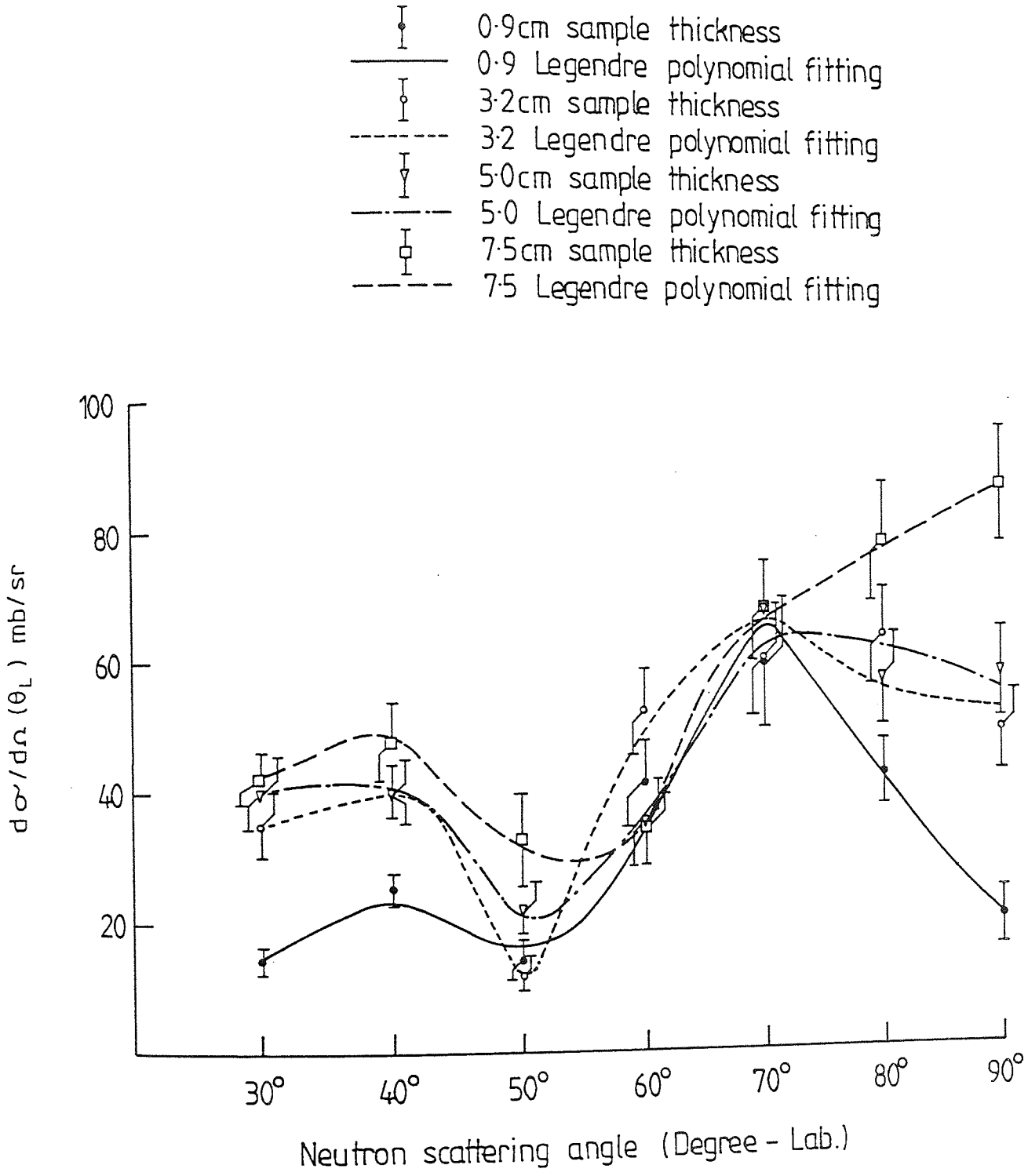

Figure 6·27 Angular distributions for the energy range 2-5 MeV at 14 MeV incident neutrons for Lead at different sample thicknesses.

6.10 THE VARIATION OF THE MEASURED DIFFERENTIAL CROSS-SECTIONS $\sigma(\theta)$ WITH THE SAMPLE THICKNESS IN LEAD

The variation of the measured differential elastic and inelastic scattering cross-sections of the lead for four different thicknesses are shown in tables (6.17) through to (6.24) analyzed as discussed in section (6.3.1.1) using equation (6.2) .

By applying the least squares method , the constant α for lead was determined as :

$$\alpha_{pb} = 0.37 \pm 0.13 \quad /mfp$$

Referring to table (6.9) , the universal constant α_{uni} was determined by combining the α-constant for both lithium and lead for all energies studied in the present work . The value of the universal constant (α_{uni}) given in table (6.25) agrees with the values obtained by AL-SHALIBI (1982) [80] AND ANVARIAN (1983) [81] .

The variation of the differential elastic and inelastic scattering cross- sections with the thickness for 14 Mev neutrons from lead samples is shown in figs (6.28) through (6.40) . For each case , the dashed and solid lines represent least squares fits to the data according to equation (6.19) , using the universal constant (α_{uni}) and lead constant respectively .

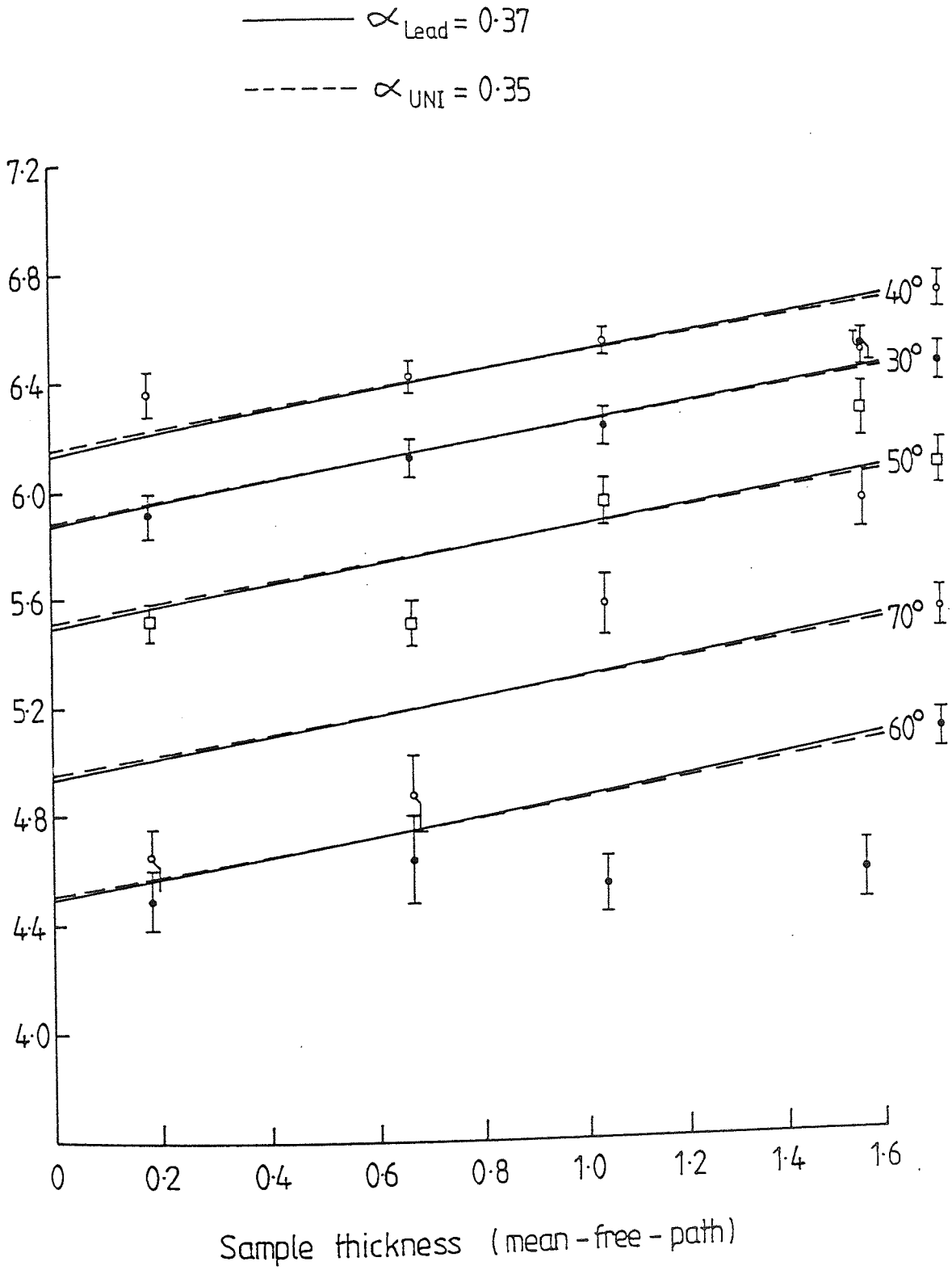

Figure 6·28 The variation of the measured differential elastic scattering cross-section for Lead samples with the sample thicknesses at various scattering angles, using equation (6.4).

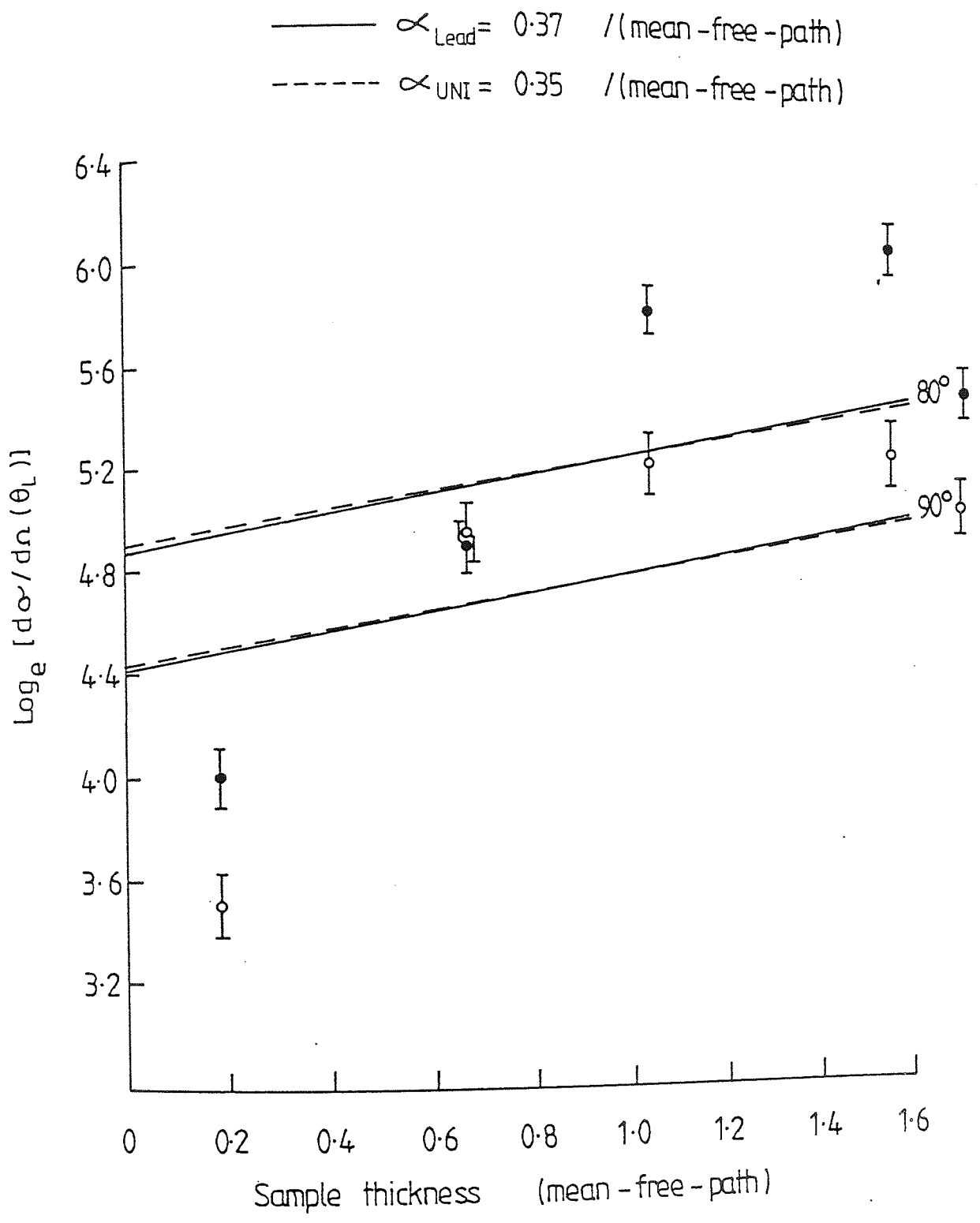

Figure 6·29 The variation of the measured differential elastic cross-section for Lead samples with the sample thicknesses at 80° and 90° scattering angles. The lines represent least squares fit using equation (6·4).

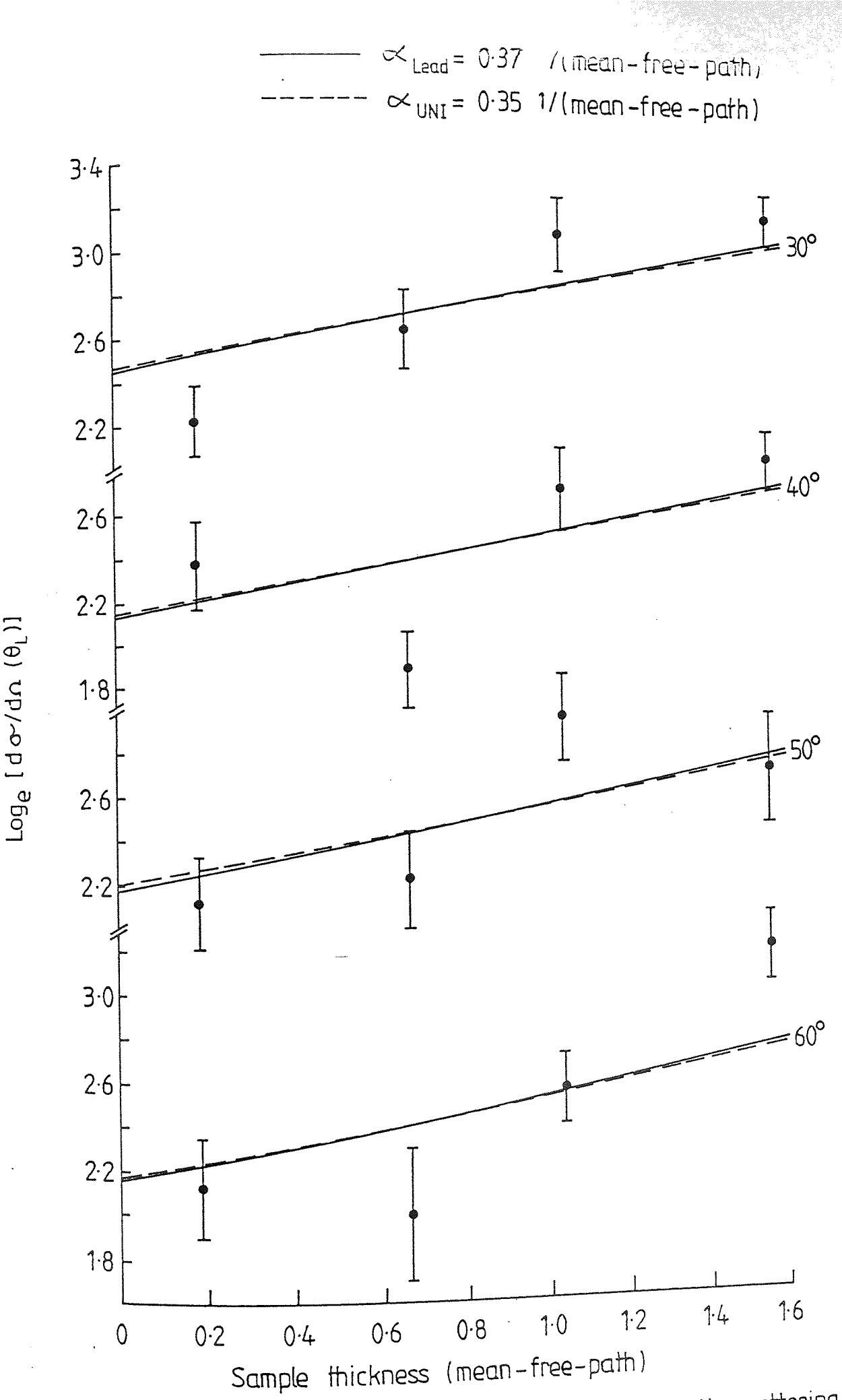

Figure 6·30 The variation of the measured differential inelastic scattering cross-sections of the excited state 2·6 MeV in Lead with the sample thicknesses at various scattering angles, using

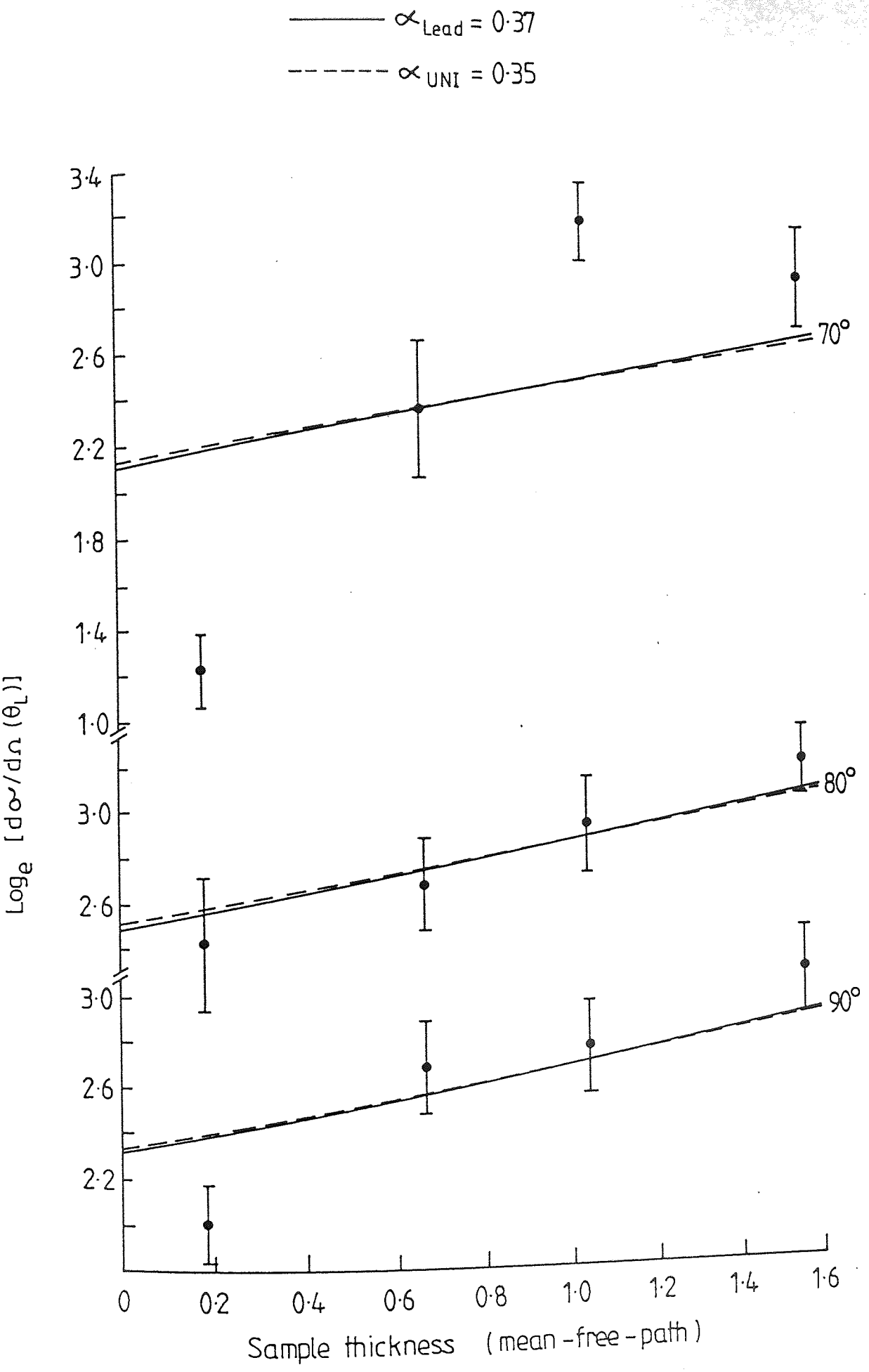

Figure 6·31 The variation of the measured differential inelastic scattering cross-sections of the excited state 2·6 MeV in Lead, with the sample thicknesses at various scattering angles, using equation (6·4).

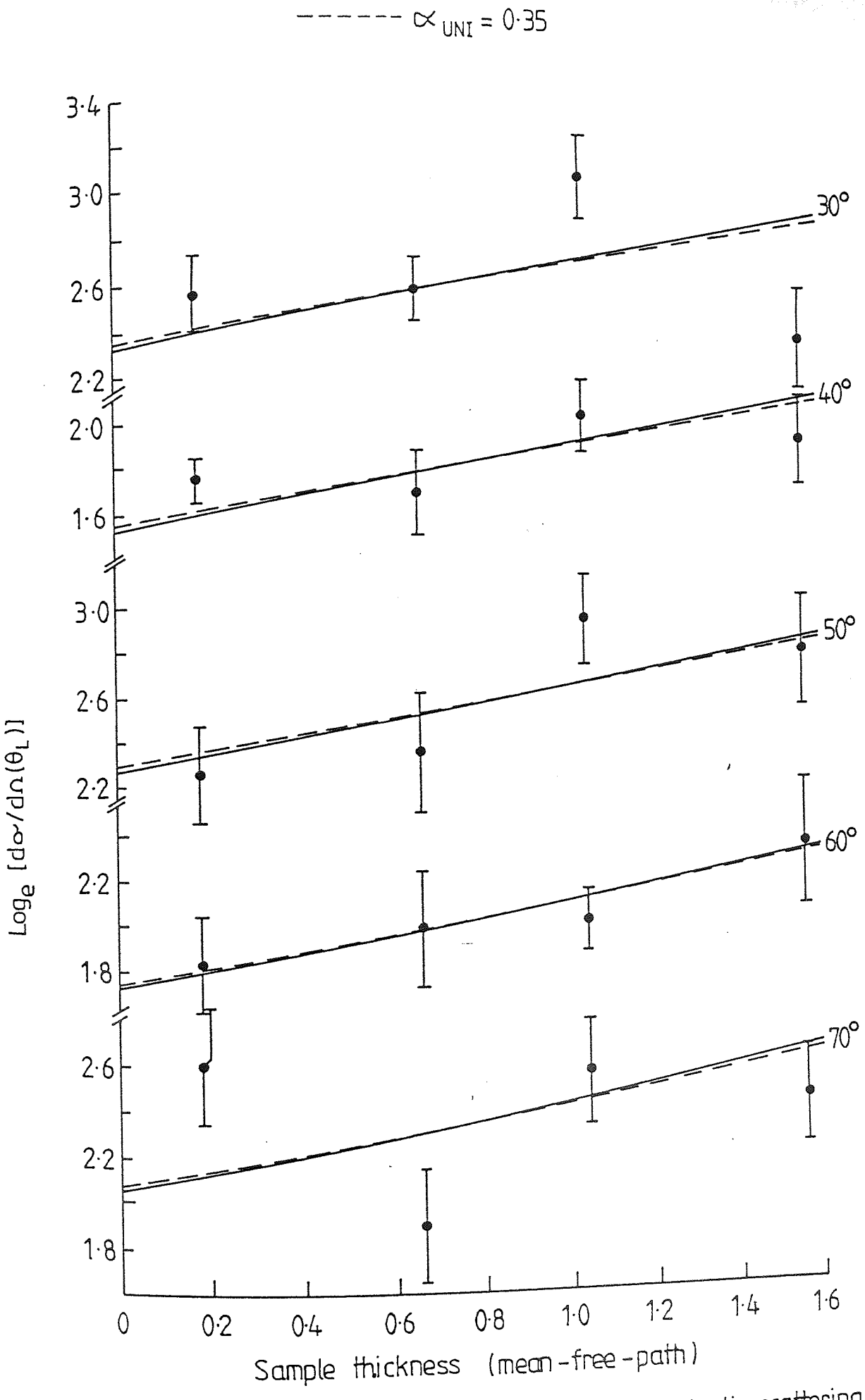

Figure 6·32 The variation of the measured differential inelastic scattering cross-sections for the excited state 4·1MeV in Lead with scattering thicknesses and at different scattering angles, using

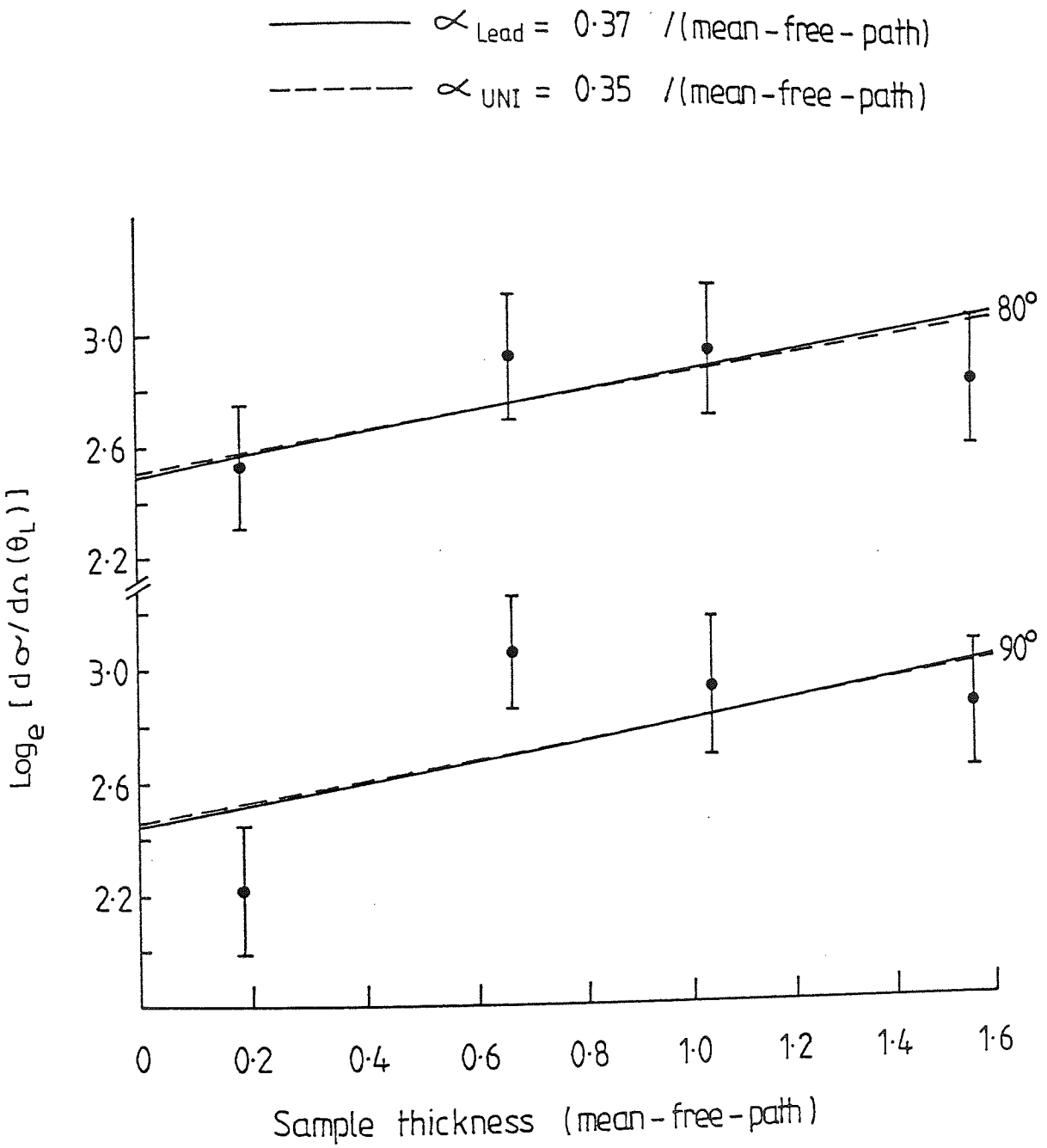

Figure 6·33 The variation of the measured differential inelastic scattering cross-sections for the excited state 4·1 MeV in Lead with the sample thicknesses and at the various scattering angles, using equation (6·4).

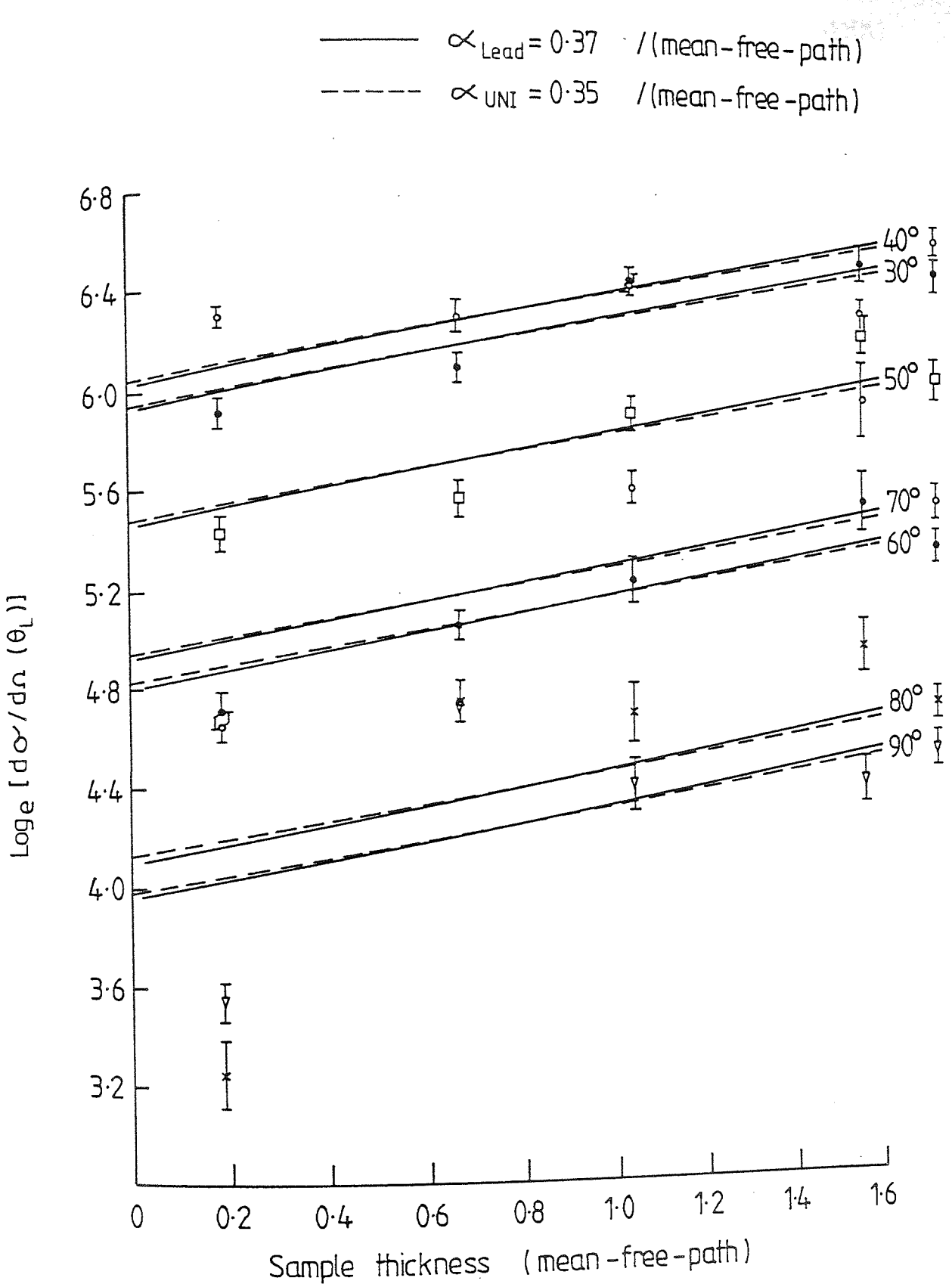

Figure 6·34 The variation of the measured differential cross-section for the energy range 11-14 MeV in Lead with sample thicknesses at different scattering angles, using equation (6·4).

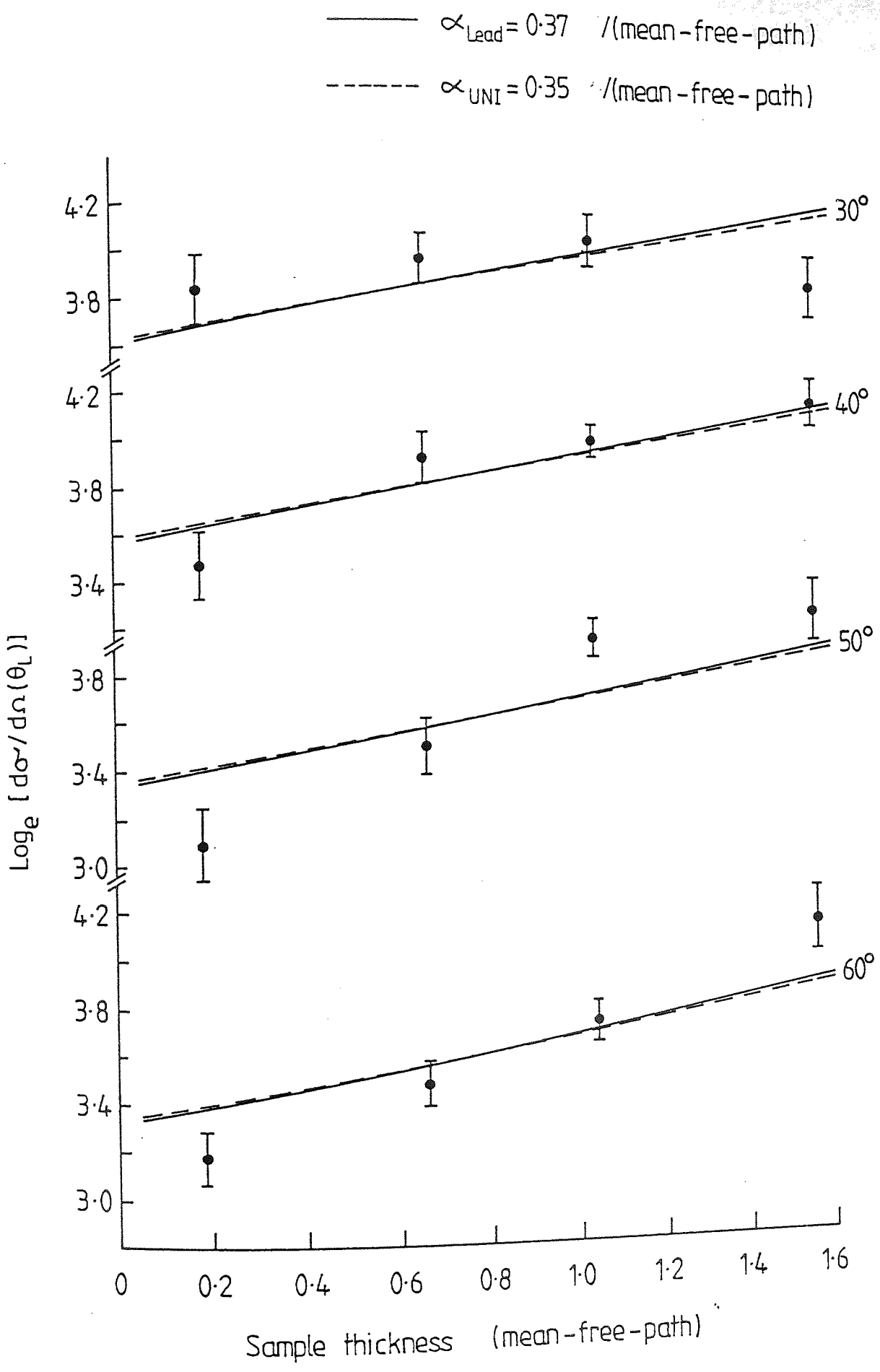

Figure 6.35 The variation of the measured differential scattering cross-sections for the energy range 8 - 11 MeV in Lead with the sample thicknesses at various scattering angles, using equation (6·4).

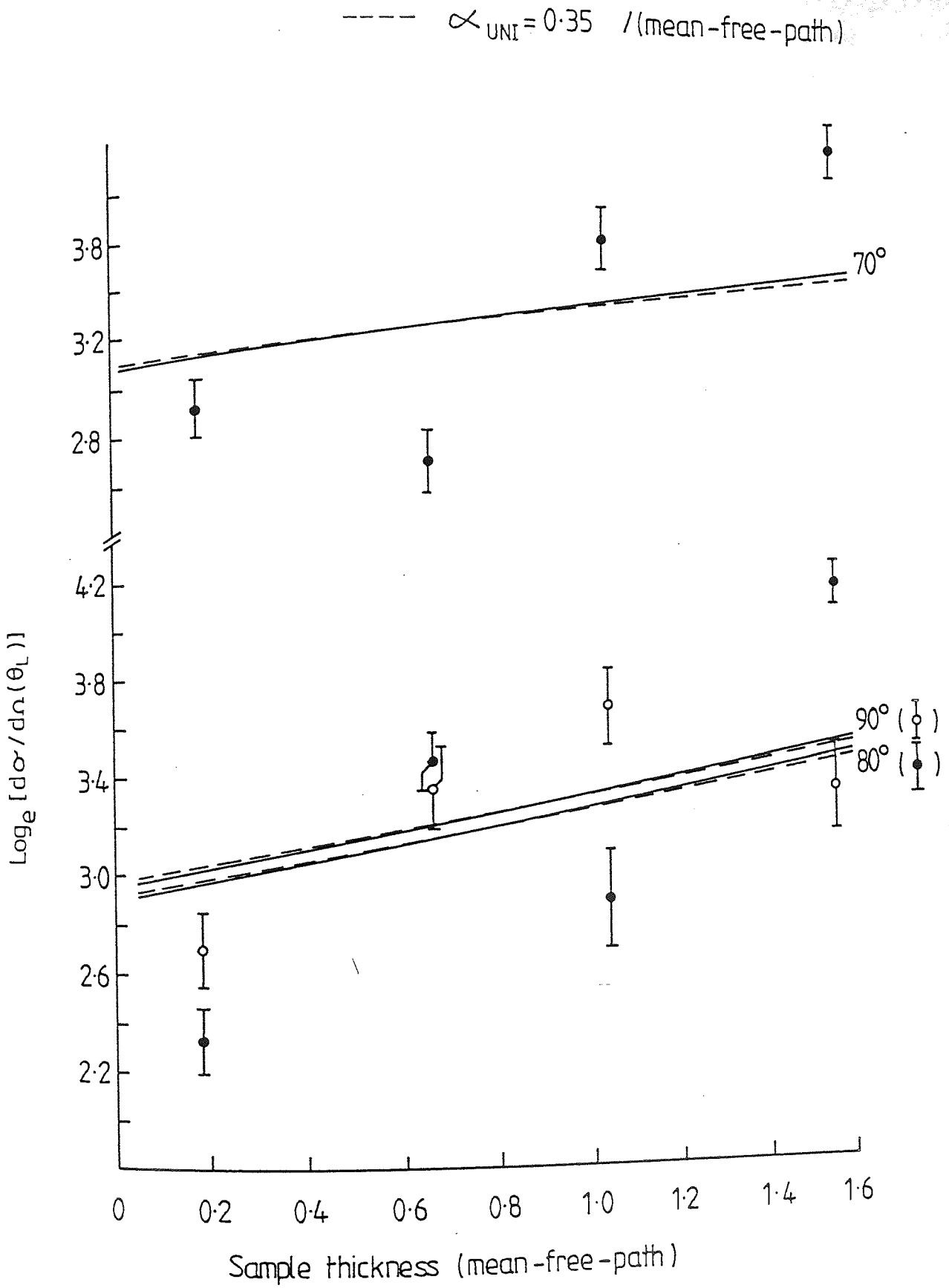

Figure 6·36 The variation of the measured differential scattering cross-sections for the energy range 8 - 11 MeV in Lead with the sample thicknesses at various scattering angles, using equation (6·4)

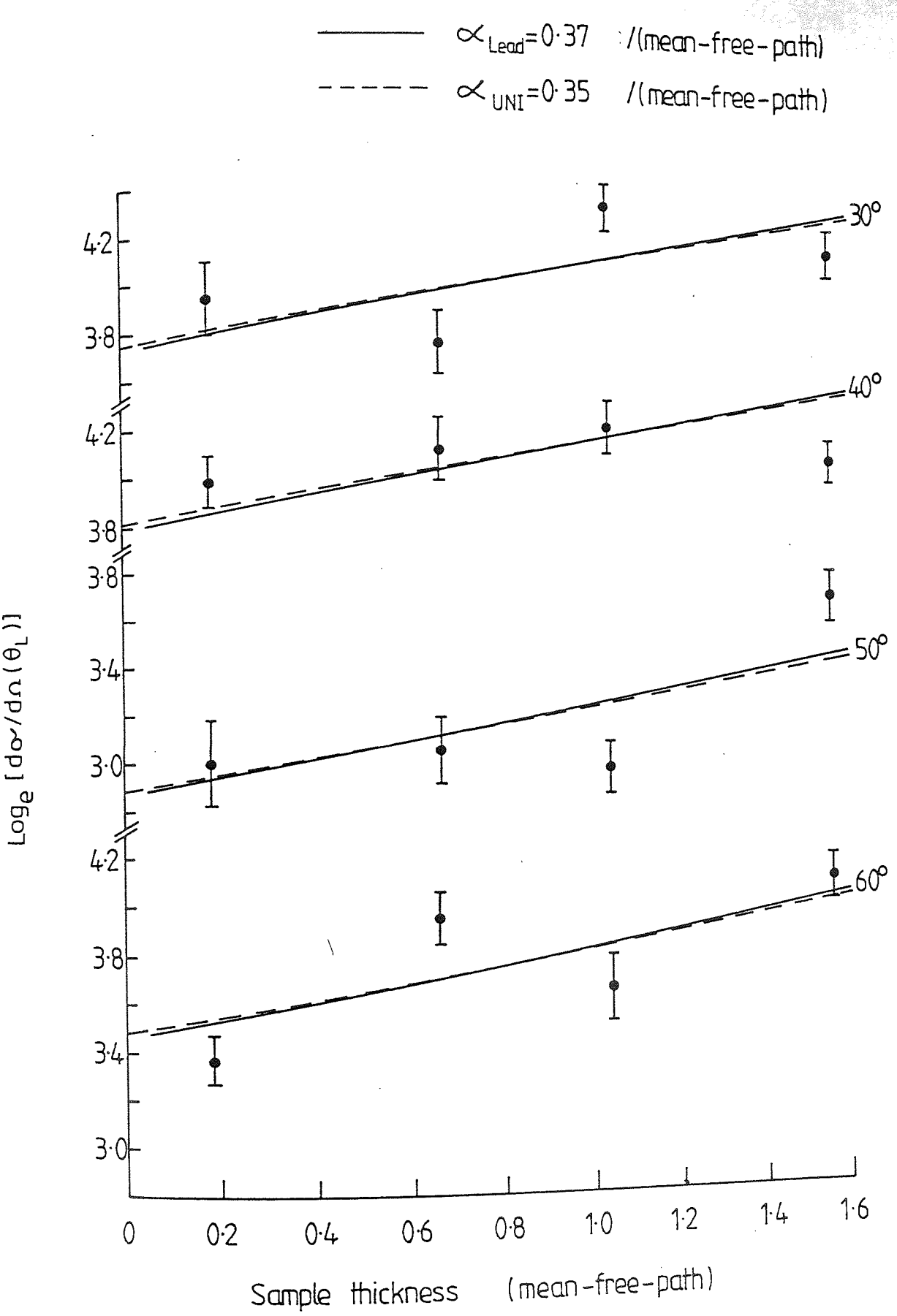

Figure 6·37 The variation of the measured differential cross-sections of the energy range 5-8 MeV in Lead with the sample thicknesses at various scattering angles, using equation (6·4)

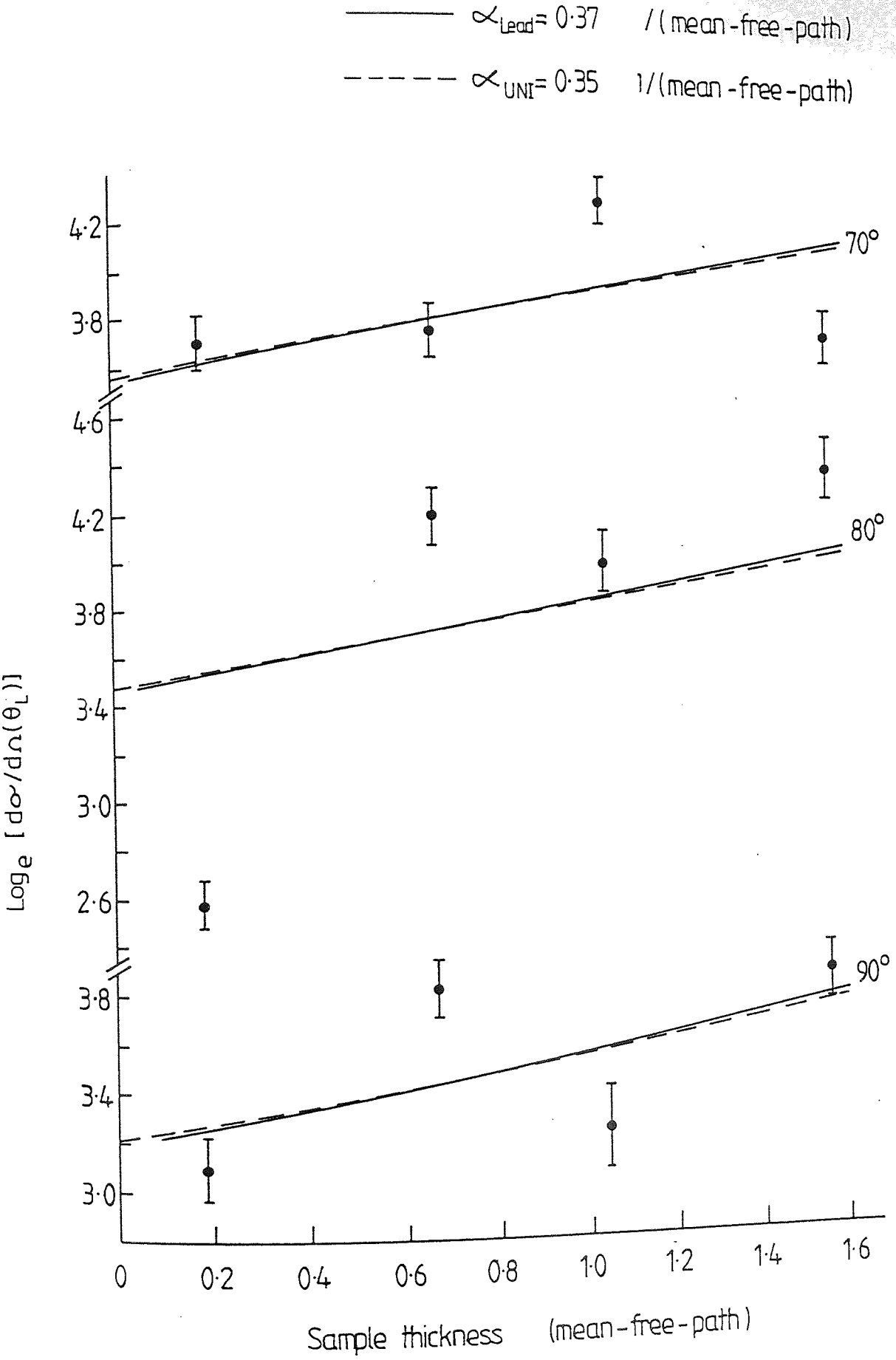

Figure 6.38 The variation of the measured differential scattering cross-sections of the energy range 5-8 MeV in Lead with the sample thicknesses at various scattering angles, using equation (6.4)

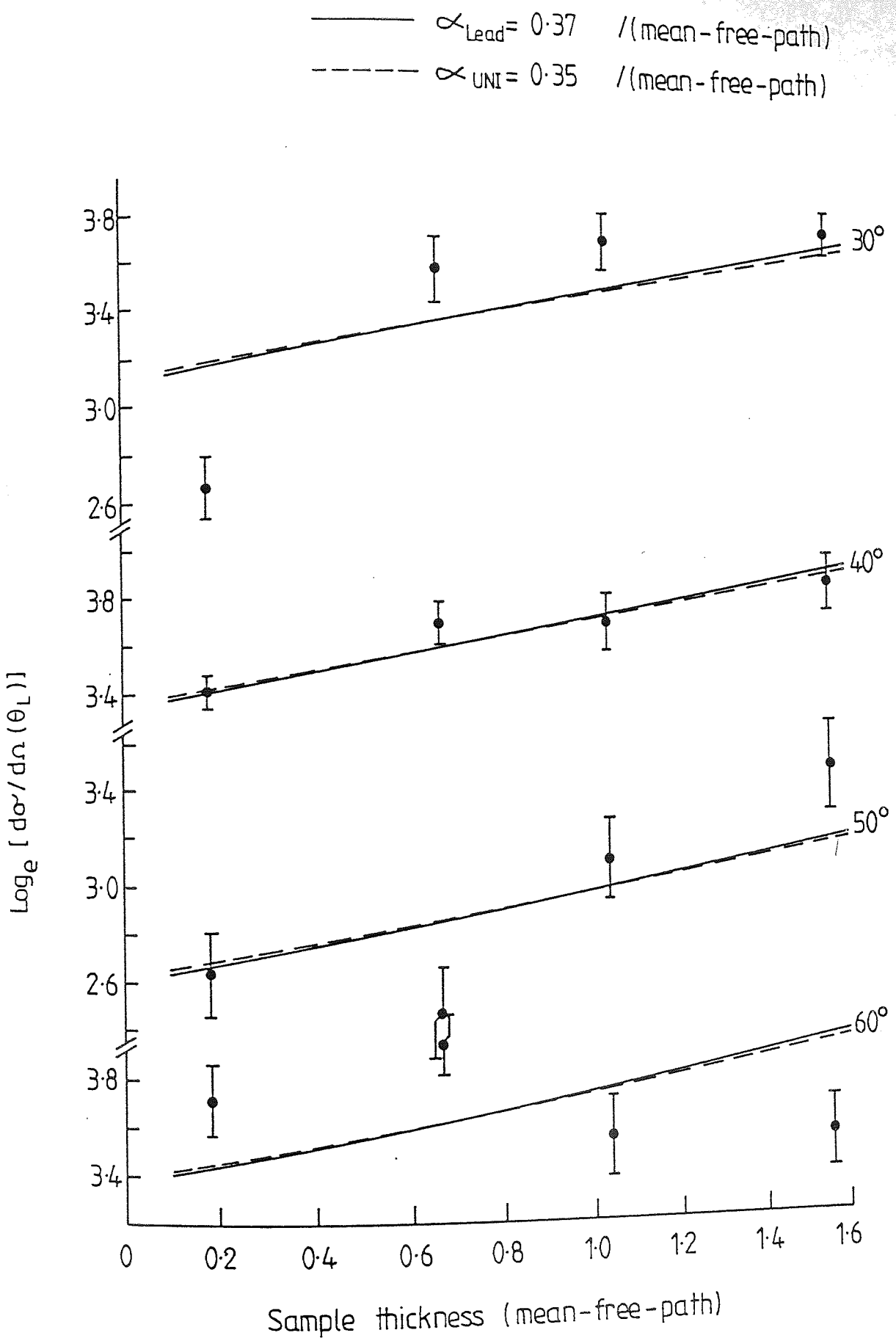

Figure 6 39 The variation of the measured differential scattering cross-sections of the energy range 2-5 MeV in Lead with the sample thicknesses at various scattering angles, using equation (6 4)

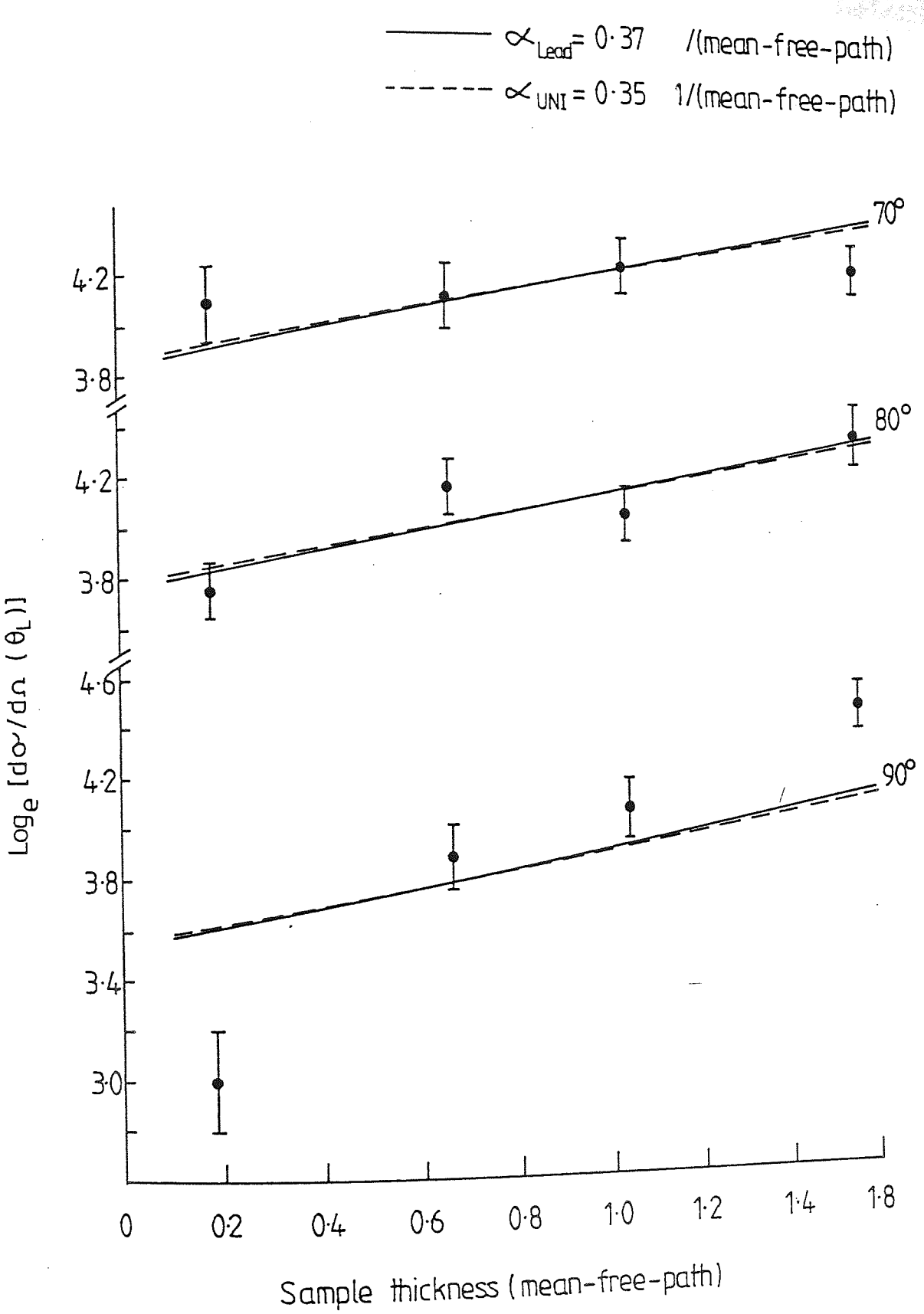

Figure 6.40 The variation of the measured differential scattering cross-sections of the energy range 5-2 MeV in Lead with the sample thicknesses at various scattering angles, using equation (6.4)

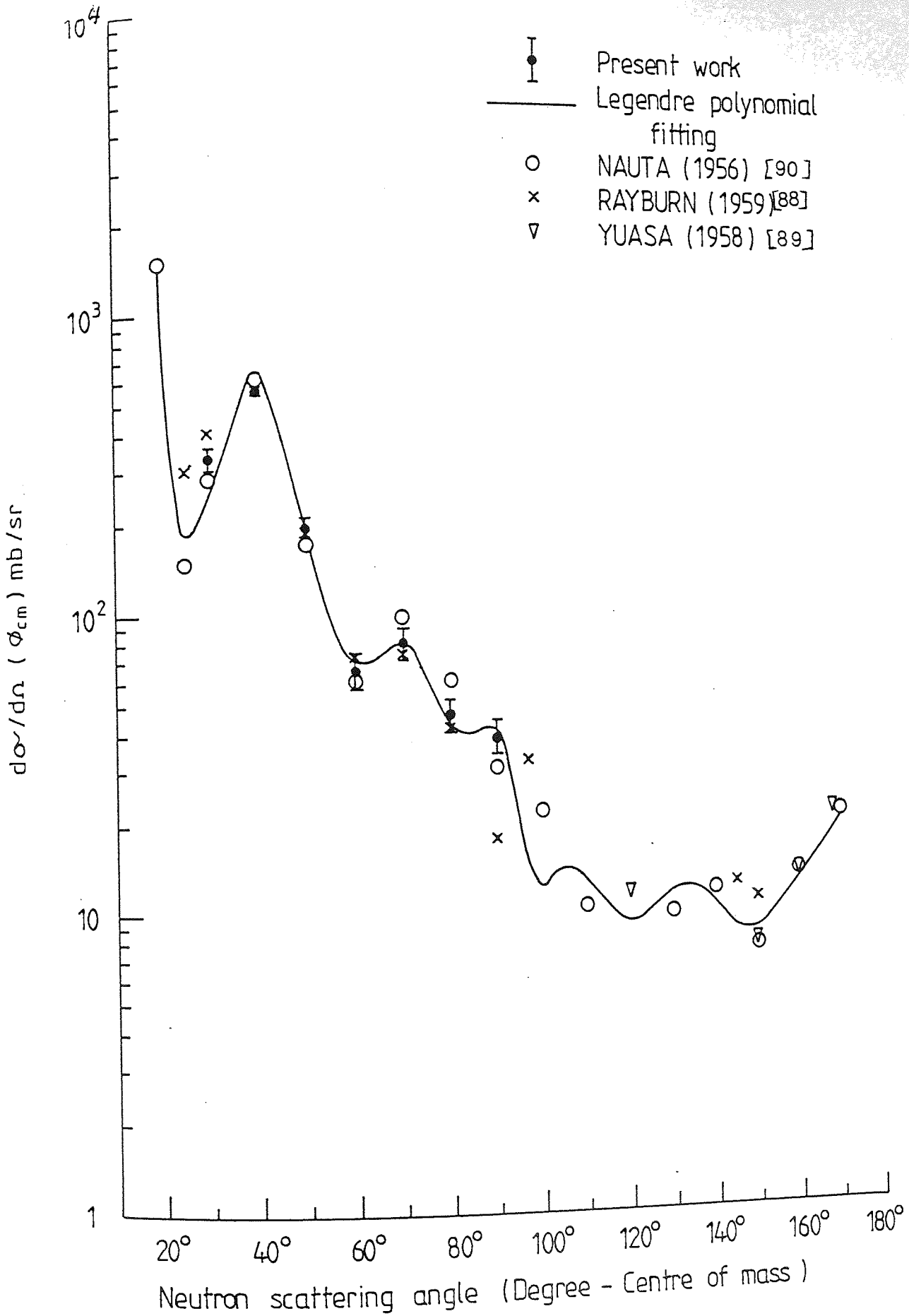

Figure 6·41 Elastic scattering angular distribution from the ground-state of Lead

Table(6·25)

UNIVERSAL CONSTANT FOR THE VARIATION OF THE $\frac{d\sigma}{d\Omega}$ vs SAMPLE THICKNESS { EQUATION (6.1)}

AUTHOR	α_{uni}(mfp)	REACTION	SAMPLES
PRESENT WORK	Ø.35±Ø.26	(n,n) , (n,n')	Lithium , Lead
AL-SHALIBI [80]	Ø.31±Ø.2Ø	(n,n'γ)	Iron , Concrete
ANVARIAN [81]	Ø.33±Ø.22	(n,n)	Iron , Concrete

6.11 THIN SAMPLE RESULTS

6.11.1 ANGULAR DISTRIBUTION OF THE ELASTIC SCATTERING CROSS SECTION

The experimental results for the differential elastic scattering cross- sections for a thin sample of lead are presented in fig(6.41) . The results are in agreement with the experimental data obtained by NAUTA (1956) [90] , RAYBURN (1959) [88] AND YUASA (1958) [89] at forward angles .

The data have been converted to the CM-system (equation(5.7)) and are presented in table (6.26) . In fig (6.41) the smooth line through the distribution is the result of fitting the data to the Legendre Polynomial series . Using the data of NAUTA (1956) [90] and YUASA (1958) [89] for scattering angles greater than 9Ø° in CM-system , a thirteen order series was found most acceptable (i.e. χ^2_ν=Ø.1) for fitting the elastic scattering cross-section .The values of the (f_l) coefficients from the present work are given in table (6.27) together with the ENDF/B-IV [91] published data .

Table (6.26)

LEAD DIFFERENTIAL ELASTIC SCATTERING

CROSS-SECTION FOR THE THIN SAMPLE

θ_{cm} (Deg)	PRESENT WORK (mb/s)	NAUTA [90] (mb/s)	RAYBURN [88] (mb/s)
20°	–	1526 ± 82	1500
25° 7′	–	149 ± 18	300
30° 8′	329 ± 28	294 ± 30	400
40° 10′	560 ± 35	604 ± 30	560 ± 55
50° 12′	194 ± 14	174 ± 30	190 ± 20
60° 14′	65 ± 10	60 ± 26	74 ± 8
70° 15′	79 ± 11	98 ± 23	74 ± 7
80° 16′	46 ± 6	60 ± 21	42 ± 6
90° 16′	40 ± 5	32 ± 23	18

Table (6.27)

LEGENDRE POLYNOMIAL COEFFICIENTS OBTAINED FROM FITS TO THE LEAD ELASTIC SCATTERING ANGULAR DISTRIBUTIONS AT 14 Mev NEUTRON ENERGY

f_l	PRESENT WORK	ENDF/IV [91]
f_0	1 ± Ø.ØØ2	1
f_1	Ø.826 ± Ø.ØØ4	Ø.8ØØ
f_2	Ø.658 ± Ø.ØØ8	Ø.618
f_3	Ø.524 ± Ø.Ø1Ø	Ø.476
f_4	Ø.436 ± Ø.Ø1Ø	Ø.397
f_5	Ø.369 ± Ø.Ø1Ø	Ø.343
f_6	Ø.325 ± Ø.ØØ8	Ø.312
f_7	Ø.294 ± Ø.ØØ6	Ø.286
f_8	Ø.269 ± Ø.ØØ4	Ø.264
f_9	Ø.233 ± Ø.ØØ4	Ø.237
f_{10}	Ø.183 ± Ø.ØØ3	Ø.195
f_{11}	Ø.125 ± Ø.ØØ2	Ø.122
f_{12}	Ø.Ø67 ± Ø.ØØ2	Ø.Ø54
f_{13}	Ø.Ø23 ± Ø.ØØ1	Ø.Ø13
INTEGRATED ELASTIC SCATTERING (Barns)	2.95 ± Ø.12	2.9

The maximum value of the coefficients (lmax) was chosen in the same way as described in section (6.5) , where the Wick's limit for setting the lower limit of the differential elastic scattering cross-section in the forward direction was obtained from equation (6.6) ; yielding σ_W= 11.8 ± Ø.8 barns . This agrees with COON et al(1958) [93] who found in practic , from the analysis of neutron scattering , that the differential cross-section in the forward direction has its limiting value within a few percent of the Wick's limit .

By applying the values of f_l , σ_t and σ_{int} data of ENDF-B-IV [91] { table (6.27) } , one obtains $\frac{d\sigma}{d\Omega}(0^\circ)$ = 9.957 barns , which disagrees markedly with Wick's limit by 15.2% { i.e. $\frac{d\sigma}{d\Omega}(\phi_{cm}=0) < \sigma_W$ (see equation(6.6) } . The integrated elastic scattering was obtained from the best fits to the experimental data and applying equation (6.8) . The results are shown in table (6.27) where they are compared with ENDF-B/IV [91] data .

6.11 .2 INELASTIC SCATTERING CROSS-SECTION

The differential inelastic scattering cross-section for 14 Mev neutrons from the excited 2.61 Mev and 4.1 Mev states are shown in tables (6.28) and (6.3Ø) .

As before the experimental yields of the inelastic scattering in Pb at 2.6 Mev and 4.1 Mev were calculated by fitting the peaks of interest with the Gaussian program (Appendix B) . The experimental measurements for the thin sample $\frac{d\sigma}{d\Omega}(\phi)\Big|_{t=0}$ and their comparison with those of STELSON (1962) [92] are shown in fig (6.42) . The uncertainties shown are the random statistical errors described in table (6.18) .

The results of the present work for 80° and 90° scattering angles are higher than that of STELSON (1958) [92] , possibly because of contributions from inelastic scattering of neighboring excited states in the lead . A further difference is that STELSON used ring geometry rather than the flat plate geometry used here .

Fig (6.42) shows the data fitted to the Legendre Polynomials (equation (6.1)) .The polynomial coefficients and the integrated cross-sections are listed in tables (6.29) and (6.31) for both excited states .

6.11.3 DIFFERENTIAL CROSS-SECTION FOR SET NEUTRON ENERGY RANGES

The measured angular distributions for the neutron non-elastic scattering (n,n') , (n,2n) and the different energy intervals are shown in fig(6.43) for scattering angles between 30° and 90° . The solid line represent a Legendre Polynomial fit of the experimental data points for even order terms in the polynomial in accordance with the predictions of the statistical model of the nucleus .

No similar measurements were found in the published literature and ; hence , it was not possible to compare the present results with the work of others .Since writing results for 40°, 60°, and 90° has been found ***) . The integrated cross-section for each energy group from the lead samples were fitted to equation (6.2) to find $(\sigma_{int})_{t=0}$ and the results are shown in table (6.33) together with the polynomial coefficients .

***) AKADEMIE DER WISSENSCHAFTEN DER DDR
ZENTRAL INSTITUT FÜR KERNFORSCHUNG ROSSENDORF BEI DRESDEN
ZfK - 227 (Ü) August (1975)
Dietrich Hermsdorf et al

Table (6.28)

DIFFERENTIAL INELASTIC SCATTERING CROSS-SECTION

FOR THE EXCITED STATE 4.1 Mev IN LEAD

ϕ_{cm} (Deg)	PRESENT WORK (mb/s)	ϕ_{cm} (Deg)	STELSON [92] (mb/s)
30° 8′	10.7 ± 2.3	31° 48′	9.5 ± 2.0
40° 10′	5.5 ± 0.5	38° 24′	8.7 ± 2.0
50° 12′	8.9 ± 2.0	50° 24′	7.0 ± 1.5
60° 14′	5.7 ± 1.2	58° 5′	8.0 ± 1.0
70° 15′	6.7 ± 2.0	70° 19′	5.2 ± 1.0
80° 16′	12.0 ± 3.1	80° 24′	4.5 ± 1.0
90° 16′	9.2 ± 2.4	90°	4.8 ± 1.2

Table (6.29)

LEGENDRE POLYNOMIAL COEFFICIENTS AND INTEGRATED INELASTC

SCATTERING OBTAINED FROM FITS TO THE EXCITED STATE Q=-4.1 Mev IN LEAD

$\sigma_{int}(E)$ (mb/s)	f_0	f_1	f_2	χ^2_ν
49 ± 16	1±0.321	0.61±0.02	-(0.28±0.06)	1.1

Table (6.3Ø)

DIFFERENTIAL INELASTIC SCATTERING CROSS-SECTION

FOR THE EXCITED STATE 2.6 Mev IN LEAD

ϕ_{cm} (Deg)	PRESENT WORK (mb/s)	ϕ_{cm} (Deg)	STELSON [92] (mb/s)
3Ø° 8′	8.6 ± 2.2	2Ø° 24′	1Ø.Ø ± 2.Ø
4Ø° 1Ø′	6.7 ± 1.3	38° 24′	6.2 ± 1.3
5Ø° 12′	7.6 ± 1.7	5Ø° 24′	7.Ø ± 1.Ø
6Ø° 14′	8.4 ± 2.1	58° 5′	8.Ø ± 1.3
7Ø° 15′	3.7 ± Ø.8	7Ø° 19′	5.Ø ± Ø.8
8Ø° 16′	1Ø.7 ± 2.5	8Ø° 24′	5.3 ± Ø.9
9Ø° 16′	7.5 ± 2.Ø	9Ø°	3.2 ± Ø.5
		112° 48′	2.1 ± Ø.5
–	–	121° 12′	2.2 ± Ø.4
–	–		

Table (6.31)

LEDENDRE POLYNOMIAL COEFFICIENTS AND INTEGRATED INELASTIC SCATTERING OBTAINED FROM FITS THE EXCITED STATE Q = -2.6 Mev IN LEAD

$\sigma_{int}(E)$ (mb/s)	f_0	f_1	f_2	X_ν^2
56 ± 9	1 ± Ø.169	Ø.374±Ø.Ø54	-(Ø.Ø4±Ø.Ø6)	Ø.8

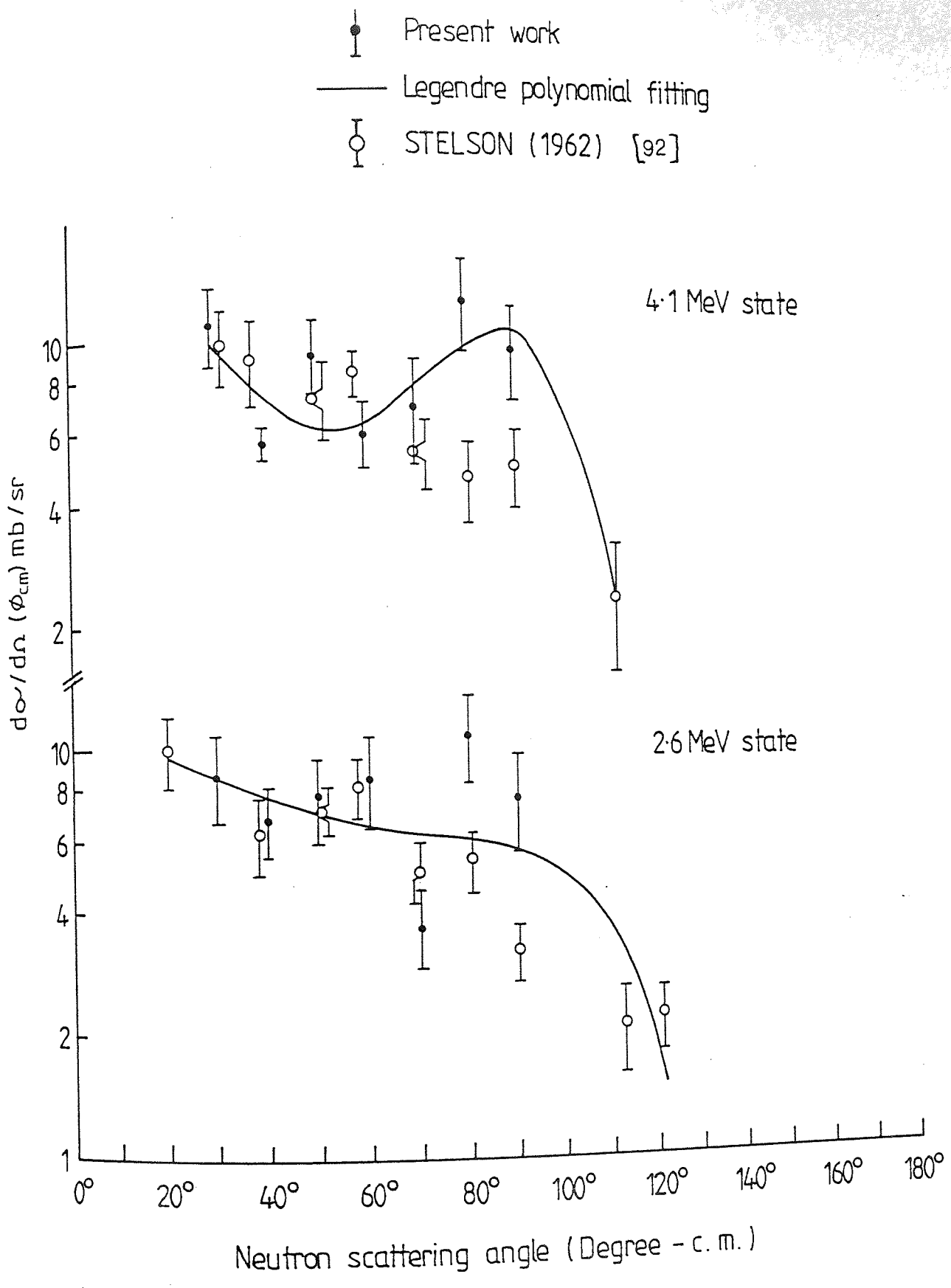

Figure 6·42 Inelastic scattering angular distributions from the excited states 2·6 MeV and 4·1 MeV in Lead.

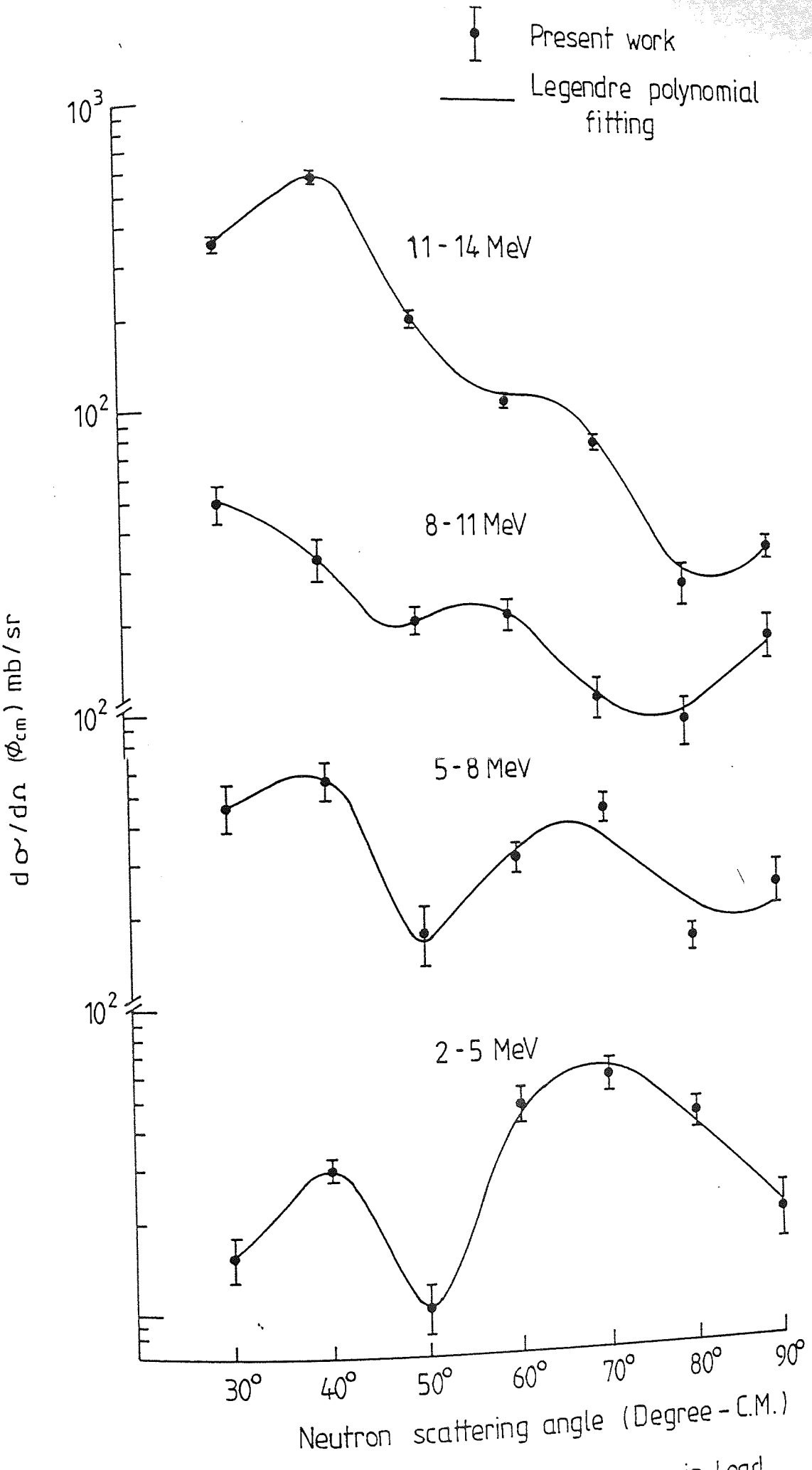

Figure 6.43 Angular distributions for the energy groups in Lead.

Table (6.32)

DIFFERENTIAL SCATTERING CROSS-SECTION FOR ENERGY RANGES 11-14 Mev , 8-11 Mev , 5-8 Mev , AND 2-5 Mev FOR A THIN SAMPLE OF LEAD

θ_{cm} (Deg)	11-14 Mev (mb/s)	8-11 Mev (mb/s)	5-8 Mev (mb/s)	2-5 Mev (mb/s)
30°8′	338.0 ± 20	49.0 ± 7.1	46.0 ± 7.8	15.6 ± 2.6
40°10′	547.0 ± 25	32.0 ± 4.6	55.6 ± 8.2	30.1 ± 2.3
50°12′	192.2 ± 14	20.3 ± 3.2	17.4 ± 3.7	10.3 ± 2.0
60°14′	103.3 ± 5.1	20.7 ± 2.1	30.6 ± 3.6	47.5 ± 6.2
70°15′	76.2 ± 4.2	11.9 ± 1.7	43.1 ± 4.0	58.1 ± 6.7
80°16′	25.8 ± 4.1	9.3 ± 1.5	16.0 ± 1.7	42.1 ± 5.0
90°16′	34.6 ± 3.1	17.3 ± 2.9	23.5 ± 3.4	19.6 ± 4.1

Table (6.33)

LEGENDRE POLYNOMIAL COEFFICIENTS AND INTEGRATED CROSS - SECTION OBTAINED FROM FITS TO THE ENERGY LEVELS IN LEAD

E (Mev)	$\sigma_{int}(E)$ (mbarn)	f_0	f_2	f_4
11-14	2347 ± 71	1 ± 0.03	0.65 ± 0.01	0.05 ± 0.01
8-11	310 ± 26	1 ± 0.08	0.49 ± 0.05	0.13 ± 0.05
5-8	391 ± 29	1 ± 0.07	0.29 ± 0.05	0.09 ± 0.04
2-5	301 ± 24	1 ± 0.07	-(0.18± 0.05)	0.03 ± 0.01

CHAPTER SEVEN

COMPARISON OF THE RESULTS AND THE THEORY

CHAPTER SEVEN

COMPARISON OF THE RESULTS WITH THEORY

7.1 OPTICAL MODEL

Differential elastic scattering cross-sections for neutrons scattered from the thin samples of Lithium and Lead have been analyzed using the optical model of the nucleus . The main objective of this analysis was to explore the possibility of finding a set of optical parameters that would reproduce the general features of neutron scattering from light and heavy nuclei . In addition , the optical model can describe the average properties of nuclear scattering both with respect to the energy of the incident partical and the mass of the target .

The optical model potential for interactions between the incident neutron and the target nucleus was assumed to have the usual form :

$$U_{op}(r) = V_R(r) + iW_v(r).f(r) + iW_D.g(r) - U_s.\frac{1}{r}\frac{df}{dr}(\sigma.I) \quad (7.1)$$

Where V_R , W_v , W_D and U_s are the real , imaginary volume , imaginary surface derivative and spin-orbit potential depths respectively ;

$$f(r) = [\ 1 + \exp(r - r_0.A^{\frac{1}{3}})\ /\ a\ ]^{-1}$$

is the WOOD-SAXON form factor with radius (r_0) and diffuseness (a) ; $g(r) = -4af'(r)$ is its normalized radial derivative ; $U_s = (V_s + iW_s)(\frac{\hbar}{m_\pi c})^2$ is the spin-orbit potential depth real and imaginary terms Vs and Wi

; $(\frac{\hbar}{m_\pi c}) \simeq 2.\emptyset\emptyset$ (fm) ; and $\sigma.I$ is spin-orbit term , where the operator is defined in terms of the spin angular momentum (s) ($s=(\frac{h}{2})\sigma$) for the neutron and I the orbital angular momentum leading to the separation of the $j=j\pm\frac{1}{2}$ states in nuclei and the increase of this separation with I. In the absence of convincing evidence to the contrary , it is usual to take $Ws=\emptyset$, leaving the three parameters Vs , Rs and as[94] to be considered .

7.2 METHOD OF ANALYSIS

The optical model analysis was carried out using a search code called RAROMP [96] , which performs optical model calculations using both the reformulated optical model of GREENLEES , PYLE AND TANG (1974) [94] and the standard form of the optical model .The analysis of a particular set of experimental data is usually carried out with the initial values of the parameters taken from previous analyses of similar data . The results of this calculation are then compared with the experimental data and a measure of the reliabity of the fit defined and evaluated . The parameters of the potential [eq. (7.1)] are then systematically varied to optimise the χ^2-fit to the data ;

$$\chi^2/\text{ point} = N^{-1} \left\{ \frac{\sigma_T(\emptyset_i) - \sigma_E(\emptyset_i)}{\Delta\sigma_E(\emptyset_i)} \right\}^2 \qquad (7.2)$$

Where $\sigma_E(\emptyset_i)$ = the measured experimental differential cross-section in the centre-of mass-system .

$\sigma_T(\emptyset_i)$ = the theoretically predicted differential cross-section

$\Delta\sigma_E(\emptyset_i)$ = the error corresponding to the measured differential cross-section .

This is done automatically by the computer program RAROMP to obtain the optimum set of parameters defined by a particular potential corresponding to a particular data set .

7.3 OPTICAL MODEL ANALYSIS OF THE LITHIUM CROSS-SECTION

The optical model parameters of BECCHETTI and GREENLEES(1969)[96] were used as initial values to predict theortical cross-section values for Li . These parameters are given by :

VR	$v_R = 56.3 - 0.32E - 24.0\,(N-Z)/A$	(7.3)
RR	$r_R = 1.17$	(7.4)
AR	$a_R = 0.75$	(7.5)
WD	$w_d = 13.0 - 0.25E - 12.0(N-Z)/A$ OR ZERO	(7.6)
RD	$r_d = 1.26$	(7.7)
AD	$a_d = 0.58$	(7.8)
WV	$w_v = 0.22E - 1.56$ OR ZERO	(7.9)
RV	$r_v = 1.26$	(7.10)
AV	$a_v = 0.58$	(7.11)
VS	$v_s = 6.2$	(7.12)
RS	$r_s = 1.01$	(7.13)
AS	$a_s = 0.75$	(7.14)

Where all potenial strengths are in Mev , E is the incident neutron energy in Mev in the laboratory system and the radius (r) and diffuseness (a) are in Fermi (10^{-13} cm) .

With the optical model defined by equation (7.1) , it is possible to obtain a good over-all fit to the experimental data by systematic adjustment of the parameters given by equations (7.3)-(7.14) . The three energies defined by equations (7.3) , (7.6) and (7.9) were evaluated for an incident energy of 14 Mev giving by :

$$VR = 48.36 \text{ Mev} , \quad WV = 1.502 \text{ Mev} , \quad WD = 7.76 \text{ Mev} \tag{7.15}$$

With all geometrical parameters fixed at the starting values of BECCHETTI and GREENLEES ,these three were optimised using a search on VR,WD,WV,(1Ø) , giving :

$$VR = 48.38 \text{ Mev} , \quad WV = Ø.13 \text{ Mev} , \quad WD = 1Ø.96 \qquad (7.16)$$

As shown in fig (7.1) the fit given by these parameters is poor because the overal parameters are not suitable for describing light nuclei . In order to obtain a better fit , the parameters of BECCHETTI et al were systematically changed .

With the real radius parameter fixed at 1.17 fm , three searchs were executed using the real potential and surface absorption potential only , i.e VR,WD,RD,(6)/ VR,AR,WD,AD,(6)/VR,AR,WD,RD,(6) . The fit obtained is shown in fig (7.2) with χ^2/point =3.1 . The search gives a good fit to the experimental data . As the χ^2 per point was minimised for a reduced number of variable parameters ,the searches on VR,AR,WD,RD,(1Ø) , VR,AR,WD,AD,(1Ø) and VR,AR,WD,RD,AD,(1Ø) were used , resulting in a further improvement and χ^2 per point for each search were found to be 3.6 , 1.2 , and Ø.7 respectively . The fits obtained are shown in figs (7.3) , (7.4) and (7.5) .

The optimum parameter values obtained for lithium are listed in table (7.1) compared with the work of HOLLAND (1974) [97] .

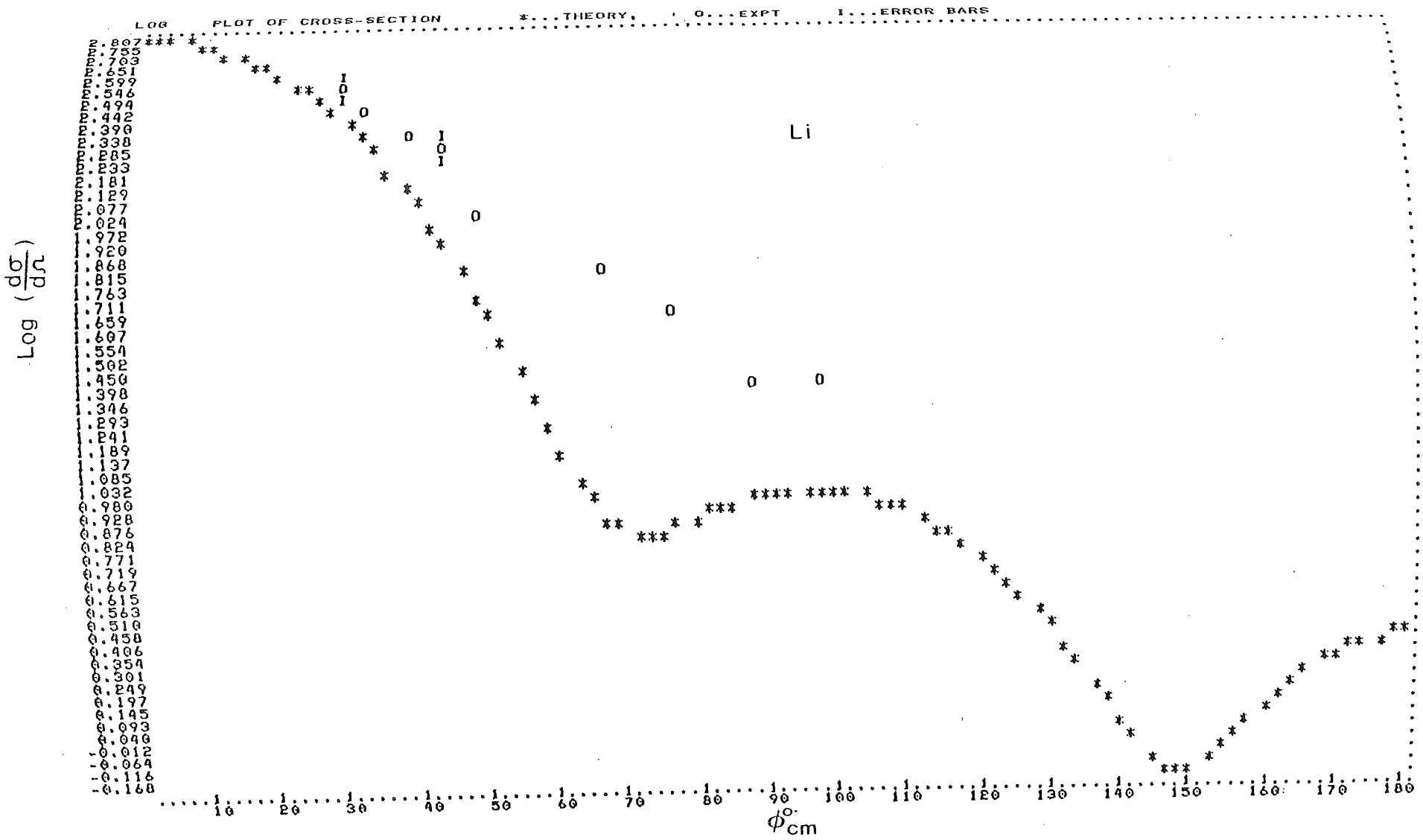

Fig (7.1) VR , WD , WV (1Ø) .

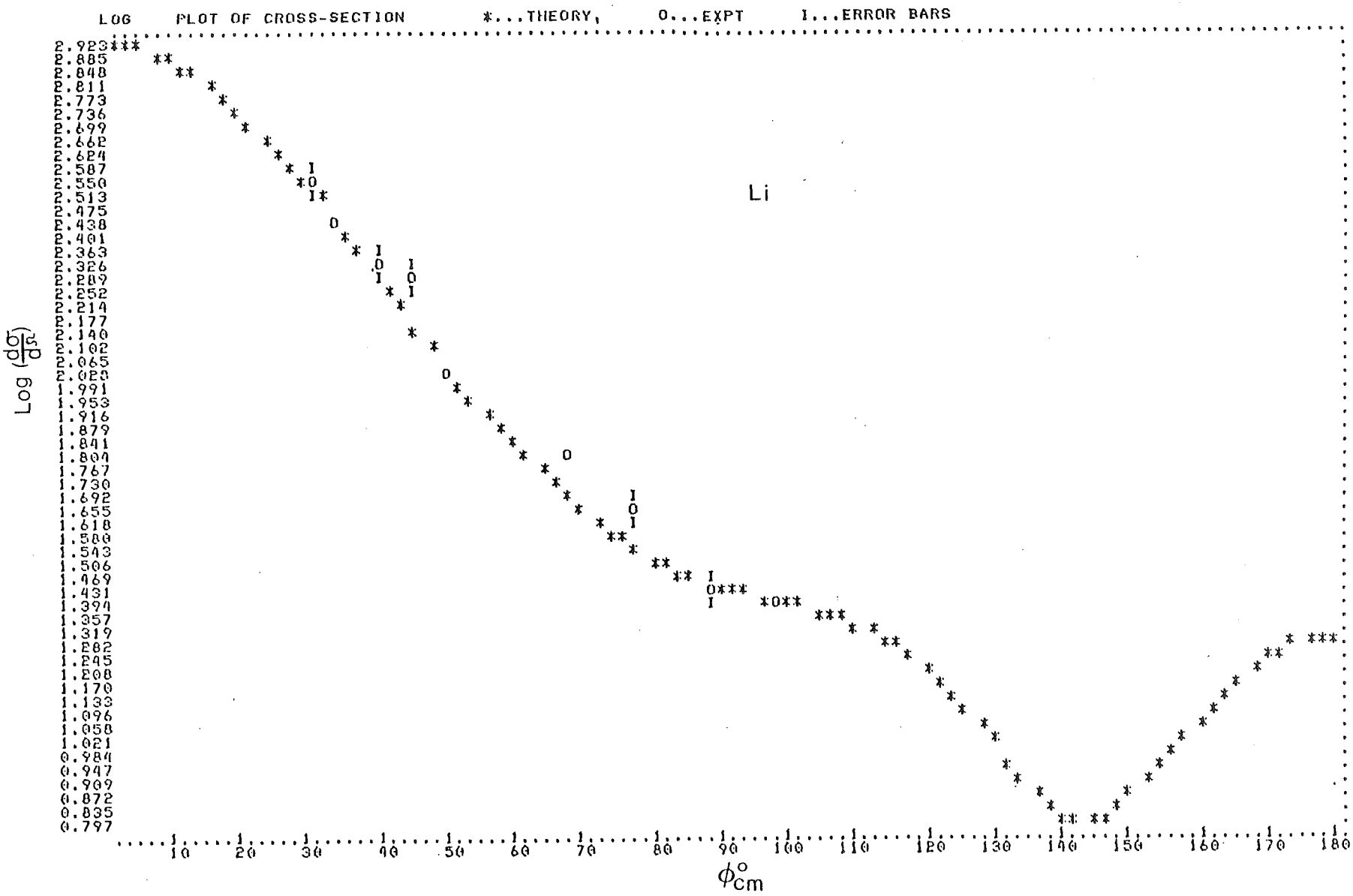

Fig (7.2) VR,WD,RD,(6)/VR,AR,WD,AD,(6)/VR,AR,WD,RD,(6)

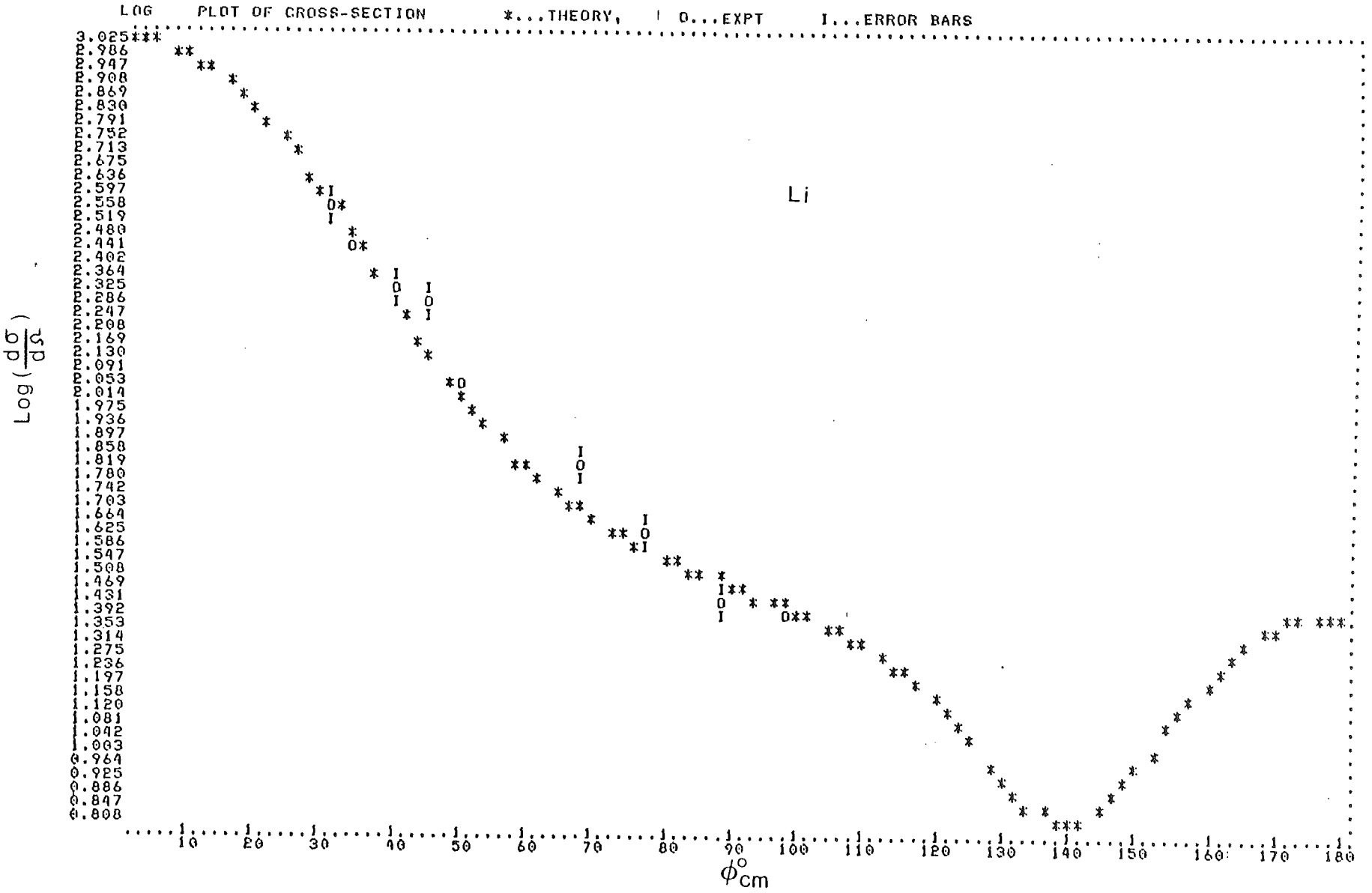

Fig (7.3) VR , AR , WD , RD , (1Ø)

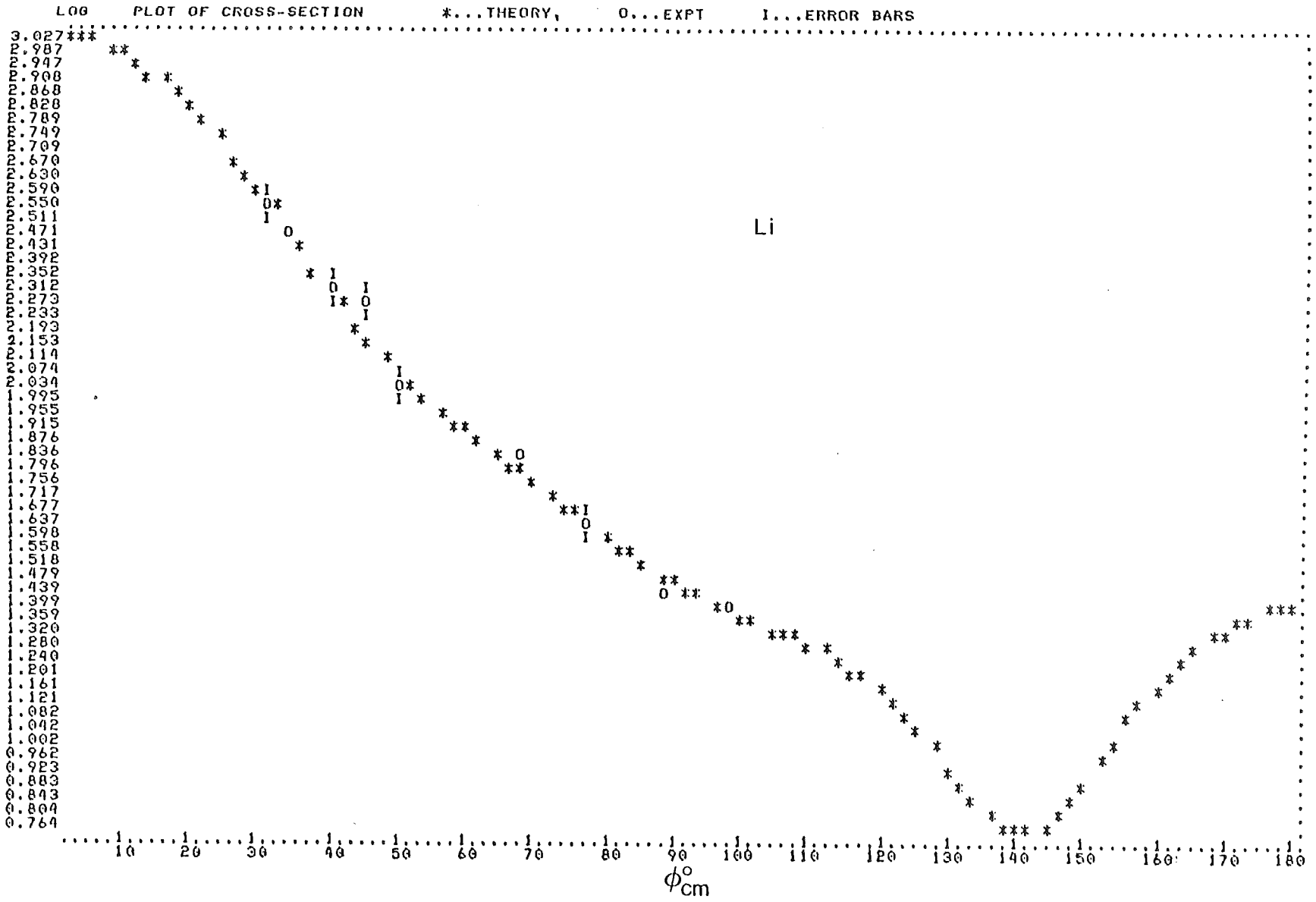

Fig (7.4) VR , AR , WD , AD , (1Ø)

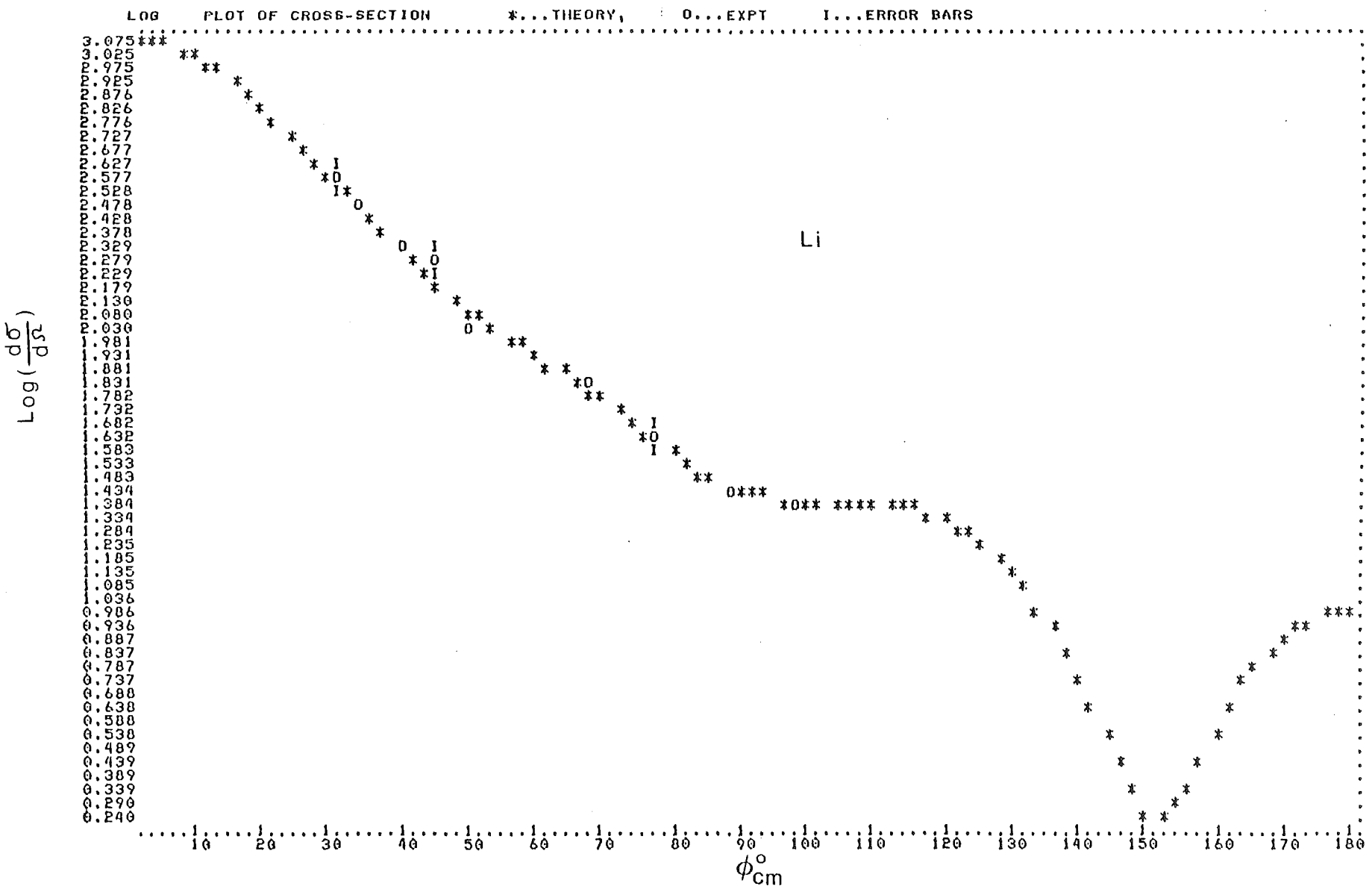

Fig (7.5) VR , AR , WD , RD , AD , (1Ø)

Table (7.1)

OPTICAL PARAMETERS USED TO FIT

LITHIUM ELASTIC SCATTERING DATA

PARAMETER	PRESENT WORK	HOLLAND etal
VR (Mev)	48.38	48.37
RR (fm)	1.424	1.356
AR (fm)	Ø.856	Ø.654
WD (Mev)	14.7ØØ	15.65Ø
RD (fm)	1.26Ø	1.278
AD (fm)	Ø.192	Ø.2ØØ
WV (Mev)	Ø.Ø5Ø	–
RV (fm)	1.26Ø	–
AV (fm)	Ø.58Ø	–
VS (Mev)	6.2ØØ	6.2
RS (fm)	1.Ø1	1.Ø1
AS (fm)	Ø.75	Ø.75
σ_R^{Th} (mb)	559.ØØ	473.3Ø
σ_R^{Ex} (mb)	453 ± 42	531 ± 1Ø2
χ^2 / point	<Ø.7	<Ø.3

7.4 OPTICAL MODEL ANALYSIS OF LEAD

The procedure for the analysis of the Lead differential cross-sections for 14.1 Mev was indentical to that used for Lithium . The values of three energy and $(\frac{N-Z}{A})$ dependent potentials using the the initial BECCHETTI and GREENLEES [96] parameters were :

$$VR = 46.783 \text{ Mev} , WV = 1.542 \text{ Mev} , WD = 6.972 \text{ Mev} \quad (7.17)$$

With all geometrical parameters kept constant at the starting values of BECCHETTI and GREENLEES , the potentials were optimised using the search VR,AR,WD,AD,(1Ø) .The optimum values were found to be :

$$VR = 44.84 \text{ Mev} , AR = Ø.915 \text{ fm} , WD = 5.33 \text{ Mev} , AD = Ø.487 \text{ fm} \quad (7.18)$$

The comparison between the experimental data and the theoretical predictions of the optical model is shown in fig (7.6) .The agreement obtained yielded χ^2 per point equal to Ø.2 .

With the volume absorption parameters fixed using equations (7.9) , (7.1Ø) and (7.11) , three searches were then executed at the same time using the real and surface absorption parameters only ie. , VR,AR,WD,RD,(6)/WD,AD,(6)/VR,AR,WD,RD,(6). The fit obtained is shown in fig (7.7) which gives good agreement between the theoretical and experimental results with a χ^2 per point of Ø.1 .

These optimum parameter values obtained for Lead in the present work are listed table (7.2) .

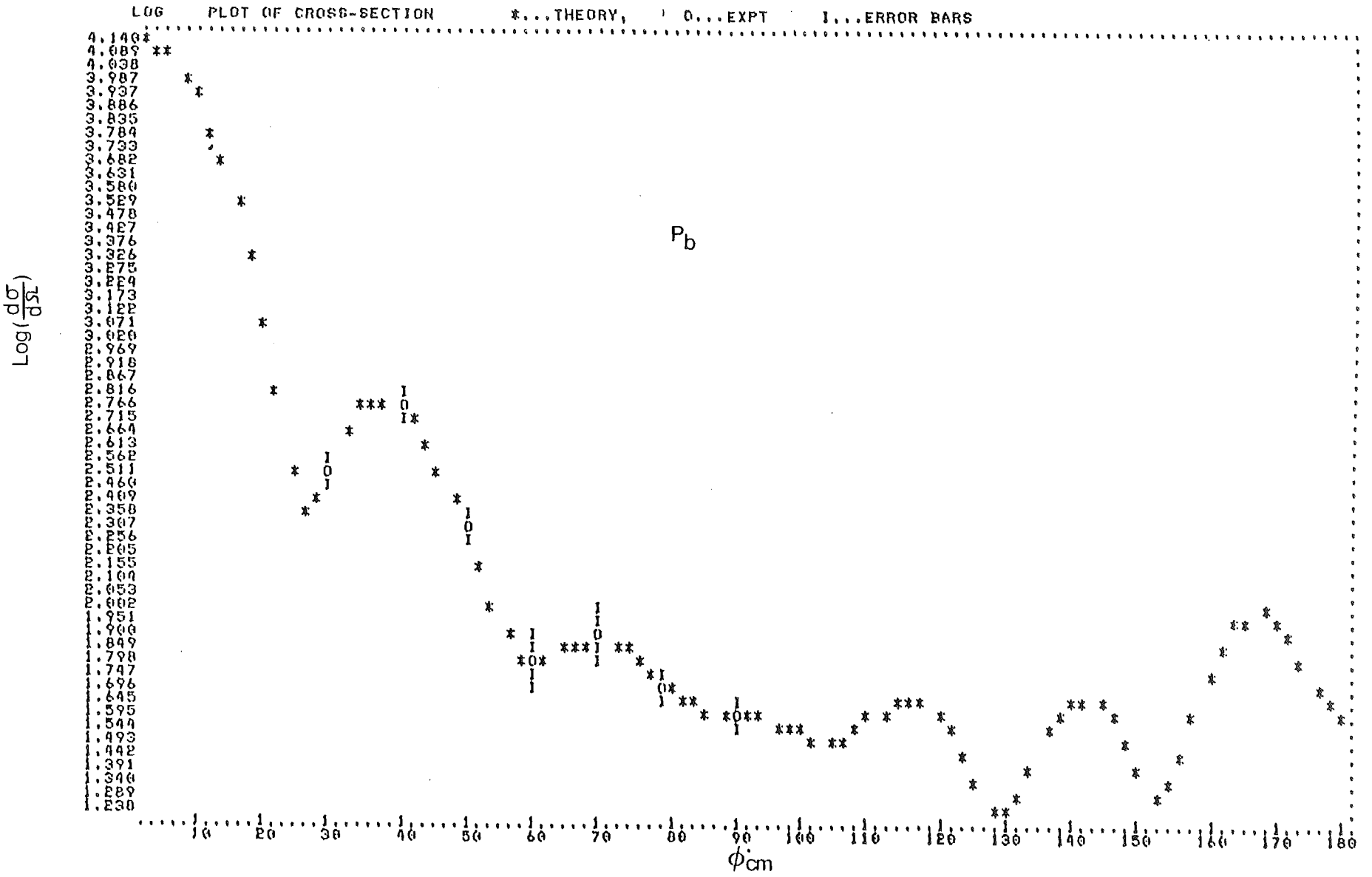

Fig (7.6) VR , AR , WD , AD , (1Ø)

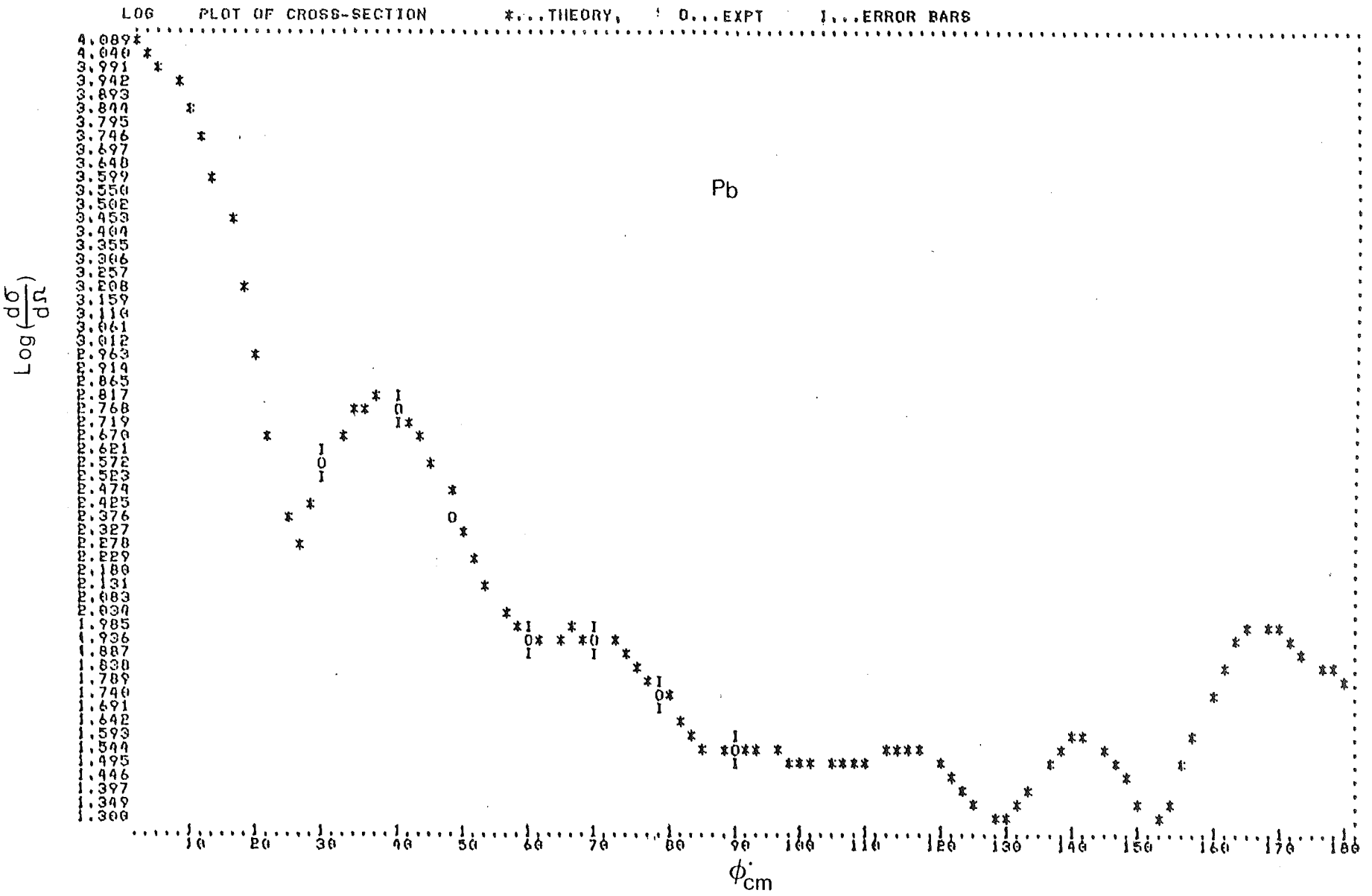

Fig (7.7) VR,AR,WD,RD,(6)/WD,AD,(6)/VR,AR,WD,RD,(6)

Table (7.2)

OPTICAL MODEL PARAMETERS USED TO

FIT LEAD ELASTIC SCATTERING DATA

PARAMETERS	PRESENT WORK	BJORKLUND etal [98] **
VR (Mev)	44.84	44.ØØ
RR (fm)	1.17	1.25
AR (fm)	Ø.915	Ø.65
WD (Mev)	5.33	11.ØØ
RD (fm)	1.189	1.25
AD (fm)	Ø.487	Ø.98
WV (Mev)	Ø.Ø5	–
RV (fm)	1.26	–
AV (fm)	Ø.58	–
VS (Mev)	6.2	8.3
RS (fm)	1.Ø1	1.25
AS (fm)	Ø.75	Ø.65
σ_R^{Th} (mb)	2.22	–
σ_R^{E} (mb)	2.45±Ø.13	–
χ^2/point	<Ø.2	–

** THEORETICAL RESULTS OF ^{208}Pb only .

7.5 THE CALCULATION PROCEDURE BASED ON THE CONTINUOUS SLOWING DOWN MODEL

The experimental results of neutrons scattered from different thickness of lithium and lead samples , were compared with the predictions of the Fermi Age Theory . This theory is based upon the continuous slowing down density , which states [99-101] that in each collision with a moderating nucleus a neutron losses an amount of energy characterized by the logarithmic energy decrement (ξ).This is the average for all collisions of $\ln E_1 - \ln E_2$,

and $$\xi = 1 - \frac{(A-1)^2}{2A} \ln\left\{\frac{A+1}{A-1}\right\} \qquad (7.20)$$

here E is the energy of the neutron before , E is that after a collision and A is the atomic mass of the scattering sample .

In the present analysis it is assumed for simplicity that :

(i) The scattering sample consists of a single nuclide .

(ii) The scattering is spherically symmetric in the centre-of-mass system .

(iii) Transport theory is valid at all energies .

(iv) The fast neutrons are produced from a source at a uniform rate.

One important aspect of the continuous slowing down density is the identification of the slowing down density [q(r,E)] which is the number of neutrons slowing down below a given energy E per unit time per unit volume . In this case the diffusion equation [51,102] can be written as :

$$\frac{D}{\xi \cdot \Sigma_s(E)} \nabla^2 q(r,E) + \frac{\partial q(r,E)}{\partial E} = \emptyset \qquad (7.21)$$

Where D = diffusion coefficient = $\frac{1}{3\Sigma_s(1-\bar{\mu})}$, $\bar{\mu} = \cos\theta_n$

ξ = the average logarithmic decrement per collision .

$\Sigma_s(E)$ = the macroscopic scattering cross-section at energy E .

and $q(r,E)$ = the slowing down density as a function of energy at the point r .

Introducing the continuous slowing down model and defining the Fermi Age :

$$\tau(E) = \int_E^{E_0} \frac{D}{\xi \cdot \Sigma_s(E)} \frac{dE}{E} \qquad (7.22)$$

Where E_0 is the energy of source neutron .

When the variable (E) is replaced by (τ) , equation (7.21) reduces to

$$\nabla^2 q(r,\tau) - \frac{\partial q(r,\tau)}{\partial \tau} = \emptyset \qquad r \neq \emptyset \qquad (7.23)$$

This is known as the Fermi Age equation which describes the spatial distribution of the slowing down density in a non-absorbing medium .

The neutron source can be considered as a planar source [see fig (5.1)] lying in the Y-Z plane at x = Ø and emitting (S) fast neutrons per cm^2/sec at the energy E_0. At the source , the age of the neutron is zero . Thus the first boundary condition is obtained ,i.e.

$$q(x,\emptyset) = S \cdot \delta(x) \qquad (7.24)$$

By assuming a product solution

$$q(x,\tau) = X(x) \cdot T(\tau) \qquad (7.25)$$

and substituting into the age equation (7.23)the general solution is obtained , i.e. :

$$q(x,\tau) = \frac{S}{\sqrt{4\pi\tau}} \cdot \exp(-x^2/4\tau) \qquad (7.26)$$

The neutron age (τ) was calculated for the neutron age between two known energies using equation (7.22).

In the present work the large scattering sample was notionally divided into slices of rectangualr shape with thickness Ø.5 cm . By applying equation (7.26) the slowing down density $q(x,\tau)$ was calculated for different neutron energies in the range Ø.1<En<14 Mev. The slowing down density from a unit point source in lithium sample {for example } as computed above is shown in fig (7.8) as a function of x for four values of τ { equation (7.22)} . As the age increases more neutrons have had an opportunity to slow down .

The sum of the slowing down density $q(x,\tau)$ after normalization gave the total number of the neutron which had been slowed down past a certain energy E in each slice of the sample .

After measuring the path length of the neutron for each slice of the sample and at certain scattering angle , the total number of neutrons of energy En incident onto the detector was determined from the equation :

$$N(\theta) = \frac{\sum_{i=1}^{m} q(x,\tau).\Delta\Omega.\xi(En).\{1-\exp(-\Sigma_t.\ t\ )\}\exp[-\Sigma_t.X(I)].\frac{d\sigma}{d\Omega}(\theta)}{\sigma_t\ .\ G} \qquad (7.27)$$

here $q(x,\tau)$ is the total number of neutrons from all slices of the sample of thickness t slowed down to a given energy from a source energy of 14 Mev , X(I) is the path length of the neutron in each slice of the sample ,the other parameters are defined in chapter five. The above procedure was written as a program called AGE shown at appendix D , where the Fermi Age τ , the slowing down density $q(x,\tau)$ and $N(\theta)$ are shown for different thicknesses of lithium and lead .The

variation of the total number of neutrons $N(\theta)$ with $(\dot{\theta}_L)$ for the lithium and lead is shown in figs (7.9) through to (7.17) . The same procedures were also used to calculate $N(\theta)$ versus (θ_L^o) for the neutrons scattered into given energy ranges from the lead samples which are shown in figs (7.18) through to (7.25) .

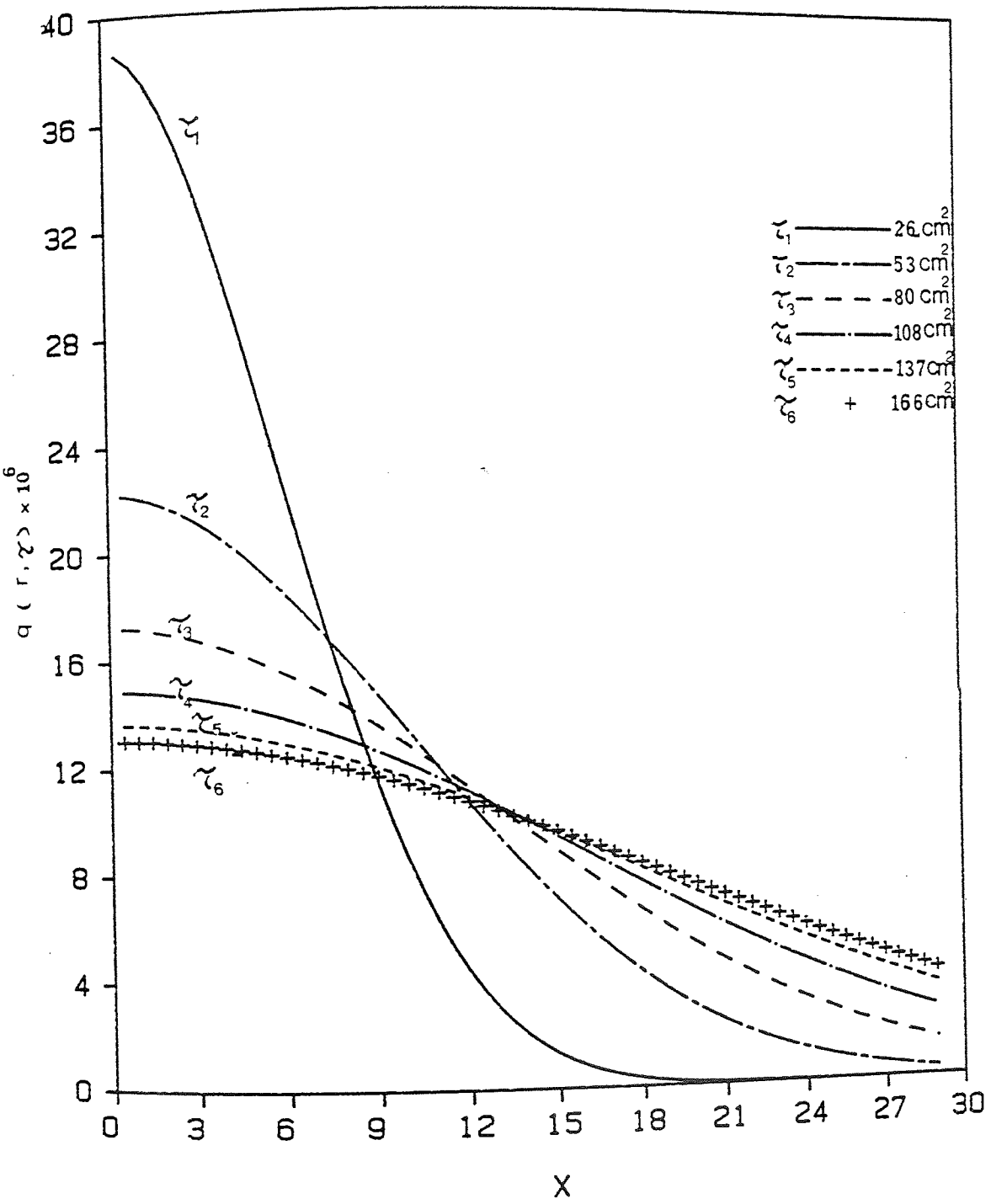

Fig (7.8) The slowing down density as a function of the distance from a unit point source of fast neutrons in Lithium sample for various values of age .

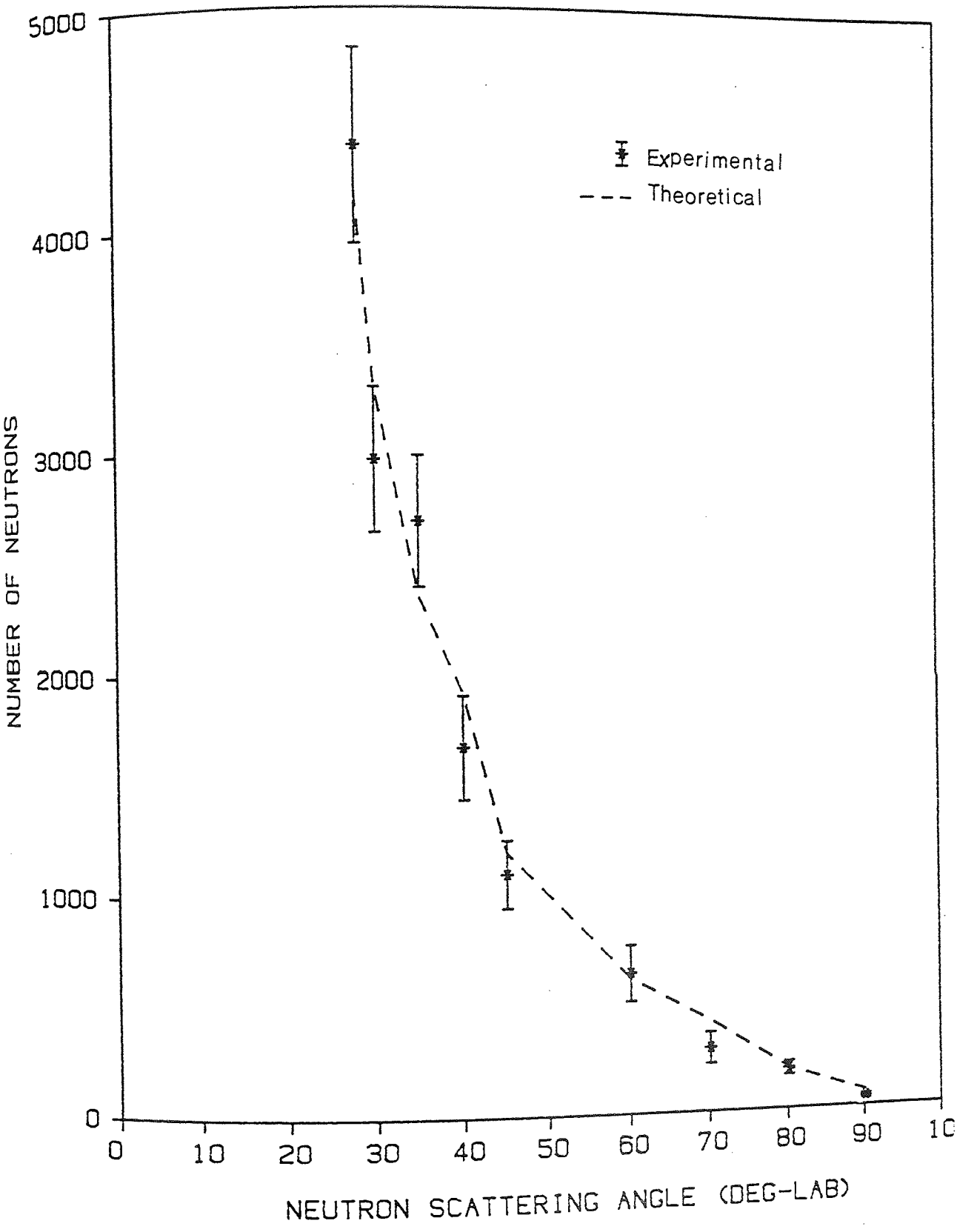

Fig (7.9) Comparison of the experimental measurement and theoretical calculation of the number of neutrons scattered from 2 cm thick Lithium sample (En = 14 Mev) .

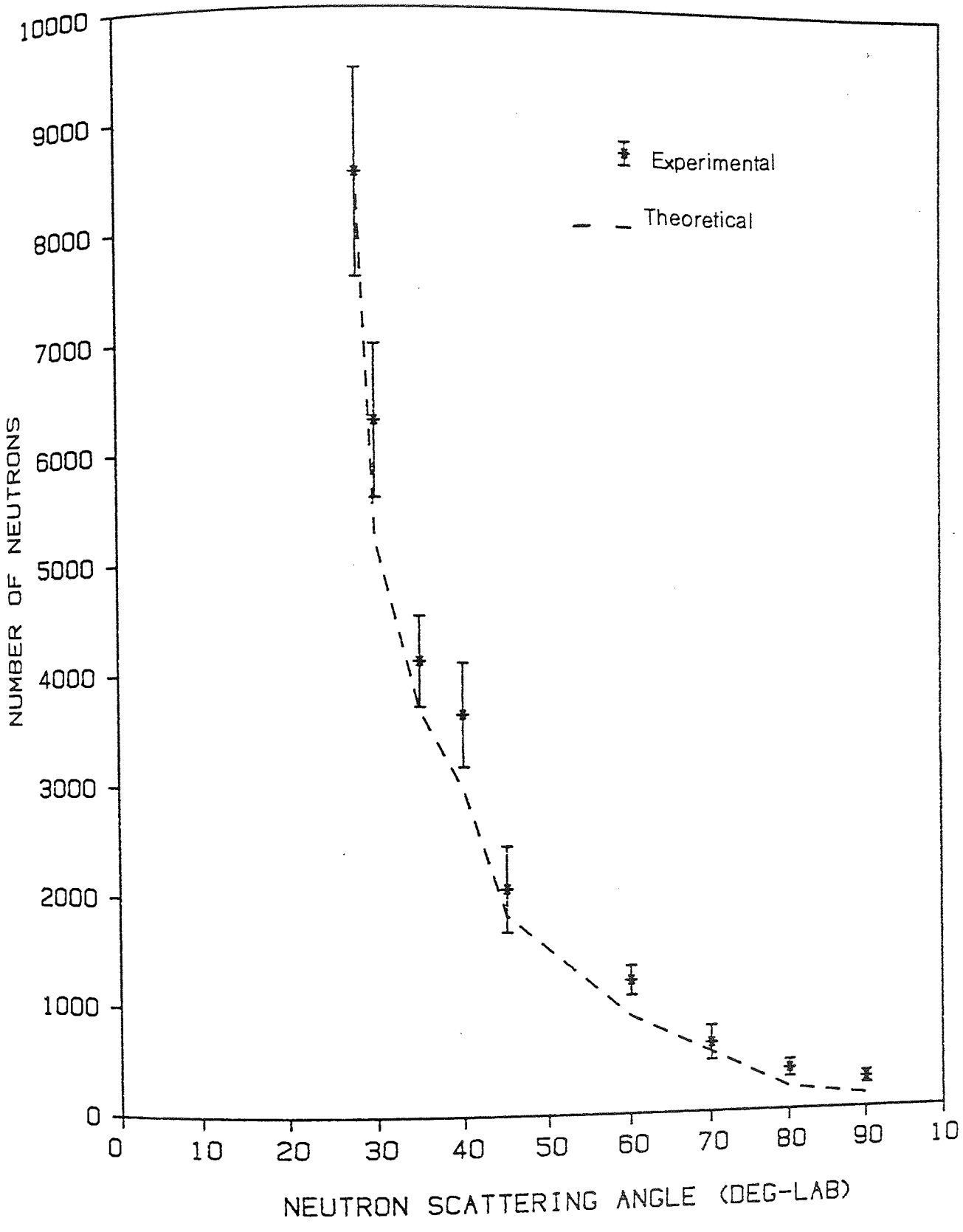

Fig (7.1Ø) Comparison of the experimental measurement and theoretical calculation of the number of neutrons scattered from 4 cm thick Lithium sample (En = 14 Mev) .

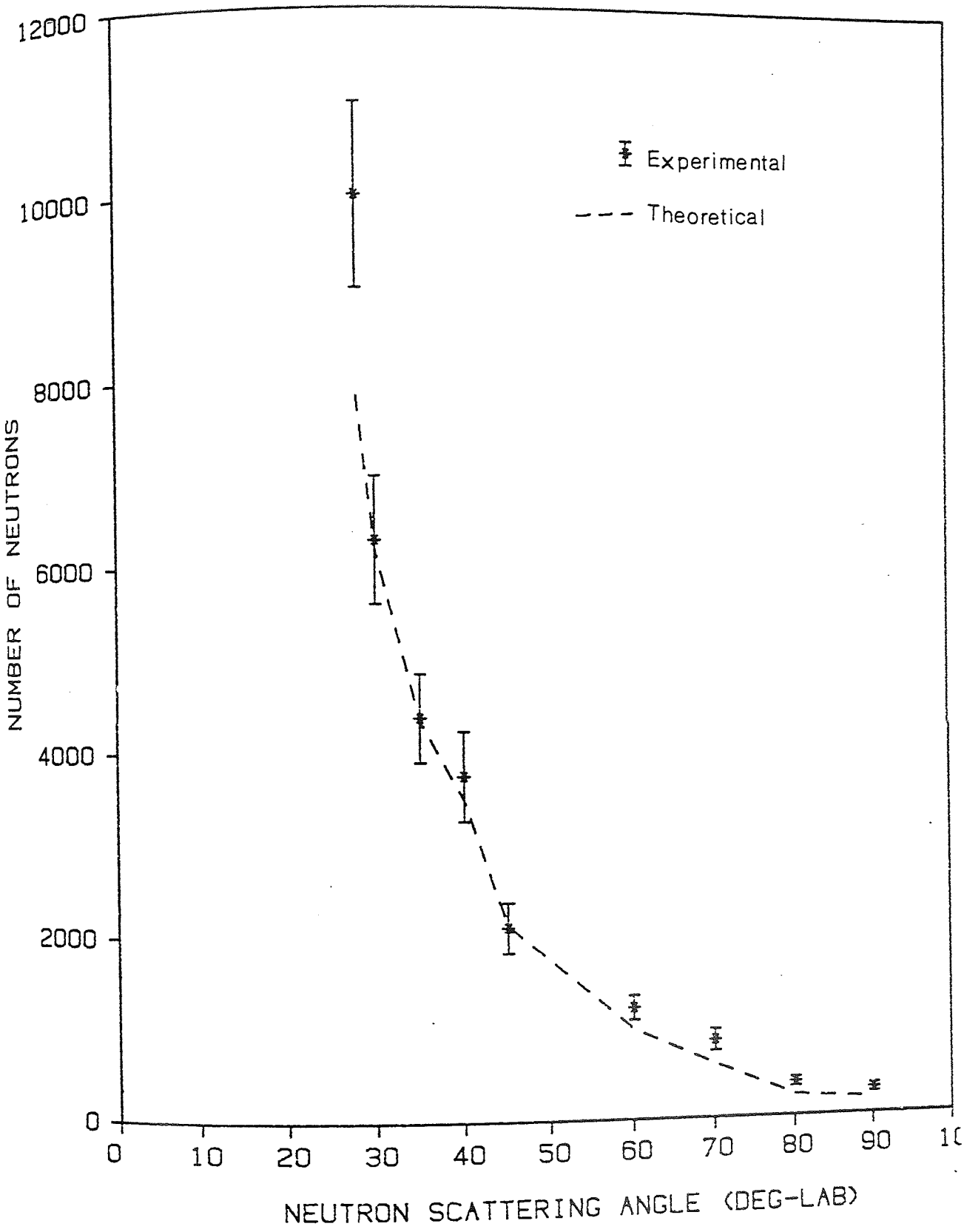

Fig (7.11) Comparison of the experimental measurement and theoretical calculation of the number of neutrons scattered from 6 cm thick Lithium sample (En = 14 Mev) .

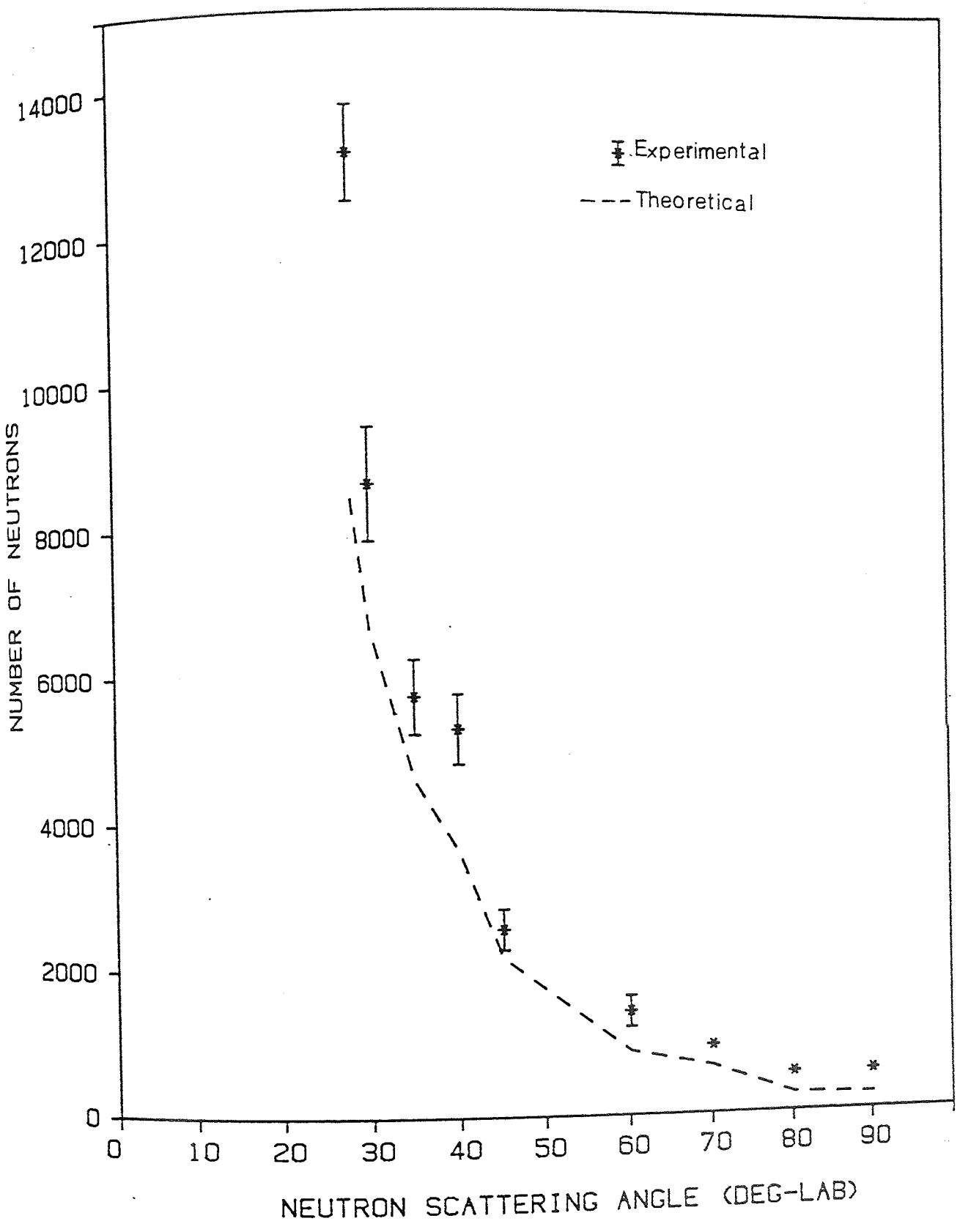

Fig (7.12) Comparison of the experimental measurement and theoretical calculation of the number of neutrons scattered from 9 cm thick Lithium sample (En = 14 Mev) .

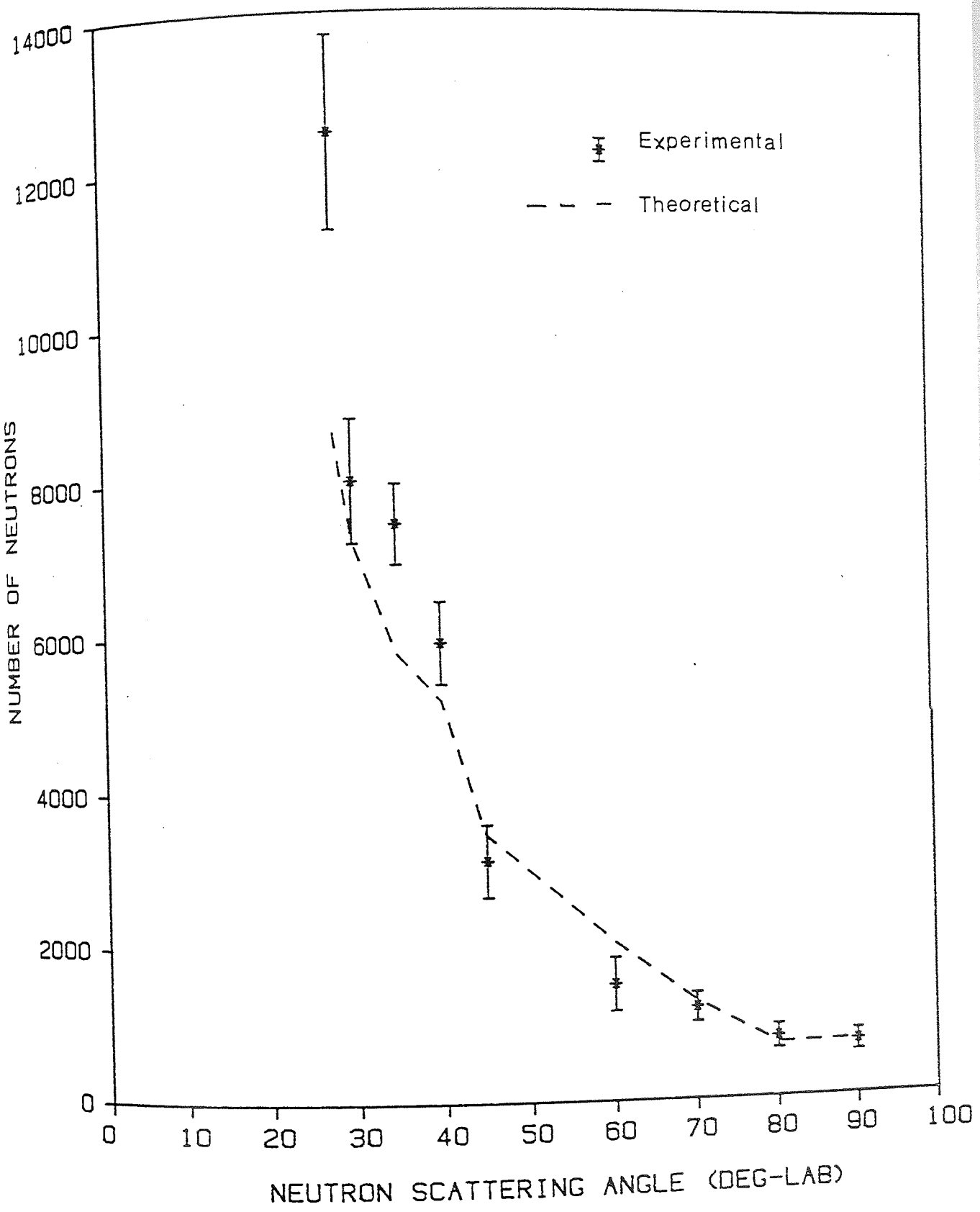

Fig (7.13) Comparison of the experimental measurement and theoretical calculation of the number of neutrons scattered from 13cm thick Lithium sample (En = 14 Mev) .

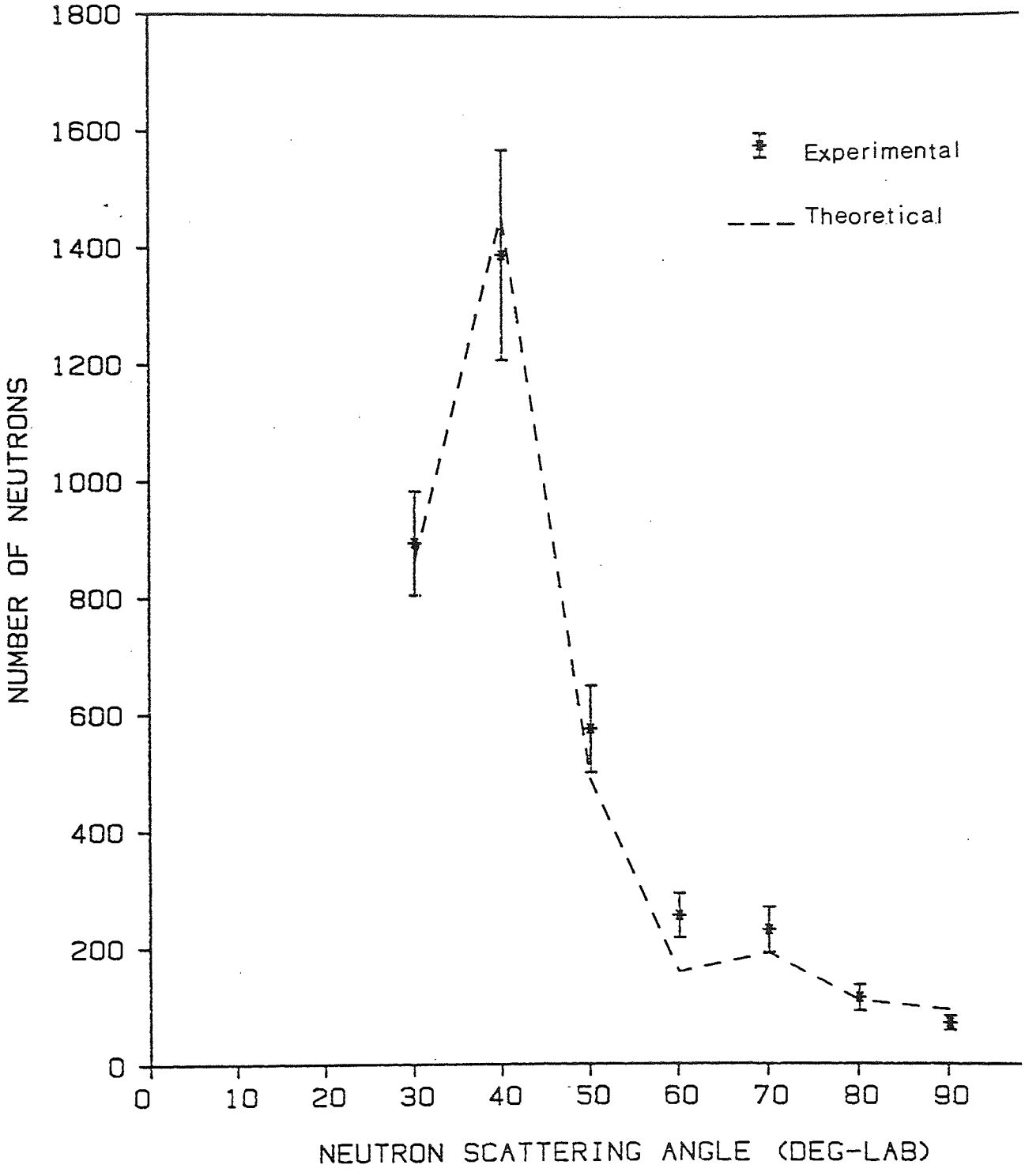

Fig (7.14) Comparison of the experimental measurement and theoretical calculation of the number of neutrons scattered from Ø.9 cm thick Lead sample (En = 14 Mev) .

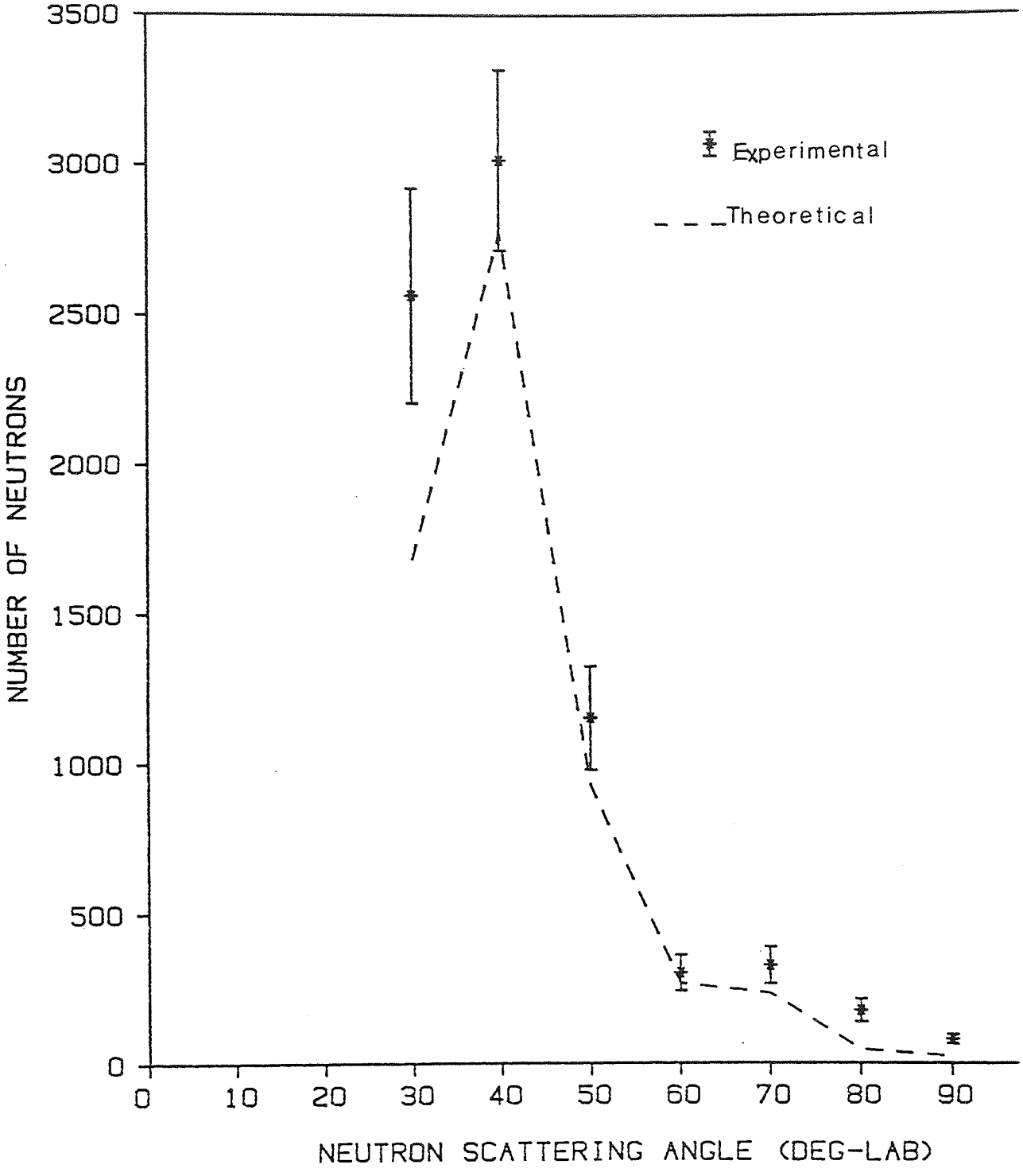

Fig (7.15) Comparison of the experimental measurement and theoretical calculation of the number of neutrons scattered from 3.2 cm thick Lead sample (En = 14 Mev) .

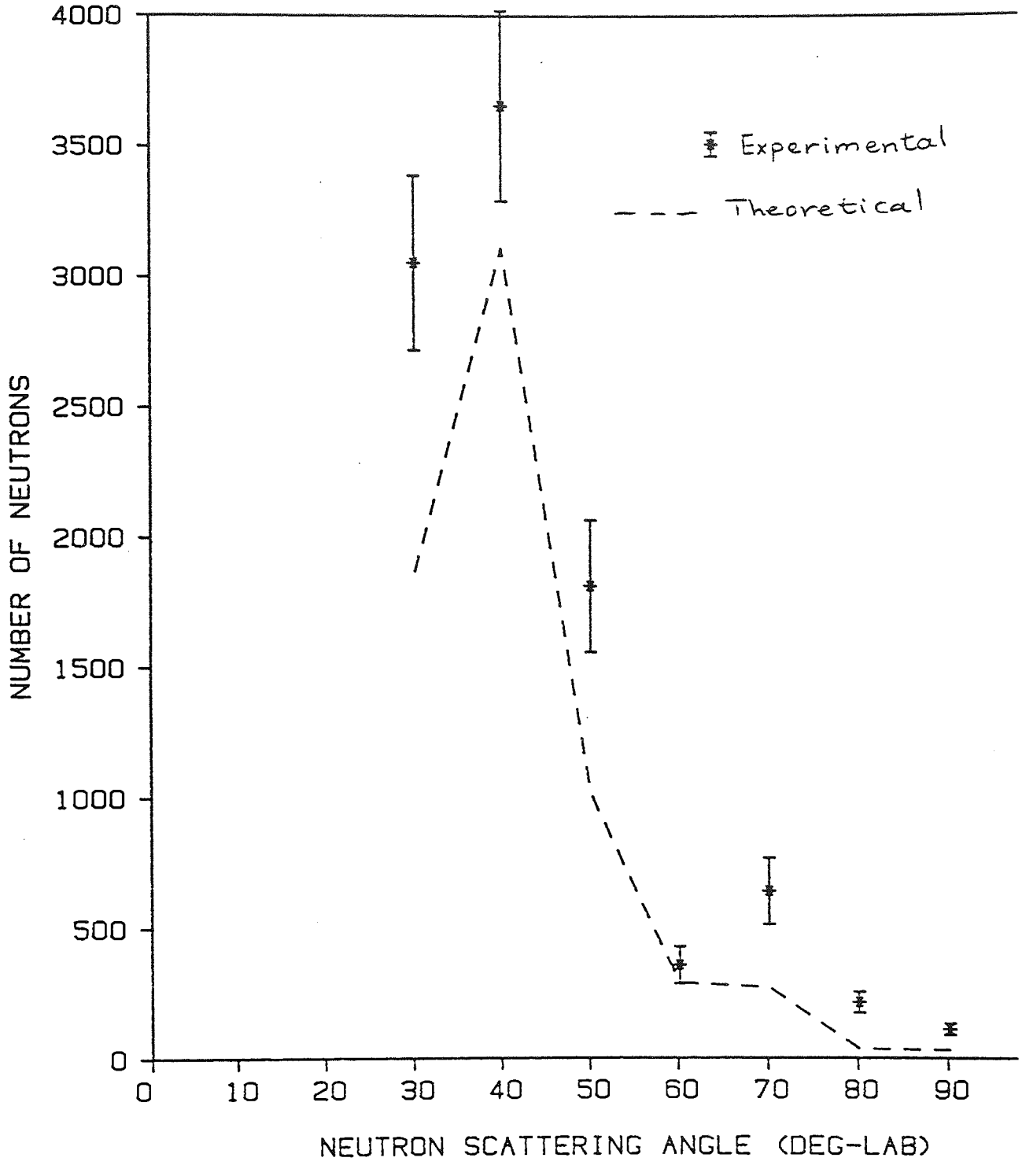

Fig (7.16) Comparison of the experimental measurement and theoretical calculation of the number of neutrons scattered from 5.0 cm thick Lead sample (En = 14 Mev) .

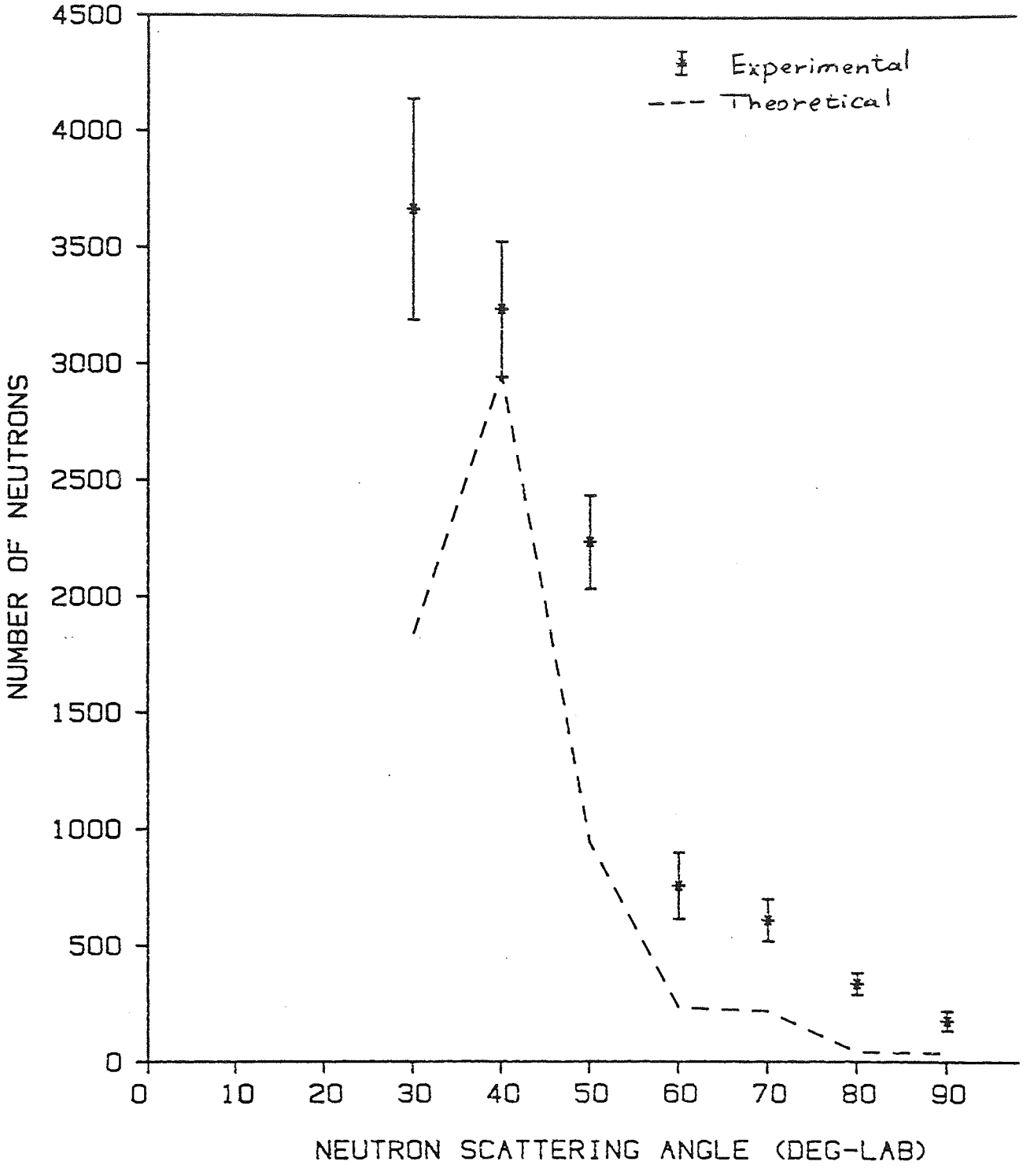

Fig (7.17) Comparison of the experimental measurement and theoretical calculation of the number of neutrons scattered from 7.5 cm thick Lead sample (En = 14 Mev) .

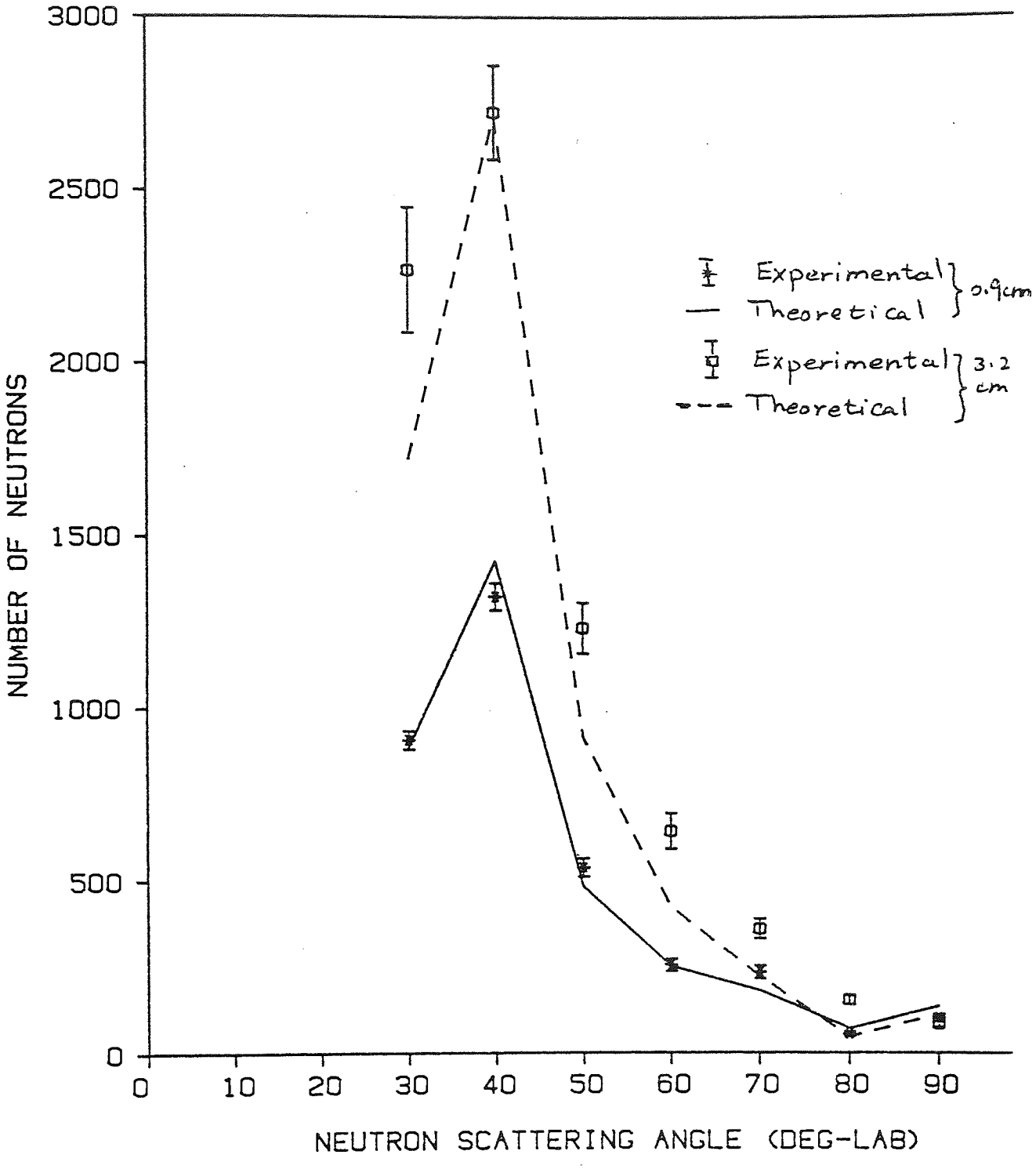

Fig (7.18) Comparison of the experimental measurement and theoretical calculation of the number of neutrons scattered from energy range 14 - 11 Mev in Lead samples of thickness Ø.9 cm and 3.2 cm .

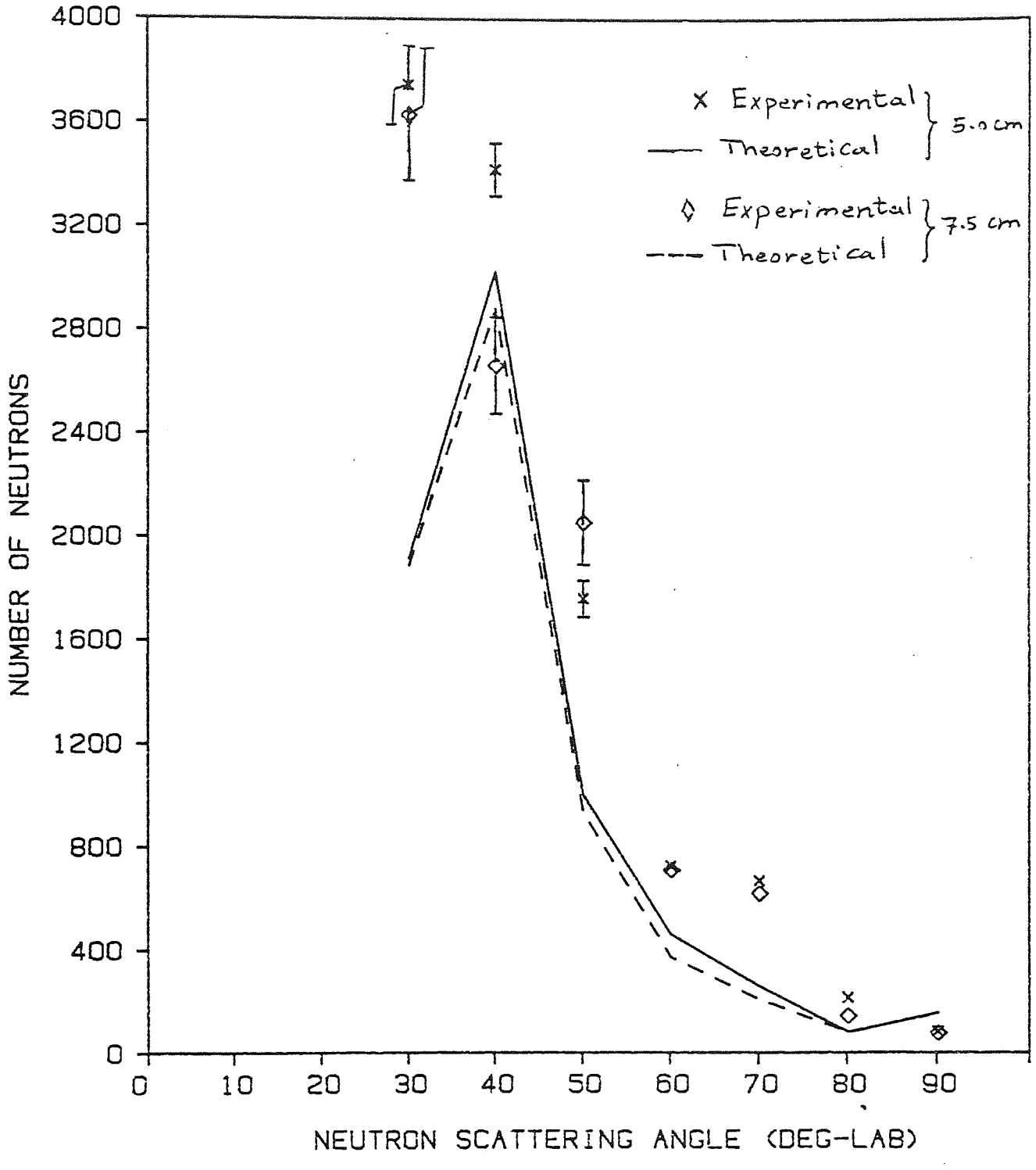

Fig (7.19) Comparison of the experimental measurement and theoretical calculation of the number of neutrons scattered from energy range 14 - 11 Mev in Lead samples of thickness 5.Ø cm and 7.5 cm .

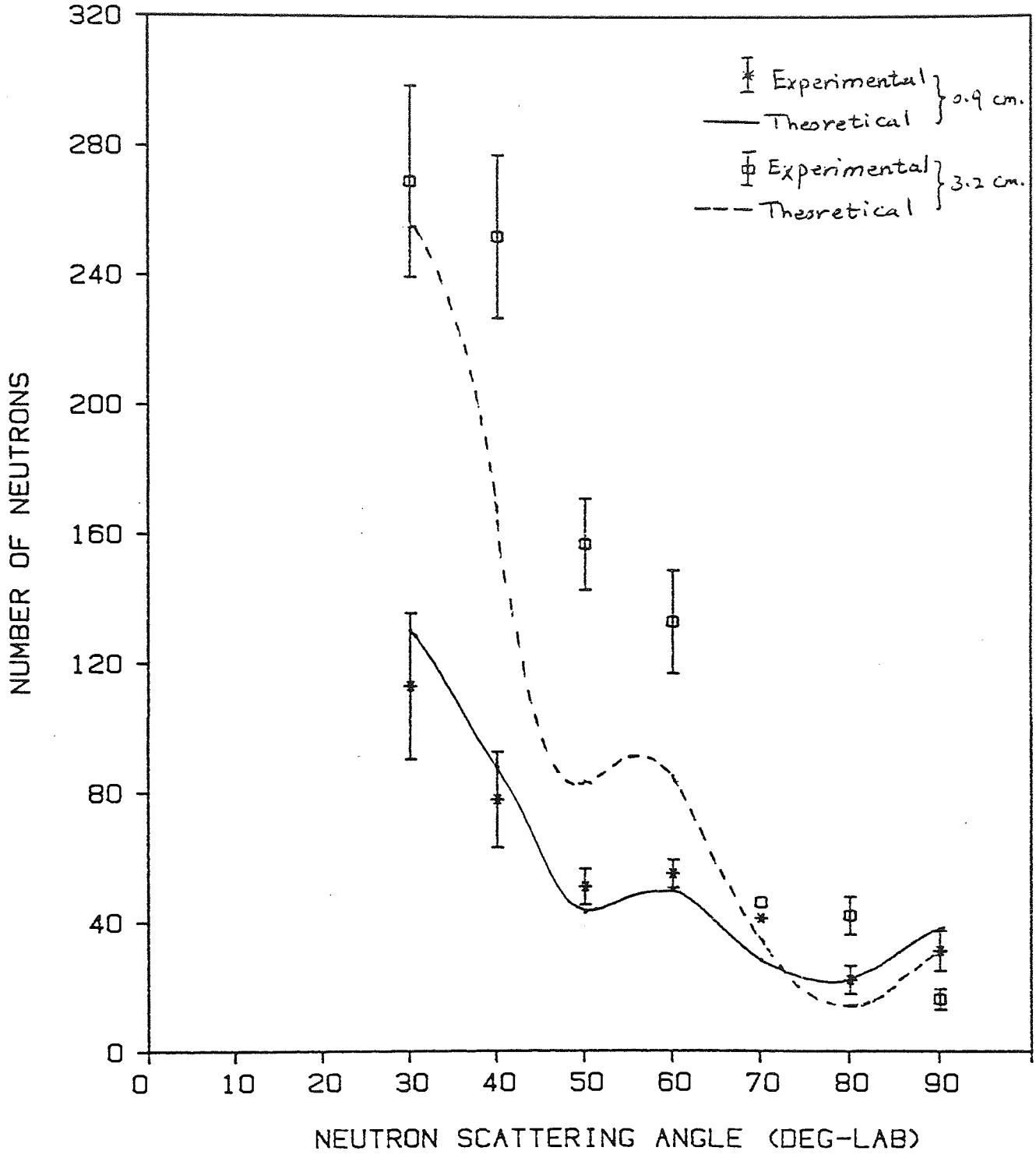

Fig (7.20) Comparison of the experimental measurement and theoretical calculation of the number of neutrons scattered from energy range 8 - 11 Mev in Lead samples of thickness 0.9 cm and 3.2 cm .

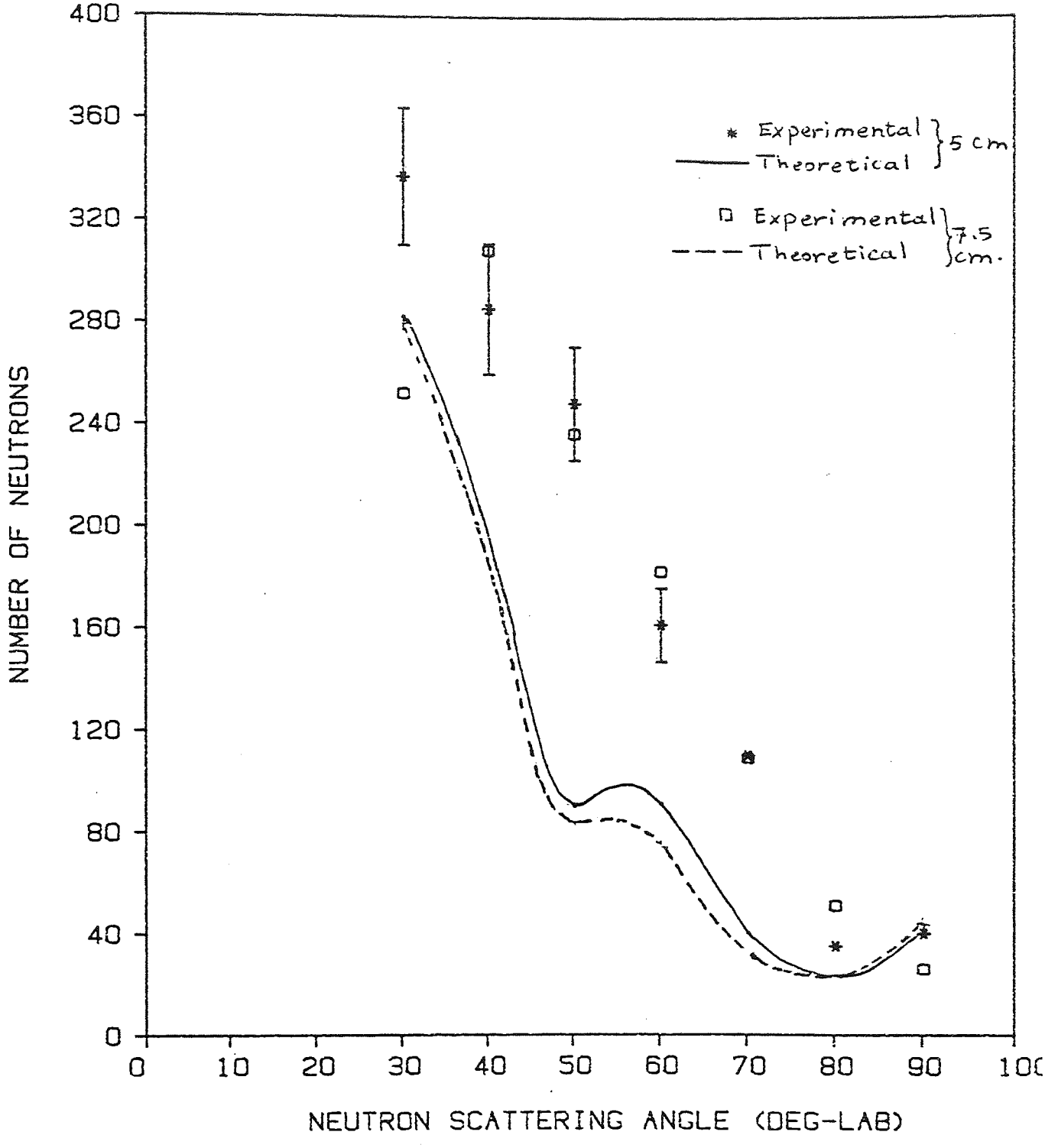

Fig (7.21) Comparison of the experimental measurement and theoretical calculation of the number of neutrons scattered from energy range 8 - 11 Mev in Lead samples of thickness 5.Ø cm and 7.5 cm .

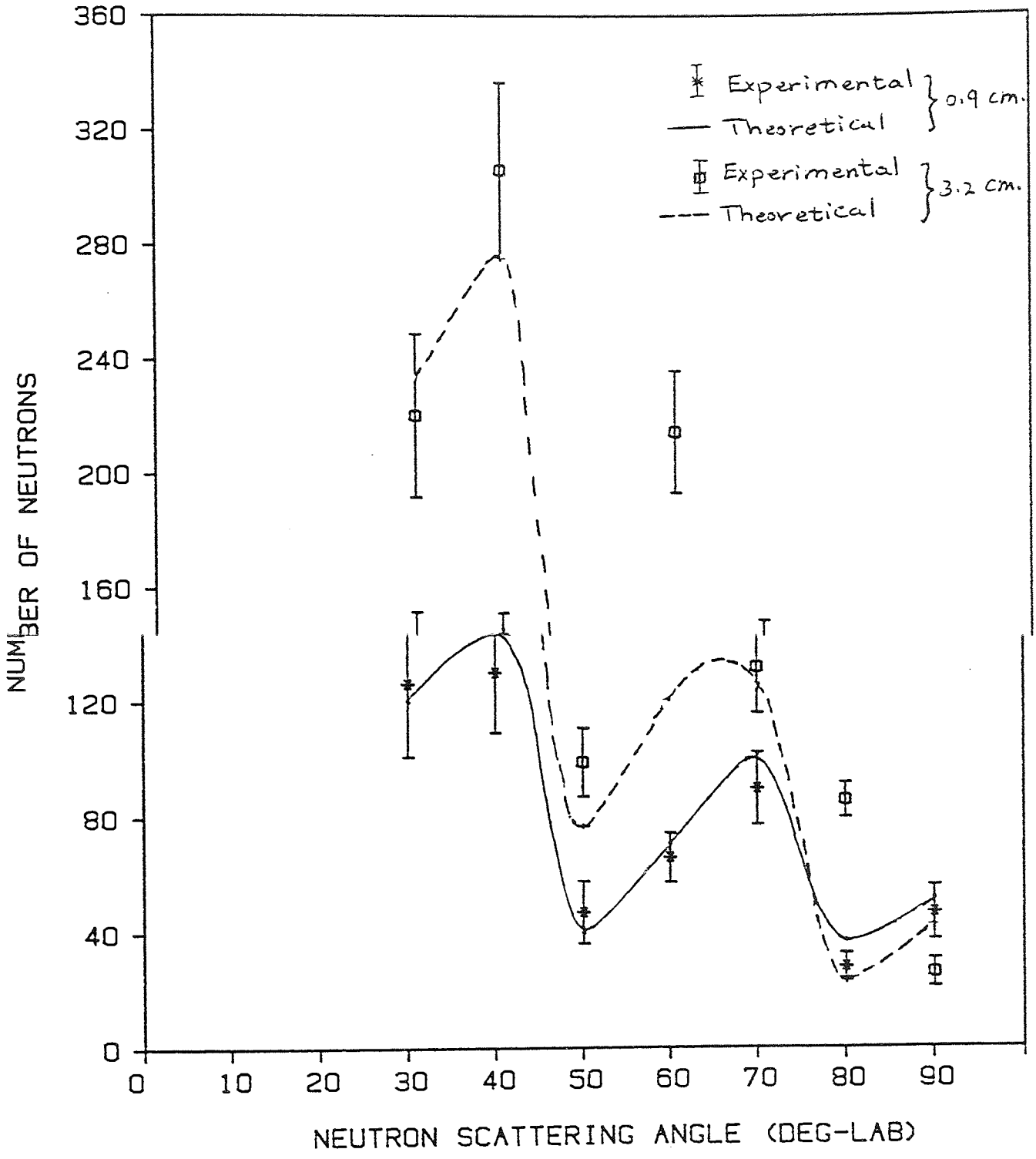

Fig (7.22) Comparison of the experimental measurement and theoretical calculation of the number of neutrons scattered from energy range 5 - 8 Mev in Lead samples of thickness Ø.9 cm and 5.Ø cm .

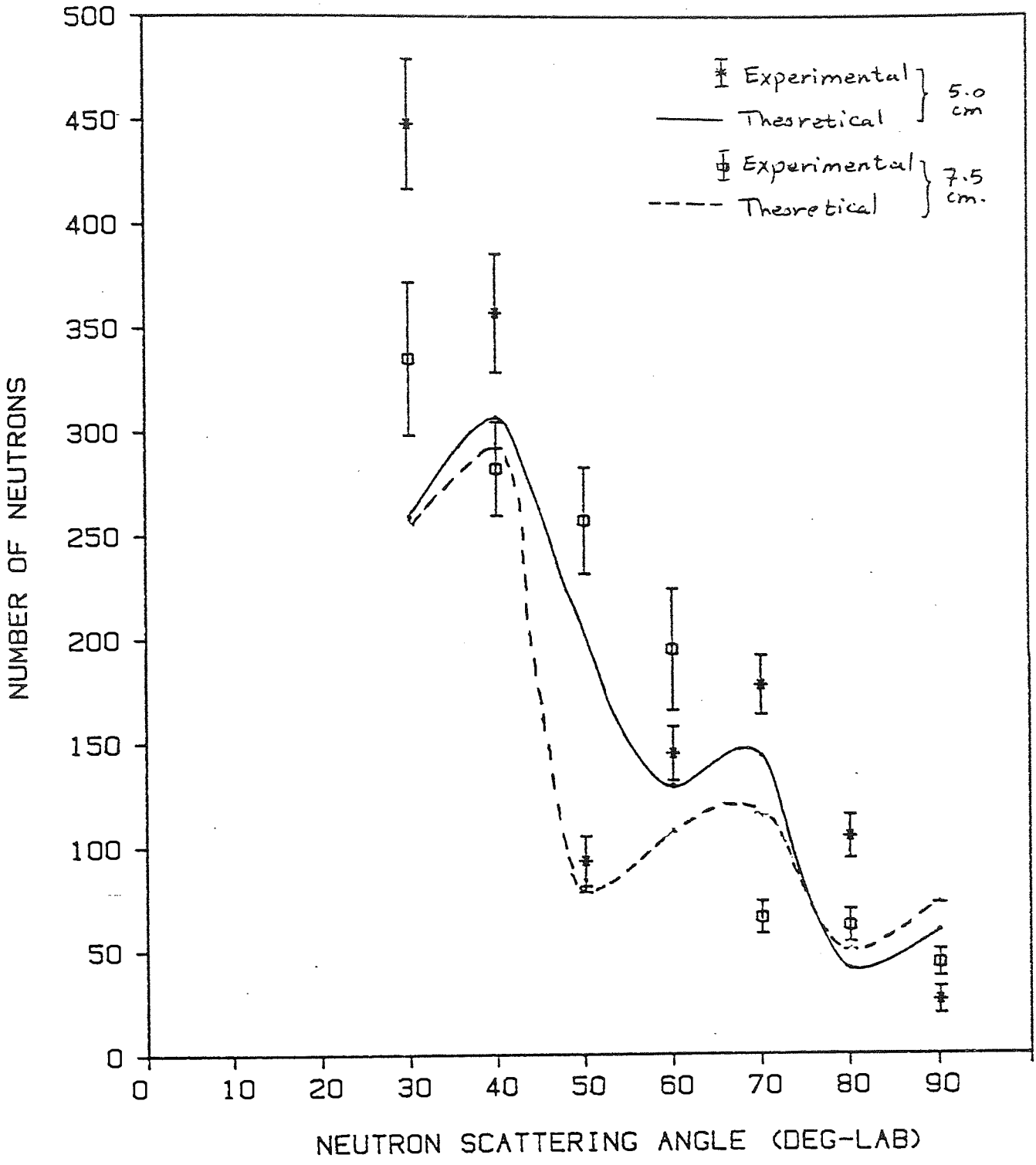

Fig(7.23) Comparison of the experimental measurement and theoretical calculation of the number of neutrons scattered from energy range 5 - 8 Mev in Lead samples of thickness 5.0 cm and 7.5 cm .

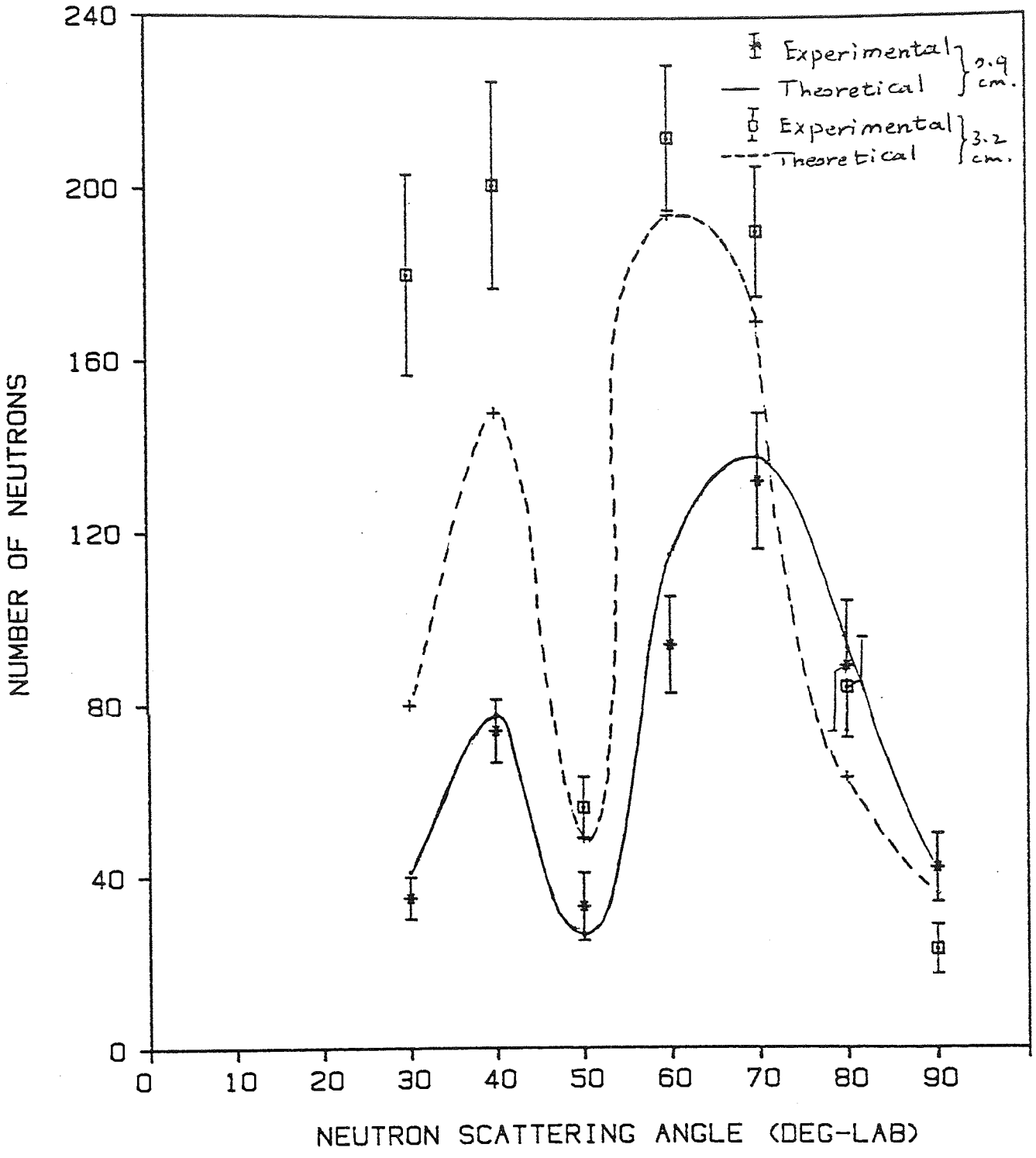

Fig(7.24) Comparison of the experimental measurement and theoretical calculation of the number of neutrons scattered from energy range 2 - 5 Mev in Lead samples of thickness Ø.9 cm and 3.2 cm .

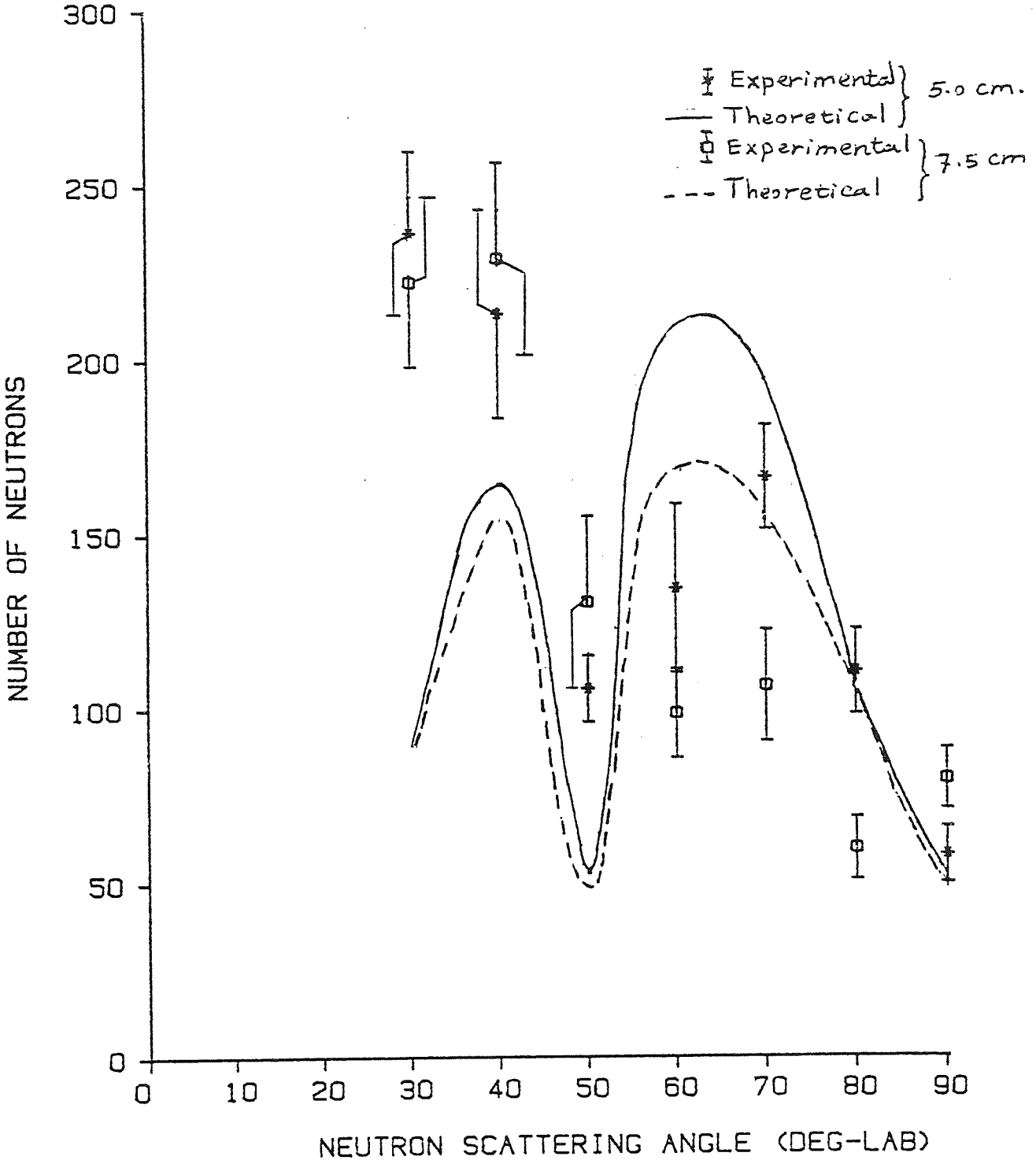

Fig(7.25) Comparison of the experimental measurement and theoretical calculation of the number of neutrons scattered from energy range 2 - 5 Mev in Lead samples of thickness 5.Ø cm and 7.5 cm .

CHAPTER EIGHT

CONCLUSIONS

CHAPTER EIGHT

CONCLUSIONS

The differential elastic and inelastic scattering cross-sections of 14 Mev and 14.44 Mev neutrons scattered from different thicknesses of slab geometry D-T fusion blanket and shielding materials , Lithium and Lead , were measured by means of a time of flight technique based on the associated particle method . The time-of-flight spectrometer provides a time resolution of 2.5 $\pm$ Ø.2 nsec for the direct 14 Mev neutron beam with a flight path of 2.13 $\pm$ Ø.Ø5 m . The limitation in the time resolution arises from the fluctuations in the transit time of electrons in the photomultiplier tube and the large dimensions of the scintillator .

Neutrons corresponding to both the elastic and inelastic scattering to the first excited state Ø.478 Mev , and to the second excited state at 4.63 Mev in Lithium were observed from thin samples at different scattering angles from Ø° to 9Ø° .

The differential cross-section data were fitted by a Legendre Polynomials and the optimum coefficients were chosen to minimize the χ^2 per point . The results of the integrated elastic and inelastic scattering measurements were in agreement within the experimental errors with the data of ENDF-B/IV and others [7Ø-74 ,76,85].

For the thick sample the variation of the differential elastic and inelastic scattering from the second excited state 4.63 Mev , with the sample thicknesses is predicted by the relation $\sigma = \sigma_o \exp(\alpha . X)$, where the value of universal constant α = Ø.35 $\pm$ Ø.26 (/mfp) in

agreement with the results of AL- SHALABY (1981)[8Ø] and ANVARIAN (1982) [81].

It seems that this equation can be used in general for all elements with extended thicknesses to predict the multiple scattering in (n,n) and (n,n') reactions .

The results of elastic scattering angular distribution for a thin lead plate geometry are in good agreement with the experimental data obtained by NATUA (1956)[9Ø] using ring geometry , RAYBURN (1959) [88] and YUASA (1958) [89] using disk-shaped scatterer .

The inelastic scattering angular distributions of the 3^- state (Q=-2.6 Mev) and 5^- state (Q=-4.1 Mev) in ^{208}Pb were compared with those of STELSON (1962) [92] . Prior to this work no reliable neutron data were avalible at this energy .

The differential cross-sections for the elastic and inelastic scattering of 14 Mev neutrons in natural Lead of different thickness was measured over the angular range between $Ø^{\circ}$ and $9Ø^{\circ}$. The non-elastic differential cross-sections (n,n') , (n,2n), for neutron energies in the range between 2-14 Mev in 3 Mev intervals were measured . No similar measurements were found in the published literature to compare with the present work . In addition Legendre Polynomial fits were produced for the elastic and non-elastic differential cross-sections these were compared to the ENDF-B/IV data.

The lower limit of the differential elastic cross-section in the forward directions [i.e. $\frac{d\sigma}{d\Omega}$ (θ_{cm} =0)] was found using the data of ENDF-B/IV and compared with the Wick's limit (σ_W) . This lower limit was found to be 15.6 % higher than the predicted Wick's limit.

The thin sample experimental results obtained for the differential

elastic and reaction cross-sections of 14 Mev neutrons on both Lithium and Lead have been compared with optical model calculations using the computer program RAROMP [95] .After iterating on the initial parameters of BECCHETTI and GREENLEES [96] , it was found that the agreement with measured angular distributions was reasonable , with χ^2/point <Ø.8 for the lithium . Therefore , the present calculation compared favourably with that of HOLLAND 1974) [79] .

The same parameters have been applied to the heavy nucleus Pb , giving a satisfactory agreement between the calculated parameters and the experimental results by χ^2/ point = Ø.2 .

In conclusion , these comparisons indicate that the optical model analysis of the n-Li and n-Pb elastic scattering can give a good description of the general features of neutron scattering from both light and heavy nuclei .

The shape of the neutron spectra from thick samples of lithium and lead when compared with the predictions of the slowing down model again show the results are in agreement with the experimental measurements.

APPENDICES

APPENDIX-A

```
 10 INPUT"P▒RITER OR VDU";Z$
 20 IFZ$="V"THEN VS=3:GOTO40
 30 IFZ$="P"THEN VS=4
 40 OPEN1,VS:CMD1
 50 DIMN(20),E0(20),PX(20),A(20),TA(20),EL1(20),RN(20),M(20)
 60 PRINT#1,CHR$(1)SPC(1)"T(D,N)AL REACTION"
 70 PRINT#1:PRINT#1:PRINT#1
 75 PRINT#1:PRINT#1:PRINT#1:PRINT#1
 80 PRINT#1,SPC(1)"E0(MV)","PN","TA","EL1","RN","M"
 90 PRINT#1,"----------------------------------------------------------------
100 READ N
110 FOR E0=.300 TO.300
120 FOR PN=20TO 23  STEP 1
130 PX=PN*π/180
140 GA=(5.9422726+174.42466/E0)
150 GB=0.5*SIN(2*PX)
160 GC=SQR(GA-SIN(PX)↑2)
170 GD=SIN(PX)*GC
180 GF=GB+GD
190 GH=COS(PX)*GC
200 GJ=(SIN(PX)↑2+3.9682193)
210 GL=GH-GJ
220 A=GF/GL
230 PA=ATN(A)*180/π
240 IF ATN(A)>=0 THEN PA=180-PA
250 IF PA<=0 THEN PA=PA*(-1)
255 TA=INT(PA*100+0.5)/100
260 EA=0.08*E0*COS(2*PX)
270 EB=0.6*E0+17.6
280 EC=0.8*EB
290 EF=SQR(0.4*E0*EB)
300 ED=0.8*COS(PX)*EF
310 EG=SQR(1-(E0*SIN(PX)↑2)/(10*EB))
320 EL=EA+EC+ED*EG
325 EL1=INT(EL*100+0.5)/100
330 RGA=SQR(1/GA)
340 RN=(RGA*(COS(PX)+GC)↑2)/GC
343 M1=SQR(1-RGA↑2*SIN(PX)↑2)
344 M2=-RGA*SIN(PX)↑2+COS(PX)*M1
345 M3=-ATN(M2/SQR(-M2*M2+1))+π/2
347 M4=M3*180/π
348 Z1=E0:Z2=3:GOSUB500:PRINT#1,Z1$SPC(3);
349 Z1=PN:Z2=3:GOSUB500:PRINT#1,Z1$SPC(3);
350 Z1=TA:Z2=3:GOSUB500:PRINT#1,Z1$SPC(3);
351 Z1=EL1:Z2=3:GOSUB500:PRINT#1,Z1$SPC(3);
352 Z1=RN1:Z2=3:GOSUB500:PRINT#1,Z1$SPC(3);
353 Z1=M4:Z2=3:GOSUB500:PRINT#1,Z1$
360 NEXT PN
370 NEXT E0
380 END
400 DATA 15
500 Z1=INT(Z1*10↑Z2+0.5)/10↑Z2
510 Z1$=LEFT$(RIGHT$("          "+STR$(Z1+0.5/10↑Z2*SGN(Z1)),10),9)
520 IFVAL(Z1$)=0 THENZ1$="      0.00"
530 RETURN
```

APPENDIX B

GAUSSIAN FUNCTION

A method for fitting the spectrum assumes that the spectral peaks can be treated as a simple Gaussian function :

$$Y(x) = Yo \cdot \exp\left[- (x - x_o)^2 / 2\sigma^2 \right] \qquad \text{(B-1)}$$

where Yo denotes the peak ght , x_o, is the peak position , and σ is the standard deviation .

Using the property of the Gaussian function :

$$Q(x) = \frac{Y(x-1)}{Y(x+1)} = \exp\left(\frac{2(x - x_o)}{\sigma^2} \right) \qquad \text{(B-2)}$$

And taking the logarithm of equation (B-2) ;

$$\log_e Q(x) = \frac{2(x - x_o)}{\sigma^2} \qquad \text{(B-3)}$$

This quantity is a linear function of x . Therefore the $\log_e Q(x)$ values defined by means of the Yi data , $\log_e\left(\frac{Y_{i-1}}{Y_{i+1}} \right)$, can be fitted to a straight line by a linear least-squares method . In this , the slope m and intercept b yield the standard deviation and the centroid xo of the Gaussian

$$\sigma = \sqrt{\frac{2}{m}} \qquad \text{and } xo = - \frac{b}{m} \qquad \text{(B-4)}$$

In making this fit , the weights associated with $\log_e Q(x)$ are chosen as :

$$Wi = \left[\frac{1}{Y_{i+1}} + \frac{1}{Y_{i-1}}\right]^{-1} \qquad \text{(B-5)}$$

Where Yi represents the content of the ith channel . However only the channels whose contents lie at least halfway up the peak were fitted because near the edges of the peak various experimental distortions make the spectrum far from Gaussian. The parameters xo and σ are determined and the peak height Yo evaluated from the weighted mean :

$$\log_e Yo = \frac{\sum_{i=1}^{N} W_i' \left\{ \log_e Y_i + (x_i - x_o)^2 / 2\sigma^2 \right\}}{\sum_{i=1}^{N} Wi'} \qquad \text{(B-6)}$$

Where the weighted factors are :

$$W_i' = \left[\frac{1}{Y_i} + \frac{(x_i - x_o)^2}{\sigma^4} \left\{ (\Delta x_o)^2 + \frac{(x_i - x_o)^2}{\sigma^2} \Delta\sigma^2 \right\} \right]^{-1} \qquad \text{(B-7)}$$

And Δxo and $\Delta\sigma$ are the estimated standard deviations of xo and σ obtained from the linear fit .

From the properties of the Gaussian curve , the total area under the peak is calculated using :

$$A = \sqrt{2\pi}\ \sigma \cdot Y_o = 2.5\ \sigma\, Y_o \qquad \text{(B-8)}$$

Where its full width at half maximum is :

$$FWHM = 2\sqrt{2\ln 2}\,\sigma = 2.355\,\sigma \qquad (B\text{-}9)$$

```
10 INPUT"PRITER OR VDU";Z$
20 IFZ$="V"THEN VS=3:GOTO 40
30 IFZ$="P"THEN VS=4
40 OPEN1,VS:CMD1
50 PRINT#1,SPC(1)CHR$(1)"NORMAL DIST."
60 PRINT#1,"-------------------------"
70 PRINT"HOWMANY DATA POINTS"
80 INPUT N
90 DIM X(N),Y(N),Q(N),U(N),W(N)
100 A1=0
110 B1=0
120 C1=0
130 D1=0
140 E=0
150 FOR I=1 TO N STEP 1
160 READ X(I):NEXT
170 FOR I=1 TO N STEP 1
180 READ Y(I):NEXT
190 DATA 300,301,302,304,305
200 DATA 100,200,300,180,95
210 FOR I=1 TO N
220 PRINT#1,ISPC(2)X(I)SPC(5)Y(I):NEXT I
230 FOR I=2 TO N-1 STEP 1
240 K=I-1
250 J=I+1
260 L=N-2
270 Q(I)=LOG(Y(K)/Y(J))
280 U(I)=(1/Y(J)+1/Y(K))
290 U(I)=1/U(I)
300 A1=A1+X(I)*U(I)
310 B1=B1+Q(I)*U(I)
320 C1=C1+X(I)*Q(I)*U(I)
330 D1=D1+X(I)*X(I)*U(I)
340 E=E+U(I)
350 NEXT I
360 M=(E*C1-A1*B1)/(E*D1-A1*A1)
370 B=(B1*D1-A1*C1)/(E*D1-A1*A1)
380 PRINT#1,"M=";M
390 PRINT#1,"B=";B
400 REM S=SIGMA
410 S=SQR(2.0/M)
420 REM X0=PEAK POSITION
430 X0=(B)/M
440 PRINT#1,"PEAK POSITION=";X0
450 REM---RESIDUAL CALCUL.
460 PRINT#1,"SIGMA=";S
470 REM S1=ERROE IN S
480 REM S2=DETERMINANT
490 A2=0
500 D2=0
510 A2=A2+X(I)
520 D2=D2+X(I)*X(I)
530 S2=(L*D2)-(A2)↑2
```

```
 540 DS=0
 550 FOR I=2 TO N-1 STEP 1
 560 Z=2*(X(I)-X0)/S↑2
 570 D=(Q(I)-Z)↑2
 580 R=DS+D
 590 NEXT I
 600 REM P=ALPHA
 610 P=(R)/(L-2)
 620 T0=SQR((L*P)/(S2))
 630 S1=(0.7071*T0)/(M)↑1.5
 640 REM S4=ERROR IN X0
 650 S3=SQR((P*D)/S2)
 660 S4=SQR((S3/M)↑2+(B*T0/M↑2)↑2)
 670 REM    X0=X0+S4
 680 REM S=S+S1
 690 REM---EVALUATION OF PEAK HEIGHT
 700 Z3=0
 710 G=0
 720 FOR I=1 TO N STEP 1
 730 V=(S4)↑2+((X(I)-X0)↑2)*((S1)↑2)/(S↑2
 740 W(I)=1/Y(I)+(((X(I)-X0)↑2)*V)/(S↑4)
 750 W(I)=1/W(I)
 760 T1=((X(I)-X0)↑2)/(2*(S)↑2)
 770 H1=(W(I)*(LOG(Y(I))+T1))
 780 H2=H1/W(I)
 790 H=H2+Z3
 800 NEXT I
 810 REM------PEAK HEIGHT Y0
 820 Y0=EXP(H)
 830 PRINT#1,"PEAK HEIGHT=";Y0
 840 A=2.507*S*Y0
 850 PRINT#1,"PEAK AREA=";A
 860 FW=2.355*S
 870 PRINT#1,"FWHM=";FW
 880 FOR X=300 TO 317  STEP 1
 890 T1=((X-X0)↑2)/(2*(S)↑2)
 900 T1=-T1
 910 Y1=Y0*EXP(T1)
 920 PRINT#1,X,Y1
 930 NEXT X
 940 END
READY.
```

APPENDIX C

LEGENDRE POLYNOMIALS

The legendre polynomial is given by :

$$y = a_o p_o(x) + a_1 p_1(x) + ... = \sum_{l=0}^{n} [\, a_l p_l(x) \,) \qquad (C.1)$$

Where $x = \cos\theta$ and the terms $p_l(x)$ in the function are given by :

$$p_l(x) = \frac{1}{l}\{ (2l-1).x.p_{l-1}(x) - (l-1).p_{l-2}(x) \} \qquad (C.2)$$

Legendre polynomials are orthogonal when averaged over all values of $x = \cos\theta$:

$$\int_{-1}^{+1} P_l(x).P_M(x).dx = \begin{cases} 1 & \text{if } L = M \\ 0 & \text{if } L \neq M \end{cases}$$

C.1 METHOD OF LEAST SQUARES

For any arbitrary function

$$y(x) = \sum_{j=0}^{n} [\, aj.Xj(x) \,] \qquad (C.3)$$

The difinition of χ^2 is :

$$\chi^2 \equiv \{ \frac{1}{\sigma_i^2} [y_i - y(x_i)]^2 \}$$

Where σ_i is the standard deviation for the experimental data $y_i(x)$, y_i are the theoretical data . Therefore by expressing the determining equations for the method of least squares in order to minimize χ^2, as

a set of (N-1) equations ,

$$\frac{\partial}{\partial a_k}\sum [\, y_i - y\,(x_i)\,]^2 = \frac{\partial}{\partial a_k}\sum \{\, y_i - \sum_{j=0}^{n} [\, a_j\, X_j(x_i)\,]\,\}^2 = 0 \qquad (C.4)$$

Where the sum without indices runs from i = 1 to N ; the sum over j runs from j=Ø to n ; and k takes on all values from Ø to n .
The coefficients aj for which χ^2 is a minimum can be determined from solution of this set of (n+1) simultaneous equations :

$$\sum y_i \cdot X_0(x_i) = a_0 \cdot \sum X_0^2(x_i) + a_1 \cdot \sum X_1(x_i)\cdot X_0(x_i) + \ldots\ldots + a_n \sum X_n(x_i)\cdot X_0(x_i)$$

$$\sum y_i \cdot X_0(x_i) = a_0 \sum X_0(x_i)\cdot X_i(x_i) + a_1 \sum X_1^2(x_i) + \ldots + a_n \sum X_n(x_i)\cdot X_1(x_i) \qquad (C.5)$$

$$\sum y_i \cdot X_n(x_i) = a_0 \sum X_0(x_i)\cdot X_n(x_i) + a_1 \cdot \sum X_1(x_i)\cdot X_n(x_i) + \ldots + a_n \cdot \sum X_n(x_i)\cdot X_1(x_i)$$

Which can be expressed as :

$$\sum [\frac{1}{\sigma_i^2}\cdot y_i \cdot X_k(x_i)] = \sum_{j=0}^{n} \{a_j \cdot \sum [\frac{1}{\sigma_i^2}\cdot X_j(x_i)\cdot X_j(x_i)]\} \qquad (C.6)$$

C.2 MATRIX INVERSION

The solution of equation (C.5) can be carried out by considering them as matrix equations which can be solved by rearragement .
Equation (C.5) becomes in matrix form :

$$\beta_k = \sum_{j=0}^{n} (a_j \cdot \alpha_{jk}) \qquad k=Ø,n \qquad (C.7)$$

Where $\beta_k = \sum [\frac{1}{\sigma_i^2}\, y_i \cdot X_k(x_i)]$

$$\alpha_{jk} = \left[\frac{1}{\sigma_i^2} X_j(x_i) \cdot X_k(x_i)\right] \qquad (C.8)$$

a_j = the coefficient matrix .

The derivative of χ^2 with respect to any arbitrary coefficient a_j is given by :

$$\frac{\partial \chi^2}{\partial a_j} = -2 \sum \left\{\frac{1}{\sigma_i^2}[y_i - y(x_i)] \cdot X_j(x_i)\right\} \qquad (C.9)$$

and the second cross partial derivative with respect to two such coefficients :

$$\frac{1}{2} \frac{\partial^2 \chi^2}{\partial a_j \cdot \partial a_k} = \sum \left[\frac{1}{\sigma_i^2} X_j(x_i) \cdot X_k(x_i)\right] = \alpha_{jk} \qquad (C.10)$$

for all j and k

Equation (C.7) can then be written

$$\beta = a \cdot \alpha$$

$$a = \beta \cdot \alpha^{-1} = \beta \cdot \epsilon \qquad (C.11)$$

and equation (C.11) becomes

$$a_j = \sum_{k=0}^{n} (\epsilon_{jk} \beta) = \sum_{k=0}^{n} \left\{\epsilon_{jk} \sum \left[\frac{1}{\sigma_i^2} y_i \cdot X_k(x_i)\right]\right\} \qquad (C.12)$$

C.3 ESTIMATIONS OF ERRORS

The unertainties in the coefficients a_j can be obtained by consideration of the standard deviation σ_{a_j} ,

$$\alpha_{a_j}^2 = \sum [\alpha_i^2 \left(\frac{\partial a_j}{\partial y_i}\right)^2] \qquad (C.13)$$

From equation (C.12) the derivatives of the right hand term are given by :

$$\frac{\partial a_j}{\partial y_i} = \sum_{k=0}^{n} [\epsilon_{jk} \frac{1}{\alpha_i^2} X_k(x_i)] \qquad (C.14)$$

and the weighted sum of the squares of the derivatives can be reduced to :

$$\sum [\alpha_i^2 \left(\frac{\partial a_j}{\partial y_i}\right)^2] = \sum_{k=0}^{n}\sum_{m=0}^{n} \{ [\frac{1}{\alpha_i^2} X_k(x_i) . X_m(x_i)]\} = \sum_{k=0}^{n}\sum_{m=0}^{n} (\epsilon_{jk}\epsilon_{jm}\alpha_{km}) = \epsilon_{jj}$$

The inverse matrix $\epsilon = \alpha^{-1}$ is called the error matrix because it contains most of the information needed to estimate the errors .

$$\alpha_{a_j}^2 = \epsilon_{jj} \qquad (C.15)$$

If the uncertainties in the data points are not known , they can be approximated from the data as in equation (C.3) .

$$\alpha_i^2 = \alpha^2 \simeq s^2 = \frac{1}{N-n-1} \sum \{ Y_i - \sum_{j=0}^{n} [a_j . X_j(x_i)]\}^2 \qquad (C.16)$$

Where s = the sample variance for the fit .

N-n-1= ν = the number of degrees of freedom after fitting N data points with n+1 parameters .

Combining equations (C.13) to (C.16) , the uncertanity in the coefficient a_j is given by :

$$\sigma_{a_j} \simeq s^2 \epsilon_{jj} (\sigma_i = 1) \qquad (C.17)$$

Where $\epsilon_{jj}(\sigma_i = 1)$ is the error matrix evaluated with $\sigma_i = 1$.

C.4 NORMALIZED POLYNOMIALS

The polynomial of equation (C.3) can be rewritten in a such a way as to separate the relative values of the coefficients from the absolute values

$$y(x) = a_0 \{ 1 + \sum_{j=1}^{n} (b_j . X_j(x_i)) \} \qquad (C.18)$$

Evaluation of the coefficients b_j of equation (C.18) is :

$$b_j = \frac{a_j}{a_0} \qquad (C.19)$$

The uncertainty in the ratio of equation (C.19) is given by :

$$\frac{\sigma_{b_j}^2}{b_j^2} = \frac{\sigma_{a_j}^2}{a_j^2} + \frac{\sigma_{a_0}^2}{a_0^2} - 2 \frac{\sigma_{a_j a_0}^2}{a_j a_0} \qquad (C.20)$$

Where the uncertainties in a_j and a_0 are given by equation (C.15) . The covariance $\sigma^2_{a_j a_0}$ follows from a derivation similar to that in equations (C.13) and (C.15)

$$\sigma^2_{a_j a_0} = \sum [\sigma_i^2 (\frac{\partial a_j}{\partial y_i}) (\frac{\partial a_0}{\partial y_i})] = \epsilon_{j0} \qquad (C.21)$$

C.5 PROGRAM LEGFIT

```
C       LEGENDRE POLYNOMIAL PROGRAM <  LEGFIT  >
C
C       PURPOSE
C          MAKE A LEAST-SQUARES FIT TO DATA WITH A LEGINDRE POLYNOMIAL
C            Y = A(1) + A(2)*X + A(3)*(3X**2-1)/2 +.....
C              = B(1) + (1. + B(2)*X +B(3)*(3X**2-1)/2 +......)
C                 WHERE X = COS(THETA)
C
C      DESCRRIBTION OF PARAMETERS
C      --------------------------
C
C        INPUT PARAMETERS
C        ****************
C
C        THETA -  ARRAY  OF ANGLES (IN DEGREES) OF THE DATA POINTS
C        Y     -  ARRAY  OF DATA POINTS FOR DEPENDENT VARIABLE
C        SIGMAY-  ARRAY OF STANDARD DEVIATIONS FOR Y DATA POINTS
C        NPTS  -  NUMBER OF PAIRS OF DATA POINTS
C        NORDER-  HIGHEST ORDER OF POLYNOMIAL ( NUMBER OF TERMS - 1 )
C        NEVEN -  DETERMINES ODD OR EVEN CHARACTER OF POLYNOMIAL
C                 +1  FITS ONLY TO EVEN TERMS
C                  Ø  FITS TO ALL TERMS
C                 -1  FITS ONLY TO ODD  TERMS
C        MODE  -  DETERMINES MODE OF WEIGHTING LEAST-SQUARES FIT
C                 +1  ( INSTRUMENTAL ) WEIGHT(I) = 1./ SIGMAY**2
C                  Ø  ( NO WEIGHTING ) WEIGHT(I) = 1.
C                 -1  ( STATISTICAL  ) WEIGHT(I) = 1./ Y(I)
C        FTEST -  ARRAY OF VALUES OF F(L) FOR AN F-TEST
C
C
C        OUTPUT PARAMETERS
C        *****************
C
C        YFIT  -  ARRAY OF CALCULATED VALUES OF Y
C        A     -  ARRAY OF COEFFICENTS OF POLYNOMIAL
C        SIGMAA-  ARRAY OF STANDARD DEVIATIONS CEOFFICIENTS
C        B     -  ARRAY OF NORMALIZED RELATIVE CEOFFICIENTS
C        SIGMAB-  ARRAY OF STANDARD DEVIATIONS FOR RELATIVE COEIFFICENTS
C        CHISQR-  REDUCED CHI SQUAREE FOR FIT
C
C        SUBROUTINES AND FUNCTION SUBPROGRAMS REQUIRED
C                MATINV (ARRAY, NTERMS, DET )
C                  INVERS A SYMMETRIC TWO-DIMENSIONAL MATRIX OF DEGREE NTREMS
C                  AND CALCULATES ITS DETERMINANT
C
C
C
      DOUBLE PRECISION COSINE , P, BETA, ALPHA, CHISQ
        DIMENSION WEIGHT(5ØØ),  P(5ØØ,24)
      DIMENSION THETA(18), Y(18), SIGMAY(18), YFIT(18), A(2Ø),B(2Ø)
       DIMENSION SIGMAB(18), SIGMAA(18), FTEST(18)
      DIMENSION BETA(2Ø), ALPHA(2Ø,2Ø)
```

```
      ACCUMLATE WEIGHT AND LEGENDRE POLYNOMIAL

     NPTS = 22
     DO 2 I= 1, NPTS
     READ(7,*)THETA(I) , Y(I)  , SIGMAY(I), FTEST(I)
 2   CONTINUE
     DO 1ØØØ NORDER = 1 , 2Ø
 11  NTERMS = 1
     NCOEFF=1
     NEVEN = Ø
     MODE =-1
     PRINT*, "NORDER=",NORDER
     PRINT*, "MODE  =",MODE
     PRINT*, "NEVEN =",NEVEN
     JMAX=NORDER+1
 2Ø  DO 4Ø I = 1, NPTS
 21  IF ( MODE ) 22, 27, 29
 22  IF ( Y(I) ) 25, 27, 23
 23  WEIGHT(I) = 1. / Y(I)
     GO TO 31
 25  WEIGHT(I) = 1. / (-Y(I))
     GO TO 31
 27  WEIGHT(I) = 1.
     GO TO 31
 29  WEIGHT(I) = 1. / SIGMAY(I)**2
 31  COSINE = COS(.Ø1745329252 * THETA(I))
     P(I,1) = 1.
     P(I,2) = COSINE
     DO 36 L = 2, NORDER
     FL = L
 36  P(I,L+1)=((2.Ø*FL-1.Ø)*COSINE*P(I,L)-(FL-1.Ø)*P(I,L-1))/FL
C
C       ACCUMULATE MATRICES ALPHA AND BETA
C
 4Ø  CONTINUE
 51  DO 54 J = 1, NTERMS
     BETA(J) = Ø.
     DO 54 K = 1, NTERMS
 54  ALPHA(J,K) = Ø.
 61  DO 66 I = 1, NPTS
     DO 66 J = 1, NTERMS
     BETA(J) = BETA(J) + P(I,J)*Y(I)*WEIGHT(I)
     DO 66 K = J , NTERMS
     ALPHA(J,K) = ALPHA(J,K) + P(I,J)*P(I,K)*WEIGHT(I)
 66  ALPHA(K,J) = ALPHA(J,K)
C
C       DELETE FIXED COEFFICIENTS
C
 7Ø  IF (NEVEN) 71, 91, 81
 71  DO 76 J = 3, NTERMS, 2
     BETA(J) = Ø.Ø
     DO 75 K = 1, NTERMS
     ALPHA(J,K) = Ø.Ø
```

```
   75  ALPHA(K,J) = Ø.Ø
   76  ALPHA(J,J) = 1.Ø
       GO TO 91
   81  DO 86 J = 2, NTERMS, 2
       BETA(J) = Ø.Ø
       DO 85 K = 1, NTERMS
       ALPHA(J,K) = Ø.Ø
   85  ALPHA(K,J) = Ø.Ø
   86  ALPHA(J,J) = 1.Ø
C
C       INVERT CURVATURE MATRIX ALPHA
C
   91  DO 95 J = 1, JMAX
       A(J) = Ø.Ø
       SIGMAA(J) = Ø.Ø
       B(J) = Ø.Ø
   95  SIGMAB(J) = Ø.Ø
       DO 97 I = 1, NPTS
   97  YFIT(I) = Ø.Ø
  1Ø1  CALL MATINV (ALPHA,NTERMS,DET)
C
C       CALCULATE COEFFICIENTS,FIT , AND, CHI SQURES
C
       IF (DET) 111, 1Ø3, 111
  1Ø3  CHISQR = Ø.Ø
       GO TO 17Ø
  111  DO 115 J = 1, NTERMS
       DO 113 K = 1, NTERMS
  113  A(J) = A(J) + BETA(K)*ALPHA(J,K)
       DO 115 I = 1, NPTS
  115  YFIT(I) = YFIT(I) + A(J)*P(I,J)
  121  CHISQ = Ø.Ø
       DO 123 I = 1, NPTS
       CHISQ = CHISQ + (Y(I) - YFIT(I))**2 * WEIGHT(I)
  123  CONTINUE
       FREE = NPTS - NCOEFF
       CHISQR = CHISQ / FREE
C
C       TEST FOR END OF FIT
C
  131    IF ( NTERMS - JMAX) 132, 151, 151
  132    IF ( NCOEFF - 2) 133, 134, 141
  133    IF (NEVEN) 137,137,135
  134    IF (NEVEN) 135, 137, 135
  135    NTERMS = NTERMS + 2
         GO TO 138
  137    NTERMS = NTERMS + 1
  138    NCOEFF = NCOEFF + 1
         CHISQ1 = CHISQ
         GO TO 51
  141    FVALUE = ( CHISQ1 - CHISQ) / CHISQR
         IF ( FTEST(NTERMS) -    FVALUE ) 134, 143, 143
  143    IF (NEVEN) 144, 146, 144
  144    NTERMS = NTERMS - 2
```

```
  144     NTERMS = NTERMS - 2
          GO TO 147
  146     NTERMS = NTERMS - 1
  147     NCOEFF = NCOEFF - 1
          JMAX = NTERMS
  149     GO TO 51
C
C        CALCULATE REMINDER OF OUTPUT
C
  151     IF (MODE) 152, 154, 152
  152     VARNCE = 1.Ø
          GO TO 155
  154     VARNCE = CHISQR
  155     PRINT*," COEFFICIENTS FOR LEAST SQURE FIT TO A LEGENDRE POLY"
        PRINT*,"-------------------------------------------------------"
        PRINT*,"           "
          DO 156 J = 1, NTERMS
        IF(ALPHA(J,J) .LE. Ø.Ø ) ALPHA(J,J)=Ø.ØØ9
          SIGMAA(J) =DSQRT(VARNCE*ALPHA(J,J))
        PRINT*,"A(J)=",A(J), "SIGMAA(J)=",SIGMAA(J)
  156     CONTINUE
  1ØØ   IF (A(1)) 162, 17Ø, 162
  162     PRINT*,"          "
          PRINT*," NORMALIZED LEGENDRE POLYNOMIAL "
          PRINT*,"--------------------------------"
          DO 166 J = 2, NTERMS
          IF (A(J)) 164, 166, 164
  164     B(J) = A(J) / A(1)
  165   SIGMAB(J) = B(J)* DSQRT((SIGMAA(J)/A(J))**2 + (SIGMAA(1)/A(1))**2
     1  - 2.Ø * VARNCE*ALPHA(J,1)/(A(J)*A(1)))


        PRINT*,"B(J)=",B(J)       ,"SIGMAB(J)=",SIGMAB(J)
  166    CONTINUE
         B(1) = 1.Ø
        PRINT *,"                                        "
        PRINT*,"    RESULTS OF FITTING "
        PRINT*,"-----------------------"
        PRINT*,"                      "
        PRINT*,"ANGLE(THETA)","YEXP","YFIT"
        PRINT*,"------------","----","----"
         DO 989 I=1, NPTS
         WRITE(6,*)THETA(I),Y(I),YFIT(I)
  989    CONTINUE

         PRINT*,"CHISQR=",CHISQR
        PRINT*,"                  "
        PRINT*,"*****************   NEXT  DEGREE  ******************"
  1ØØØ  CONTINUE
   17Ø  STOP
        END
```

```
      SUBROUTINE MATINV


        PURPOSE
          INVERT A SYMMETRIC MATRIX AND CALCULATE ITS DETERMINANT

        DESCRIBTION OF PARAMETERS
          ARRAY   -  INPUT MATRIX WHICH IS REPLACED BY ITS INVERS
          NORDER  -  DEGREE OF MATRIX (ORDER OF DETERMINANT)
          DET     -  DETERMINANT OF INPUT MATRIX

      SUBROUTINE MATINV (ARRAY, NORDER, DET)
      DOUBLE PRECISION ARRAY, AMAX, SAVE
      DIMENSION ARRAY(20,20), IK(20), JK(20)
10        DET = 1.
11        DO 100 K = 1, NORDER

       FIND LARGEST ELEMENT ARRAY(I,J) IN REST OF MATRIX

          AMAX = 0.0
21        DO 30 I = K, NORDER
          DO 30 J = K, NORDER
23        IF (ABS(AMAX) - ABS(ARRAY(I,J))) 24, 24, 30
24        AMAX = ARRAY(I,J)
          IK(K) = I
          JK(K) = J
30        CONTINUE

       INTERCHANGE THE ROWS AND COLUMNS TO PUT AMAX IN ARRAY(K,K)

31        IF (AMAX) 41, 32, 41
32        DET = 0.0
          GO TO 140
41        I = IK(K)
          IF ( I - K ) 21, 51, 43
43        DO 50 J = 1, NORDER
           SAVE = ARRAY(K,J)
        ARRAY(K,J) = ARRAY(I,J)
50         ARRAY(I,J) = -SAVE
51        J = JK(K)
          IF (J-K) 21, 61, 53
53        DO 60 I=1, NORDER
          SAVE = ARRAY(I,K)
          ARRAY(I,K) = ARRAY(I,J)
60        ARRAY(I,J) = -SAVE

       ACCUMULATE ELEMENTS OF INVERSE MATRIX

61        DO 70 I = 1, NORDER
           IF (I-K) 63, 70, 63
63        ARRAY(I,K) = -ARRAY(I,K) / AMAX
70        CONTINUE
```

```
 71          DO 80 I = 1, NORDER
             DO 80 J = 1, NORDER
             IF (I-K) 74, 80, 74
 74          IF (J-K) 75, 80, 75
 75          ARRAY(I,J) = ARRAY(I,J)+ ARRAY(I,K)*ARRAY(K,J)
 80          CONTINUE
 81          DO 90 J = 1, NORDER
             IF (J-K) 83, 90, 83
 83          ARRAY(K,J) = ARRAY(K,J) / AMAX
 90          CONTINUE
             ARRAY(K,K) = 1.0/AMAX
100          DET = DET*AMAX
C
C       RESTORE ORDERING OF MATRIX
C
101          DO 130 L = 1, NORDER
             K = NORDER - L +1
             J = IK(K)
             IF (J-K) 111, 111, 105
105          DO 110 I = 1, NORDER
             SAVE = ARRAY(I,K)
             ARRAY(I,K) = - ARRAY(I,J)
110          ARRAY(I,J) = SAVE
111          I = JK(K)
             IF ( I - K ) 130, 130, 113
113          DO 120 J = 1, NORDER
             SAVE = ARRAY(K,J)
             ARRAY(K,J) = - ARRAY(I,J)
120          ARRAY(I,J) = SAVE
130          CONTINUE
140          RETURN
     END
```

APPENDIX - D

```
INPUT "PRINTER OR VDU";Z$
IF Z$ = "V" THEN  VS = 3 : GOTO 130
IF Z$ = "P" THEN  VS = 4
OPEN 1,VS : CMD 1
DIM  E(16),T(16),C(16),R(16),Q(50,16),A(50),B(50),S(16),W(50,16
DIM Q$(50,16),W$(50,16),Y(28)
PRINT#1,CHR$(1) SPC(8)"SLOWING DOWN DENSITY" : PRINT#1
PRINT#1, SPC(3)" LITHIUM SAMPLE"
PRINT#1,"********************" : PRINT#1 : PRINT#1
READ  N,N1
B = 0
M = .119 : E0 = 1
FOR  J = 1 TO  N1 : READ  E(J) : NEXT  J
FOR  J = 1 TO  N1 : READ  C(J) : NEXT  J
NN = 5.4E8 : T2 = 0 : S(J) = 0
FOR  J = 1 TO  N1
R(J) = (E0/E(J))
T(J) = (360.39*R(J)/C(J)↑2)
T2 = T2+T(J)
PRINT#1
PRINT#1,J":AGE="T2"CM↑2"
PRINT#1, SPC(4)"ENERGY ="E(J)"MEV"
PRINT#1
PRINT#1, SPC(5)"X" SPC(12)"Q*1E6"
PRINT#1, SPC(3)"----------------------"
FOR I = 1 TO N : X = I/2
A(I) = NN*EXP(-(X↑2)/(4*T2))
B(I) = SQR(4*3.1415926*T2)
Q(I,J) = (A(I)/B(I))/1E6
S(J) = S(J)+Q(I,J)
Z = X : GOSUB 1000 : X$ = Z$ : PRINT#1,X$;
Z = Q(I,J) : GOSUB 1010 : Q$(I,J) = Z$ : PRINT#1, SPC(5)Q$(I,J)
NEXT I
PRINT#1, SPC(3)"**********************"
PRINT#1, SPC(30)"S(J)="S(J)
NEXT J
PRINT#1 : PRINT#1
PRINT#1,CHR$(1) SPC(15)" AFTER NORMALIZATION " : PRINT#1
FOR J = 1 TO N1
PRINT#1,"ENERGY="E(J)
PRINT#1, SPC(5)"X" SPC(6)"Q*1E6" SPC(5)"W*1E6"
PRINT#1, SPC(3)"----------------------"
FOR I = 1 TO N : X = I/2
W(I,J) = (Q(I,J)*NN/S(J))/1E6
Z = X : GOSUB 1210 : X$ = Z$ : PRINT#1,X$;
Z = Q(I,J) : GOSUB 1220 : Q$(I,J) = Z$ : PRINT#1,Q$(I,J);
Z = W(I,J) : GOSUB 1220 : W$(I,J) = Z$ : PRINT#1,W$(I,J)
NEXT I
NEXT J
READ N2,N3
PRINT#1 : PRINT#1 : PRINT#1 : PRINT#1
PRINT#1,CHR$(1) SPC(8)"TOTAL NUMBER OF NEUTRONS" : PRINT#1
PRINT#1, SPC(5)"A" SPC(9)"SOURCE" SPC(7)"AA*1E6" SPC(9)"TN" SPC
PRINT#1, SPC(4)"-----------------------------------------------
FOR K = 1 TO N2
READ X1,EF
```

```
660 PRINT#1,"X=";X1;"CM"
670 PRINT#1,"==========="
680 PRINT#1
690 FOR  L = 1 TO  N3
700 READ  X2,A,NA,XS
710 AA = (NN*EXP(-M*X2))/1E6
720 BB = (1-EXP(-M*X1))
730 FOR  I = 1 TO  NA : READ  Y(I) : NEXT I
740 DD = 213.2
750 SA = (25*3.1415926)/(DD)↑2
760 P = 0
770 FOR  I = 1 TO  NA
780 J = 9
790 U = EXP(-M*Y(I))
800 P = P+(W(I,J)*U)
810 NEXT  I
820 F1 = .95 : F2 = .94
830 TN = AA+P
840 DT = (P*1E6*SA*EF*BB*XS*F1*F2)/1490
850 Z = A : GOSUB 1720 : A$ = Z$ : PRINT#1,A$;
860 Z = P : GOSUB 1730 : P$ = Z$ : PRINT#1, SPC(4)P$;
870 Z = AA : GOSUB 1740 : AA$ = Z$ : PRINT#1, SPC(4)AA$;
880 Z = TN : GOSUB 1750 : TN$ = Z$ : PRINT#1, SPC(4)TN$;
890 Z = DT : GOSUB 1760 : DT$ = Z$ : PRINT#1, SPC(4)DT$
900 NEXT L
910 NEXT K
920 CLOSE 1,4
930 END
940 DATA 56,15
950 DATA 13.9,13,12,11,10,9,8,7,6,5,4,3,2,1,.1
960 DATA .98,1.027,1.058,1.075,1.117,1.169,1.202,1.301,1.504,1.91,2.065
970 DATA 1.833,1.56,1.418,1.054
980 DATA 1,10
990 REM ***************** 2 CM ********************
1000 DATA 2,.1,2.2,28,3,414.86,1.65,1.1,.53,2.3,30,3,360,1.65,1.1,.55
1010 DATA 2.4,35,3,257.231,1.75,1.15,.58,2.6,40,3,247.855,1.9,1.25,.6
1020 DATA .6,45,3,125.709,2,1.35,.7,2.6,50,3,72.504,2.2,1.5,.75,2.6,60,3
1030 DATA 67.338,2.7,1.9,1.05,2.6,70,3,33.194,3.8,2.75,1.52,2.6,80,3
1040 DATA 29.031,6.6,5.4,3.6,2.6,90,3,17,12.5,12.5,12.5
1050 REM ***************** 4 CM ********************:
1060 DATA 4,.1,4.5,28,7,500.47,3.8,3.3,2.75,2.25,1.65,1.1,.55,4.6,30,7
1070 DATA 408,3.75,3.25,2.75,2.25,1.7,1.2,.6,4.8,35,7,303.936,4.05,3.5,2.9
1080 DATA 2.35,1.8,1.2,.6,4.8,40,7,257.506,4.25,3.7,3.15,2.55,1.95,1.35
1090 DATA .65,4.8,45,7,135.224,4.2,3.75,3.25,2.8,2.2,1.65,.95,4.8,50,7
1100 DATA 82.6,4.45,4,3.5,3,2.5,1.95,1.15,4.8,60,7,74.632,5.1,4.7,4.3
1110 DATA 3.8,3.45,2.9,1.9,4.8,70,7,55.077,7.55,7.05,6.45,5.75,4.9,3.85
1120 DATA 2.3,4.8,80,7,23.233,12.5,10.6,10.85,11.3,12.2,12.5,12.5,4.8,90
1130 DATA 7,17.9,12.5,12.5,12.5,12.5,12.5,12.5,12.5
1140 REM******************** 6CM ********************:
1150 DATA 6,.1,6.7,28,11,513,5.8,5.25,4.75,4.3,3.75,3.35,2.8,2.35,1.8,1.3
1160 DATA .7,6.8,30,11,408.763,5.95,5.45,4.95,4.45,3.9,3.45,2.85,2.3,1.75
1170 DATA 1.2,.6,6.8,35,11,286.584,6.2,5.7,5.15,4.65,4.1,3.6,3.05,2.5,1.9
1180 DATA 1.3,.65,6.8,40,11,249.311,6.45,6,5.45,4.9,4.4,3.9,3.3,2.7,2.1,1.
1190 DATA .7,6.8,45,11,142.593,6.8,6.3,5.8,5.2,4.7,4.2,3.6,3,2.3,1.6,.85
1200 DATA 6.8,50,11,146.774,7.2,6.7,6.2,5.7,5.15,4.6,4,3.4,2.65,1.85,.95
1210 DATA 6.8,60,11,79.9,8.4,7.9,7.45,7,6.45,5.95,5.35,4.7,3.85,2.9,1.6
1220 DATA 6.8,70,11,73.236,10.4,10.1,9.75,9.4,9.1,8.7,8.4,7.9,7.2,6.4
1230 DATA 4.7,6.8,80,11,44.91,13.3,13.15,12.95,12.9,12.75,12.65,12.6,12.5
1240 DATA 12.5,12.45,12.45,6.8,90,11,33.383,12.5,12.5,12.5
1241 DATA 12.5,12.5,12.5,12.5,12.5,12.5,12.5,12.5
```

REFERENCES

REFERENCES

BETHE , H.A.
Physics Rev. 47 (1935) 747

FODERARO , A. " The Elements Of Neutron Interaction Theory "
The MIT Press (1971)

BOHR , N.
Nature , Lond 137 (1936) 344

FESCHBACH ,H. ; PORTER ,C.E. ; and WEISSKOPF ,V.F. " The Theory Of The 'Cloudy Crystal Ball' Model Is Presented In Its Original Form As A Sharp-Edged Potential Well"
Physics Rev. 46 (1954) 448

HUGHES ,D.J. " Neutron Cross Sections "
PERGAMON Press (1957)

SERBER ,R.
Physics Rev. 72 (1947) 1008

FERNBACH , H. ; SERBER ,R. and TAYLOR , T.B.
Physics Rev. 75 (1949) 1352

FESHBACH , H. ; PORTER , C.E. and WEISSKOPF , V.F. "Model For Nuclear Reactions With Neutrons "
Physics Rev. 96 (1954) 448

FESHBACH , H. and WEISSKOPF , V.F. "A schematic Theory Of Nuclear Cross Sections "
Physics Rev. 76 (1949) 1550

0] BENVENISTE , J. and ZENGER , J. "Information On The Neutrons Produced In The $T(d,n)^4He$ reaction "
UCRL - 4266 (1954)

1] GUNNERSEN , E.M. and JAMES , G. " On The Efficiency Of The Reaction $T(d,n,)^4He$ In Titanium Tirtide Bombarded With Deuterons"
Nuclear Instrument and Method 8 (1960) 173-184

2] GRANATA , L. and LAGONEGRO , M. " On the shape of a neutron beam produced by means of the $T(d,n)^4He$ reaction using a thick target and the associated-partical method "
Nuclear Instruments And Method 70 (1969) 93-97

3] BENVENISTE , J. etal " The problem of measuring the absolute yield of 14 Mev neutrons by means of an alpha counter "
Nuclear Instruments and methods 7 (1960) 306-314

4] FEWELL , T.R. "An evaluation of the alpha counting technique for determining 14 Mev neutron yields "
Nuclear instruments and methods 61(1968)61-71

5] PAULSEN , A. and LISKIEN , H. " An evaluation for cross-sections of the $T(d,n)^4He$ reaction "
EANDC (E) -144 "L" Joint Nuclear Research Centre Geel Establishment - Belgium (1972)

6] LISKIEN , H. and PAULSEN , A.
Nuclear Data Tables , Vol. 11 , No. 7 , (1973)

17] Technical Bulletin Societe Anonym de Machines Electrostateques , Grenoble , France , June (1961) .

18] BAYNHAM , D.F. , Ph.D. Thesis (1971) University of ASTON in Birmingham .

[19] TAYLOR , A. , I.E.E.E. (Inst. Elec. Electron Engrs.) ,
Trans. Nucl. Sci. NS-18 , No.3 , 79 (1971) .
[20] Technical Proposal For DYNAMITRON ACCELERATOR Model RPEA 3.0
RDI No. 67-11-1-155 Vovember 17,1967 .
[21] ENGLAND , J.B.A. ,"Techniques In Nuclear Structure Physiscs "
part I , The Macmillan Press Ltd. , 1974 .
[22] LANGSDORF ,JR A. ; LANE , R.O. and MONAHAN ,J.E.
"Angular Distributions of scattered neutrons "
Physics Rev. 107 (1957) 1077 .
[23] TAYLOR ,N.B. ; PARLCES ,W.H. and LANGENBERG , D.N.
Rev. Mod. Phys. 41 (1969) 375 .
[24] BETTS ,R.R. "Time-Of-Flight Detectors For Heavy Ions "
Nuclear Instrument and Methods 162 (1979) 531-538 .
[25] SMITH ,A.B. etal "Multi-angle Fast Neutron Time-Of-Flight
system"
Nuclear Instrument And Methods 50 (1967) 277-291 .
[26] SMITH , D. L.
Nuclear Instrument And Methods 64(1968) 157
[27] NARGOLWALLA , S.S. etal " Activation Analysis With Neutron
Generators" copy right (c) 1973 By John Wiley and Sons , Inc.
[28] MARION ,J.B. and FOWLER ,J.L. " Fast Neutron Physics " part I
copy right (c) 1963 By John Wiley and Sons , Inc.
[29] OKHUYSEN ,P.L. etal "Detection Of Fast Neutrons By The
Associated Particle Methods"
The Review Scientific Instruments Vol.29 , No 11, 1958 .
[30] WAKUTA,Y. etal " A Fast Neutron Time-Of-Flight Spectrometer With
Neutron Gamma-ray Discrimination "
Nuclear Instrument and Methods 71 (1969) 133-136 .
[31] HAOUAT ,G. ; LACHKAR ,J. etal " Measurement Of The Differential
Elastic And Inelastic Neutron scattering Cross-sections Of
Carbon From 8.0 to 14.5 Mev "
Nuclear Science and Engineering 65 (1978) 331-346 .
[32] MOSZYNSKI ,M. and BENGTSON ,B. "Status Of Timing With Plastic
scintillation detectors "
Nuclear Instrument and Methods 158 (1979) 1-31
[33] CONNEL ,K.A. Ph.D. Thesis (1972) University Of ASTON in
Birmingham .
[34] GLASGOW , D.W. etal " Shielding For Fast Neutron Scattering
Experiments Of High Sensitivity"
Nuclear Instrument And Method 114 (1974) 521-534 .
[35] HOPKINS ,J.C. etal " Shadow-Bar Design For Fast Neutron
Scattering Experiments "
Nuclear Instruments and Method 56 (1967) 175-176 .
[36] JAEGER ,R.G. etal"Engineering Compendium On Radiation
Shielding"
Vol.II , Spring-Verlag Berlin Heidelberg NY. 1975
[37] ENDF/B-VI "Data For H, Li, B, Fe, Cu, w and Pb "
[38] MUGA ,M.L. etal
Nuclear Instruments and Method 104 (1972) 605-610 .
[39] GEISSEL ,H. etal
Nuclear Instruments and Method 144 (1977) 465-468
[40] DEARNALEY ,G. and WHITEHEAD ,A.B.
Nuclear Instruments and Method 12 (1961)205-226

[41] HANSER ,F.A. and SELLERS ,B.
Review Science Instruments 41 (1970) 780
[42] Nuclear Enterprises Limited Catalogue (1970)
[43] MARION ,J.B. and YOUNG ,F.C. " Nuclear Reaction Analysis , Graphs and Tables " , North Holland , Amesterdam and Wieley ,NY 1968 .
[44] WARNER ,P.C. Ph.D. Thesis (1984) University Of ASTON in Birmingham .
[45] WHALING ,W. "Handbook der Physik " Vol.XXXIV (1930)
[46] CLYDE ,S.Z. "A Method For Energy-Loss and Range calculations Based on Empirical Approximations" Nuclear Instruments and Method 120 (1974) 125-129
[47] BROOKS ,F.D. "Development of Organic Scintillators " Nuclear Instruments and Method 162 (1979) 477-505 .
[48] BIRKS ,J.B. "The Theory and Practice of Scintillation counting" Pergamon Press 1964 .
[49] TOMS ,M.E. "A Computer Analysis to obtain neutron Spectra From An Organic Scintillator ." Nuclear Instruments and Method 92 (1971) 61-70
[50] SWARTZ ,C.D. and OWEN ,G.E. "Recoil Detection In Scintillator " Fast Neutron Physics part I (eds. J.B. Marion and J.L. Fowler Interscience pub. , Inc. , New York 1960 .)
[51] LAMARSH ,J.R. "Inroduction to Nuclear Reactor Theory" Addison-Wesely Publishing Co. Inc. (1966)
[52] HUGEHES ,D.J. "Neutron Cross-Sections " BNL-325 Vol. II , third Ed. 1976
[53] BIRKS ,J.B. Proc. Phys. Soc. A64 (1951) 874-877
[54] PRESCOTT ,J.R. and RUPAAL ,A.S. "The Specific Fluorescence Of Plastic Scintillator NE102 " Can. j. of Physics 39 (1961) 221
[55] BIRKS ,J.B. Physics Review 86 (1952) 569
[56] CHOU ,C.N. Physics Review 87 (1952) 367 and 904
[57] WRIGHT ,G.T. Physics Review 91 (1953) 1282
[58] RICHARD,R.and MADEY ,R. "Range Energy Tables " UCRL-2301 (1954)
[59] ANDERSON ,H.H. and ZIEGLEER ,J.F. (1977) "Hydrogen Stopping power and Range in all Elements " Pergamon Press 1977 Vol.3
[60] GOODING , T. J. and PUGH , H. G. Nuclear Instruments and Method 7 (1960) 189
[61] GROOM , D.E. etal " A Note on the Relationship Between Energy Loss And Light Output For Plastic Scintillator NE102 " Nuclear Instruments and Method 46 (1967) 301-304
[62] EVANS ,H.C. and BELLAMY ,E.H. Proc. Phys. Soci. 74 (1959) 483-485
[63] FLYNN ,K.F. etal Nuclear Instruments and Method 27 (1964) 13-17
[64] GARG ,J.B. "A Fast Neutron TOF Spectrometer" Nuclear Instruments and Method 6 (1960) 72-82
[65] KNOLL , G.F. " Radiation Detection and Measurements " John Wiley and Sons 1979

[66] STEWART , L. , etal " Hydrogen free Atom Cross-Sections "
LA-4574 October 1970
[67] ALLENBY ,K. Ph.D. Thesis (1974) University Of ASTON In Birmingham
[68] MUKOYAMA , T. "Fitting Of Gaussian To Peaks By Non-iterative Method ."
Nuclear Instruments And Method 125 (1975) 289-291
[69] KOKTA , L. " Determination Of Peak Area "
Nuclear Instruments And Method 112 (1973) 245-251
[70] WONG ,C. etal
Nuclear Physics 33 (1962) 680
[71] MERCHEZ , F. etal
Proc. First Int. Conf. Nuclear Data for Reactors , Paris . October 17-21 , 1966 , Vol. I p393 IAEA (1966) .
[72] ARMSTRONG , A.H. etal
Nuclear Physics 52 (1964) 505 .
[73] HYAKUTAKE , M. etal
J. Nuclear Sicence and Tech. 11(10) (1974) 407-421
[74] HOGUE , H.H. etal
Nuclear Sicence and Engineering 69 (1979) 22-29
[75] CONLON ,T.W.
AERE - R7166 1972 .
[76] PENDLEBURY , E.D.
AWRE Report No. 0-61/64 (1964) .
[77] BONAZZOLA ,E.D. etal " The F(n,n') Reaction At 14 Mev "
Nuclear Physics 86 (1966) 378-384
[78] CLARK , R.L. and PERRIN , P. " Elastic and Inelastic Scattering Of 14.1 Mev neutrons from Fluorine "
Nuclear Physics A147 (1970) 174-182 .
[79] HOLLAND , D. and COX , A.J. "Scattering of 14.1 Mev Neutrons By Potasium and Lithium"
Nuclear Physics Vol.3 , No. 10 , 1977 , p 1431-1441
[80] AL-SHALABI , B. Ph.D. Thesis (1982) , University Of ASTON In Birmingham .
[81] ANVARIAN , S.P.T. Ph.D. Thesis (1983) , University Of ASTON In Birmingham .
[82] WICK ,G.C.
Physics Review 75 (1949) 1459
[83] BEVINGTON ,P.R. " Data Reduction And Error Analysis For The Physical Science " , McGraw-Hill (1969)
[84] ENDF/B-IV data file for ^{7}Li (Mat 1272) , Brookhoven National Laboratory ; evaluation By R.J. LABAUVE , L. STEWART and M. BATTAT , LOS ALAMOS SCIN. LAB. (1974)
[85] GUANREN , S. "Measurements Of Differential 14.7 Mev neutron Scattering Cross-Sections of Lithium-7 and Beryllium"
Nuclear Science and Engineering 86 (1984) 184-190
[86] HODGSON , P.E. "Nuclear Reactions and Nuclear Structure "
Oxford University Press (1971)
[87] FU , C.Y. and PEREY , F.G.
Atomic Data and Nuclear Data Tables 16 (1975) 409-450
[88] RAYBURN , L.A.
Physics Review 116 (1959) 1157

[89] YUASA , K.
J. Physics Soc. Japan 13 (1958) 1248
[90] NAUTA , H.
Nuclear Physics 2 (1956-1957) 124-131
[91] ENDF/B-IV Data File for Pb (MAT 1288) , Brookhoven National Laboratory ; evaluation By C.Y. FU and F.G. PEREY Nov. (1974)
[92] STELSON , P.H. and ROBINSON ,R.L.
Bull. Am. Physics Soc. 7 (1962) 335
[93] COON , J.H. etal
Physics Review 111 (1958) 250
[94] GREENLEES , G.W. ; PYLE ,G.J. and TANG , Y.C. "Nuclear Matter Radii From a Reformulated Optical Model "
Physical Review 171 (1968) 1115
[95] RAROMP , { Regular And Reformulated Optical Model Program }
By G.J. PYLE
[96] BECCHETTI , F.D. and GREENLEES , G.W. " Nucleon-Nucleus Optical-Model Parameters , A>40 , E<50 Mev "
Physical Review 182 (1969) 1190-1209
[97] HOLLAND ,D. Ph.D. Thesis (1974) , University Of ASTON In Birmingham
[98] BJORKLUND , F. and FERNBACH , S.
Physical Review 109 (1958) 1295
[99] MARSHAK , R.E. "Theory Of The Slowing Down of Neutrons By Elastic Collision With Atomic Nuclei "
Review Of Modern Physics 19(3) (1947) 185-238
[100] ZWEIFEL , P.F. "REACTOR PHYSICS "
McGraw-Hill Kogakusha Ltd. (1973)
[101] GLASSTONE , S. and SESONSKE , A. "Nuclear Reactor Engineering "
Van Nostrand Reinhold co. (1967)
[102] PLACZEK ,G. "On the theory of the slowing down of neutrons in heavy substances "
Phy. Rev. 69 (1946) 423
[103] WOODS ,R.D. and SAXON , D. S.
Phy. Rev. 95 (1954) 577-578
[104] HUNT , S . E. " Fission , Fusion and The Energy Crisis "
Pergamon Press 1974
[105] CRAUN , R.L. and SMITH , D.L.
Nuclear Instr. and Meth. 80 (1970) 239
[106] FOWLER , J.L. and BROLLEY , J.E. "Monoenergetic Neutron Techniques in the 10-to-30 Mev range"
Rev. of Modern Physics (19)
[107] ALLRED , J.C. etal " The Interaction of 14 Mev neutrons with protons and deuterons "
Phy. Rev. 91 (1953) 90-99
[108] SEAGRAVE , J.D. "Recoil Deuterons Disintigration Protons "
Phy. Rev. 97 (1955) 757
[109] The University Of ASTON in Birmingham Computer Centre , 1904S Information sheet 4 , Program Curve fitting UA01 .